

Thesis

Friedrich-Alexander Universität Erlangen-Nürnberg

Helmholtz Institut Erlangen-Nürnberg

Dynamics of thin liquid film flows studied with the
lattice Boltzmann method

September 10, 2023

Stefan Zitz

Abstract

Fluid dynamics is a part of our everyday life. The governing equations describe not only large weather systems on planetary scales (10^6m) but also reach down to wetting problems on the nanometric scale (10^{-9}m). That a single theory can describe both the movement of atmospheric layers as well as the displacement of the contact line of a droplet with a diameter smaller than a micrometer (10^{-6}m) is highly non trivial and related to the scale invariant nature of flow problems.

The lubrication approximation was first thought of by Osborn Reynolds in the 19th century. He understood that a lubrication layer is essentially a thin layer of fluid between mechanical components. This thin layer offered some novelties which made it possible to simplify the Navier-Stokes equation. From that time onwards the functional formulation of the lubrication approximation, the so-called thin film equation, has shed new light on problems such as wetting, coating and printing to name but a few.

Today the thin film equation is used to understand several phenomena in nature and on the other hand to optimize various industrial applications. Insects for example need to have a water-repellent exoskeleton. Due to their size they would not be able to overcome the surface tension of water and therefore could become trapped inside a drop. In agriculture the distribution of pesticides relies on the adhesion between the pesticide's transport fluid and the plant's surface. Having a too low affinity would just wash off the pesticide, however by reducing the surface tension via so-called surfactants it is more likely that the pesticide sticks to the plant. Another application relates to the production of computer chips. The process itself is fairly complex, however at some point the yield on the wafer heavily relies on the homogeneous distribution of photoresist, and therefore on wetting.

Over the past six decades numerical methods have become more and more essential to study fluid dynamics. Culminating in a topic of research of its own called computational fluid dynamics (CFD). Not only is it used in an academic environment but also in areas that do not come to mind at first glance, e.g. computer games and animated movies. One numerical approach among the vast zoo of CFD methods is the lattice Boltzmann method (LBM). Instead of a direct simulation of the fluid's density and velocity the LBM uses a statistical approach based on the Boltzmann equation. We make use of this approach and derive a model that is capable of solving the thin film equation. The starting point is the shallow water lattice Boltzmann method. Interestingly enough with well defined approximations the shallow water dynamics can be recast to the thin film equation. This approach is tested and in agreement with known numerical and experimental results such as instabilities, droplet dynamics and dewetting.

Dewetting, i.e. the process when a liquid retracts from a surface, is extensively studied in this thesis. When it comes to dewetting one mostly ignored effect of experiments is the presence of thermal fluctuations. Theoretically this poses a different and more complex problem as the resulting equation is no longer deterministic. The resulting stochastic thin film (STF) equation can however be treated with the here

developed LBM. Including fluctuations do in fact accelerate dewetting, which is in agreement with previous studies, but can also lead to novel couplings when the substrates' wettability is heterogeneous.

Dewetting can also be addressed using a time and spatially dependent wettability. The priority program SPP 2171 of the German Research Foundation (DFG) aims to deepen our understanding of liquid-substrate interactions. Our contribution to this program is the study of so-called switchable substrates. With simple arguments it is shown that a morphological transition during dewetting can be induced. Instead of several droplets fewer rivulets are present based on the dynamics of the local wettability.

Kurzfassung

Hydrodynamik, als solches die Bewegung von Flüssigkeiten, ist ein wichtiger Teil unseres Alltags. Die definierenden Gleichungen beschreiben nicht nur die Dynamik von Wettersystemen planetarer Ordnung (10^6m), sondern auch die Benetzung fein strukturierter Oberflächen (10^{-9}m). Es ist erstaunlich, dass die Theorie der Hydrodynamik sowohl die Bewegung von atmosphärischen Schichten als auch die Verschiebung der Kontaktline eines Tropfens mit einer Größe kleiner als einem Mikrometer (10^{-6}m) beschreiben kann. Diese Eigenschaft der Skaleninvarianz macht die Hydrodynamik zu einem äußerst interessanten Forschungsgebiet.

Osborn Reynolds hatte sich bereits im 19. Jahrhundert mit der Frage der Schmiermittelreibung beschäftigt. Dabei stellte er fest, dass ein Schmiermittel einen dünnen Film zwischen den Mechanischen Komponenten bildet. Diese Tatsache, dass der Film nur eine geringe Höhe zwischen den Komponenten einnehmen konnte macht es möglich die Navier-Stokes Gleichung zu vereinfachen. Diese Lubrikationsapproximation fand ihre Anwendung in der Dünnfilmgleichung, die seit mehr als 100 Jahren neues Licht auf diese vermeintlich einfachen Probleme wirft.

Heutzutage wird die Dünnfilmgleichung genutzt, um Phänomene in der Natur zu studieren und um industrielle Prozesse zu optimieren. Insekten würden zum Beispiel in einem Wassertropfen ertrinken wenn, Sie von einem Tropfen benetzt würden. Als Antwort auf dieses Problem ist ein Insektenpanzer nur schwer benetzbar oder einfacher gesagt "wasserabweisend". In der Landwirtschaft wiederum sollten Pestizide an den Pflanzen haften und nicht einfach im Boden versickern. Ob die Pestizide an der Pflanze haften oder nicht hängt von den Benetzungseigenschaften der Trägerflüssigkeit des Pestizids ab. Um eine bessere Benetzung zu garantieren, wird mit Oberflächenspannungsreduzierenden Komponenten, sogenannten Tensiden, gearbeitet. Ein anderer industrieller Sektor, der auch noch in Zukunft wichtiger werden wird, beschäftigt sich mit der Herstellung von Computerchips. Der Prozess vom Silizium Einkristall zum logischen Schaltkreis ist hochkomplex, aber an einem Punkt der Produktion wird per Lithographie eine Struktur aufgedruckt. Dieser Schritt ist unter anderem dadurch begrenzt wie gleichmäßig sich einen bestimmte chemische Beschichtung, der sogenannte Photoresist, am Wafer verteilt hat. Ein Problem das zwar auf den ersten Blick nicht viel mit dem Verteilen von Pestiziden gemein hat, aber dessen Problemstellung auch im Gebiet der Benetzungsprobleme angesiedelt ist.

In den letzten sechzig Jahren sind numerische Methoden zur Untersuchung von hydrodynamischen Problem immer wichtiger geworden. Kulminiert ist dieser Trend in einem eigenen Forschungsfeld der numerischen Strömungsmechanik, oder colorful fluid dynamic (CFD). Aber auch außerhalb der Forschung findet die CFD ein breites Anwendungsspektrum. Zum einen werden CFD Simulationen genutzt um Flugzeugflügel oder Motoren von Kraftfahrzeugen zu optimieren, zum anderen findet CFD auch Anwendung in Filmen und Computerspielen. Eine von vielen Methoden der numerischen Strömungsmechanik ist die Gitter Boltzmann Methode (LBM), die sich der Boltzmann Gleichung der Statistischen Physik bedient. Um die Dynamik dünner Flüssigkeitsfilme mit der LBM zu simulieren bedarf es einiger Annahmen und

Erweiterungen. Ausgangspunkt für unser Model ist die LBM für seichte Gewässer (shallow waters). Mit ein paar Annahmen und etwas Algebra lässt sich das Gleichungssystem des seichten Gewässers in die Dünnfilmgleichung umformen. Das so entstandene Model wird mit bekannten Problem der Dünnfilmgleichung getestet und validiert. Diese “benchmark”-Probleme reichen von Instabilitäten über Tropfodynamik bis hin zur Entnetzung von Oberflächen.

Entnetzung wird hier verstanden als das aufbrechen eines Flüssigkeitsfilms. Anstelle einer homogenen Flüssigkeitsschicht entstehen beim Entnetzen einzelne Tropfen. Im Laufe dieser Arbeit wird Entnetzung ein immer wiederkehrendes Thema sein. Üblicherweise wird in Entnetzungsexperimenten die Rolle der thermischen Fluktuationen nicht berücksichtigt. Der hier definierte Ansatz macht es möglich, mit simplen Erweiterungen deren Effekt zu simulieren und zu klassifizieren. Die somit gewonnenen Erkenntnisse können vorherige Studien reproduzieren und teilweise ergänzen.

Entnetzung von Flüssigkeiten kann viele Gründe haben, zum Beispiel durch räumliche und zeitliche Änderungen der Benetzbartkeit der Oberfläche. Dieses Problem ist in keiner Weise trivial was sich auch darin äußert, dass die Deutsche Forschungsgemeinschaft (DFG) ein Schwerpunktsprogramm fördert welches sich unter anderem mit dieser Fragestellung widmet. Konkret beschäftigt sicher der SPP 2171 mit dem dynamischen Benetzen von flexiblen, adaptiven and schaltbaren Substraten. Deswegen findet sich in diese Arbeit auch der Themenkomplex der schaltbaren Substrate, also Oberflächen die ihre Benetzungseigenschaft durch z.B. Beleuchtung ändern. Mit einem einfachen Modell wird gezeigt, dass es möglich ist die Entnetzungsmorphologie des dünnen Films zu ändern. Anstatt von Tropfen, wie es zu vermuten wäre auf einem gemusterten Substrat, werden Bandstrukturen gebildet. Dieser bisher unerforschte Übergange zu Bandstrukturen hängt nicht nur von den schaltbaren Eigenschaften des Substrates ab, sondern auch von z.B der Oberflächenspannung der Flüssigkeit.

Prolog

My time as a student hopefully and finally ends with this work, my thesis. I started studying physics quite some time ago and honestly doing research for my doctorate feels very different from what university was before. While there are many things to write here as objective as possible, most of it is tainted with my style. Therefore I want to use this prologue as a short but to me important personal summary. Working on problems nobody has solved or thought about is hard. Creativity is an essential skill to perform research. Often it is easy to do the same over and over again, most of the time following orders is also easy. Finding my very own way to approach problems and designing computational experiments was unbelievable hard work. Not only did I do far more things wrong than right, but I also had a naive and idealistic view of science. But science is done by humans. Doing research can be fairly disappointing on the one hand but also very rewarding on the other. For me it was mostly the former and while failures or null results are an integral part of science they are rarely communicated. A situation which at least from my point of view does not improve the quality of research and in fact does inevitably lead to recurring mistakes and thus wasted effort. It is well known that most of academia's staff is showing symptoms of burnout and are exposed to constant elevated levels of stress [Gew21; Bil06; WR11; Sat+21]. I am just a PhD student, but even I felt guilty during weekends for not working and instead engaged in leisure activities. Why did I feel guilty, because projects did not work the way they should have and results did not agree with hypotheses. That put pressure on me, because whatever we do we want to see progress. If nothing adds up and you hit a dead end after another it is hard to see progress.

Of course my situation was still good, I for example didn't have to acquire funding for my position. Truth is that the situation of scientists in academia is not optimal and chain contracts are only one issue. The requirement of moving to different countries, acquiring funds and publishing research all at the same time is by all means an unhealthy one. It is also remarkable that plenty of studies showed that the situation is far from being good, yet scientist world wide accept the status quo.

While this may sound depressing, I think it is an opportunity. An opportunity to make things better, healthier and the first step is to talk openly about the situation. That is why I choose to add quotes at the start of every chapter. These quotes are not famous words from important people, they are parts of lyrics from pop songs. Songs that highlight that our society is flawed. Singing about problems such as the requirement to be perfect out of the box or the constant repression of minorities for example. I think these lyrics are quite fitting to describe the state I found myself in during the time as a student and even more so during the writing of this thesis.

Contents

1	Introduction	1
1.1	Thin Liquid Films	1
1.2	Thin film application	3
1.3	Literature Overview	6
1.4	Scientific Software	9
1.5	Outline	13
2	Theory	16
2.1	The Navier-Stokes equation	16
2.2	Shallow Water Theory	20
2.2.1	Definition	20
2.2.2	Scaling analysis	22
2.2.3	Integration along the vertical dimension	25
2.2.4	Poiseuille flow	27
2.3	Lubrication theory and thin films	29
2.3.1	Scaling and boundary conditions	32
2.3.2	Vertical integration	35
2.3.3	Linear stability analysis	36
2.4	Differences and Overlap	38
3	Method	42
3.1	Numerical Methods	44
3.1.1	Finite differences	44
3.1.2	Spectral methods	46
3.1.3	Molecular dynamics	47
3.2	The Lattice Boltzmann Method	48
3.2.1	The Boltzmann equation and macroscopic conservation equations	50
3.2.2	From continuum to lattice	53
3.2.3	Shallow water equations on the lattice	58
4	Swalbe.jl: A lattice Boltzmann solver for thin film hydrodynamics	61
4.1	Summary	61
4.2	Statement of need	62
4.3	State of the field	63
4.4	Use Case	64
4.5	Author Contribution Statement	65
4.6	Acknowledgements	65

5 Lattice Boltzmann method for thin-liquid-film hydrodynamics	66
5.1 Introduction	66
5.2 Numerical Model	67
5.3 Results	72
5.3.1 The Rayleigh-Taylor instability	72
5.3.2 A spreading droplet	75
5.3.3 A Sliding droplet	78
5.3.4 Dewetting of liquid films	80
5.4 Computational Aspects	80
5.5 Conclusions	81
5.6 Acknowledgements	81
5.7 Appendix	82
6 Lattice Boltzmann simulations of stochastic thin film dewetting	84
6.1 Introduction	84
6.2 Linear Stability Analysis of the Stochastic Thin-Film Equation	86
6.3 Thin Film Lattice Boltzmann Model	87
6.3.1 Lattice Boltzmann Method	87
6.3.2 Modelling Thermal Fluctuations	89
6.3.3 Fluid-substrate interactions: the contact angle	89
6.4 Results	90
6.4.1 Testing the stochastic term	91
6.4.2 Droplet size distributions	92
6.4.3 Rupture times and role of contact angle	93
6.4.4 Patterned substrates	96
6.4.4.1 Sine wave pattern	96
6.4.4.2 Square wave pattern	101
6.5 Summary and Conclusions	104
6.6 Acknowledgements	105
7 Controlling the dewetting morphologies of thin liquid films by switchable substrates	106
7.1 Introduction	106
7.2 Method	107
7.3 Results	110
7.4 Conclusions	115
7.5 Acknowledgements	116
7.6 Supplemental Material	117
7.6.1 Minkowski's structure metric q_2 in an extended parameter space.	117
7.6.2 Droplet shape	117
8 Conclusion and outlook	120
Bibliography	125

List of Figures

1.1	Illustrative examples of thin film flows. In (a) rain drops seem to choose random paths running down a window, during their motion they leave behind smaller drops which is called pearling. Tile (b) displays the interaction between water and a plant leaf. Drops are formed quickly and due to the curvature of the leafs surface the coalescence of droplets is enhanced. Soap bubbles are a prime example of a thin film flow, as shown in (c). A small amount of liquid is enclosed between two gas phases. Inside the film fluid is drained to the bottom of the bubble due to gravity.	2
1.2	Film dewetting of a surface in the spinodal regime. Series (a) are experimental measurements with an AFM, while series (b) is generated using a numerical approach with the same parameters taken from [Bec+03].	4
1.3	(a) Schematics of the dip coating process. A substrate is withdrawn from a fluid bath and due to capillarity and solid-liquid interactions (adhesion) some liquid adheres to the substrate. Balancing between adhesion and viscous drag most of the liquid is left in the bath. Depending on the surface tension and atmospheric pressure, evaporation can further thin the drawn film. (b) Schematics of a slot die coating process. A die is placed on top of a constantly moving foil. Through that die a liquid is pumped onto the moving foil.	5
1.4	A drawing from Osborn Reynolds on slipper bearing lubrication. The four figures are taken from Ref. [Rey86] and cropped together in a single image. In (a) surface CD is fixed while surface AB moves to the left with velocity U. The fluid between the surfaces feels the force $F = \mu \frac{U}{h}$, with h being the separation distance. The velocity profile changes uniformly from U at AB to zero at CD. Panel (b) displays the case when two parallel surfaces approach each other. The pressure acting on surface CD is shown on top of the surface. Each line between the surfaces shows the tangential forces and thus indicates the fluid velocity profile. Allowing surface AB to move to the left while surface CD approaches with the same pressure distribution as in (b) it is shown in (c). This case is a combination of (a) and (b) with non-uniform force distribution between the surfaces. The last panel (d) displays the case when the surfaces are not parallel. Surface CD is kept constant while surface AB is moved to the left. The curve on top displays the pressure the fluid exerts on surface CD.	6

1.5 (a) Equilibrium state of a dewetting thin film on a patterned substrate, i.e. droplets inside of the contact angle minima. The color corresponds to the contact angle. Yellow shows a high and blue a low contact angle, ranging from 10° to 30° . (b) Similar to the left panel a dewetting thin film on a “switchable” substrate. Due to the function that controls the contact angle field liquid rivulets are formed.	9
2.1 Schematic description of the shallow water problem. A liquid column with position of the free surface $\eta(x, y, t)$ covers a bottom topography $b(x, y)$. The liquid’s height with the addition of the elevation of the topography defines the resulting height or z-component of the free surface.	20
2.2 a) Schematic, cut through the center, velocity profile of a pipe flow with wall friction and no slip boundary condition. The flow velocity u_x can be calculated using Eq. (2.60). b) Similar case in terms of a shallow water geometry. The upper wall is replaced with a pressure free boundary while the lower wall induces friction according to a no-slip boundary condition.	28
2.3 Liquid droplet placed on a smooth substrate. The three phase contact line which is the interface between the vapor, the solid and liquid phase is displayed as thick black line.	30
2.4 Wetting behaviour for different fluid substrate interactions. If the affinity between fluid and substrate is very large the substrate is said to be fully wetting with a vanishing contact angle. Reducing this affinity, which is usually the case for real substrates, leads to a measurable contact angle and is called partially wetting. Surface treatment or complex surface structure can lead to non wetting surfaces, therefore with contact angles of close to π	32
2.5 Dispersion relation of a spinodally dewetting thin film with and without thermal fluctuations. Where $S(q)$ is the structure factor depending on the wavemode q . The dots and triangles are generated using the here presented numerical method. Full and dashed lines are the theoretical prediction based on Eq. (2.65) and its fluctuating extension, Eq. (6.29).	39
3.1 Discretization of a continuous function y (in red) along a discrete space x (x_0, x_1, x_2, \dots). Consecutive points on the x-axis are separated by a uniform distance h	44
3.2 Schematic display of how different approaches relate to different length and time scales. The finer the system is resolved the more computing resources are needed.	49
3.3 Number of lattice Boltzmann method related publications measured from 1990 to 2018 according to Ref. [Li+20]. The red bars indicate the total number of publications per year. The green, blue and lavender lines show the number of publications for the most “productive” countries, respectively China, USA and the UK.	54

4.1 Dewetting simulation on a patterned substrate, letters have a higher wettability than the rest of the substrate.	62
4.2 Coalescence of sessile droplets on a partially wetting substrate. The upper panel shows the time evolution for a single experiment (lowest surface tension). In the lower left panel we plot the evolution of the bridge height for the four different surface tensions. To the right we normalize the data with characteristic quantities and show that the bridge height grows as $\propto t^{2/3}$	65
5.1 Schematic sketch of a model system: a thin liquid film deposited on a flat substrate. The air-liquid interface is represented by the <i>height</i> $h(x, y, t)$. The characteristic thickness of the film is given by H	68
5.2 Time evolution of the free surface for the Rayleigh-Taylor instability at $\tau_{\text{cap}} \approx 50, 75, 100, 188$, corresponding to the lattice Boltzmann time steps [9000, 14000, 19000, 35000] Δt in (a) - (d) respectively. For a more clear visualization we only show a small patch of size 256×256 centered in the middle of the 2048×2048 domain. The fluctuations of earlier states still follow the linear stability analysis (See Fig. 5.3 for the power spectrum of the height fluctuations versus wavenumber).	73
5.3 Power spectrum of the height fluctuations versus wavenumber.	74
5.4 Relaxation of an out-of-equilibrium droplet. The initial state (a) is shown with a contact angle of $\theta = \pi/6$. Towards the end of the simulation (b) the droplet relaxes to the equilibrium contact angle.	75
5.5 Difference of cubed instantaneous and equilibrium contact angles, $\theta_{\text{num}}^3 - \theta_{\text{eq}}^3$, vs. capillary number Ca for a spreading droplet; the dashed line shows a linear dependence (consistent with the Cox-Voinov law). The different symbols represent different viscosities, while the dashed line is a linear function of the capillary number.	77
5.6 Time evolution of the droplet base radius of a spreading droplet; the dashed red line shows a $\tilde{t}^{1/10}$ power law (In consistence with Tanner's law). As in Fig. 5.5 different symbols refer to different viscosities. The radius clearly grows with the predicted power law until it saturates. Upon rescaling the time with τ_{cap} the curves of all three viscosities collapse into a single one.	77
5.7 Ca vs Bo for a sliding droplet: notice that a finite minimum forcing (corresponding to Bo_c) is needed to actuate the droplet. For $Bo > Bo_c$ a linear relation, $Ca \sim Bo$, is observed. In the insets we show the shape of the droplet for both, the pinned (upper left) as well as the sliding (lower right) case.	78

5.8	Time evolution of the free surface on a chemically patterned substrate on a $512 \times 512 \Delta x^2$ domain. Varying the contact angle between the letters and the rest of the substrate yields the shown dewetting pattern. The letters are more wettable than the rest. To emphasize the process we use a color gradient ranging from dark blue to light blue. Starting from a randomly perturbed film height, the fluid starts to dewet the pattern (a) and after $2400\Delta t$ the letters and a surrounding rim structure are clearly visible. In (b) at $16800\Delta t$ a depletion around the letters is already very prominent. Towards the end of the simulation (c) at $97200\Delta t$, the instability of the thin film also leads to film rupture. Holes form between the letters E, R and N.	79
5.9	Time evolution of the L_2 norm (as defined by equation (5.34)) of the x -component of the terms appearing on the right hand side of the second of equations (5.15). The plot is in log-lin scale. The panels refer to three different numerical experiments: (a) spreading droplet, (b) sliding droplet and (c) thin film dewetting. The symbols correspond to: film pressure gradient, $-h\partial_x p_{\text{film}}$, (\star); friction, $-\nu\alpha(h)u_x$, (\bullet); longitudinal dissipation terms $\nu\nabla^2(hu_x) + 2\nu\partial_x(\nabla \cdot (hu))$, (\blacktriangle).	82
6.1	Height fluctuations spectra from deterministic (circles) and stochastic (triangles) simulations at $t = 0.2t_0$ (filled symbols) and $t = 0.7t_0$ (empty symbols), on a substrate with $\theta = \pi/9$. The theoretical predictions, Eq. (6.29), are reported with solid ($\sigma = 0$) and dashed ($\sigma = \sigma_0$) lines.	91
6.2	Histograms of the droplet height distributions from the deterministic (blue, line-patterned) and stochastic (orange, dot-patterned) simulations with $\theta = \pi/9$, at $t \approx 20t_0$; the corresponding Gaussian kernel density estimations are also plotted, as a guide to the eye, with solid blue (dashed orange) curve for the deterministic (stochastic) data.	92
6.3	Time evolution of $\Delta h(t) = \max_x\{h(x, t)\} - \min_x\{h(x, t)\}$ for the athermal (bullets) and fluctuating (triangles) systems with $\theta = \pi/9$. The blue dashed-dotted line depicts an exponential fit of the data for the athermal case ($\sigma = 0$). The vertical lines mark the rupture times for the deterministic (solid) and stochastic (dotted) simulations.	94
6.4	Ratio of rupture times from athermal and fluctuating dewetting, $\chi_{\sigma_0}(\theta)$ (Eq. (6.32)), as a function of the contact angle θ . The dashed line is Eq. (6.36) for $\sigma = \sigma_0$. Inset: Rupture times τ_r normalized by t_0 (see Tab. 6.1) vs θ , for the deterministic (orange bullets \bullet) and stochastic (green triangles \blacktriangle) simulations.	96
6.5	Time dependence of the maximum wavenumber q_m for various contact angles θ and $\sigma = \sigma_0$, using $\delta = 0$. The full blue, orange and green lines correspond to theoretical curve $q_m(t)$ derived from Eq. (6.29) for $\theta = \pi/9, 5\pi/36, \pi/6$. The dashed lines show the corresponding $q_0(\theta)$. In the inset we show that the data collapse onto a single curve upon rescaling each q_m by its respective q_0	97

6.6 Space-time plot of the height field $h(x, t)$ evolution over a sinusoidally patterned substrate undergoing athermal (panel (a)) and fluctuating (panel (b)) dewetting, respectively. In panel (c) we report the contact angle profile $\theta(x)$ (Eq. (6.37))	98
6.7 Height profiles from deterministic dewetting ($\sigma = 0$) over the sinusoidally patterned substrate, Eq.(6.37) at $t = 0.26t_0$ (panel a)) and $t = 0.66t_0$ (panel b)) and corresponding spectra (panel c)). In panel c) also the initial spectrum, $S_0(q)$, is reported; the vertical lines indicate the pattern wavemode q_θ (solid) and its multiples $2q_\theta$ (dashed) and $3q_\theta$ (dashed dotted). As explained in the text, the convention $t_0 = t_0(\pi/6)$ and $q_0 = q_0(\pi/6)$ applies.	99
6.8 Height profiles from stochastic dewetting ($\sigma = \sigma_0$) over the sinusoidally patterned substrate, Eq.(6.37) at $t = 0.26t_0$ (panel a)) and $t = 0.66t_0$ (panel b)) and corresponding spectra (panel c)). In panel c) also the initial spectrum, $S_0(q)$, is reported; the vertical lines indicate the pattern wavemode q_θ (solid) and its multiples $2q_\theta$ (dashed) and $3q_\theta$ (dashed dotted).	100
6.9 Space-time plot of the height field $h(x, t)$ evolution over a square-wave patterned substrate undergoing athermal (panel (a)) and fluctuating (panel (b)) dewetting, respectively. In panel (c) we report the contact angle profile $\theta(x)$ (Eq. (6.38))	101
6.10 Panel a) and b): Space-time plots showing the evolution of the height field for athermal, a), and fluctuating, b), dewetting over the square-wave patterned substrate, in a neighbourhood of the instant of time at which the first rupture event (in the athermal case) occurred; for the sake of visualization we mark the rupture events with red bullets (●). Panel c): Distribution of times of occurrence of rupture events for the athermal ($\sigma = 0$, blue, line-patterned) and fluctuating ($\sigma = \sigma_0$, orange, dot-patterned) dewetting.	103
6.11 Spectra of the dewetting film on the $\theta^{(2)}(x)$ pattern, Eq.(6.38), at $t = 0.1t_0(\pi/6)$, with ($\sigma = \sigma_0$, ▲) and without ($\sigma = 0$, ●) thermal fluctuations. The vertical lines indicate the substrate wavemode q_θ (solid) and its multiples $2q_\theta$ (dashed), $3q_\theta$ (thin dashed-dotted) and $7q_\theta$ (thick dashed-dotted).	104
7.1 Stationary film thickness field ($t > t_0$) showing the formation of droplets. The color map indicates the contact angle pattern (Eq. (7.3) with $v_\theta = 0$), with lower (higher) values coded in light blue (yellow).	109
7.2 Rupture times, τ_r , as a function of the pattern wavelength λ , for $v_\theta = 0$ (●) and $v_\theta = 20v_0$ (★). The continuous and dashed lines indicate the linear, $\sim \lambda$, and quadratic, $\sim \lambda^2$, scaling laws, respectively.	111

- 7.3 MAIN PANEL: Time evolution of the height fluctuations, $\Delta h(t)$, during the dewetting process on the patterned substrate given by Eq. (7.3) with $v_\theta = 0$ and $\lambda = 512h_0$ (blue circles), $\lambda = 256h_0$ (orange squares) and $\lambda = 170h_0$ (green stars). The dashed lines indicate the geometrically expected values of the droplet height h_d , assuming monodispersity and a perfect spherical cap shape. INSET: Number of droplets, $N(t)$, as a function of time. The three horizontal dashed lines indicate the number of minima of Eq. (7.3), which is $2\left(\frac{L}{\lambda}\right)^2$. In the insets, we display snapshots of the stationary droplet states as grey-scale images of the film thickness field, $h(\mathbf{x}, t)$ 112
- 7.4 Time evolution of the second order Minkowski structure metric, $q_2(t)$ (see text for details), for different Γ values, on a substrate with pattern wavelength $\lambda = 256h_0$. The grey-scale insets supply snapshots of the film thickness field associated to the various curves. 113
- 7.5 MAIN PANEL: Rivulets life-times, τ_{riv} , for various Γ values. The dashed line is plotted as a guide to the eye to highlight the logarithmic dependence, in agreement with the theoretical prediction, Eq. (7.6). INSET: Height fluctuations, $\Delta h(t)$, vs time, computed along the rivulet axis, for three different Γ values. 114
- 7.6 LEFT PANEL. Minkowski's structure metric q_2 for three different wavelengths $\lambda = 64h_0$, $\lambda = 128h_0$ and $\lambda = 256h_0$ (as in figure 4 of the main text) and for $\Gamma = 1.5$ (all other parameters are as in the main text). The time interval during which $q_2 \approx 1$ signals the emergence of rivulets, also for $\lambda = 64h_0$ which is comparable with the spinodal wavelength $\lambda_s \approx 70h_0$. RIGHT PANEL. Comparison of the Minkowski's structure metric q_2 for $\delta\theta = 5^\circ$ and $\delta\theta = 10^\circ$, $\Gamma = 15$ and $\lambda = 256h_0$ 117

1 Introduction

So kaputt kriegst du mich nie, das schaff ich nur ganz alleine

Von Wegen Lisbeth

1.1 Thin Liquid Films

Thin liquid films appear in multiple forms. We find them in ordinary situations such as washing our hands, where a thin water layer adheres to our skin. Another example can be found inside fully automatic coffee machines. In the inner tubs of these machines coffee grounds are mixed with hot water to brew coffee. Small amounts of this mixture stays inside the tubes leading to the growth of a so called biofilm, making it necessary to clean them regularly. Of course, some thin film phenomena will be explained in a more detailed manner throughout this thesis. A visual representation of some thin film flows can be found in Fig. 1.1.

To describe thin film problems, however, one has to start somewhere. And the starting point for me and this thesis was to learn about the governing equations of fluid dynamics. Those equations are called the Navier-Stokes equations and they resemble the dynamics of a fluid constraint due to several symmetries [Nav23; Sto42], e.g. conservation of mass and momentum. Solving these equations in a strict mathematical manner, therefore showing existence and smoothness of a solution is an elusive quest. Although being around for roughly two centuries this equation¹ is one of the seven problems which are considered to be worth a million dollars when solved. The collection of these problems is called “Millenium problems” and the Navier-Stokes equation poses one of the six unsolved problems. A quality that differentiates physics from mathematics is the understanding of an approximation. While it is true that we can not strictly solve the Navier-Stokes equation, we still have a rather good understanding due to well working approximations. Helping this statement is the constant innovation in computing techniques and, more so, computing hardware. Todays algorithms are able to *brute force* an approximate solution to a wide class of problems. Some examples to be named are the air flow around an airfoil or the catamaran boat structure to reduce drag. The main topic of my work, however, is the dynamics of thin liquids film which admits a crucial simplification to the Navier-Stokes equation.

¹Strictly speaking the Navier-Stokes equation is a momentum equation, however it is often accompanied with an continuity equation



Figure 1.1: Illustrative examples of thin film flows. In (a) rain drops seem to choose random paths running down a window, during their motion they leave behind smaller drops which is called pearling. Tile (b) displays the interaction between water and a plant leaf. Drops are formed quickly and due to the curvature of the leaf's surface the coalescence of droplets is enhanced. Soap bubbles are a prime example of a thin film flow, as shown in (c). A small amount of liquid is enclosed between two gas phases. Inside the film fluid is drained to the bottom of the bubble due to gravity.

Nevertheless it should be noted that theoretical and computational fluid dynamics (CFD) is by all means a complex but also a vibrant and constantly evolving field.

Generally there are three paths to study the dynamics of thin liquid films. One can work with the partial differential equations and derive the dynamics from them. This is the theoretical approach which uses analytical calculus to derive solutions. On the other hand it is possible to study fluid dynamics with experiments. Studying thin film flows by experiment can be a tedious task. Although the experimental system is quite approachable, a thin liquid layer on a substrate, the devil lies in the details. Preparation of films with uniform thickness of only a few nanometers is not a trivial task. Measurements are often a series of images with frame rates that allow to document dynamics in the region of $\approx 10^{-5}$ seconds. This series of images or other control parameters allow then to derive results from observations. Both however, theory as well as the experiment, have shortcomings. Theoretical assumptions can be wrong or the resulting system of equations can be too complex to be solved. Experiments often do not allow for the very fine grained control and independent change of different parameters. The third approach, which is used throughout this thesis lies in between the experiment and a purely theoretical one. Numerical modelling or computational fluid dynamics allows to approximate the complicated partial differential equations while also allowing for fine grained parameter studies.

To study thin films and in the end to write this thesis I had to broaden my understanding of (numerical) modelling. Which solver, algorithms and simplifications

are used in common fluid dynamic research? How do they compare with each other and which of those are relevant for the model I used and developed? I had to learn about algorithms and numerical techniques and among them I focused on the lattice Boltzmann method(LBM) [CD98; HL97; GZS02; Krü+17]. But I also learned how approachable the thin film research can be. Whenever some liquid is pushed onto a dry surface, for example watercolor on a white canvas, thin film theory can help to shine light on the distribution of paint [Thi14; ODB97; Edw+16]. At some point in our life most of us watched rain drops run down a transparent window [Wil+17], as shown in Fig. 1.1a. The question of why a drop chooses its very own path has a lot to do with the window's surface topology and the three phase contact line (TPC) of the droplet [CB44; Suz+08; LX15]. Why droplets form at all, e.g. after a foggy morning can be studied in the framework of the thin film equation as well [Zha+15; Shi+18]. Although these phenomena happen in many situations their theoretical understanding is far from being complete. Just to highlight one of the above-mentioned situations, the wetting of a dry surface is a highly sophisticated problem. Using the thin film equation as a mathematical model comes short in explaining the wet-dry transition. Even worse, to move the liquid on top of a dry surface one would need an infinite amount of energy. This has to do with boundary conditions and is called the *Huh-Scriven paradox*, which states: "Not even Herakles could sink a solid if the physical model were entirely valid" [HS71]. In fact, the quote has to be understood in two ways. First and foremost, the thin film equation is rather a powerful tool in modelling a lot of fluid dynamics problems. Second is the criticism on the rough approximations, i.e. about the *no-slip* boundary condition, which requires a vanishing flow velocity at the substrate. Of course, nature finds a way around and does not use infinite amounts of energy to make a droplet slide. In the end the *no-slip* boundary condition is just a model. Definitely one of the better models, but one that comes short of explaining wetting sufficiently well.

In the following chapters of this thesis I discuss what kind of problems can be modelled with approaches similar to the thin film equation. Showing how broad the use cases are and where possible extensions can lead to. Having these use cases, both academic and industrial, is of utmost importance to justify the further development of thin film models. Following this short illustrative part will be, of course, the introduction of the mathematical models with their partial differential equations (PDE). However, this is nothing more than an efficient way of describing the problem. Strictly speaking mathematics as well as algorithms serve as tools not as the goal of this thesis. Therefore, the **KISS** concept, keep it simple stupid, is one core concept that is used throughout. Most mathematical models are accompanied with explanatory figures.

1.2 Thin film application

Applications of the thin film equation cover a wide range of use cases. There is for example the problem of pesticide distribution in agriculture, a problem that requires that the pesticide sticks to the plant. From a medical perspective, our lung and in

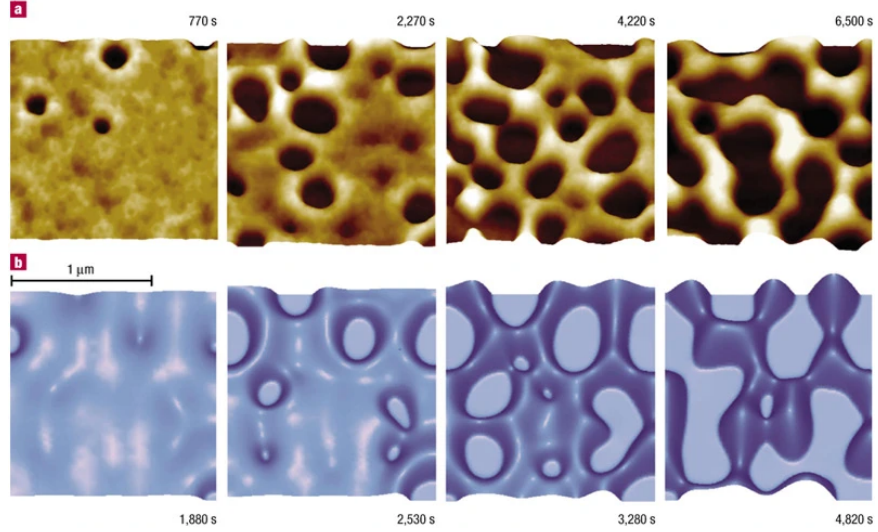


Figure 1.2: Film dewetting of a surface in the spinodal regime. Series (a) are experimental measurements with an AFM, while series (b) is generated using a numerical approach with the same parameters taken from [Bec+03].

particular the alveoli need to be covered with a thin film with a well defined concentration of biological surfactants [Her+15]. Certain disease inhibit the surfactant production and therefore threaten partial or full collapse of the lung [Gro94].

Coatings of surfaces is one of the problems that has been scientifically investigated for the last few decades. There are various ways to coat a surface with arbitrary kinds of liquids. What is common to all of them is the fact that the process heavily relies on the affinity between the to be coated surface and the coating agent [Bon+09]. If this affinity is too small the coating is unstable and therefore making the film prone to wrinkling [da +99] or eventually even rupture [ODB97; CM09; Bec+03], as shown in Fig 1.2.

For different length scales (m, cm, mm) and for different materials (metals, glasses, polymer compounds) there exists different coating approaches. The industrial coating process of a five by five meter aluminium plate differs significantly from the process to coat a millimetric biological sensor. Among the various coating approaches one is the so called dip coating, as displayed in Fig. 1.3(a). Much like the name suggests the to be coated object is dipped into a reservoir of coating liquid [Scr88; Dar+00; Gro11]. While the process itself is straightforward the *art* of dip coating is far from being trivial, meaning that this process requires tight tolerances on extraction velocity, material parameters and if possible a vibration free extraction.

From a theoretical point of view this problem has first been addressed by Landau and Levich [LL88] as well as Derjaguin [Der93]. In their fundamental work they derived two limits concerning the dynamics of the film during the extrusion. The low extrusion velocity limit assumes that gravity and as such inertia is small and can be neglected, at least for a simple plate geometry. The resulting equation leads to a balance between capillary and viscous forces. The film that is drawn with the object is

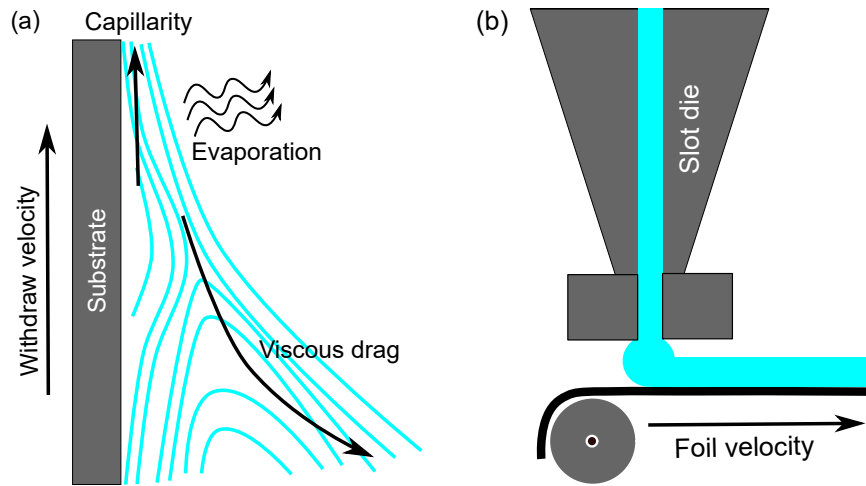


Figure 1.3: (a) Schematics of the dip coating process. A substrate is withdrawn from a fluid bath and due to capillarity and solid-liquid interactions (adhesion) some liquid adheres to the substrate. Balancing between adhesion and viscous drag most of the liquid is left in the bath. Depending on the surface tension and atmospheric pressure, evaporation can further thin the drawn film. (b) Schematics of a slot die coating process. A die is placed on top of a constantly moving foil. Through that die a liquid is pumped onto the moving foil.

usually very thin and the resulting meniscus between the object and the fluid reservoir is in size proportional to the capillary length. In fact the thickness of the coating film is roughly given as $h_\infty \propto l Ca^{2/3}$, where l is the capillary length and Ca the capillary number. The capillary number Ca is one among many non-dimensional numbers in fluid dynamics. It compares viscous drag with surface tension, whereas the capillary length l is a length scale that separates between gravity and capillary driven dynamics. This can be understood simply by looking at droplets. As long as the volume is small the droplet will form a spherical cap. If the volume becomes too large, a paddle will form with a distinct difference in shape from a spherical cap, because gravity can no longer be neglected. In the converse limit of high extrusion velocity the capillary forces become subdominant. Therefore viscous forces are being balanced with gravity. Using the same scaling argument as before the coating thickness can be approximated with $h_\infty \propto l Ca^{1/2}$. Clearly these two regimes show that the extrusion velocity of the coated object has a significant impact, assuming that the surface tension and viscosity are constant parameters.

In case of die or slot die coating the to be coated object is not immersed into a reservoir of coating liquid. Instead the coated material is usually an elastic foil which moves with constant velocity under a die. A film is created because the coating fluid is pumped through the die which is placed on top of the foil with some distance d . Similar to the illustration in Fig. 1.3(b), a film is drawn due to balance between capillary and viscous forces. The thickness of the resulting film however does not

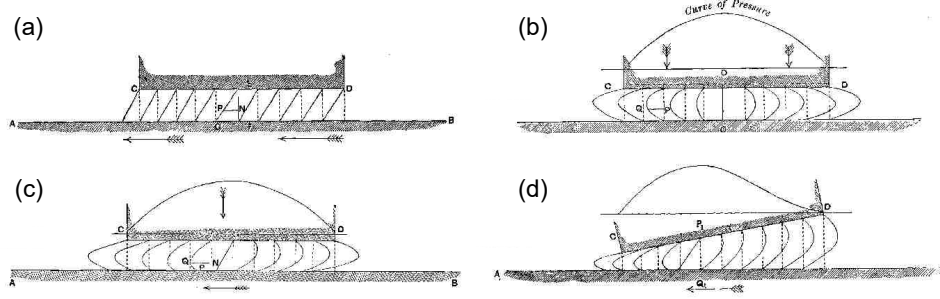


Figure 1.4: A drawing from Osborn Reynolds on slipper bearing lubrication. The four figures are taken from Ref. [Rey86] and cropped together in a single image. In (a) surface CD is fixed while surface AB moves to the left with velocity U . The fluid between the surfaces feels the force $F = \mu \frac{U}{h}$, with h being the separation distance. The velocity profile changes uniformly from U at AB to zero at CD. Panel (b) displays the case when two parallel surfaces approach each other. The pressure acting on surface CD is shown on top of the surface. Each line between the surfaces shows the tangential forces and thus indicates the fluid velocity profile. Allowing surface AB to move to the left while surface CD approaches with the same pressure distribution as in (b) it is shown in (c). This case is a combination of (a) and (b) with non-uniform force distribution between the surfaces. The last panel (d) displays the case when the surfaces are not parallel. Surface CD is kept constant while surface AB is moved to the left. The curve on top displays the pressure the fluid exerts on surface CD.

depend on gravity in this case. Ruschak showed that similar to the low extrusion velocity limit of the dip coating problem the film thickness after die coating can be approximated using $h_\infty = d Ca^{2/3}$ [Rus76].

These two examples highlight an important behaviour. The solution consists of some variable, here the capillary number, that scales with a well defined exponent, e.g. 2/3 in the low and 1/2 in the high extrusion velocity scenario. These results can be addressed as dimensional analysis, a rather fancy word for matching dimensions on both sides of the equation. In the end the height or thickness needs to be of the dimension of a length. They often support so-called self similar behaviour, meaning under change of one or more parameters it is possible to collapse data in a master curve. Another dynamic problem that exhibits self similar behaviour is droplet coalescence, which is shortly discussed in Chapter 4 and liquid lens coalescence [Hac+20].

1.3 Literature Overview

Fluid dynamics in general is mathematically described by the Navier-Stokes equation [Nav23; Sto42]. Interestingly, this equation was not the starting point for the

lubrication approximation. Only in 1886, more than half a century after Navier's derivation, Osborn Reynolds started looking into a mechanical problem. He was the first to work on the dynamics of a slider bearing, as shown in Fig. 1.4. The idea of the slider bearing is to reduce the wear of moving mechanical components due to a lubricating fluid in Reynolds' case this fluid was olive oil [Rey86]. Within this work Reynolds developed what is called today the lubrication approximation. Instead of solving the problem in all its glory, Reynolds derived that due to constraints the problem can be simplified. The first constraint is the fact that the film's thickness H is much smaller than its lateral extension L and therefore $\varepsilon = H/L \ll 1$. Besides this ratio the liquid's inertia can be neglected as the acceleration of the fluid is slow. Variations along the liquid interface are smooth and thus the gradient $|\partial h/\partial x_i| \ll 1$ for both lateral dimensions. This clean and novel deduction dates back already to the year 1886 and will be further discussed in Chapter 2.

Since the 19th century the theory of lubrication has gained a lot of attention and got extended to account for more complex problems. Over time, it became clear that problems such as wetting and capillarity can be studied within this framework [de 85; ODB97; CM09]. To this end the term "thin film equation" was introduced, which is nothing more than taking the assumption of the lubrication approximation and removing the upper wall of Fig. 1.4. A thin film is therefore a liquid layer with a free liquid/vapour interface and the thin film equation is an evolution equation for a film thickness. It is possible to derive one more model based on the lubrication approximation which is the viscous sheet model, as the name suggests this model describes a liquid layer with two free interfaces [SB09].

By now it should be clear that contact line motion and thus wetting strongly depends on the affinity between liquid and solid. The DLVO potential is one potential which allows to account for these interaction forces [V41; Ver]. DLVO is an acronym from the names of the four scientists Derjaguin, Landau, Verwey and Overbeek who developed this theory. Based on the theory one can derive an interaction potential which was used to understand the stability of colloidal suspensions, however for thin film theory it offers a quantification of the disjoining pressure [ODB97; Pes+19; ML13; DKB00]. Pierre-Gilles de Gennes, who was awarded with the Nobel Prize in physics in 1991 for his seminal work on soft matter physics and his students were ones of the first who understood that "*dirty*" soft matter physics can be useful in understanding thin film problems [de 85; de 02; dBQ04]. The term dirty in the above sentence is an expression that de Gennes used to distinguish soft matter systems from pure gas, liquid or solids. He and his students developed the theoretical tools to derive forces and potential and created the term "soft interface". A soft interface is for example the surface of a thin film, because it is deformable and feels interaction with both the gas phase above and solid phase below [dBQ04]. De Gennes not only found the soft matter field, but also made large contributions to our understanding of wetting, interface dynamics and among other things liquid crystals.

Of course, by the end of the 20th century there were already some yet unexplained experimental findings associated to the thin film equation, e.g. the spectrum of capillary waves [VO68]. While the spectrum was quickly connected with thermal fluctu-

ations it wasn't an easy challenge to find a consistent theoretical description. From a theoretical point of view one has to account for the stochastic nature of thermal fluctuations. The entry point for this problem is not the Navier-Stokes equation but the Landau-Lifshitz Navier-Stokes (LLNS) equation [LL13]. While the mass flux is conserved at all times, heat transfer can violate Fourier's law at molecular scales [BGW07]. Landau and Lifshitz derived a consistent stochastic stress term that accounts for these fluctuations and they added it to the Navier-Stokes equation. Their stochastic term has zero mean, therefore the fluctuations do not create or destroy energy, and covariance proportional to thermal energy and viscosity. The stochastic thin film equation is then, again, derived from the LLNS equation by integration along the minor dimension, usually considered the vertical dimension. This step however poses a hard problem, because the stochastic stress tensor in principle depends on the vertical dimension. Grün and coworkers found an elegant way to circumvent the problem with a single multiplicative Gaussian term [GMR06; MR05; Fet+07b; ZSL20; ZSL19; Nes+15]. This idea will be revisited in Chap. 6. Around the same time Davidovitch et al., came up with a similar form for the stochastic thin film equation, studying the spreading of a droplet [DMS05]. The addition of a Gaussian noise term made it therefore possible to reproduce the observed capillary wave spectrum and explain the difference in spreading behaviour. A further impact of this term was the reduction of rupture times for spinodal dewetting thin films [GMR06; Fet+07b]. Becker et al. pointed out that the classical thin film equation comes short in the prediction of the experimentally measured rupture times [Bec+03]. In fact the rupture time is overestimated by the classical thin film equation, adding however thermal fluctuations do lead to decreased rupture times [Dur+19; Sha+19].

Additions of complex dynamics on top of the partial differential equation that defines the thin film problems is not limited to thermal fluctuations. On the one hand it is possible to add degrees of freedom to the fluid. For example one can study the effect of non-Newtonian shear behaviour [ZL05; Mye05]. Non-Newtonian liquids have a different response to stress than e.g. water. A short discussion about shear thickening, thinning liquids, such as toothpaste, follows in Chap. 2. Other than the liquids' rheology it is possible to include arbitrary concentration fields and introduce Marangoni-like flows [SBA05; Her+15; SWB04]. Thermal fluctuations pose another addition of complexity as shown above [GMR06; MR05; DMS05; ZSH21].

On the other hand the substrate can be e.g. chemically or topographically patterned. A modified substrate can lead to a very different understanding of wetting behaviour as shown in Refs. [CB44; WBS08]. Several research programs revolved around wetting, capillarity and the thin film equation. Within Europa the German Research Foundation (DFG) funded the priority program 1052: "Wetting and Structure Formation" from 1998 to 2004. Karin Jacobs as project leader, one particularly interesting outcome was the fundamental work about dewetting morphology which was carried out by Becker et al. [Bec+03]. Recently, in 2019, the DFG funded another priority program on wetting, called priority program 2171: "*Dynamic wetting of flexible, adaptive and switchable surfaces*". The goal of this program is to enlarge the understanding concerning the dynamics of thin liquid films on complex

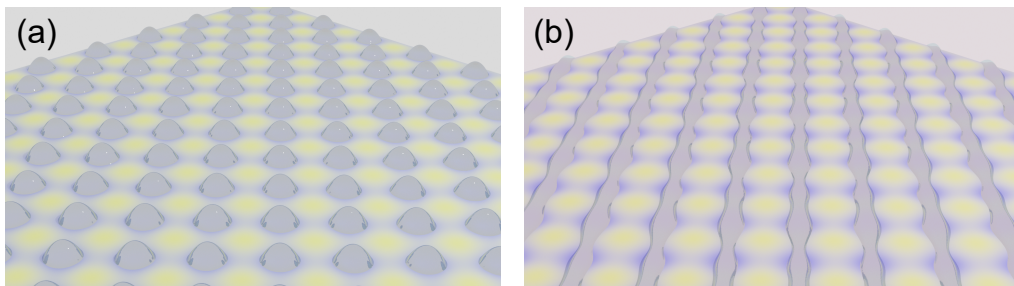


Figure 1.5: (a) Equilibrium state of a dewetting thin film on a patterned substrate, i.e. droplets inside of the contact angle minima. The color corresponds to the contact angle. Yellow shows a high and blue a low contact angle, ranging from 10° to 30° . (b) Similar to the left panel a dewetting thin film on a “switchable” substrate. Due to the function that controls the contact angle field liquid rivulets are formed.

substrates. Complex substrates can for example be substrates with grafted polymer brushes [TH20]. These brushes can swell somewhat similar to a sponge, allowing for special wetting and dewetting behaviour on such substrates. One treatment the substrate to generate a self-cleaning superhydrophobic surface similar to the lotus leaf [Li+21; Won+20]. Picking up the example of the lotus leaf, it is not necessary that the substrate is stiff. In fact most organic structures are not as stiff as a silica substrate (or the glass of a window), therefore wetting of soft materials is as well considered in this priority program [AS20; AM21; CKB11]. More so with special surface treatment it is possible to control the substrates surface chemistry [XH10; WSJ07]. These stimuli responsive substrates are collected under the umbrella of the term *switchable substrates*. Allowing for the dynamic control of the substrates wettability with e.g. light sources [ION00; Sek18]. This opens up a new avenue for microfluidic devices. In Chap. 7 we discuss the influence a switchable wettability can have on the dewetting of a thin film. In fact the switching can induce morphological transitions as depicted in Fig. 1.5.

1.4 Scientific Software

The way thin liquid films are studied in this thesis is by using analytical models for computer simulations. Therefore I build and use software to run numerical experiments. Software is a central part of our society. The interaction with an operating system, the quick information distribution over emails and the web calls via e.g. Zoom have become standard rituals of our work life (because due to Corona we had to change the way we usually interact with people). Most of the time these applications work. When they do not work it induces stress², because we rely on them and

²Just the outage of a computational infrastructure for running simulations lead repeatedly to elevated levels of stress.

yet have barely any control.

While it is easy to say that “*software should work*” it is hard to guarantee. The complexity of writing good source code and working applications is at least comparable to that of a scientific problem. In fact, good software has become so complex that the workforce of a huge margin of employees of a company can be used up on a problem as “simple” as a search engine. To make it possible to work in cooperation at this scale it is necessary to use so called *best practises* and *style guides* [Som15]. Such style guides could for example define how to add and test new functions.

Scientific software is often seen as a secondary or by-product of research and sadly often threaded that way. In contrast to the peer review process for scientific findings and publications, software that generated scientific results is rarely tested by reviewers. While there are high standards to industrial software, e.g. Ansys Fluent [Mat22], these standards are quite low for the average scientifically developed source code. This however is fairly troubling for two reasons.

Software or source code is prone to bugs because it is a creative process. One approach to overcome the issues of bugs is the so called test driven development (TDD) approach [Bec03]. The simple idea is that, whenever a function is written it is accompanied with one or more test cases. To illustrate this idea, let’s discuss an example written in Julia:

```
function add(a, b)
    return a + b
end

@test add(5, 3) == 8
```

The function **add** returns the value of variable *a* plus variable *b*. Below the definition is a test, that passes if $5 + 3 = 8$ and fails if this not the case. At first glance the test does not add any value, but at second thought one can imagine a scenario where *a* and *b* are complex numbers, or even worse where their type is not numerical. The misuse of the simple function **add**, could in principle break a program. Debugging of this situation may be straightforward, but with a test one knows exactly which function returns an error. A more specific example to this thesis is collision operation in the shallow water lattice Boltzmann method. On a two dimensional grid where each point has eight neighbours the function reads:

```
function BGKandStream!(state::LBM_state_2D, sys::SysConst)
    # All distribution functions
    fe0, fe1, fe2, fe3, fe4, fe5, fe6, fe7, fe8 = viewdists(state.feq)
    ft0, ft1, ft2, ft3, ft4, ft5, ft6, ft7, ft8 = viewdists(state.ftemp)
    fo0, fo1, fo2, fo3, fo4, fo5, fo6, fo7, fo8 = viewdists(statefout)

    omeg = 1-1/sys.tau

    # Collision for the nine populations
```

```

# Zeroth, no forcing!
fo0 .= omeg .* ft0 .+ 1/sys.tau .* fe0
# Straight ones, force correction is 1/3, 3*1/9
fo1 .= omeg .* ft1 .+ 1/sys.tau .* fe1 .+ 1/3 .* state.Fx
fo2 .= omeg .* ft2 .+ 1/sys.tau .* fe2 .+ 1/3 .* state.Fy
fo3 .= omeg .* ft3 .+ 1/sys.tau .* fe3 .- 1/3 .* state.Fx
fo4 .= omeg .* ft4 .+ 1/sys.tau .* fe4 .- 1/3 .* state.Fy
# Diagonal ones, force correction 1/24 -> 3/2*1/36
fo5 .= omeg .* ft5 .+ 1/sys.tau .* fe5 .+ 1/24 .* (state.Fx .+ state.Fy)
fo6 .= omeg .* ft6 .+ 1/sys.tau .* fe6 .+ 1/24 .* (state.Fy .- state.Fx)
fo7 .= omeg .* ft7 .+ 1/sys.tau .* fe7 .- 1/24 .* (state.Fx .+ state.Fy)
fo8 .= omeg .* ft8 .+ 1/sys.tau .* fe8 .+ 1/24 .* (state.Fx .- state.Fy)

# This is the streaming step with implicite periodic boundarys
circshift!(ft0, fo0, (0, 0))
circshift!(ft1, fo1, (1, 0))
circshift!(ft2, fo2, (0, 1))
circshift!(ft3, fo3, (-1, 0))
circshift!(ft4, fo4, (0, -1))
circshift!(ft5, fo5, (1, 1))
circshift!(ft6, fo6, (-1, 1))
circshift!(ft7, fo7, (-1, -1))
circshift!(ft8, fo8, (1, -1))

# Overwrite fout with ftemp
statefout .= stateftemp
return nothing
end

```

What is going on inside this function is not trivial to understand. To quickly summarize it, there is a data structure which called state who's fields represent the fluids state. The distribution functions, ft and fe as well as the forces acting on the fluid are used to update the fluids state which is computed from $fout$. Assuming periodic boundary conditions, thus what leaves the domain to the right is fluxed in at the left, one distribution function is streamed by a well defined velocity vector. Writing tests for this function has two benefits, on the one hand any test is some documentation. A test is build on a mathematical expression, therefore it shows inside the source code what happens when certain parameters are used. On the other hand tests make it harder to add errors to functions. To test the **BGKandStream!** function one appropriate test could be,

```

# Without forces, tau = 1
feq = ones(5,5,9)
ftemp = ones(5,5,9)
fout = ones(5,5,9)

```

```
feq[1,1,:] .= 2.0
Swalbe.BGKandStream!(fout, feq, ftemp, zeros(5,5), zeros(5,5))
@test all(fout[:, :, 1] == feq[:, :, 1])
@test all(fout[:, :, 2] == circshift(feq[:, :, 1], (1, 0)))
```

These tests would, however, come short when τ_{a} , the socalled relaxation time, is different from one. The tests would further not catch issues with the implementation of the forcing. Therefore, some more tests must be added,

```
# With forces, tau /= 1
fout = ones(5,5,9)
feq[1,1,:].= 2.0
onebytau = 1.0/0.75
omega = 1.0 - 1.0/0.75
Swalbe.BGKandStream!(fout, feq, ftemp, fill(0.1,5,5), fill(-0.1,5,5), 0.75)
@test all(fout[:, :, 1] == omega .* 1.0 .+ onebytau .* feq[:, :, 1])
@test all(fout[:, :, 2] == circshift(omega .* 1.0 .+
    onebytau * feq[:, :, 1] .+ 1/30, (1,0)))
```

Now there is an exact mathematical relation that **BGKandStream!** has to satisfy, which can be tested every time changes are made to the code. The test further shows how to use **BGKandStream!** and users unfamiliar with the code could alter tests to learn more about the function. Apart from testing the exactness of each function individually it is important to add tests that perform simulations of a physical problem. One of these problems could be the relaxation of a droplet towards its equilibrium contact angle,

```
# Relaxation simulation of a droplet
h, A = Swalbe.run_dropletrelax(sys, "CPU", radius=rads, verbose=false)
@test h == h_res
@test A == A_res
```

run_dropletrelax performs a CFD simulation of a relaxing droplet. The function returns a spatially resolved thickness and an area of the droplet after relaxation. The output can be compared against known results, which in fact should ensure that the dynamics of the droplet relaxation are modelled correctly. In this case the test actually provide a guideline of how to set up a simulation for a relaxing droplet, it can therefore be used as a tutorial case.

Using this principle creates a testing suite that (hopefully) ensures that functionality is not broken if changes to the source code are made. For mature software projects, e.g. OpenFOAM [JJT; Jas09; Che+14], these suits can and should be even integrated into the continuous development/continuous integration (CD/CI) step and therefore be automated. Often however when a student starts a new software project, functionality or performance is the main point of interest. During the development step tests and even more important documentation are left aside. Ultimately this does not only open the gate for various bugs but to some extent it also renders the

software useless for other researchers. Needless to say, my very own CFD solver, see Chap. 4, generated correct results due to the cancellation of two bugs. Defining a test suite from the beginning of the project would have spared me valuable time and effort.

On the other hand, research became more than ever dependent on computational resources. Clearly the main topic of this thesis, CFD is a compute heavy subdomain of fluid dynamics. However, recent advances in artificial intelligence show a rising trend to their applicability for industrial and scientific problems [AR18; Bei+20]. These advances comes at a price, leaving aside the discussion if artificial intelligence is of value at all. One of the main pillars that generates trust in scientific results is their reproducibility. Independent of the number of trials a stone, when flung up in the air, will fall to the ground following a well defined path³. Generating huge amounts of data without labels and explanation makes it by definition impossible to verify any given finding or result from that experiment. Mislabeling data is not something new, it always happened from time to time with e.g. laboratory journals. However, exa-scaling computing pushes this problem to new severity. Now or never is the time to install protocols. Guides on how to deal with scientific software such that data can be reproduced or even more important reused. While this may not be of interest for most readers, to me it is an essential point. That said, Chap. 4 describes the software developed and used for this thesis. One can find the open source software repository that hosts the code, tests and documentation. Upon pull or merge requests an automated testing suite performs tests to ensure no bugs break necessary functionality. Furthermore by definition of version control it is possible to reproduce all results generated with that software, called *Swalbe.jl*.

1.5 Outline

Following this short introduction are chapters on theory, the numerical method, results and finally a conclusion. Starting with the next Chap. 2 a detailed explanation of the theoretical ideas is presented. Thus the starting point will be the equation of motion of a fluid, the Navier-Stokes equation. Using real world observations and strong assumptions the Navier-Stokes equation can be reduced to the Saint-Venant or shallow water equation [B71]. Similar arguments also play a critical role in the derivation of the thin film equation. However, these two systems describe different physical phenomena. Still, as will be shown, this is a direct consequence of *long-scale, long-wave* phenomena [ODB97]. Chap. 2 will then end with a short section of differences and intersections between these two theories.

In Chap. 3 numerical frameworks for solving differential equations are presented. Starting with a short overview on different methods to be used to solve the thin film problem. Specifically, the concept of discrete differentiation is introduced as a consequence of a discrete computational domain. One strategy to avoid differentiation is to use spectral methods which operate via Fourier transformation. Lastly one method

³Given the stone is not flung with earth's escape velocity, $v \approx 11.2\text{km/s}$

that offers a lot of value for nanometric thin films is molecular dynamics (MD). As it turns out different length and time scales can be a pitfall for either of these methods. In between the macro (classical Navier-Stokes solvers) and micro (MD) scale is the lattice Boltzmann method (LBM), a so-called meso-scale approach. The underlying differential equation that is solved is the Boltzmann equation. LBM is therefore not another discretization scheme for the Navier-Stokes equation. However, as will be shown the Navier-Stokes equation can be approximated using the lattice Boltzmann method [Ens17; CC90; CD98; Krü+17]. Not only is it possible to approximate the Navier-Stokes but also the shallow water equations, of course with a different set of constraints [Sal99; Zho04; van+10; Del02].

Following that argumentation is the published article for the *Journal of Open Source Software*. Highlighting the implementation and development of the lattice Boltzmann solver called **Swalbe** (shallow water lattice Boltzmann solver) in Chap. 4. Key aspects are the automated continuous integration (CI) with a test suite and web-hosted documentation, as motivated in Sec. 1.4. The Julia package allows for either fast iterative model development in two dimensions or large scale simulations in three dimensions with GPU acceleration. It allows for prototyping and testing which is fast and easy to use, but also a framework for large three dimensional simulations with minor to no code changes.

Use cases and a derivation of the model can be found in Chap. 5. In this chapter the mandatory modelling assumptions are introduced that allow to match the shallow water system with the thin film equation. It further highlights which modifications are made to the shallow water lattice Boltzmann algorithm. With some emphasis on the numerical implementation of e.g. the computation of gradients and the Laplacian in agreement with Ref [JK00; Tha+13]. After the derivation, numerical experiments are displayed to validate the model. Among those are the Rayleigh-Taylor instability, an instability that occurs when a heavy fluid is on top of light fluid. Spreading dynamics is tested against the Cox-Voinov and Tanner's laws. The linear relation between Bond and Capillary number is validated with the sliding of a droplet. And for completeness a discussion on the performance of the algorithm and applicability for accelerated computing at the end of the chapter.

In the next chapter, Chap. 6, a functional extension to the lattice Boltzmann model is shown. Instead of approximating the deterministic thin film equation the stochastic thin film equation (STF) is the topic of interest in this chapter. Thermal fluctuations are often neglected in simulations while their existence in the experiment cannot be denied. For nanometric thin films fluctuations can accelerate the time scales of instabilities. Interestingly the time scales of these instabilities and resulting film ruptures are in fact contact angle dependent. Depending however on the substrate properties (patterning), it is still likely that fluctuations are only subdominant.

Dynamics during dewetting can either be generated due to forces, as shown in Chaps. 5-6 or it can be induced due to time dependent potentials. Giving the recent interest in dynamics of simple liquids on complex substrates and the dynamic wetting of flexible, adaptive and switchable surfaces, Chap. 4 is dedicated to the question: "What happens during dewetting with a spatio-temporal evolving wettability gradi-

ent?" To study this problem a series of three dimensional simulations is performed with varying spatial as well as temporal evolution of the wettability. On the one hand the wettability dynamics has a small but measurable stabilizing effect on the spinodal dewetting of the thin film leading to a net increase in rupture times if the dynamic wetting is switched on. On the other hand after the rupture of the film a clear morphological transition is observable. Having only a static wettability gradient results in stationary droplets in regions of high wettability. Making the wettability gradient dynamic can lead to metastable rivulet states. These rivulets can be explained using a simple model that balances the capillary with the wettability wave velocity, introducing a cutoff parameter ($\Gamma > 1$) for which rivulets are to be observed.

In the last Chap. 8 a summary and conclusion of the work collected in this thesis is given. Summarizing the scientific results that have been achieved during the duration of the PhD. Because this work can be seen as an "*exploratory*" work, some outlook is presented with possible extensions as well as further dynamical variables to study more complex thin film flows.

2 Theory

*Wir wollen immer da hin, wo
jeglicher Druck mal ein Ende hat
Ha'm immer tausend Sachen auf'm
Zettel, sach' ma', kennst du das?*

Deichkind

The starting point to study fluid dynamics is the Navier-Stokes equation [Cla27; Sto48], as motivated in Chap. 1. Both Claude Navier in 1823 as well as Gorge G. Stokes in 1842 derived the momentum equation for a Newtonian liquid. Historically these two were not the only ones. Siméon Denis Poisson and Barré de Saint-Venant came to the same conclusion around the same time [Poi31; Sai43; JA98]. But history is written and Navier as well as Stokes are identified with the derivation of the momentum of a fluid element.

2.1 The Navier-Stokes equation

Mathematically the Navier-Stokes equation can be derived from one definition and two constraints. The two constraints are mass and momentum conservation. Mass conservation simply states that mass cannot be lost or created. The same argument holds for the momentum. By Noethers theorem every conserved quantity yields a symmetry and vice versa. In this case conservation of momentum allows us to use the constraints on the solutions that translational symmetry requires. Put simply a sliding drop experiment has to yield the same result in any laboratory on earths surface, independent of the exact location of the laboratory. The last ingredient for the derivation is the definition of a fluid. A fluid is “*a substance that flows and is not solid*“ according to the Cambridge Dictionary. This definition can be refined, because a fluid is either a gas or a liquid that continuously deforms under shear stress, at least in the case of a Newtonian fluid. And as such there is a linear relation between shear rate and shear velocity for a Newtonian fluid. Clearly there are other liquids (which encloses granular systems to some extent) that exhibit different behaviour, for example toothpaste. As long as there is no force applied to the tube the toothpaste does not flow. Even the acceleration due gravity when pointing the tube towards the ground does not exert enough force to generate a flow. In contrast to Newtonian liquids those liquids have a different response function to shear, they can be addressed as *power law* fluids. While the phenomenology of these fluids, e.g. shear thinning or

thickening, is very interesting and important in many industrial applications it is beyond the scope of this work. That said, in Chap. 6 an extension towards more complex flows is presented. Instead of however changing the shear response we model thermal fluctuations to approximate the stochastic thin film equation (STF). In fact, the step to derive an extension to our approach are nicely summarized in Chap. 6. It should serve as a guideline for further features, such as viscoelasticity for non-Newtonian liquids [BB13].

Knowing what a fluid is and taking into account the conservation of mass and momentum it is possible to derive the Navier-Stokes equation. By applying a continuity equation we assume that the fluid itself is a continuum and therefore ignoring the underlying molecular structure for now. This allows us to describe the fluids state with a density $\rho(\mathbf{x}, t)$, instead of describing every atom or molecule individually. Assuming an infinitesimal small volume of fluid V_0 its density can only change if there is a flow through the boundaries of the volume ∂V_0 ,

$$\partial_t \int_{V_0} \rho dV = - \oint_{\partial V_0} \rho \vec{u} \cdot d\vec{A}, \quad (2.1)$$

where $\vec{u}(\vec{x}, t)$ is the fluid's velocity, A is the area that encloses the volume V_0 and $d\vec{A}$ are the normals pointing outwards of the volume. Violations of this Eq. (2.1) are equivalent to generation or destruction of mass.

Thanks to Gauss the integral over a closed surface can be written as divergence of a volume and thus the above equation becomes [Kön11]

$$\partial_t \int_{V_0} \rho dV = - \int_{V_0} \vec{\nabla} \cdot (\rho \vec{u}) dV. \quad (2.2)$$

Since both sides are integrals over the volume V_0 we drop them and work with the differential equation

$$\partial_t \rho + \vec{\nabla} \cdot (\rho \vec{u}) = 0, \quad (2.3)$$

which will be addressed as the continuity equation throughout the thesis. Actually one finds this equation not only in fluid dynamics for mass conservation but as well in electrodynamics for charge conservation, where the second term is often referred to as flux [Jac21; Gri13].

For the momentum equation the same line of arguments is applied, however momentum can change for different reasons. Momentum can for example be advected with the flow from or into the volume V_0 . Pressure on the other hand can be a source of momentum change and of course forces that are applied to the fluid are as well sources [Krü+17]. Collecting these terms and writing down an equation for the momentum we have,

$$\partial_t \int_{V_0} \rho \vec{u} dV = - \oint_{\partial V_0} (\rho \vec{u} \vec{u}) \cdot d\vec{A} - \oint_{\partial V_0} p d\vec{A} + \int_{V_0} \vec{F} dV, \quad (2.4)$$

where $\vec{u}\vec{u}$ is used to denote the outer product

$$\vec{u}\vec{u} = \begin{bmatrix} u_x u_x & u_x u_y & u_x u_z \\ u_y u_x & u_y u_y & u_y u_z \\ u_z u_x & u_z u_y & u_z u_z \end{bmatrix}. \quad (2.5)$$

Using the divergence theorem again to reformulate everything in terms of volume integrals and dropping the integration the above equation becomes

$$\partial_t(\rho\vec{u}) = -\vec{\nabla} \cdot (\rho\vec{u}\vec{u}) - \vec{\nabla} p + \vec{F}. \quad (2.6)$$

This however is not yet the Navier-Stokes equation, in fact this is the Euler equation [BB67]. In the derivation there is one term missing, because the momentum of a fluid can also change due to internal friction, or put simply, due to viscosity. These viscous contributions are collected in the viscous stress tensor $\hat{\sigma}$ as

$$\hat{\sigma}_{\alpha\beta} = \mu \left(\frac{\partial u_\alpha}{\partial x_\beta} + \frac{\partial u_\beta}{\partial x_\alpha} \right) + \lambda \delta_{\alpha\beta} \frac{\partial u_\gamma}{\partial x_\gamma}, \quad (2.7)$$

This tensor introduces a lot of the complexity of the Navier-Stokes equation as in principle neither μ nor λ need to be constants and in fact they are tensors themselves.

For the sake of clarity however here it is assumed that both μ and λ are constants. Inclusion of pressure to $\hat{\sigma}$ yields the total stress tensor $\tilde{\sigma}$. Due to symmetries of the problem there are various constraints on this tensor. A fluid element can be rotated similar to a solid body, but it can also be stretched. In contrast to a solid body a fluid element is allowed to deform. Working out these constraints we find that the pressure has to be a diagonal term and thus

$$\tilde{\sigma}_{\alpha\beta} = -p\delta_{\alpha\beta} + \mu \left(\frac{\partial u_\alpha}{\partial x_\beta} + \frac{\partial u_\beta}{\partial x_\alpha} \right) + \lambda \delta_{\alpha\beta} \frac{\partial u_\gamma}{\partial x_\gamma}. \quad (2.8)$$

Now to get from the Euler equation (Eq. (2.6)) to the Navier-Stoke we add the viscous stress tensor and rearrange terms,

$$\partial_t(\rho\vec{u}) + \vec{\nabla} \cdot (\rho\vec{u}\vec{u}) = -\vec{\nabla} p + \vec{\nabla} \left[\mu(\vec{\nabla}\vec{u} + \vec{\nabla}\vec{u}^T) + \left(\eta - \frac{2\mu}{3} \right) \vec{\nabla} \cdot \vec{u} \right] + \vec{F}, \quad (2.9)$$

where we have used the differential form of Eq. (2.8) and $\lambda = \eta - 2/3\mu$.

Instead of trying to solve this straight away, let's first discuss what we try to archive. The main goal of this thesis is to model the dynamics of thin film flows. An area of fluid dynamics usually addressed as creeping flows. The flow velocities in this regime are in fact much slower than the speed of sound c_s ($c_s^{\text{H}_2\text{O}} \approx 1500\text{m/s}$). This allows for the simplification of an incompressible medium. For such media or fluids one can assume that $\rho = \text{const.}$ and therefore by Eq. (2.3)

$$\vec{\nabla} \cdot \vec{u} = 0. \quad (2.10)$$

A note of caution: While a constant density ($\rho = \text{const.}$) does satisfy the incompressibility constraint it is not unique to the underlying thermodynamics. The thermodynamic compressibility κ measures the change of volume with pressure and is given by

$$\kappa = \left(\frac{\partial V}{\partial p} \right)_T. \quad (2.11)$$

Strictly speaking a fluid is incompressible as long as its density does not depend on the pressure p or $\kappa = 0$.

Inserting this constraint Eq. (2.10) into Eq. (2.9) yields therefore the Navier-Stokes equation for an incompressible fluid as

$$\rho(\partial_t \vec{u} + \vec{\nabla} \cdot \vec{u} \vec{u}) = -\vec{\nabla} p + \mu \Delta \vec{u} + \vec{F}, \quad (2.12)$$

where the symbol Δ denotes the laplace operator ($\Delta f = \vec{\nabla} \cdot \vec{\nabla} f$). The left hand side can be rewritten using the material derivative

$$D_t = \partial_t + \vec{u} \cdot \vec{\nabla}, \quad (2.13)$$

which is a convenient measure for following a fluid element instead of a single point. Inserting this, Eq. (2.12) can be written as

$$\rho D_t \vec{u} = -\vec{\nabla} p + \mu \Delta \vec{u} + \vec{F}. \quad (2.14)$$

Eqs. (2.3, 2.12) cannot be solved because there are too few equations for too many unknowns. So far there are five unknowns (ρ, \mathbf{u}, p) for four equations. The clever way out of this misery is to use an equation of state that relates pressure, density, temperature, energy and entropy. Especially the relation between pressure, density and temperature helps in closing the system of equations. To define an equation of state is far from trivial. It requires a thermodynamically consistent approach that is based on observations or theoretical assumptions. The equation of state for an ideal gas was born from theoretical assumptions, e.g. non-interacting gas molecules, and reads [Sch06]

$$p = \rho R T, \quad (2.15)$$

where R is the specific gas constant and T is the temperature. Having a well defined state in the thermodynamical sense allows to relate pressure and density and therefore to close the system of equations. The equation of state for an ideal gas, see Eq. (2.15), will be revisited in Chap. 3 where we discuss the lattice Boltzmann method.

The Navier-Stokes equation, see Eqs. (2.3, 2.12), offers a general framework to deal with fluid dynamics problems. In the case of an incompressible non turbulent flow we have a solid understanding of the velocity field. For compressible flows with developed turbulence on the other hand we still miss fundamental knowledge, as mentioned in Chap. 1. This missing information is the reason that the automotive as well as aviation industry invests heavily in both real world experiments and CFD. For the concrete example of thin film flows, however, there is no need to “solve” the Navier-Stokes equation. That is why in the next two sections different theories that build upon the Navier-Stokes are introduced. Both of these theories using a scaling argument to severely simplify the resulting system of equations.

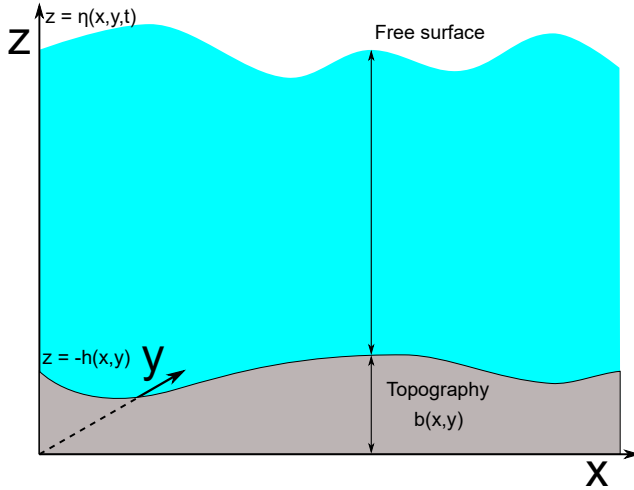


Figure 2.1: Schematic description of the shallow water problem. A liquid column with position of the free surface $\eta(x, y, t)$ covers a bottom topography $b(x, y)$. The liquid's height with the addition of the elevation of the topography defines the resulting height or z-component of the free surface.

2.2 Shallow Water Theory

Solving the Navier-Stokes equation for the problems discussed in Chaps. 4-7 is not needed. Looking at Figs. 1.1-1.5 one can identify that the height or thickness of the fluid layer is much smaller than the horizontal extension of the substrate. This statement together with some more approximations allows to derive another system from the Navier-Stokes equation and the continuity equation which is called the shallow water or Saint-Venant equations [B71].

2.2.1 Definition

The shallow water equations are a well working approximation to describe *shallow* flows [Tan92] and illustrated in Fig. 2.1. “Shallow” by definition of the Cambridge dictionary means “*having only a short distance from the top to the bottom*”, which in fact describes quite well what the model does. Instead of having a fully resolved three-dimensional model of the fluid’s density and velocity the shallow water approach assumes that the degrees of freedom in the vertical direction can be integrated out. Therefore all dynamics of the system are effectively captured by the evolution based on the horizontal degrees of freedom (x, y).

Such strong assumptions require to take a look at the system at hand. Coming back to the meaning of the word shallow, a shallow flow with a liquid column of height h and horizontal length scale L needs to satisfy

$$\varepsilon := \frac{h}{L} \ll 1, \quad (2.16)$$

where ε is a measure for the difference between horizontal and vertical scales. An illustrative example that satisfies this inequality is any of the three major oceans. On average the oceans are about $3000m$ deep. They cover about 71% of the earth's surface area which is approximately $361000000km^2$. Dividing this number by three, to separate between Atlantic, Pacific and Indian ocean one gets a square with a side length of $11000km$. Inserting numbers in Eq. (2.16) yields a ratio $\varepsilon \approx 3 \cdot 10^{-4}$. The average height of the fluid column is negligibly small as compared to its horizontal scales. Therefore, the dynamics in the vertical direction can be considered instantaneous. The oceans are not the only dynamical system that with such a relation, the atmospheric layer also has a small ε . Atmospheric dynamics can be described with the shallow water model, at least to some extent.

Secondly comes the assumption of the pressure free surface. Putting it simply, the shallow water model does not know what happens above the fluid. The assumption is that the density of the layer above the fluid column is small when compared to the fluid density. The oceans are mostly filled with water, the density of (salt) water is around a thousand times higher than the density of the air above ($\rho^{H_2O} \approx 1000\text{kg/m}^3$, $\rho^{\text{air}} \approx 1,25\text{kg/m}^3$). To some extent this is, again, actually true for the atmospheric layer. Using the barometric formula to relate the density with altitude,

$$\rho(h_1) = \rho(h_0)e^{-\frac{\Delta h}{h_s}}, \quad (2.17)$$

with $\Delta h = h_1 - h_0$ and $h_s = RT/Mg$ is the scale height. Of course, the model can be refined with a so called multi layer approach [TT09; PSR13], but by definition the assumption is that the upper end of the fluid column does not feel any pressure from above [Tan92; Jam+19].

Third, the horizontal velocity of the fluid has to vanish at the “solid” ground, or in terms of Fig. 2.1 looking down from the free surface at $-h(x, y)$. Although there is a viscosity associated with the fluid, friction with the bottom topography is the dominating dissipation channel. This kind of boundary condition has been introduced in Chap. 1 is called **no-slip** boundary condition [Ric73; de 02; Sal99]. While this may seem counterintuitive because fluid has no problem to flow over yet dry surfaces, modelling wetting or the wet-dry transition is a complex task, as seen later in this chapter and in Chap. 5. After all, a theoretical model which is defined as a set of partial differential equations cannot account for the true complexity of nature [Scr88]. We come back to the idea of the no-slip boundary condition in Sec. 2.3.

The big circular flow systems in the oceans like the Gulf Stream have much larger velocity components in the horizontal directions as compared to the vertical one. This is actually crucial to know because in the following mathematical modelling it is taken into account and will allow for further reduction of complexity. We therefore assume that the vertical velocity component is small as compared to the horizontal ones.

The task now is to make, Eq. (2.12), aware about these constraints. Although this sounds straightforward partial differential equations are complex. They are one of the topics in mathematics where researchers are satisfied with the irritating result that an equation cannot be solved, an undesired outcome for most Physicists. Nevertheless, to come up with consistent strategies to solve them one can classify them,

e.g. hyperbolic, parabolic, linear, nonlinear, initial value problem or boundary value problem. There is in fact overlap between those terms, however to keep things simple it is sufficient to talk about initial or boundary value problems. The former can be solved knowing the initial configuration which then defines the evolution, e.g. the initial coordinates and velocity of a pendulum. For the latter ones it is mandatory to know the solution at the boundaries. If we know the current temperature distribution on a metallic plate and the heat flux on the boundaries then we are able to calculate the temperature field on that plate at later times. The shallow water system can be derived from the Navier-Stokes equation using both well defined boundary conditions and system specific approximations. For example the statement *pressure free surface* translates to the fact that there is a boundary condition requiring $p = 0$ at $z = \eta$. Therefore no pressure is acting on liquids interface.

2.2.2 Scaling analysis

Starting with the system specific approximations, in Eq. (2.16) a so-called scaling parameter ε has been introduced. We use this parameter to rescale the velocities according to

$$u_x = \tilde{u}_x, \quad u_y = \tilde{u}_y, \quad u_z = \varepsilon \tilde{u}_z. \quad (2.18)$$

For an incompressible fluid with vanishing density gradient Eq. (2.3) therefore becomes

$$\vec{\nabla} \cdot \vec{u} = \partial_x u_x + \partial_y u_y + \varepsilon \partial_z u_z = 0. \quad (2.19)$$

To satisfy that all terms of this equation are the same order in ε the coordinates need to be rescaled as well. This choice however is not unique and offers two possibilities [Jam+19]. There is on the one hand the long wave approximation [ODB97],

$$x = \frac{\tilde{x}}{\varepsilon}, \quad y = \frac{\tilde{y}}{\varepsilon}, \quad z = \tilde{z}, \quad t = \frac{\tilde{t}}{\varepsilon}, \quad (2.20)$$

which again is encountered in Sec. 2.3.1 and has the effect of smoothing out spatial and temporal variations. On the other hand is the thin layer scaling

$$x = \tilde{x}, \quad y = \tilde{y}, \quad z = \varepsilon \tilde{z}, \quad t = \tilde{t}, \quad (2.21)$$

which corresponds to the classical scaling of boundary layer theory [Mil96].

In Eqs. (2.18-2.21) there is no distinct difference between both horizontal dimensions (x, y). For the sake of clarity and to simplify the derivation of the shallow water model we neglect the y -components. Of course, to study large oceanic systems or Coriolis forces one needs both horizontal dimensions, see e.g. [DS05; Mar07], but for the following derivation it is sufficient to use only one. Furthermore we use Eq. (2.20), which represents long wave theory or scaling. We make use of this approach once more in the derivation of the thin film equation. The benefit of this choice is the smoothing effect on variations which makes them more gradual. But not only the gradients in

horizontal dimensions are multiplied with ε^{-1} . The time is scaled with ε^{-1} as well which smears the dynamics. Inserting Eqs. (2.18,2.20) into Eq. (2.3) yields

$$\tilde{\nabla} \cdot \tilde{\mathbf{u}} = \partial_{\tilde{x}} \tilde{u}_x + \partial_{\tilde{z}} \tilde{u}_z = 0, \quad (2.22)$$

where two dimensional vectors, such as $\mathbf{u} = (u_x, u_z)$ are bold while three dimensional ones are denoted with an arrow symbol.

Scaling analysis and renormalization are key concepts in modern physics [YO86; Pes18b]. One of the key concepts of this idea are symmetries, and therefore transformations under which a given state does not change. Fluid dynamics to some extent admits a conformal symmetry. The governing equations describe the flow through a nanotube as well as the circular currents in oceans [Sec+16; Mar07]. Some features however such as the drag on an airfoil do not simply scale with the size of the system. Therefore while a miniaturised model may create enough lift force, simply scaling up the size is not sufficient to ensure enough lift. In the following it will be helpful to introduce dimensionless numbers [Ruz08; NS19]. These numbers have a long history in fluid dynamics. The Reynolds number for example is a measure if a flow is turbulent or not, it depends only on proportions and not on an exact experiment. With the knowledge of these number comparing experiments is straightforward, even if the experiments differ in many aspects. The two dimensionless numbers of interest for the shallow water theory are the Reynolds number and the Froud number

$$Re = \frac{\rho L v_0}{\mu}, \quad Fr = \frac{v_0}{\sqrt{gL}}, \quad (2.23)$$

where L is a characteristic length scale of the problem, e.g. the mean water depth, v_0 and g are a characteristic velocity and the gravitational acceleration ($g = 9.81 \text{ m/s}^2$), respectively. A characteristic velocity can be for example the inflow velocity from a boundary, or the speed of a certain wave type such as a tsunami. Both numbers measure the magnitude of certain effects, in the case of the Reynolds number the inertial forces are compared against viscosity. The Froud number is a measure to compare kinetic (v_0) with potential energy (gL).

In the next step both Fr and Re are used to make Eq. (2.14) dimensionless. For convenience the vector equation is split into two respective equations with gravity being the only force present. Writing the full equation with all components yields

$$\partial_t u_x + u_x \partial_x u_x + u_z \partial_z u_x = -\partial_x p + \frac{1}{Re} \Delta u_x, \quad (2.24)$$

$$\partial_t u_z + u_z \partial_x u_x + u_z \partial_z u_z = -\partial_z p - \frac{1}{Fr^2} + \frac{1}{Re} \Delta u_z, \quad (2.25)$$

with the two dimensional Laplacian $\Delta = (\partial_x^2 + \partial_z^2)$. Using long wave scaling, Eq. (2.20) and the rescaled length and time variables (e.g. \tilde{x}),

$$\varepsilon(\partial_{\tilde{t}} \tilde{u}_x + \tilde{u}_x \partial_{\tilde{x}} \tilde{u}_x + \tilde{u}_z \partial_{\tilde{z}} \tilde{u}_x) = -\varepsilon \partial_{\tilde{x}} \tilde{p} + \frac{1}{Re} (\varepsilon^2 \partial_x^2 \tilde{u}_x + \partial_z^2 \tilde{u}_x), \quad (2.26)$$

$$\varepsilon^2(\partial_t \tilde{u}_z + \tilde{u}_x \partial_{\tilde{x}} \tilde{u}_x + \tilde{u}_z \partial_{\tilde{z}} \tilde{u}_z) = -\partial_{\tilde{z}} \tilde{p} - \frac{1}{Fr^2} + \frac{\varepsilon}{Re}(\varepsilon^2 \partial_x^2 \tilde{u}_z + \partial_{\tilde{z}}^2 \tilde{u}_z). \quad (2.27)$$

We now assume that terms with higher orders in ε are negligible and therefore $O(\varepsilon^2) \rightarrow 0$, collecting only terms with up to $O(\varepsilon)$

$$\partial_{\tilde{t}} \tilde{u}_x + \tilde{u}_x \partial_{\tilde{x}} \tilde{u}_x + \tilde{u}_z \partial_{\tilde{z}} \tilde{u}_x = -\partial_{\tilde{x}} \tilde{p} + \frac{\partial_{\tilde{z}}^2 \tilde{u}_x}{\varepsilon Re}, \quad (2.28)$$

$$0 = -\partial_{\tilde{z}} \tilde{p} - \frac{1}{Fr^2} + \frac{\varepsilon \partial_{\tilde{z}}^2 \tilde{u}_z}{Re}. \quad (2.29)$$

Interestingly in the first of the two above equations the term associated to the horizontal viscosity is $O(\varepsilon^2)$ and can be dropped. On the other hand with the assumption of the long wave scaling the second of the above equations yields the hydrostatic pressure, taking only $O(1)$ terms

$$\partial_{\tilde{z}} \tilde{p} = -\frac{1}{Fr^2}, \quad (2.30)$$

which can be readily integrated, given Fr is a constant, using the upper bound at the liquid air interface $\eta(x)$

$$\tilde{p} = \frac{1}{Fr^2}(\tilde{\eta} - \tilde{z}). \quad (2.31)$$

This implies that $\partial_{\tilde{x}} p$ does not depend on \tilde{z} and therefore states that the pressure gradient is conserved along z .

Summarizing the impact of the approximation, on the continuity equation Eq. (2.22) and Eqs. (2.28-2.30) and dropping the tilde we get

$$\partial_x u_x + \partial_z u_z = 0, \quad (2.32)$$

$$\partial_t u_x + u_x \partial_x u_x + u_z \partial_z u_x = -\partial_x p + \frac{\partial_z^2 u_x}{\varepsilon Re}, \quad (2.33)$$

$$\partial_z p = -\frac{1}{Fr^2} \left(+ \frac{\varepsilon \partial_z^2 \tilde{u}_z}{Re} \right), \quad (2.34)$$

with the addition of boundary conditions at the liquid air interface ($z = \eta$)

$$\partial_t \eta + u_x \partial_x \eta - u_z = 0, \quad (2.35)$$

$$p = 0, \quad (2.36)$$

$$\partial_z u_x = 0, \quad (2.37)$$

as well as the no slip condition at the liquid solid interface ($z = b$)

$$u_x = 0, \quad (2.38)$$

$$u_z = 0. \quad (2.39)$$

One interesting limit is the case when $\varepsilon Re \rightarrow \infty$. In this limit both the continuity equation as well as the boundary conditions are untouched. The only part that is modified is the momentum equation Eq. (2.33),

$$\partial_t u_x + u_x \partial_x u_x + u_z \partial_z u_x = -\partial_x p, \quad (2.40)$$

which describes the hydrostatic Euler equations [Bre08].

2.2.3 Integration along the vertical dimension

The classical approach to obtain the shallow water equations is to integrate the system of Eqs. (2.32-2.34) along the vertical dimension. Having already neglected the y -component, the integration will also integrate out degrees of freedom in z . The resulting system will therefore only vary with a x dependency. Analogous to Fig. 2.1 by integration along the vertical direction of the three dimensional density field ρ , the height of the fluid column emerges as a dynamic quantity,

$$h(x) = \eta(x) - b(x). \quad (2.41)$$

Therefore it is a reduction of complexity and effectively enslaves the vertical dynamics to the horizontal one.

In terms of velocity a new variable needs to be defined which accounts for the averaging along the vertical

$$hU = \int_b^\eta u_x dz, \quad (2.42)$$

where h is the height (Eq. (2.41)) and U the height averaged velocity. The pair hU , thus height that is transported with velocity U , can also be addressed as discharge Q [Sal99]. Having introduced the height h and the discharge Q the next step is to integrate the continuity and momentum equations, Eqs. (2.32, 2.33). Starting with the former

$$0 = \int_b^\eta (\partial_x u_x + \partial_z u_z) dz, \quad (2.43)$$

$$= \int_b^\eta (\partial_x u_x dz) + u_z|_{z=\eta} - u_z|_{z=b}, \quad (2.44)$$

where the z dependent velocity can be integrated. For the x -component we make use of the integration rule of Leibniz,

$$\partial_x \int_{A(x)}^{B(x)} F(x, y) dy = \int_{A(x)}^{B(x)} \frac{\partial F(x, y)}{\partial x} dy + \frac{dB(x)}{dx} F(x, B(x)) - \frac{dA(x)}{dx} F(x, A(x)), \quad (2.45)$$

which upon inserting yields

$$0 = \partial_x \left(\int_b^\eta u_x dz \right) - u_x|_{z=\eta} \partial_x \eta + u_x|_{z=b} \partial_x b + u_z|_{z=\eta} - u_z|_{z=b}. \quad (2.46)$$

Simplifying this equation by making use of Eq. (2.35) and Eqs. (2.38-2.39) yields

$$0 = \partial_x \left(\int_b^\eta u_x dz \right) + \partial_t \eta, \quad (2.47)$$

where the integral is simply the discharge hU . Assuming that the river or shallow water bed $b(x)$ is time independent the equation can be condensed to

$$\partial_t h + \partial_x(hU) = 0. \quad (2.48)$$

This is equal to the statement whenever height changes it has to flow somewhere and therefore ensures mass conservation. Rivers such as the Colorado River change their bed quite significantly with time, the same is true for coastlines as we know that they erode with time. The reason we use $b(x)$ and not $b(x, t)$ is the mismatch in time scales between the erosion and the flow. For example, the Grand Canyon is about 5-6 million years old and roughly 1.9km deep, the Colorado River flows however with a velocity of $\approx 3.5\text{km/h}$ [Gra97].

Performing the horizontal integration to the depth averaged momentum equation, see Eq. (2.33) we have

$$\int_b^\eta \left(-\partial_x p + \frac{\partial_z^2 u_x}{\varepsilon Re} \right) dz = \int_b^\eta (\partial_t u_x + u_x \partial_x u_x + u_z \partial_z u_x) dz. \quad (2.49)$$

The two terms on the left hand side can be integrated straight away. We know that the pressure gradient $\partial_x p$ is conserved along the vertical dimension. The other term ($\propto \partial_z^2 u$) has a similar shape as the viscous term in Eq. (2.12). Performing the integral therefore yields

$$\int_b^\eta \left(-\partial_x p + \frac{\partial_z^2 u_x}{\varepsilon Re} \right) dz = -h \partial_x p + \frac{\partial_z u_x|_{z=\eta} - \partial_z u_x|_{z=b}}{\varepsilon Re}, \quad (2.50)$$

with the boundary condition that fluid does not accelerate into the air phase, see Eq. (2.37), the left hand side reduces to

$$\int_b^\eta \left(-\partial_x p + \frac{\partial_z^2 u_x}{\varepsilon Re} \right) dz = -h \partial_x p - \frac{\partial_z u_x|_{z=b}}{\varepsilon Re}. \quad (2.51)$$

The right hand side of Eq. (2.49) reads

$$\begin{aligned} \int_b^\eta (\partial_t u_x + u_x \partial_x u_x + u_z \partial_z u_x) dz &= \int_b^\eta (\partial_t u_x) dz \\ &\quad + \int_b^\eta (u_x \partial_x u_x + u_z \partial_z u_x) dz, \end{aligned} \quad (2.52)$$

where the integral is split into two separate integrals for convenience. The time dependent part can be easily integrated using Eq.(2.45)

$$\int_b^\eta (\partial_t u_x) dz = \partial_t \int_b^\eta u_x dz - \partial_t \eta u_x|_{z=\eta} - \partial_t b u_x|_{z=b} = \partial_t(hU) - \partial_t \eta u_x|_{z=\eta} - \partial_t b u_x|_{z=b}. \quad (2.53)$$

The other integral is somewhat more tricky. First, the $u_z \partial_z u_x$ term is integrated by parts

$$\int_b^\eta u_z (\partial_z u_x) dz = [u_x u_z]_b^\eta - \int_b^\eta (\partial_z u_z) u_x dz. \quad (2.54)$$

We use this intermediate result, Eq. (2.32) and the integration rule of Leibnitz to perform the integral of the second line of Eq.(2.52)

$$\begin{aligned} \int_b^\eta (u_x \partial_x u_x + u_z \partial_z u_x) dz &= 2 \int_b^\eta u_x \partial_x u_x dz + [u_x u_z]_b^\eta, \\ &= \partial_x \left(\int_b^\eta u_x^2 dz \right) + \partial_t \eta u_x|_{z=\eta} + u_x (u_x \partial_x b - u_z)|_{z=b}, \end{aligned} \quad (2.55)$$

where the same line of arguments as in Eq. (2.46) has been used. Applying the boundary condition to this equation and using the definition for height and discharge we have

$$\partial_t (hU) + \partial_x (\beta hU^2) = -h\partial_x p - \tau_b, \quad (2.56)$$

where two new variables appear. The first one is Boussinesq coefficient β which is defined by the equation

$$\int_b^\eta u_x^2 dz = \beta h U^2, \quad (2.57)$$

and the second one is the friction or the shear stress at the bottom of the fluid column τ_b

$$\tau_b = \frac{\partial_z u_x|_{z=b}}{\varepsilon Re}. \quad (2.58)$$

Both β as well as τ_b do depend on u , therefore to know their exact contribution one needs to know about the flow. Without the concrete knowledge of u there is however one observation concerning Eq. (2.57)

$$\beta = 1 + \frac{1}{h} \int_b^\eta \left(1 - \frac{u}{U} \right)^2 dz, \quad (2.59)$$

and therefore $\beta \geq 1$. To understand the implications of these terms we discuss an instructive example.

2.2.4 Poiseuille flow

The Poiseuille flow is one amongst those few problems that can be solved analytically [Sut93]. To have an idea about the flow, one can think of a circular pipe. The pipe is fully filled with a (Newtonian) liquid, see Fig. 2.2 a) for an oversimplified illustration. By an external pressure gradient, for example a pump, a continuous flow is

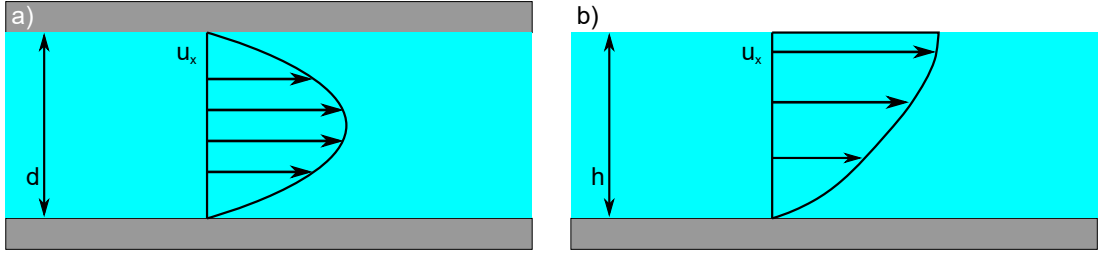


Figure 2.2: a) Schematic, cut through the center, velocity profile of a pipe flow with wall friction and no slip boundary condition. The flow velocity u_x can be calculated using Eq. (2.60). b) Similar case in terms of a shallow water geometry. The upper wall is replaced with a pressure free boundary while the lower wall induces friction according to a no-slip boundary condition.

generated. The velocity profile of this flow can be explained with the equation [BB67; Krü+17]

$$u_x(y) = -\frac{\partial_x p}{2\mu} y(y-d), \quad (2.60)$$

where d is the diameter of the pipe. The profile is parabolic with vanishing u_x at the walls and a maximum at $d/2$. Thus the above equation defines the balance between the driving force, here the pressure difference, and the friction at the walls.

In Fig. 2.2 b) the flow is not enclosed between two boundaries but has a pressure free surface. The solution is not anymore given by Eq. (2.60) but reduces to the half-Poiseuille or Nusselt solution with a new self similar quantity \bar{h} [Jam+19]

$$\bar{h} = \frac{z-b}{h}, \quad \frac{u}{U} = 3 \left(\bar{h} - \frac{\bar{h}^2}{2} \right), \quad (2.61)$$

where \bar{h} is constructed to be in the interval between 0 and 1. Inserting \bar{h} into Eq. (2.59) reveals that the Boussinesq coefficient is given as $\beta = 6/5$, where the integration can be performed using a transformation of the integral measure. The friction term Eq. (2.58) becomes

$$\tau_b = \frac{3}{\varepsilon Re} \frac{U}{h}. \quad (2.62)$$

The friction term τ_b depends linearly on U the mean flow velocity. Interestingly for large Reynolds numbers the friction can become negligible, with the transition to the inviscid shallow water regime.

A word of caution when using τ_b . Friction forces in real experiments are very dependent on the actual boundary condition at $z = b$. Both the topography and the specific type of material at the bottom will influence the measured value of τ_b . By modelling a dissipative force such as friction we make an error, sometimes this error is negligible. It is therefore often simpler and more accurate to use data from empirical studies or real world experiments. Within the shallow water literature an often encountered coefficient is the one of Manning, the empirical law that connects flow velocity with friction can be found in Ref. [Stu21].

To close this section we quickly collect the equations that form the shallow water system, see Eqs. (2.48, 2.56). The generalization of these equations towards a second horizontal dimension is straightforward and can be written as [Sal99; Del02; TSB07]

$$\partial_t h + \nabla \cdot (h \mathbf{u}) = 0, \quad (2.63)$$

$$\partial_t (h \mathbf{u}) + \nabla \cdot (p \mathbb{1} + h \mathbf{u} \mathbf{u} - S) = 0, \quad (2.64)$$

where $\mathbf{u} = (u_x, u_y)$ and the only unknown S is a yet undefined source term. The system Eqs. (2.63-2.64) concludes the shallow water model. In Chap. 5 we show how this translates into a numerical solver.

Following in this chapter are two more sections. The next section and the main point of interest of this work is a short and phenomenological oriented derivation of the thin film model. In the last section the chapter concludes with a comparison of shallow water with thin film theory.

2.3 Lubrication theory and thin films

Thin liquid films are an interesting problem to study. Their dynamics is seemingly easy to explain but bares a lot of complexity. Many of us have played with soap bubbles and experienced their bursting. Rain drops on plant leafs form fascinating shapes and sometimes when we shake those leafs they seem to fall off without any resistance. Complexity is generated due to the shape of the equation that describes the thin film dynamics, usually a non linear forth order partial differential equation of the film thickness. When the thickness of a film becomes small, e.g. only a few tens of nanometers the complexity can even be enhanced. Complex behaviour can arise due to thermal fluctuations or strictly speaking the mathematical unsolvable problem of moving contact lines e.g. when a wet to dry transition happens. Similar to the above section's scaling argument and the long wave theory, the Navier-Stokes equation can be reduced to the thin film equation. Although with the difference to the shallow water system, see Eqs. (2.63-2.64), that the thin film equation does only admit a continuity like equation and no accompanying momentum equation [ODB97; de 85; CM09].

Similar to the shallow water system, the thin film equation only considers the dynamics of a thin liquid *layer*. In principle this layer can be unsupported, it can as well be placed on top of a yet undefined surface or substrate. Within this thesis we consider exclusively supported thin films on substrates. The defining equation that describes the dynamics of a thin liquid film can be written as [Thi14; ODB97; CM09; Bon+09]

$$\partial_t h = \nabla \cdot (M(h) \nabla p). \quad (2.65)$$

On the left hand side we have the change in thickness ($\partial_t h$), that can only be achieved by applying a pressure gradient (∇p). In Eq. (2.65) two unknowns are introduced. The first one is the mobility $M(h)$ which determines the exact velocity boundary

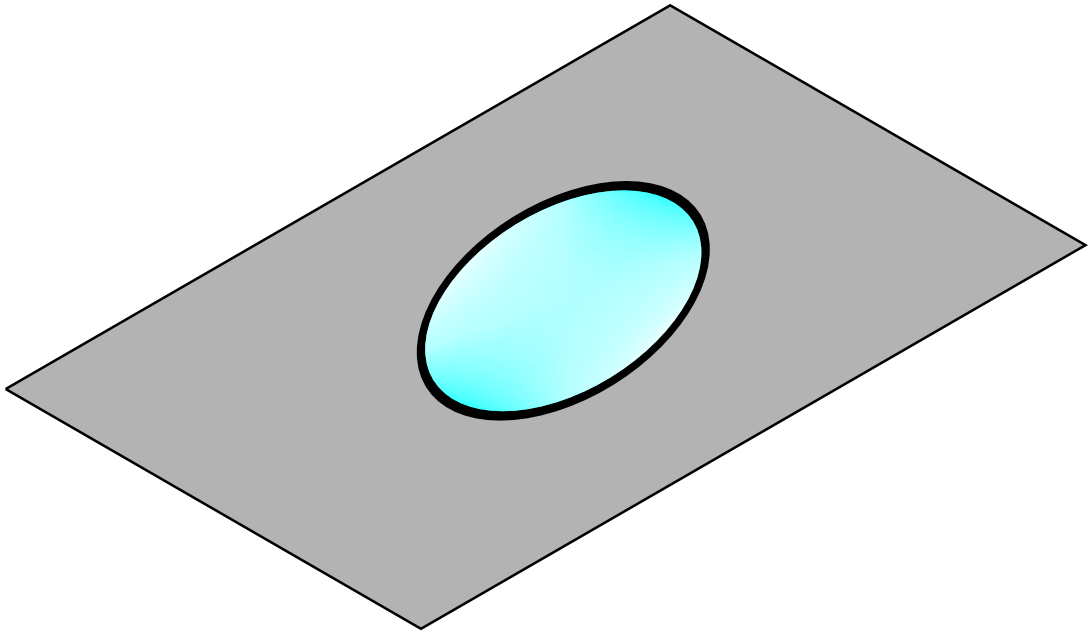


Figure 2.3: Liquid droplet placed on a smooth substrate. The three phase contact line which is the interface between the vapor, the solid and liquid phase is displayed as thick black line.

condition for $h = 0$. Using the no-slip boundary condition [BG05], see Eq. (2.38), we have

$$M(h) = \frac{h^3}{3\mu}, \quad (2.66)$$

with μ being the (dynamic) viscosity. Therefore the mobility is inversely proportional to the viscosity. Of course the velocity boundary condition can be relaxed which is often desired e.g. for contact line movement. For problems such as dewetting¹ it is actually a known approximation to relax the velocity boundary condition at the liquid solid interface [Mün05; MWW05; Fet+05]. The term contact line or to be precise three-phase contact line defines the single one dimensional interface that connects all three phases involved in the problem, as displayed in Fig. 2.3. The addition of a “slip length” (δ) makes it possible to interpolate the height of vanishing fluid velocity into the substrate. Using this interpolation the mobility function Eq. (2.66) can be extended towards a slip like behaviour in the proximity of $h \approx 0$ as

$$M(h) = \mu^{-1} \left(\frac{h^3}{3} + \delta h^2 \right). \quad (2.67)$$

The second unknown is the pressure, to be more specific the thin film pressure. So far the terms surface tension (γ) or equilibrium contact angle (θ_{eq}) did not ap-

¹Dewetting usually refers to an unstable film which by so-called film rupture recedes into separated droplets. Depending on the film’s properties different modes of dewetting can be identified, such as spinodal dewetting or hole nucleation.

pear. When we derived the Navier-Stoke equation we did not consider multiphase or multicomponent problems. In the derivation of the shallow water equations we encountered an interface, but its shape was solely determined by the hydrostatic pressure. Both theories therefore are not well-equipped to account for either surface tension or balances between surface energies and as such contact angles. The thin film pressure introduces both of them and can be modelled using

$$p = -\gamma \Delta h - \Pi(h), \quad (2.68)$$

where $\Delta h = \partial_x^2 h + \partial_y^2 h$ denotes the two-dimensional Laplacian of the thickness and $\Pi(h)$ is the disjoining pressure functional. The first term ensures that the fluid's enclosing surface area, the interface between the fluid and vapor phase, is minimal. The surface tension is therefore the strength with which the surface area minimization is enforced. The disjoining pressure ($\Pi(h)$) on the other hand takes into account the inter-molecular interactions that can arise, e.g. the interaction between solid substrate and film [CM09; ML13]. Independent of the exact model the disjoining pressure can be understood as a derivative of an interaction potential. The model used for this work was first derived by Schwartz and Eley [SE98] and consists of two contributions

$$\Pi(h) = K(\theta, \gamma) f(h), \quad (2.69)$$

where K is a function of material parameters, such as surface tension and the contact angle,

$$K(\theta, \gamma) = \gamma(1 - \cos \theta) \frac{(n-1)(m-1)}{(n-m)}, \quad (2.70)$$

and can be motivated from inter-molecular interactions [MAK15]. The second term $f(h)$ is a function of the film thickness. Here we use a power law with a characteristic height h_* for which $\Pi(h_*) = 0$,

$$f(h) = \frac{1}{h_*} \left[\left(\frac{h_*}{h} \right)^n - \left(\frac{h_*}{h} \right)^m \right], \quad (2.71)$$

with the constraints that $n > m$ as well as $m > 0$. This is an effective model for wetting of partially wettable substrates, see Fig. 2.4, with a spreading coefficient $S = \gamma_{vs} - \gamma_{ls} - \gamma$ and can be computed as [Pes+19]

$$S = \int \Pi(h)|_{h=h_*} dh, \quad (2.72)$$

where different γ 's denote the different surface energies, e.g. γ_{vs} is the surface energy between the vapour and the solid phases. By the very construction of $\Pi(h)$ everything cancels but the factor that contains the equilibrium contact angle

$$S = -\gamma(1 - \cos \theta_{eq}), \quad (2.73)$$

where we have used Young's law [You05]

$$\gamma \cos \theta_{eq} = \gamma_{vs} - \gamma_{ls}, \quad (2.74)$$

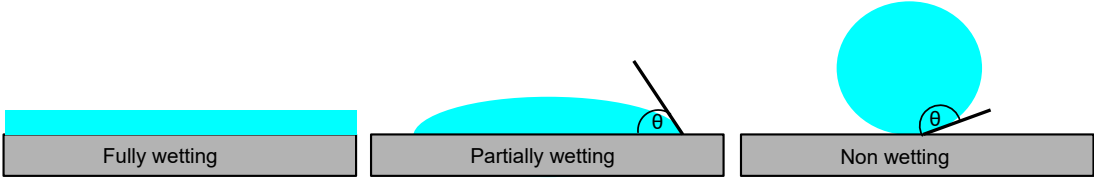


Figure 2.4: Wetting behaviour for different fluid substrate interactions. If the affinity between fluid and substrate is very large the substrate is said to be fully wetting with a vanishing contact angle. Reducing this affinity, which is usually the case for real substrates, leads to a measurable contact angle and is called partially wetting. Surface treatment or complex surface structure can lead to non wetting surfaces, therefore with contact angles of close to π .

as an approximation to the surface energies at equilibrium. For a perfectly wettable substrate the contact angle vanishes and thus $S = 0$. While we can easily formulate Eq. (2.74) it is almost impossible to measure the different γ_s experimentally. What can be measured in experiments on the other hand are the spreading parameter S and/or the Hamaker constant [Ham37; Bon+09; DGF16; Pes+19]

In contrast to the previous section we started this section with the result the thin film equation. What follows now is the derivation of Eq. (2.65) from the Navier-Stokes equation.

2.3.1 Scaling and boundary conditions

Thin liquid films are *thin*, there is always a spatial dimension which is much smaller than the other ones. Some instructive everyday example that enforces this understanding would be the thickness of an oil film in a frying pan. The pan is about 30cm in diameter while the thickness of the oil film is not even 1cm. Assuming that the oil is covering the whole surface of the pan $\varepsilon < 10^{-1}$. While this example is very illustrative it also displays interesting physics. When the pan is heated the film usually ruptures in the middle and a ring-like structure is left as shown in Ref. [FH21].

The basic assumption is, again, the absence of strong slopes and therefore

$$|\nabla h| \ll 1, \quad (2.75)$$

meaning that the thickness changes gradually along the two horizontal dimensions.

Before we start the derivation we rescale length and velocity components to have dimensionless quantities. We use a similar scaling as in Eq. (2.16) and get

$$\begin{aligned} \tilde{x} &= \frac{x}{L}, & \tilde{y} &= \frac{y}{L}, & \tilde{z} &= \frac{z}{H}, \\ \tilde{u}_x &= \frac{u_x}{U}, & \tilde{u}_y &= \frac{u_y}{U}, & \tilde{u}_z &= \frac{u_z}{V}, \\ \tilde{t} &= \frac{L}{U} t, & \tilde{p} &= \frac{H^2 p}{\mu U L}, \end{aligned} \quad (2.76)$$

where U and V are characteristic velocities and L and H are characteristic length scales in horizontal and vertical dimension. The scaling factor in front of the pressure can be calculated assuming stationary unidirectional flow with $\mathbf{u} = (u(z), 0, 0)$. It is this scaling factor ($\mu UL/H^2$) that requires that inertial effects are small and $Re < 1$. In many applications the small Reynolds number limit is a good approximation, however for e.g. spin coating inertia is not negligible. To account for inertial effects the scaling, Eq. (2.76), must be modified. For example the pressure scaling would change to $p = \rho U^2 \tilde{p}$ [CM09].

In the shallow water section, we quickly reduced the problem to two dimensions (one horizontal and one vertical). Here we keep the second horizontal dimension (\tilde{y}, \tilde{u}_y), because most numerical experiments in Chaps. 4–7 are computed in a two dimensional domain.

The first step in the derivation is to insert the dimensionless variables into the continuity equation, Eq. (2.10)

$$\vec{\nabla} \cdot \vec{u} = \partial_{\tilde{x}} \tilde{u}_x + \partial_{\tilde{y}} \tilde{u}_y + \frac{VL}{UH} \partial_{\tilde{z}} \tilde{u}_z = 0, \quad (2.77)$$

which means that $V = UH/L$ to ensure all terms are of the same order in ε . Upon inserting them into the Navier-Stokes equation for the x-component only we get

$$\begin{aligned} \rho L \partial_t \tilde{u}_x + \rho \left[\frac{U^2}{L} (\tilde{u}_x \partial_{\tilde{x}} \tilde{u}_x + \tilde{u}_y \partial_{\tilde{y}} \tilde{u}_x) + \frac{UV}{H} \tilde{u}_z \partial_{\tilde{z}} \tilde{u}_x \right] = \\ - \frac{\mu U}{H^2} \partial_{\tilde{x}} \tilde{p} + \mu \left[\frac{U}{L^2} (\partial_{\tilde{x}}^2 \tilde{u}_x + \partial_{\tilde{y}}^2 \tilde{u}_x) + \frac{U}{H^2} \partial_{\tilde{z}}^2 \tilde{u}_x \right]. \end{aligned} \quad (2.78)$$

For the y and z component we refer to the review by Oron et al. [ODB97]. Although the equation is now non-dimensional it is instructive to multiply both sides with $H^2/\mu U$ and collect the characteristic quantities in dimensionless numbers, here the Reynolds number $Re = (\rho HU)/\mu$, see Eq. (2.23), and ε

$$\varepsilon Re (\partial_t \tilde{u}_x + \tilde{u}_x \partial_{\tilde{x}} \tilde{u}_x + \tilde{u}_y \partial_{\tilde{y}} \tilde{u}_x + \tilde{u}_z \partial_{\tilde{z}} \tilde{u}_x) = -\partial_{\tilde{x}} \tilde{p} + \varepsilon^2 (\partial_{\tilde{x}}^2 \tilde{u}_x + \partial_{\tilde{y}}^2 \tilde{u}_x) + \partial_{\tilde{z}}^2 \tilde{u}_x. \quad (2.79)$$

By definition ε is small and terms with higher order in ε are at most subleading. Collecting only the term of $O(1)$ and performing the same scaling for the two other directions leads to the non-dimensional momentum equation of a thin film on a solid substrate

$$-\partial_{\tilde{x}} \tilde{p} + \partial_{\tilde{z}}^2 \tilde{u}_x = 0, \quad (2.80)$$

$$-\partial_{\tilde{y}} \tilde{p} + \partial_{\tilde{z}}^2 \tilde{u}_y = 0, \quad (2.81)$$

$$\partial_{\tilde{z}} \tilde{p} = 0. \quad (2.82)$$

For the last of the above equations the analogy to the shallow water model can be drawn using Eq. (2.34) which states that the pressure gradient does not depend on z .

The system so far does not resemble Eq. (2.65). Therefore, some more derivation is in order, starting with the application of the boundary conditions. Between the fluid

and solid phase a no-slip boundary condition is used, therefore analogue to Eq. (2.38) and (2.39) we have

$$\mathbf{u}|_{z=0} = \mathbf{0}, \quad (2.83)$$

and for the vapour fluid interface a stress balance needs to be satisfied [Lea07]

$$(\tilde{\sigma}_l - \tilde{\sigma}_v) \cdot \mathbf{n} + \nabla_S \gamma - \gamma \mathbf{n} (\nabla \cdot \mathbf{n}) = 0, \quad (2.84)$$

where $\tilde{\sigma}_{l,v}$ are the stress tensors for the liquid (l) and the vapour (v) phase. Furthermore, we have the normal vector \mathbf{n} along the fluid interface and the surface gradient ∇_S . The two surface tension terms account for changes along the surface (∇_S) and the Laplace pressure due the curvature (κ) of the liquid vapour interface $2\kappa = \nabla \cdot \mathbf{n}$. The stress tensor for a Newtonian liquid has been defined in Eq. (2.8) and for the sake of completeness is given in matrix notation as

$$\tilde{\sigma} = \begin{bmatrix} -p + 2\mu\partial_x u_x & \mu(\partial_y u_x + \partial_x u_y) & \mu(\partial_z u_x + \partial_x u_z) \\ \mu(\partial_x u_y + \partial_y u_x) & -p + 2\mu\partial_y u_y & \mu(\partial_z u_y + \partial_y u_z) \\ \mu(\partial_x u_z + \partial_z u_x) & \mu(\partial_y u_z + \partial_z u_y) & -p + 2\mu\partial_z u_z \end{bmatrix}. \quad (2.85)$$

The normal vector \mathbf{n} along the interface is defined as

$$\mathbf{n} = \frac{1}{\sqrt{1 + (\partial_x h)^2 + (\partial_y h)^2}} (-\partial_x h, -\partial_y h, 1). \quad (2.86)$$

Computing the inner product of Eq. (2.84) with the normal vector \mathbf{n} yields

$$p_v - p - (\mathbf{n} \cdot \mathbf{T}) \cdot \mathbf{n} + \gamma \mathbf{n} (\nabla \cdot \mathbf{n}) \cdot \mathbf{n} = 0, \quad (2.87)$$

where p_v is the pressure in the vapour phase and $\mathbf{T} = \mu(\nabla \mathbf{u} + \nabla \mathbf{u}^T)$. In fact only the contribution from the liquid is considered, because $\mu_l \gg \mu_v$. Assuming a water/air interface (which not too different from a water/water vapour interface) we have a ratio of dynamic viscosity $\mu_{air}/\mu_{H_2O} = 0.018 \text{ mPa} \cdot \text{s}/1.0016 \text{ mPa} \cdot \text{s} \approx 0.02$. Inserting the scaling defined in the Eq. (2.76) and collecting only leading order contributions we have

$$\tilde{p} = p_v + P - \gamma(\partial_{\tilde{x}}^2 h + \partial_{\tilde{y}}^2 h), \quad (2.88)$$

where P accounts for all additional contributions to the pressure, e.g. the hydrostatic pressure, see for examples Eq. (2.31), but as well for the disjoining pressure $\Pi(h)$ Eq. (2.69).

Now that the normal stresses are balanced at the fluid vapour interface the same has to be done for the tangential stresses. Again we use Eq. (2.84) and compute the inner product with the tangential unit vectors \mathbf{t}_i

$$\mathbf{t}_i (\mathbf{T}_l - \mathbf{T}_v) \cdot \mathbf{n} + \mathbf{t}_i \cdot \nabla_S \gamma = 0. \quad (2.89)$$

The high viscosity contrast between the liquid and vapour allows us to neglect contributions from \mathbf{T}_v . Collecting leading order terms we have

$$\mu \partial_{\tilde{z}} \tilde{u}_x = \tau_x, \quad (2.90)$$

$$\mu \partial_{\tilde{z}} \tilde{u}_y = \tau_y. \quad (2.91)$$

Having defined the leading order equations for the flow velocity, the next step is to integrate them along the vertical dimension.

2.3.2 Vertical integration

The system of equations so far do not resemble Eq. (2.65). To get to Eq. (2.65) we still need to perform the integration along the vertical dimension. Dropping the tilde for now as all variables are dimensionless we have,

$$\iint (-\partial_x p + \partial_z^2 u_x) d^2 z = 0, \quad (2.92)$$

$$\iint (-\partial_y p + \partial_z^2 u_y) d^2 z = 0. \quad (2.93)$$

From Eq. (2.82) we know that the pressure gradient is conserved along z . Therefore integrating Eqs. (2.80, 2.81) twice with respect to z yields

$$u_x = \frac{\partial_x p}{2\mu} (z^2 - 2hz) + \frac{\tau_x z}{\mu}, \quad (2.94)$$

$$u_y = \frac{\partial_y p}{2\mu} (z^2 - 2hz) + \frac{\tau_y z}{\mu}, \quad (2.95)$$

where we used Eqs. (2.83, 2.90, 2.91) to determine the integration constants. In the following, many steps are fairly similar to the derivation of Sec. 2.2, however, it is instructive to proceed step by step. Performing another integration of the velocities with respect to the thickness to compute the discharge Q or volume flux

$$Q_x = \int_0^h u_x(z) dz = -\frac{h^3}{3\mu} \partial_x p + \frac{h^2}{2\mu} \tau_x, \quad (2.96)$$

$$Q_y = \int_0^h u_y(z) dz = -\frac{h^3}{3\mu} \partial_y p + \frac{h^2}{2\mu} \tau_y, \quad (2.97)$$

where due to the no slip boundary condition the mobility function $M(h)$, Eq. (2.66) naturally arises.

Now that the horizontal velocities are known we can simply integrate the continuity equation Eq. (2.10)

$$\int_0^h (\partial_x u_x + \partial_y u_y + \partial_z u_z) dz = 0, \quad (2.98)$$

making use of the Leibniz rule one more time and showing only the x component

$$\int_0^h \partial_x u_x(z) dz = \partial_x \int_0^h u_x dz + \partial_x 0 u_x(0) - \partial_x h u_x(h) = \partial_x Q_x - \partial_x h u_x(h), \quad (2.99)$$

where Eq. (2.96) was used. Inserting the above equation for the x and y -component into the Eq. (2.98) and performing the integration of $\partial_z u_z$ yields

$$\partial_x Q_x - (\partial_x h) u_x(h) + \partial_y Q_y - (\partial_y h) u_y(h) + u_z(h) - u_z(0) = 0. \quad (2.100)$$

Since the no-slip boundary condition holds for all velocity components we set $u_z(0) = 0$. The upper bound $u_z(h)$ can be computed using the material derivative, see Eq. (2.13). We apply the same transformation as in Eq. (2.41) with $f(\mathbf{x}, t) = h(\mathbf{x}, t) - z$, which is 0 at the interface yields

$$D_t f = \partial_t h + u_x \partial_x h + u_y \partial_y h - u_z = 0. \quad (2.101)$$

Inserting the found result for $u(h)$ into Eq. (2.100) we get

$$\partial_x Q_x + \partial_y Q_y + \partial_t h = 0, \quad (2.102)$$

which is almost the same as Eq. (2.65). Inserting Q_x and Q_y , Eqs. (2.96) and (2.97), we have

$$\partial_t h(\mathbf{x}, t) = \nabla \cdot \left(\frac{h^3}{3\mu} \nabla p + \frac{h^2}{2\mu} \tau \right), \quad (2.103)$$

which compared to Eq. (2.65) includes the shear contribution τ . Assuming the interface is not accelerated (e.g. in case of dewetting) the shear term can be neglected and the resulting equation is

$$\partial_t h(\mathbf{x}, t) = \nabla \cdot \left(\frac{h^3}{3\mu} \nabla p \right), \quad (2.104)$$

which completes the task to derive the thin film equation from the Navier-Stokes equation. To sum up the approach in one sentence, we non dimensionalized the variables, collected terms in orders of ε , used our boundary conditions and performed an integration along the vertical dimension to average out the vertical dynamics. Of course this derivation comes short if there are additional forces to consider such as thermal fluctuations, that said in Chap. 6 we discuss the effect of thermal fluctuations on dewetting and show how the thin film equation has to be modified.

Because the thin film equation is the main theoretical framework for the following Chaps. it is instructive to derive some more phenomenology of Eq. (2.104). One helpful tool is the so called linear stability analysis. The idea is to slightly perturb the system, Eq. (2.104), and derive its response to the perturbation.

2.3.3 Linear stability analysis

The concept of the linear stability analysis is a rather interesting one. One takes a stable solution of a mathematical system, in our case the thin film equation, and perturbs the stable solution. Will the system come back to the stable solution and therefore damp out the perturbation or will the system become unstable and open up a new branch in the phase space of solutions?

A simple example for this can be the string of a guitar. In the rest case, which forms a stable solution for the length of the string, the string is flat. If one gently touches the string a small perturbation is added and will undulate the string such that it starts to vibrate. The vibrations will turn into waves with well defined wavelengths. Most of them will be damped and usually only one wavemode will survive. The sound related to that wavemode defines the eigenmode of the string. Due to friction and

boundary conditions the string will come go back to be flat, which means that the string is linearly stable.

Using this analysis for the thin film equation we simply add a small perturbation to a flat film with

$$h(\mathbf{x}, t) = h_0 + \delta h(\mathbf{x}, t), \quad (2.105)$$

where h_0 is the thickness of the flat film and δh is the small, but dynamic perturbation. Small in this sense that $\delta h \ll h_0$. Now we follow the development of the perturbation and therefore quantify the stability of the system. The name “linear stability analysis” comes from the fact that one considers only terms up to $O(\delta h)$, but neglects higher orders of δh [LP00].

Inserting Eq. (2.105) into Eq. (2.104) yields

$$\partial_t(h_0 + \delta h) = \nabla \cdot \left\{ \frac{(h_0 + \delta h)^3}{3\mu} \nabla [-\gamma \Delta(h_0 + \delta h) - \Pi(h_0 + \delta h)] \right\}, \quad (2.106)$$

where the pressure term has been written explicitly in terms of the Laplace and the disjoining pressure. Using the fact that h_0 is constant and thus $\nabla h_0 = \partial_t h_0 = 0$ we can compute the derivatives

$$\partial_t \delta h = \frac{h_0^3}{3\mu} \left[-\Pi'(h_0) \nabla^2 \delta h - \gamma \nabla^4 \delta h \right], \quad (2.107)$$

where $\Pi'(h_0)$ is a short notation for

$$\Pi'(h_0) = \left. \frac{\partial \Pi(h)}{\partial h} \right|_{h=h_0}. \quad (2.108)$$

Instead of solving this equation in real space it is simpler to solve it in Fourier space. This further means that a wavelength λ in real space becomes a wavemode q in Fourier space. Fourier transforming the perturbation δh we have

$$\tilde{\delta h}(\mathbf{q}, t) = \int_{-\infty}^{\infty} \delta h(\mathbf{x}, t) e^{-i\mathbf{x}\cdot\mathbf{q}} d\mathbf{x}. \quad (2.109)$$

Under the Fourier transformation the derivatives become wavevectors (\mathbf{q}) and Eq. (2.107) reads

$$\partial_t \tilde{\delta h}(\mathbf{q}, t) = \frac{h_0^3}{3\mu} \left[-\Pi'(h_0) \mathbf{q}^2 \delta h - \gamma \mathbf{q}^4 \delta h \right]. \quad (2.110)$$

From the above equation one can readily read the dispersion relation $\omega(q)$ as

$$\partial_t \tilde{\delta h} = \omega(q) \tilde{\delta h}, \quad (2.111)$$

$$\omega(q) = \frac{h_0^3}{3\mu} \left[-\Pi'(h_0) q^2 - \gamma q^4 \right], \quad (2.112)$$

where $q = \sqrt{q_x^2 + q_y^2}$. To find the fastest growing unstable wavemode q_0 which is also called the eigenmode of the (spinodally dewetting) film we set the left hand side equal to 0 and solve for q

$$\partial_t \tilde{h} = 0, \quad (2.113)$$

$$\frac{h_0^3}{3\mu} q^2 [-\Pi'(h_0)\delta h - \gamma q^2 \delta h] = 0, \quad (2.114)$$

$$-\Pi'(h_0) - \gamma q^2 = 0, \quad (2.115)$$

$$q_0 = \sqrt{\frac{-\Pi'(h_0)}{\gamma}}. \quad (2.116)$$

An example of a dispersion relation which follows the above equation is shown in Fig. 2.5. In this figure we can identify two relevant wave numbers, on the one hand there is q_0 which is the fastest growing mode indicated by a dotted line and there is $q_m = \sqrt{2}q_0$ which is the largest wave number that is not damped. Wavemodes larger than q_m are therefore damped out. A characteristic time scale of the problem is given as

$$t_0 = \frac{3\mu}{\gamma h_0^3 q_0^4}, \quad (2.117)$$

which is used to normalize the time in Fig. 2.5. Because the concept of linear stability is such an important one, we encounter it again in Chap. 5 see Fig. 5.3 as well as in Chap. 6 see Figs. 6.1, 6.7, 6.8, 6.11. Chap. 6 focuses only on the addition of a fluctuating term and the so called stochastic thin film equation. The new term due to thermal fluctuations offers some interesting features on both the structure factor as well as the dispersion.

2.4 Differences and Overlap

The theoretical starting point of this chapter is the Navier-Stokes equation. This equation relates the change of momentum of the fluid to various effect, e.g. viscous contributions. As of today, nobody has solved the Millennium problem and showed that there exist a unique and smooth solution to this equation. A well defined solution would have the benefit that even complex flow fields could be computed using analytical methods, such as pen and paper. What we can do, is computing approximative results of this equation using numerical techniques. This is in fact the idea of the following chapter. Mathematically the incompressible Navier-Stokes equation is a second order partial differential vector equation. It can be considered hyperbolic if the flow is advection dominated or parabolic if it is diffusion dominated. The Reynolds number is the one dimensionless number that helps to distinguish between these two regimes.

For many flows we actually do not need to solve the Navier-Stokes equation. In Sec. 2.2 we introduce the concept of dimensional reduction by integrating out the horizontal degrees of freedom. This reduction is build on the fact that we consider

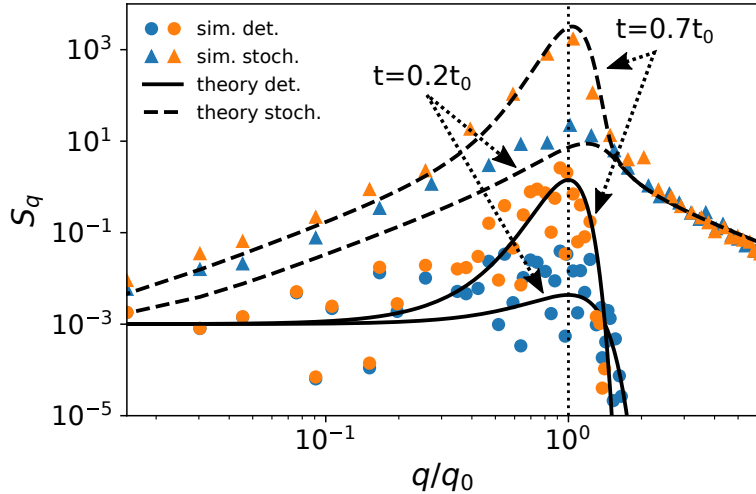


Figure 2.5: Dispersion relation of a spinodally dewetting thin film with and without thermal fluctuations. Where $S(q)$ is the structure factor depending on the wavemode q . The dots and triangles are generated using the here presented numerical method. Full and dashed lines are the theoretical prediction based on Eq. (2.65) and its fluctuating extension, Eq. (6.29).

two length scales, a vertical and horizontal scale, with a scaling parameter ε . Applying this scaling and collect terms in orders $O(\varepsilon)$ we derive a different continuity and momentum equation, see Eqs. (2.63-2.64). We exchange the fluid density $\rho(\mathbf{x}, t)$ for a fluid “height” $h(\mathbf{x}, t)$, which is measured from the bottom topography to the fluid/vapour interface. The resulting set of equations, Eqs. (2.63-2.64), are hyperbolic partial differential equations. Assuming that \mathcal{S} in Eq. (2.64) is a Newtonian viscous stress analogue to Eq. (2.7) we have a second order vector equation in (h, u_x, u_y) . The shallow water equations covers a wide ranges of geophysical flow problems, from slowly creeping lava to quickly evolving weather systems. At no point in the derivation of the theory we required that dimensionless numbers, such as the Reynolds number, are small or vanishing. In fact it straightforward to derive the inviscid shallow water equations for large Reynolds numbers. An interesting phenomenon that can be explained with the inviscid shallow water equations are soliton like solutions. These solutions are stable travelling waves with a constant velocity and no dispersion, famous examples are tsunamis and river bora. One word of caution these solutions are valid in “open” water, as soon as these waves come close to shore the breaking wave dynamics cannot be explained with the simple set of equations we derived here. In most of the shallow flows considered here the fluids viscosity is at most subleading. Which does not mean that there are no models considering viscosity, see for example Ref. [Mar07]. The main source of friction and thus dissipation is however the interaction with the bottom topography, we for example required that the flow velocity vanished at $z = -h(x, y)$. Lastly, in our derivation we did not consider surface tension as a leading order contribution to the shallow water equations. The shape of the fluid/vapour interface is driven by the hydrostatic pressure.

The last model we introduce in this chapter is the thin film equation, Eq. (2.104). In Sec. 2.3 we start with a discussion on the phenomenology of thin film flows and peculiarities of modelling wetting and contact line dynamics. If we leave aside the disjoining pressure $\Pi(h)$, see Eq. (2.69), and only consider the capillary pressure (Δh), the thin film equation is a degenerate, fourth order parabolic partial differential equation of the film thickness $h(\mathbf{x}, t)$ [Pes18a]. In contrast to the shallow water equations and the Navier-Stoke equation, the thin film equation is a single scalar equation. Therefore there is no momentum equation, but only a continuity equation for the film thickness. The thin film equation is a highly non-linear equation similar to both the Navier-Stoke and the shallow water equations. One example for these non-linearities is the dynamics of droplet formation after rupture of an unstable thin film. The equation allows for many instabilities such as fingering, tearing and pearling [CM09; Wil+17]. The steps to derive the thin film equation are in parts similar to the shallow water system. Starting with a rescaling of the continuity equation, Eq. (2.10), and the Navier-Stokes equation, Eq. (2.14) (with $\mathbf{F} = 0$) and assuming that one dimension is much smaller than the others. However, in contrast to shallow water system this scaling ansatz we choose is only suitable for negligible inertial contributions. Terms are then collected in orders of ε similar to the shallow water derivation. The boundary condition at $z = 0$ is another shared feature between the shallow water equations and the thin film equation, at least for the no-slip mobility Eq. (2.66). If we relax this boundary condition, which is the case in the following chapters, then we introduce a so-called slip length which is not accounted for in the shallow water equations. The stress balance at the liquid/vapour interface is another difference between the shallow water equation and the thin film equation, for the normal stress component we have Eq. (2.84). We have another balance equation for the tangential stress with Eq. (2.89). Balancing the surface stresses also introduces the surface tension, a contribution that keeps the liquid/vapour interface minimal. To reduce the dimensionality of the problem we perform an integration along the vertical direction, similar to the shallow water derivation. In the last step we use the material derivative, Eq. (2.13), to compute a relation between the flow velocity at the liquid/vapour interface and the discharge \mathbf{Q} . Because of Eqs. (2.96-2.96) we know that the discharge is pressure dependent, and thus we end up with Eq. (2.104). The velocities are therefore effectively captured by a pressure gradient and if applicable a shear rate τ .

While there are many similarities between the thin film equation and the shallow water equations, there are also some major difference. The most pressing difference between these two models is the fact that the shallow water equation is a vector equation while the the thin film equation is a scalar equation. In the shallow water equations the liquid/vapour interface is driven by hydrostatic pressure while in the thin film equation we neglect the hydrostatic pressure and introduce surface tension and capillarity. The question that naturally arise here is: can one model be translated into the other one? Although this question seems odd at first it is actually of great significance to show that problems can be solved with different approaches. There are several numerical methods to iteratively solve the thin film equation. There are as

well several different numerical methods to approximate the Navier-Stokes equation. The important contribution to our understanding of CFD is that methods build to solve the shallow water equations can actually be used to solve the thin film problem, as discussed in Chap. 5

3 Method

Du bist schön, aber dafür kannst du nichts. Weder Lesen, noch Schreiben, noch was anderes.

Alligatoah

Based on the theory discussed in the previous chapter it is possible to build a model for numerical simulations. Numerical simulations have been at the heart of fluid dynamics for a long time. This is mainly because of two statements. On the one hand we cannot find an analytical solution to every given flow problem, which is due to the shape and the structure of the Navier-Stokes equations. In fact there are only a few flows that admit an analytical solution. They are often referred to as benchmark problems. One of those is the famous "Hagen–Poiseuille flow", see Sec. 2.2, which is an analytical solution for a flow field in a canal and was first derived by Poiseuille and Haagen in the 18th century [Sut93]. There are a few other benchmark problems, especially in the low Reynolds number regime with a small or vanishing Stokes number¹. The so called Stokes flows admit time reversal symmetry and many have theoretical solutions. But going from laminar to turbulent flows with high Reynolds numbers poses still a problem, or as R. Feynman once said: "... the most important unsolved problem of classical physics."

On the other hand solving differential equations with numerical tools is a story of success. Long before any computer was build, iterative methods for approximating a solution to a given differential or integral equation have been developed. Leonhard Euler published his findings about what we call today the "Euler-method" already in the 18th century [BW12]. On the blink to the 20th century Carl Runge and Martin Kutta developed the method nowadays called "Runge-Kutta Method" which is of better accuracy than a plain Euler solver [W01; Run95].

Several physics problems are being studied to large extent with numerical tools, quantum field theory [MM94], solid mechanics [CD21], and as outlined in the introduction Chap. 1 computational fluid dynamics (CFD) is one of those fields. Although chip manufacturers have a hard time to keep up with Moore's law, computing power is still growing rapidly [Sch97]. Of course instead of ever faster processors (measured in clock rate), the trend goes in the direction of parallel and accelerated computing. Several accelerator designs hit the market around 2020, one design that works par-

¹The Stokes number is a dimensionless number that defines the behaviour of particles suspended in a flow and can be calculated with $St = \frac{t_0 u_0}{l_0}$, where t_0 is a relaxation time of the particles, u_0 is a characteristic velocity and l_0 is a characteristic length scale.

ticularly well as accelerators are graphics processing units (GPUs). While a GPU lacks the complexity of a CPU it excels at doing simple task over and over again. For example the generation of colorful pixels for a monitor. It turns out that several algorithms developed for solving differential equations are well suited to be calculated on the GPU. Among them is the lattice Boltzmann method, at least a very basic implementation of the method. GPUs however are not the only devices to be used as accelerators. Intel for example used a different approach to accelerator computing and already some time ago developed the Xenon Phi. However with lack of performance as compared to Nvidia's graphics cards and company intern decisions Intel ended the Xenon Phi project in 2020. The successor of the Xenon Phi project is the very recent *oneAPI* approach and its hardware [CS20]. Shifting the focus towards heterogeneous compute architectures, or as Rick Stevens² said: "The future of advanced computing requires heterogeneous hardware to maximize the computing power needed for exascale-class workloads. The oneAPI industry initiative Intel is spearheading will ensure that programming across diverse compute architectures is greatly simplified." Not only is this Intel's idea but a general trend in high performance computing (HPC) moving from CPU only clusters to heterogeneous hardware. Apart from Intel more and more companies joined the development of workload optimized hardware. Which is possible not only but also due to the technological inventions from arm (Advanced RISC Machines) and other system on a chip (SoC) design companies. SoC designs optimized for specific workloads is the key business of arm, which is a paradigm change of the industry. For the longest time established chip manufactures also defined the designs of a chips. Today SoC designs can be manufactured at project manufacturers with TSMC (Taiwan Semiconductor Manufacturing Company Limited) being one of them. TSMC is also the world leader in the production of semiconductors for computer chips. They moved the resolution limit for single transistors from 12nm to about 5nm in roughly 5 years. These technological steps allowed on the other hand companies such as Apple to design SoCs for their specific needs. The M1 Max is from this perspective a very interesting device, although it is not an x86 design.

Coming up in this chapter is a short overview of numerical methods to iteratively solve the thin film equation, Eq. (2.104). Starting with the straightforward finite differences approach and an introduction of the Courant Friedrichs Lewy (CFL) condition [CFL28]. We then discuss the possibility to use the bottom up approach and solve Newton's equation of motion for every molecule. Followed by a short introduction to the main method of this work, the lattice Boltzmann method [FHP86; Krü+17; Suc01]. The mathematical framework as well as its link to kinetic theory will be discussed and the idea of the Chapman-Enskog expansion will be outlined [CC90; Ens17]. Based on this mathematical model we can define a numerical approach. Using assumptions, mainly concerning the collision operator, the resulting algorithm is fairly easy to implement and shows good scalability. This closes the loop with the above statement that the resulting source code is a perfect candidate for GPU programming.

²Rick Stevens is Professor at the Department of Computer Science and Associate Laboratory Director, Computing, Environment and Life Sciences at Argonne National Laboratory.

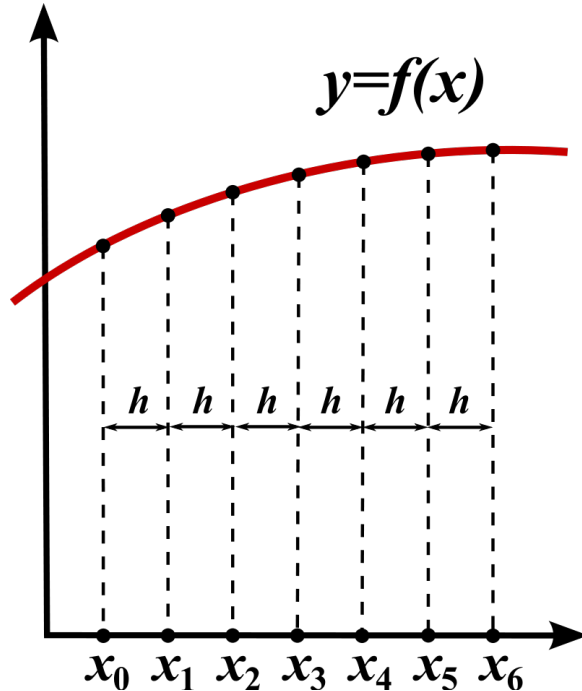


Figure 3.1: Discretization of a continuous function y (in red) along a discrete space x (x_0, x_1, x_2, \dots). Consecutive points on the x-axis are separated by a uniform distance h .

3.1 Numerical Methods

The lattice Boltzmann method is one among many to simulate the behaviour of a fluid. Especially when it comes to numerical simulations of the thin film equation, see Eq. (2.65), other numerical approaches are more established and have been successfully applied for more than thirty years [Bec+03; Pes+19; DMS05; MR05; DKB00; SE98]. The thin film equation is a non-linear (stiff) fourth order PDE which requires choosing an appropriate scheme, because not every numerical scheme will be able to provide first stability and second a correct approximation of the solution. A numerical scheme is a blue print of how to discretize derivatives and arrange terms such that an iterative process converges towards a solution. That said, developing new numerical schemes for PDEs is still a very active research area. One way to compute this differential operators on a computer is via finite differences.

3.1.1 Finite differences

Using finite differences means nothing more than discretizing the continuous problem into small (infinitesimal) discrete segments. Figure 3.1 illustrates a discretization approach where the function $f(x)$ is approximated by a finite set of points which are shown as black dots on the red line. At every point x_i along the x-axis we know the value of the function $f(x_i)$. This however does not mean that we know the value

of $f(x)$ at arbitrary x values and even worse we do not know $\partial_x f(x_i)$ at x_i . For a continuous function, e.g. the film thickness $h(\mathbf{x}, t)$, we can analytically compute the derivatives. Here we are left with a discrete set of point and have yet to come up with an idea to calculate $\nabla h(\mathbf{x}_i, t)$, which is crucial to compute the film pressure, Eq. (5.11).

Discretization of a derivative is a long studied problem [BM72; JJ65]. The Taylor expansion gives us a tool to approximate the solution to a differential. In one spatial dimension there are three different methods to compute the derivative, neglecting boundary conditions there is

$$\partial_x f(x_i) = \frac{f(x_{i+1}) - f(x_i)}{h}, \quad (3.1)$$

where h is the spacing between two consecutive points as introduced in Fig. 3.1. Subtracting the value of the function $f(x_{i+1})$ from $f(x_i)$ is called forward difference. Changing the interval the backward difference is given as

$$\partial_x f(x_i) = \frac{f(x_i) - f(x_{i-1})}{h}. \quad (3.2)$$

Both the forward as well as the backward differential are first order in their error, beyond first order is the central difference approach

$$\partial_x f(x_i) = \frac{f(x_{i+1}) - f(x_{i-1})}{2h}, \quad (3.3)$$

where the value of the derivative is averaged over a larger interval. The second derivative is than simply applying the differential operator (forward, backward, central) to the first derivative, in case of central difference this yields

$$\partial_x^2 f(x_i) = \frac{f(x_{i+1}) - 2f(x_i) + f(x_{i-1})}{2}. \quad (3.4)$$

However all finite difference schemes suffer from the concrete choice of the discretization, which is often referred as discretization artifacts. The starting equation is usually a continuous one in both space and time, but the numerical solver requires a discretized system. This can be done as shown in Fig. 3.1 by introducing a grid for the spatial dimensions. For now we assume that we can the same to the time and put the temporal dimension into a discrete grid. To understand the error one makes using finite difference we use the example of a sine wave. We mark two points along the curve and connect them, which yields a straight line. Therefore all information in between the points is lost, instead of $y(x) = \sin(x)$ one would guess $y(x) = kx + d$ for the points. Besides the fact that information about the function is lost it still could be a good enough approximation for the derivative, especially if the points are not too far apart. Increasing the number of points along the curve, thus making h smaller, will increase the accuracy of the resulting approximation as displayed in Fig. 3.1. A good approximation for $y(x) = \sin(x)$ requires therefore more than just two points.

Which explains the so called fidelity of the finite difference method [Gur02]. One needs a fine enough grid to resolve the to be studied dynamics, but the smaller the spacing h gets the more numerically demanding is the calculation.

In fact there are further limitations to the problem of numerically approximating a PDE. Numerical methods for PDEs, e.g. the thin film or the wave equation, need to satisfy the CFL condition [CFL28]. Beyond other things it states that choosing an increment for time cannot be independent of the spatial resolution. This condition can be formalized as

$$C = \Delta t \left(\sum_{i=1}^n \frac{u_{x_i}}{\Delta x_i} \right) \leq C_{max}, \quad (3.5)$$

with Δx_i and Δt being the spatial and temporal increment, respectively and u_{x_i} being the magnitude of the velocity in the respective direction. In case of Fig. 3.1 we have $\Delta x = h$. Behind this concept is the idea that propagation of information has an upper limit. For fluid dynamic problems this upper limit is the speed of sound, in electrodynamics it would be the speed of light. Any propagation larger than this upper limit introduces stability issues. These issues are purely numerical as we know that air can flow with velocities larger than the speed of sound, however by doing so the flow creates a so called shock.

Thinking about a wave package, numerically it should be ensured that several time iterations are computed before the package has reached the next spatial point of the grid. The maximal value that the Courant number can reach for an explicit solver, to which for example the lattice Boltzmann method belongs (assuming a BGK collision operator), is $C_{max} = 1$. For implicit methods the maximal Courant number can be larger than one. The iteration from $u(x_i, t_0)$ to $u(x_i, t_1)$ is called a time step. The “distance” between consecutive time values, here $\Delta t = t_1 - t_0$ must ensure that forces and therefore acceleration are well within the stability condition Eq. (3.5).

A very specific finite difference scheme with good stability features is the Crank-Nicolson method [CN47; Pre+07]. This method is second order in time and implicit and has been successfully applied to thin film problems, see for example Refs. [DKB00; DGF16; Mün05].

3.1.2 Spectral methods

Another strategy to solve a differential equation is to perform a transformation. One rather famous transformation is the Fourier Transformation (FT), which we have used to find the dispersion relation in Sec. 2.3 and will encounter again in Chap. 6. The set of solvers using a FT to solve a given differential equation is called spectral methods. Doing so has the advantage of interchanging the derivatives with simple multiplications. For example the term $\partial_x f(x)$ transforms to

$$\partial_x f(x) = q \cdot \tilde{f}(q), \quad (3.6)$$

where $\tilde{f}(q)$ is the Fourier transformed of $f(x)$, e.g. $\tilde{f}(q) = \delta(q - a/2\pi)$ for $f(x) = e^{i a x}$. Instead of solving a differential equation one solves an algebraic equation, or a set of

algebraic equations. While it is often straightforward to perform the transformation it can become problematic to perform the backward transformation. Usually the expressions are fairly complicated and often the backward transformation into real space is not easy to perform. In Chap. 6 we arrive at such an expression for the structure factor $\mathcal{S}(q, t)$. A structure factor is a measure of the distribution of length scales, roughly speaking. In this specific case there is no need for a backward transformation because (scattering) experiments usually supply data in Fourier space.

However, when simulating the thin film equation we may be interested in forces, pressures or simply the thickness $h(\mathbf{x}, t)$, which is why we need a backward transformation. Numerically speaking the operators for transformations are matrices, which depend on the explicit problem. Solutions in real space are generated by inversion of these operators and therefore by inversion of an (arbitrary) matrix. Computing the inverse of a matrix is a demanding problem. Nevertheless, these transformation approaches are often quite helpful finding an exact solution. One rather prominent example is the computation of Green's functions, e.g. in electrostatics [Gre89]. For the shallow water theory, see Sec. 2.2, one class of effective methods are the (discontinuous) Galerkin methods [EG04] and to some extent the related finite element method (FEM).

Literature concerning simulations of the thin film equation using spectral solvers is rather sparse. That does however not mean that spectral methods are ill suited for this specific problem. Durán-Olivencia, M. et al. have shown that a spectral method is not only able to simulate the thin film equation but also they also included thermal fluctuations and were able to simulate the stochastic thin film equation [Dur+19].

3.1.3 Molecular dynamics

The third approach we discuss in this section is the molecular dynamics method (MD) [Hai97; ZSL19; Wen+00]. When we solve the equations of motion of molecules we do not per se think of a **thin** film flow, however molecular dynamics can be very insightful when dealing with thin film problems. In Sec. 2.3 we introduced the term wetting and the three phase contact line. Advancement of the three phase contact line can be boiled down to the interaction between fluid molecules and substrate molecules, therefore MD is perfectly suited to study e.g. slip [JAT99; Seg+13]. Instead of working with macroscopic fields, such as density ρ or velocity \mathbf{u} , the method uses a bottom up approach. The main idea is to compute the trajectory of every particle using Newton's equation of motion, therefore to assume that particles are classical objects. Interactions as well as boundary conditions can be added via pair potentials. A common interaction potential is the Lennard-Jones potential

$$U(r_{ij}) = 4\epsilon \left[\left(\frac{\sigma}{r_{ij}} \right)^{12} - \left(\frac{\sigma}{r_{ij}} \right)^6 \right], \quad (3.7)$$

where ij denotes the particle pair, ϵ and σ are the model dependent energy and length parameters, respectively. Clearly this approach is rather elegant. Knowing the correct

values for σ and ε , the simulations show good agreement with experiments [ZSL19]. Which is quite impressive if we take into account that the method is considered noisy.

However there is no free lunch. Because of the microscopic nature of this method it is compute intensive. Per definition the method needs to know the phase space coordinates, thus the position and the velocity, of every particle. While it is possible to arrange this information efficiently, the computation of the pair potential quickly becomes quite resource demanding in terms of computational power. The results from the computation of pair potentials are forces which act on the particles. This surmounts to a lot of computational resources for small physical volumes, which is in the context of fluid flows and film formation problematic. Assuming a box of a few nanometers in all directions and a physical time of about a picosecond ($10^{-12}s$) is already a lot to do for a common laptop. Clearly a lot is depending on the implementation of the algorithm. There are well developed, open source and supported software solutions that not only scale well but have a mature user interface, e.g. LAMMPS and GROMACS [Pli95; Bvv95; LHv01]. However all this development cannot overcome that this method is suited only for relatively small systems and not for macroscopic scales.

Another problem that is inherent to MD simulations is the vast zoo of interaction potentials. Water for example is not a Lennard-Jones liquid and therefore the potential Eq. (3.7) cannot be used or water-water interactions. Although water seems to be a simple molecule with just two hydrogen atoms and one oxygen atom it is in fact a rather complex substance to simulate. There exists not a single model for how water should interact but several, all with very fine tuned adjustments. Some include for example the polarity of the water molecule while others neglect it. Without knowing why a certain water model is more suited than another one, this approach can come down to a black box. This method therefore requires a lot of literature knowledge and validation with both theory and where possible with experiments. That said apart from Zhang et al. [ZSL19] MD has been used on a diverse set of thin film related problems such as pearling [Kop+06], dewetting [Ber+07] or dynamics of droplets [LX15; Wan+15] to name just a few.

3.2 The Lattice Boltzmann Method

The lattice Boltzmann method is as the name suggests a discretization approach to the Boltzmann equation [Krü+17; Suc01; Wol04]. Boltzmann more than a hundred years ago introduced a model that was built on the assumptions that atoms and molecules move classically. This was actually just a small portion of his groundbreaking work which forms a whole subsection of physics called statistical mechanics. He as well knew that there are a lot of oxygen, nitrogen and other atoms that make up the content of air we inhale with a single breath. In 1811 already Avogadro calculated that rough number of molecules and around fifty years later Loschmidt came to a

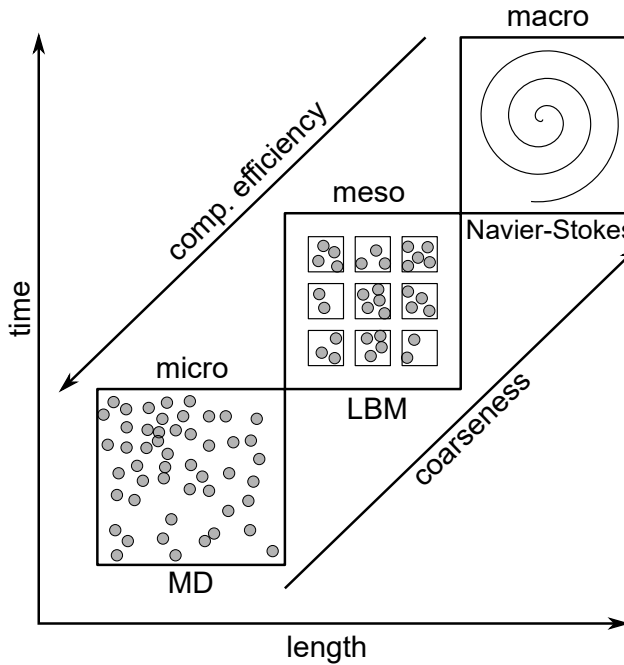


Figure 3.2: Schematic display of how different approaches relate to different length and time scales. The finer the system is resolved the more computing resources are needed.

similar result [Ava11; Los66]

$$n = \frac{pN_A}{RT}, \quad (3.8)$$

where n is the number density, p the pressure, R the gas constant and T the temperature. The constant named after Avogadro (N_A) states that a mole of any substance has about $6 \cdot 10^{23}$ atoms. Boltzmann's ingenious idea, this adjective is justified as even mathematicians find statistical mechanics appealing, to solve the dynamics of this complex coupled system was to use a statistical ansatz. Instead of solving the equations of motion for every particle, which is the idea of MD, Boltzmann decided to introduce distribution functions $f(\vec{x}, \vec{\xi}, t)$, which depend on position, momentum and time and generate an ensemble. However, to introduce these distribution functions $f(\vec{x}, \vec{\xi}, t)$ we must make a guess how the atoms or molecules behave in a gas. We actually shortly discussed one of these guesses in Sec. 2.1 already. The ideal gas is a well working model that assumes that the atoms or molecules in a gas are indistinguishable point particles. Furthermore these particles do not attract or repel each other, neglecting e.g. electrostatic forces. The mean free path of these particles is much larger than their physical size. Both of these assumptions are actually quite good, because a gas at room temperature and ambient pressure of one bar is a very dilute fluid. The particles move in random directions with velocities given by a distribution that depends on temperature. The only way to transfer energy between particles is via elastic collisions. This model works exceptionally well for many problems and has

been validated experimental numerous times. Clearly there are shortcomings to the ideal gas, for example at low temperature and high pressures when intermolecular interactions become important. However for the scenarios considered in this thesis, the ideal gas serves as a good foundation to the lattice Boltzmann method.

Figure 3.2 illustrates the idea coming from either a macroscopic system or a microscopic system. Instead of dealing with every atom or molecule, which is displayed in the bottom left of the figure, it is also possible to use a more coarse approach which is shown in the centre of the figure where distributions over ensembles of particles are used [Raa04]. Therefore instead of working in the microscopic world the lattice Boltzmann method works in a mesoscopic regime. Making it computationally more efficient than e.g. MD for a larger class of problems. Of course, it is also possible to use a coarser approach and in fact a lot of the classical Navier-Stokes solvers operate in the upper right of Fig. 3.2, see Sec. 4.2 for some example solvers.

3.2.1 The Boltzmann equation and macroscopic conservation equations

The dynamics of these distributions f can be formalized and put into an evolution equation which is called the Boltzmann equation

$$\partial_t f + \vec{\xi} \cdot \vec{\nabla} f + \frac{1}{\rho} \vec{F} \cdot \partial_{\vec{\xi}} f = \Omega(f), \quad (3.9)$$

where $\vec{\xi}$ is the momentum. The first two terms describe the advection of the distribution due to the atoms and the third term measures the effect of a force \mathbf{F} on the momentum [Krü+17]. On the right side of the equation is an arbitrary complex term, the collision operator. This operator accounts for all collisions the atoms or particles perform at any given instance of time. In principle this operator cannot be computed analytically, because one would need to take into account all possible collision terms from two up to n-point interactions.

However with a smart ansatz it is possible to find a suitable approximation to the collision operator. One ansatz we can make is,

1. The fluids state is not far from its equilibrium.
2. During the collision it approaches its equilibrium with a relaxation time τ .

Bhatnagar, Gross and Krook (BGK) were the first ones who worked out the mathematical model behind this ansatz [BGK54]. This model can be formalized quite simply and reads

$$\Omega(f) = -\frac{1}{\tau}(f - f^{eq}), \quad (3.10)$$

where f^{eq} denotes the equilibrium distribution function,

$$f^{eq}(\vec{x}, |\vec{v}|, t) = \rho \left(\frac{1}{2\pi RT} \right)^{3/2} e^{-|\vec{v}|^2/(2RT)}, \quad (3.11)$$

which is called Maxwell-Boltzmann distribution. The moments of the BGK collision operator satisfy the following set of equations

$$\int \Omega(f) d^3\xi = 0, \quad (3.12)$$

$$\int \vec{\xi} \Omega(f) d^3\xi = \vec{0}, \quad (3.13)$$

$$\int |\vec{\xi}|^2 \Omega(f) d^3\xi = 0, \quad (3.14)$$

$$\int |\vec{v}|^2 \Omega(f) d^3\xi = 0. \quad (3.15)$$

The first of the above equations states that the mass is conserved, while Eq. (3.13) ensures momentum conservation. Eqs. (3.14, 3.15) tell us that both that the total energy as well as the internal energy are conserved. Note that \vec{v} is a relative velocity which measures the deviation $\vec{v}(\vec{x}, t) = \vec{\xi}(\vec{x}, t) - \vec{u}(\vec{x}, t)$.

Taking this four constraints into consideration as well as the two points above one finds that the BGK operator is the simplest one to satisfy them all. With one side note however, the full collision operator from Boltzmann does predict a different Prandtl number (Pr) than the BGK yields. The Prandtl number $Pr = \nu/\alpha$ measures viscosity against thermal diffusivity (α). Using BGK one gets $Pr = 1$ while monoatomic gases or Boltzmann's operator showing $Pr \approx 2/3$ [Cer88; Krü+17].

The Boltzmann equation, Eq. (3.9), was developed as an evolution for a gas and is build upon distributions of microscopic particles, e.g. Eq. (3.11). Using the BGK approximation for the collision operator we found that its moments conserve mass, momentum and energy. The next step is to show that the Boltzmann equation with the BGK operator obeys macroscopic conservation equations, as such Eq (2.3) and Eq. (2.14). For the mass conservation we compute the zeroth moment of Eq. (3.9), therefore integrate it over the velocity space

$$\partial_t \int f d^3\xi + \partial_{x_\beta} \int \xi_\beta f d^3\xi + \frac{F_\beta}{\rho} \int \partial_{\xi_\beta} f d^3\xi = \int \Omega(f) d^3\xi, \quad (3.16)$$

with moments of f given by

$$\Pi_0 = \int f d^3\xi = \rho, \quad (3.17)$$

$$\Pi_\alpha = \int \xi_\alpha f d^3\xi = \rho u_\alpha, \quad (3.18)$$

$$\Pi_{\alpha\beta} = \int \xi_\alpha \xi_\beta f d^3\xi, \quad (3.19)$$

$$\Pi_{\alpha\beta\gamma} = \int \xi_\alpha \xi_\beta \xi_\gamma f d^3\xi. \quad (3.20)$$

From Eq. 3.12 we know that the right hand side of Eq. (3.16) is zero, furthermore the force term is vanishing as well, because [Krü+17]

$$\int \partial_{\xi_\beta} f d^3\xi = 0. \quad (3.21)$$

The non vanishing contributions, thus the first two integrals on the left hand side are given by Eqs. (3.17-3.18) and therefore we get

$$\partial_t \rho + \partial_{x_\beta} (\rho u_\beta) = 0, \quad (3.22)$$

which is the macroscopic continuity equation, see Eq. (2.3). This is actually a quite remarkable result, because we did not need to specify f during this derivation and therefore any distribution function f satisfies mass conservation.

For the momentum conservation we take the first moment of Eq. (3.9), thus we multiply with ξ and integrate

$$\partial_t \int \xi_\alpha f d^3\xi + \partial_{x_\beta} \int \xi_\alpha \xi_\beta f d^3\xi + \frac{F_\beta}{\rho} \int \xi_\alpha \partial_{\xi_\beta} f d^3\xi = \int \xi_\alpha \Omega(f) d^3\xi. \quad (3.23)$$

The right hand side is vanishing according to Eq. (3.13). The first two integrals on the left hand side can be found from Eqs. (3.18-3.19). For the force term we use integration by parts and get

$$\int \xi_\alpha \partial_{\xi_\beta} f d^3\xi = - \int \partial_{\xi_\beta} \xi_\alpha f d\xi^3 = -\rho \delta_{\alpha\beta}. \quad (3.24)$$

Collecting the non zero contributions we have

$$\partial_t (\rho u_\alpha) + \partial_{x_\beta} (\Pi_{\alpha\beta}) = F_\alpha, \quad (3.25)$$

with $\Pi_{\alpha\beta}$ being the momentum flux tensor, which can be decomposed into

$$\Pi_{\alpha\beta} = \rho u_\alpha u_\beta + \int v_\alpha v_\beta f d^3\xi, \quad (3.26)$$

with

$$\sigma_{\alpha\beta} = - \int v_\alpha v_\beta f d^3\xi, \quad (3.27)$$

being a stress tensor. Inserting Eqs.(3.26-3.27) into Eq. (3.25) we have,

$$\partial_t (\rho u_\alpha) + \partial_{x_\beta} (\rho u_\alpha u_\beta) = \partial_{x_\beta} \sigma_{\alpha\beta} + F_\alpha. \quad (3.28)$$

This equation is rather similar to Eq. (2.6) or Eq. (2.14), however we cannot solve it yet as we are not able to compute the stress tensor without further knowledge on f .

For completeness let us also compute the energy conservation. We therefore multiply Eq. (3.9) with $\xi_\alpha \xi_\alpha$, thus the trace of the second moment, and integrate

$$\partial_t \int \xi_\alpha \xi_\alpha f d^3\xi + \partial_{x_\beta} \int \xi_\alpha \xi_\alpha \xi_\beta f d^3\xi + \frac{F_\beta}{\rho} \int \xi_\alpha \xi_\alpha \partial_{\xi_\beta} f d^3\xi = \int \xi_\alpha \xi_\alpha \Omega(f) d^3\xi. \quad (3.29)$$

The collision term vanishes again and for the force term we apply integration by parts once more,

$$\int \xi_\alpha \xi_\alpha \partial_{\xi_\beta} f d^3\xi = - \int \partial_{\xi_\beta} (\xi_\alpha \xi_\alpha) f d^3\xi = -2\rho u_\beta. \quad (3.30)$$

Collecting all non zero terms yields

$$\partial_t(\rho E) + \frac{1}{2} \partial_{x_\beta} \Pi_{\alpha\alpha\beta} = F_\beta u_\beta, \quad (3.31)$$

where ρE is the total energy density. Decomposing $\Pi_{\alpha\alpha\beta}$ similarly to Eq. (3.26) we find

$$\partial_t(\rho E) + \partial_{x_\beta}(\rho u_\beta E) = \partial_{x_\beta}(u_\alpha \sigma_{\alpha\beta}) + F_\beta u_\beta - \partial_{x_\beta} q_\beta, \quad (3.32)$$

where we used

$$q_\beta = \int v_\alpha v_\alpha v_\beta f d^3\xi, \quad (3.33)$$

with \vec{q} being the heat flux.

Both the stress tensor, Eq. (3.27), and the heat flux, Eq. (3.33), cannot be derived without specifying f . However, the only distribution we have readily available is the equilibrium distribution f^{eq} , Eq. (3.11). This marks the starting point for the famous Chapman-Enskog expansion, which was derived around a hundred years ago [CC90; Ens17]. The idea is to use a perturbative expansion for f around f^{eq} and ∂_t ,

$$f = f^{eq} + \epsilon f^{(1)} + \epsilon^2 f^{(2)} + O(\epsilon^3), \quad \partial_t = \partial_{t_0} + \epsilon \partial_{t_1} + O(\epsilon^2), \quad (3.34)$$

where $\epsilon \approx Kn$ and Kn is the Knudsen number³. Already at zeroth order, therefore $f \approx f^{eq}$, we find that Eq. (3.28) resembles the Euler equation, Eq. (2.6), from Sec. 2.1. The time scale t_0 can be understood as advective time scale while t_1 marks the diffusive time scale [Del02]. The missing viscous contributions are not covered by the zeroth order. However already at first order of the expansion, thus $f \approx f^{eq} + \epsilon f^{(1)}$, the Navier-Stokes equation can be recovered [CD98]. In the next section we use this result and discretize the Boltzmann equation with the BGK operator.

3.2.2 From continuum to lattice

In 1986 Frisch, Hasslacher and Pomeau published their groundbreaking article on the simulation of the Navier-Stokes equation using lattice gas automata (LGA) [FHP86]. The LGA model is in contrast to the lattice Boltzmann method a purely boolean model, thus a lattice site hosts a particle or not [MZ88]. Due to the usage of boolean states the simulations suffered a serious noise problem.

The lattice Boltzmann method is the successor of the LGA, where among other things the boolean lattice state was abandoned in favour of a distribution function $f_i(\vec{x}, t)$ which in simulations is represented by a real number [CD98]. Since the method got first developed in the late 1980s it has gained more and more popularity, as shown in Fig. 3.3 [Li+20]. Due to the simplicity of the method a lot has been worked out over last forty years. The reason why the lattice Boltzmann method is lacking behind when it comes to thin film flows is due to its origin as an approximation to the Navier-Stokes equation. That said, there are of course studies of wetting and sliding droplets using

³ $Kn = \lambda/L$ is a measure to compare the mean free path to a characteristic length scale, i.e. ballistic and diffusive regime.

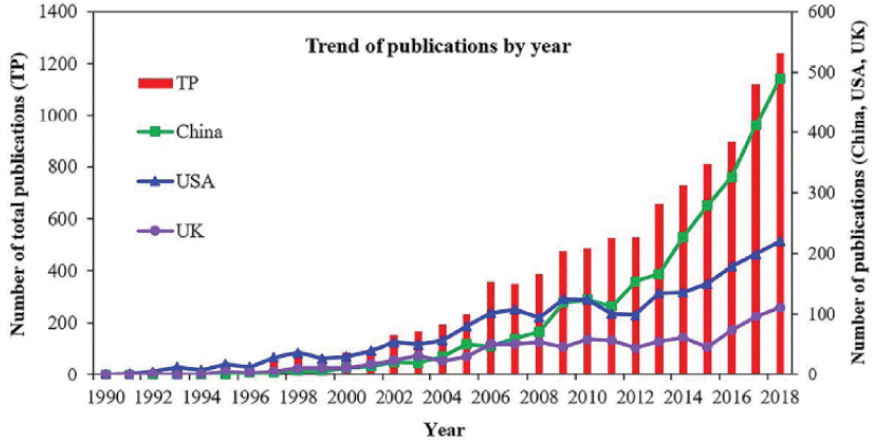


Figure 3.3: Number of lattice Boltzmann method related publications measured from 1990 to 2018 according to Ref. [Li+20]. The red bars indicate the total number of publications per year. The green, blue and lavender lines show the number of publications for the most “productive” countries, respectively China, USA and the UK.

the lattice Boltzmann method, e.g. Sbragaglia et al. [Sbr+14]. However they rely on additional contributions for either multiphase or multicomponent models [SC93; Che+95; SYC06].

The discretization of Eq. (3.9) using the lattice Boltzmann method is straightforward and does not require complex meshing. In fact this one of the strengths the lattice Boltzmann method inherited from the LGA. As the name suggests a lattice with lattice constants Δx and Δt for spatial and temporal discretization is the desired numerical domain. The discretized Boltzmann equation without force term reads,

$$f_i(\vec{x} + \vec{c}_i \Delta t, t + \Delta t) - f_i(\vec{x}, t) = -\frac{\Delta t}{\tau} (f_i(\vec{x}, t) - f_i^{eq}(\vec{x}, t)), \quad (3.35)$$

where the \vec{c}_i form a discrete set of α velocities that upon special symmetry considerations replace $\vec{\xi}$ of the previous section [RL08]. This equation is also called lattice Boltzmann equation (LBE). The perturbative expansion around the equilibrium distribution, Eq. (3.34) does also hold for a discretized velocity space, therefore

$$f_i = f_i^{eq} + \epsilon f_i^{(1)} + \epsilon^2 f_i^{(2)} + O(\epsilon^3). \quad (3.36)$$

Introducing the non-equilibrium part of the discretized distribution f_i as $f_i^{neq} = f_i - f_i^{eq}$. From Eqs. (3.12-3.13) we know that the non-equilibrium part has to satisfy,

$$\sum_i f_i^{neq} = 0, \quad (3.37)$$

$$\sum_i \vec{c}_i f_i^{neq} = \vec{0}, \quad (3.38)$$

where due to discretization the integral becomes a sum. The moments of the equilibrium functions obey the following relations [CD98]

$$\Pi^{eq} = \sum_i f_i^{eq} = \rho, \quad (3.39)$$

$$\Pi_\alpha^{eq} = \sum_i c_{i\alpha} f_i^{eq} = \rho u_\alpha, \quad (3.40)$$

$$\Pi_{\alpha\beta}^{eq} = \sum_i c_{i\alpha} c_{i\beta} f_i^{eq} = \rho u_\alpha u_\beta + \rho c_s^2 \delta_{\alpha\beta}, \quad (3.41)$$

$$\Pi_{\alpha\beta\gamma}^{eq} = \sum_i c_{i\alpha} c_{i\beta} c_{i\gamma} f_i^{eq} = \rho c_s^2 (u_\alpha \delta_{\beta\gamma} + u_\beta \delta_{\gamma\alpha} + u_\gamma \delta_{\alpha\beta}), \quad (3.42)$$

where the greek indices refer to the spatial dimensions (x, y, z). For the zeroth and first moment we also require that,

$$\sum_i f_i^{eq} = \sum_i f_i = \rho, \quad (3.43)$$

$$\sum_i c_{i\alpha} f_i^{eq} = \sum_i c_{i\alpha} f_i = \rho u_\alpha. \quad (3.44)$$

Clearly Eqs. (3.39-3.42) resemble Eqs. (3.17-3.20) at zeroth order of Eq. (3.36). As a solvability condition for the upcoming derivation we use,

$$\sum_i f_i^{(n)} = 0, \quad (3.45)$$

$$\sum_i \vec{c}_i f_i^{(n)} = \vec{0}, \quad (3.46)$$

which basically insures mass and momentum conservation of the collision operator.

Performing a Taylor expansion of Eq. (3.9) with a discrete set of velocities assuming no force is present yields [Krü+17]

$$\Delta t (\partial_t + c_{i\alpha} \partial_\alpha) f_i + \frac{\Delta t^2}{2} (\partial_t + c_{i\alpha} \partial_\alpha)^2 f_i + O(\Delta t^3) = -\frac{\Delta t}{\tau} f_i^{neq}. \quad (3.47)$$

Leaving higher orders aside one finds that this is actually a slow mode expansion of f_i . The distribution functions f_i , therefore only changes with macroscopic time scales. If this statement is violated higher orders need to be considered. Subtracting $\Delta t/2(\partial_t + c_{i\alpha} \partial_\alpha)$ from both sides yields

$$\Delta t (\partial_t + c_{i\alpha} \partial_\alpha) f_i = -\frac{\Delta t}{\tau} f_i^{neq} + \Delta t (\partial_t + c_{i\alpha} \partial_\alpha) \frac{\Delta t}{2\tau} f_i^{neq}, \quad (3.48)$$

which is first order in derivatives. Here we use the second expansion of Eq. (3.34) and expand the time derivative in orders of Kn ,

$$\Delta t \partial_t f_i = \Delta t (\epsilon \partial_t^{(1)} + \epsilon^2 \partial_t^{(2)} + O(\epsilon^3)) f_i. \quad (3.49)$$

For the spatial deviates it is sufficient to use

$$\Delta t c_{i\alpha} \partial_\alpha f_i = \Delta t (\epsilon c_{i\alpha} \partial_\alpha^{(1)}) f_i. \quad (3.50)$$

With a note of caution for Eq. (3.49) as only the sum of all orders in ϵ resembles the real time derivative. Applying both expansions Eq. (3.36) and Eq. (3.49) to Eq. (3.48) we have

$$(\partial_t^{(1)} + c_{i\alpha} \partial_\alpha) f_i^{eq} = -\frac{\Delta t}{\tau} f_i^{(1)} \quad (3.51)$$

at first order in ϵ and

$$\partial_t^{(2)} f_i^{eq} + (\partial_t^{(1)} + c_{i\alpha} \partial_\alpha) \left(1 - \frac{\Delta t}{2\tau} \right) f_i^{(1)} = -\frac{\Delta t}{\tau} f_i^{(2)}, \quad (3.52)$$

for $O(\epsilon^2)$.

Taking the moments of Eq. (3.51), see Eqs.(3.39-3.42) yields

$$\partial_t^{(1)} \rho + \partial_\beta^{(1)} (\rho u_\beta) = 0, \quad (3.53)$$

$$\partial_t^{(1)} (\rho u_\alpha) + \partial_\beta^{(1)} \Pi_{\alpha\beta}^{eq} = 0, \quad (3.54)$$

$$\partial_t^{(1)} \Pi_{\alpha\beta}^{eq} + \partial_\gamma^{(1)} \Pi_{\alpha\beta\gamma}^{eq} = -\frac{1}{\tau} \Pi_{\alpha\beta}^{(1)}, \quad (3.55)$$

for which the moments Π are

$$\Pi_{\alpha\beta}^{eq} = \sum_i c_{i\alpha} c_{i\beta} f_i^{eq} = \rho u_\alpha u_\beta + \rho c_s^2 \delta_{\alpha\beta}, \quad (3.56)$$

$$\Pi_{\alpha\beta\gamma}^{eq} = \sum_i c_{i\alpha} c_{i\beta} c_{i\gamma} f_i^{eq} = \rho c_s^2 (u_\alpha \delta_{\beta\gamma} + u_\beta \delta_{\gamma\alpha} + u_\gamma \delta_{\alpha\beta}), \quad (3.57)$$

$$\Pi_{\alpha\beta}^{(1)} = \sum_i c_{i\alpha} c_{i\beta} f_i^{(1)}, \quad (3.58)$$

where Eqs. (3.39-3.42) have been used. Similar to Eq. (3.22) and Eq. (3.28) the discretized equations, therefore Eq. (3.53) and Eq. (3.54) resemble the continuity and Euler momentum equation.

Computing the moments of Eq. (3.52) we have

$$\partial_t^{(2)} \rho = 0, \quad (3.59)$$

$$\partial_t^{(2)} (\rho u_\alpha) + \partial_\beta^{(1)} \left(1 - \frac{\Delta t}{2\tau} \right) \Pi_{\alpha\beta}^{(1)} = 0. \quad (3.60)$$

As there is now an equation for $\Pi_{\alpha\beta}^{(1)}$ it is possible to collect the mass and momentum equation for both $O(\epsilon)$ and $O(\epsilon^2)$

$$(\epsilon \partial_t^{(1)} + \epsilon^2 \partial^{(2)}) \rho + \epsilon \partial_\alpha^{(1)} (\rho u_\alpha) = 0, \quad (3.61)$$

$$(\epsilon \partial_t^{(1)} + \epsilon^2 \partial^{(2)}) (\rho u_\alpha) + \epsilon \partial_\beta^{(1)} \Pi_{\alpha\beta}^{eq} = -\epsilon^2 \partial_\beta^{(1)} \left(1 - \frac{\Delta t}{2\tau} \right) \Pi_{\alpha\beta}^{(1)}. \quad (3.62)$$

This system in fact resembles the Navier-Stokes with the small pitfall that the viscous stress tensor

$$\sigma = - \left(1 - \frac{\Delta t}{2\tau} \right) \Pi^{(1)}, \quad (3.63)$$

is as of now still unknown. Cut the last part short for an isothermal equation of state and f_i^{eq} as function of $O(u^2)$ for example

$$f_i^{eq} = \rho(a + bc_{i\alpha}u_\alpha + d(c_{i\alpha}u_\alpha)^2 + eu^2), \quad (3.64)$$

then the tensor is given as

$$\Pi^{(1)} = -\rho c_s^2 \tau (\partial_\beta^{(1)} u_\alpha + \partial_\alpha^{(1)} u_\beta) + \tau \partial_\gamma^{(1)} (\rho u_\alpha u_\beta u_\gamma), \quad (3.65)$$

which concludes the expansion part. The continuity and the Navier-Stokes equation can be derived by inserting Eq. 3.65 into Eqs. (3.61-3.62) and reverting the expansion such that,

$$\partial_t \rho + \partial_\gamma (\rho u_\gamma) = 0, \quad (3.66)$$

$$\partial_t (\rho u_\alpha + \partial_\beta (\rho u_\alpha u_\beta)) = -\partial_\alpha p + \partial_\beta [\eta(\partial_\beta u_\alpha + \partial_\alpha u_\beta)], \quad (3.67)$$

where we have neglected the $O(u^3)$ (error) term and used $p = \rho c_s^2$ as well as $\eta = \rho c_s^2 (\tau - \frac{\Delta t}{2})$ [Krü+17].

So far however no assumptions on the lattice distributions are made and the discrete equilibrium distribution function has not been specified. Paving work by He and Luo as well as group theoretical arguments derived by Rubinstein and Luo showed that based on dimensionality just a few (discrete) velocities are sufficient [HL97; RL08]. In fact in Chap. 5 all numerical experiments were performed on a D2Q9 lattice therefore \mathbf{c}_i is

$$\mathbf{c}_i = \begin{cases} (0, 0) & \alpha = 0 \\ \left[\cos \frac{(i-1)\pi}{4}, \sin \frac{(i-1)\pi}{4} \right] & i = 1, 3, 5, 7 \\ \sqrt{2} \left[\cos \frac{(i-1)\pi}{4}, \sin \frac{(i-1)\pi}{4} \right] & i = 2, 4, 6, 8 \end{cases} \quad (3.68)$$

The only missing pieces are a, b, c, d of Eq. (3.64). Using the set of equations (3.39-3.42) one quickly finds

$$a = 1, \quad b = \frac{1}{c_s^2}, \quad d = \frac{1}{2c_s^4}, \quad e = \frac{1}{2c_s^2}, \quad (3.69)$$

with lattice weights

$$w_i = \begin{cases} 4/9 & i = 0 \\ 1/9 & i = 1, 2, 3, 4 \\ 1/36 & i = 5, 6, 7, 8 \end{cases}, \quad (3.70)$$

such that the equilibria can be written as

$$f_i^{eq} = w_i \rho \left(1 + \frac{c_{i\alpha} u_\alpha}{c_s^2} + \frac{(c_{i\alpha} u_\alpha)^2}{2c_s^4} + \frac{u^2}{2c_s^2} \right). \quad (3.71)$$

Together with the evolution equation Eq. (3.35) it is therefore possible to approximate the Navier-Stokes equation, at least in regimes of small Knudsen and Mach numbers, $Kn \& Ma \ll 1$.

Many articles about the lattice Boltzmann method mention a collision step and a streaming step. This can be achieved by splitting Eq. (3.35) into a purely local part,

$$f_i^*(\vec{x}, t) = \left(1 - \frac{\Delta t}{\tau}\right) f_i(\vec{x}, t) + \frac{\Delta t}{\tau} f_i^{eq}(\vec{x}, t), \quad (3.72)$$

and a non-local propagation step

$$f_i(\vec{x} + \vec{c}_i \Delta t, t + \Delta t) = f_i^*(\vec{x}, t). \quad (3.73)$$

This rearrangement offers the unique computational advantage, because Eq. (3.72) is perfectly suited for parallel computation.

3.2.3 Shallow water equations on the lattice

The idea however of this thesis is not to approximate the Navier-Stokes equation but have a numerical solver for the thin film equation. Luckily for me and as outlined in Sec. 2.2 there is a system which has some similarities with the thin film equation, namely the shallow water equations, Eqs. (2.63-2.64). In fact it is possible to derive with a similar ansatz, the shallow water equations from the Boltzmann equation [Sal99; Zho04; Del02]. The starting point are the two equations for mass and momentum conservation from Sec. 2.2,

$$\partial_t h + \partial_{x_\alpha} (u_\alpha h) = 0, \quad (3.74)$$

$$\partial_t (u_\alpha h) + \partial_{x_\beta} (P_{\alpha\beta} - \mathcal{S}_{\alpha\beta}) = 0, \quad (3.75)$$

where \mathcal{S} can be thought of as a Newtonian viscous stress of the form,

$$\mathcal{S} = \mu \left[\partial_{x_\beta} u_\alpha + \partial_{x_\alpha} u_\beta - \frac{2}{3} \delta_{\alpha\beta} \partial_{x_\gamma} u_\gamma \right], \quad (3.76)$$

and the pressure $P_{\alpha\beta}$,

$$P_{\alpha\beta} = \frac{1}{2} gh^2 \delta_{\alpha\beta} + hu_\alpha u_\beta, \quad (3.77)$$

with g being the gravitational constant [Sal99]. The momentum flux tensor can simply be read from Eq. (3.75) and is given by $\Pi = P - \mathcal{S}$ [Del02]. The equilibrium distribution, Eq. (3.11), is build upon the equation of state of an ideal gas and is as such not applicable to the shallow water system. However by introducing the hydrostatic pressure as an equation of state Xu was able to simulate the shallow water equations with the equilibrium distribution [Xu99; Del02],

$$f^{eq}(\mathbf{x}, \mathbf{v}, t) = \rho \frac{1}{(\pi g \rho)^{D/2}} e^{-\mathbf{v}^2/(g\rho)}, \quad (3.78)$$

where D accounts for the spatial dimensions.

The derivation of the lattice Boltzmann method for the shallow water system is very similar to the lattice Boltzmann method for the Navier-Stokes equation. The starting

point for both models is Eq. (3.35) and the expansion of f , see Eq. (3.36). Instead of repeating all calculations from the previous section, Dellar [Del02] showed a rather direct approach to compute the stress tensor. The idea is to use the non-dimensional discretized (force free) Boltzmann equation,

$$\partial_t f_i + c_i \cdot \nabla f_i = -\frac{1}{\epsilon\tau} (f_i - f_i^{eq}), \quad (3.79)$$

and compute its moments straight away such that,

$$\partial_t \sum_i f_i + \partial_\alpha \sum_i c_{i\alpha} f_i = -\frac{1}{\epsilon\tau} \left(\sum_i f_i - \sum_i f_i^{eq} \right), \quad (3.80)$$

$$\partial_t \sum_i c_{i\alpha} f_i + \partial_\beta \sum_i c_{i\alpha} c_{i\beta} f_i = -\frac{1}{\epsilon\tau} \left(\sum_i c_{i\alpha} f_i - \sum_i c_{i\alpha} f_i^{eq} \right). \quad (3.81)$$

The discretized moments given by,

$$\sum_i f_i^{eq} = \sum_i f_i = h, \quad (3.82)$$

$$\sum_i c_{i\alpha} f_i^{eq} = \sum_i c_{i\alpha} f_i = hu_\alpha, \quad (3.83)$$

$$\sum_i c_{i\alpha} c_{i\beta} f_i^{eq} = \sum_i c_{i\alpha} c_{i\beta} f_i = \Pi_{\alpha\beta}, \quad (3.84)$$

where we simply used Eqs. (3.17-3.19) with the discrete velocity set \mathbf{c}_i and the shallow water equilibrium function Eq. (3.78). Inserting the expansion of f , Eq. (3.36), into Eq. (3.80) we have,

$$\partial_t h + \partial_\alpha (hu_\alpha) = 0, \quad (3.85)$$

where we have used the solvability condition, Eqs. (3.45-3.46). For the first moment we get,

$$\partial_t (hu_\alpha) + \partial_\beta \left(\Pi_{\alpha\beta}^{eq} + \epsilon \Pi_{\alpha\beta}^{(1)} + \epsilon^2 \Pi_{\alpha\beta}^{(2)} + O(\epsilon^3) \right) = 0, \quad (3.86)$$

with $\Pi^{(n)} = \sum_i \mathbf{c}_i \mathbf{c}_i f_i^{(n)}$. To compute the unknown stress tensor $\Pi_{\alpha\beta}^{(1)}$ we use Eq. (3.79) and take its second moment

$$\partial_t \left(\sum_i c_{i\alpha} c_{i\beta} f_i \right) + \partial_\gamma \left(\sum_i c_{i\alpha} c_{i\beta} c_{i\gamma} f_i \right) = -\frac{1}{\epsilon\tau} \left(\sum_i c_{i\alpha} c_{i\beta} f_i - \sum_i c_{i\alpha} c_{i\beta} f_i^{eq} \right). \quad (3.87)$$

If we cut the expansion of f at $O(\epsilon)$ we get

$$\partial_t \left(\Pi_{\alpha\beta}^{eq} + \epsilon \Pi_{\alpha\beta}^{(1)} \right) + \partial_\gamma \left[\sum_i c_{i\alpha} c_{i\beta} c_{i\gamma} (f_i^{(0)} + \epsilon f_i^{(1)}) \right] = -\frac{1}{\epsilon\tau} \left(\Pi_{\alpha\beta}^{eq} + \epsilon \Pi_{\alpha\beta}^{(1)} - \Pi_{\alpha\beta}^{eq} \right), \quad (3.88)$$

where at $O(1)$ we find,

$$\partial_t \Pi_{\alpha\beta}^{eq} + \partial_\gamma \left(\sum_i c_{i\alpha} c_{i\beta} c_{i\gamma} f_i^{(0)} \right) = -\frac{1}{\tau} \Pi_{\alpha\beta}^{(1)}. \quad (3.89)$$

The stress term $\Pi_{\alpha\beta}^{(1)}$ is therefore given by,

$$\Pi_{\alpha\beta}^{(1)} = -\tau \partial_t^{(0)} \Pi^{eq} = \partial_t^{(0)} \left(\frac{1}{2} h^2 g \delta_{\alpha\beta} + h u_\alpha u_\beta \right) = \partial_t^{(0)} P_{\alpha\beta} \quad (3.90)$$

$$= -\tau [\theta h (\partial_\beta u_\alpha + \partial_\alpha u_\beta) + (\theta - gh) (\delta_{\alpha\beta} \partial_\gamma h u_\gamma + u_\alpha \partial_\beta h + u_\beta \partial_\alpha h)], \quad (3.91)$$

where we neglected the term $O(u^3)$ and used $\theta = 1/3$ as a constant non-dimensional reference temperature [Del02]. At leading order, therefore at $f_i = f_i^{eq}$ we recover Eqs. (3.74-3.75) from Eqs. (3.80-3.81) assuming $\mathcal{S} = 0$.

The lattice speeds introduced in Eq. (3.68) are already two dimensional and so are the weights W_i , see Eq. (3.70), therefore the last missing piece are the discretized equilibrium distributions f_i^{eq} . In principle we could adopt a form similar to Eq. (3.71), however Dellar showed this approach is unstable and in fact suggested to use the equilibrium distributions derived by Salmon [Del02; Sal99],

$$f_0^{eq} = h + w_0 h \left(-\frac{15}{8} gh - \frac{3}{2} u^2 \right), \quad (3.92)$$

$$f_i^{eq} = w_i h \left(\frac{3}{2} gh + 3c_{i\alpha} u_\alpha + \frac{9}{2} (c_{i\alpha} u_\alpha)^2 - \frac{3}{2} u^2 \right), \quad i \neq 0. \quad (3.93)$$

In Chap. 5 we will recap the main ideas of this derivation. We will then discuss constructive matching conditions between the shallow water model and the thin film equation. The shallow water lattice Boltzmann model is not sufficient for thin film dynamics, we also have to introduce forces. These forces account for wetting dynamics, such as contact angles, and the velocity boundary condition at $h = 0$.

The derivation of the lattice Boltzmann method for the Navier-Stokes equation as well as the shallow water system concludes this chapter. Following is a chapter about the sustainable approach I choose to keep the software first open source and maintainable for the future. After the introduction of *Swalbe.jl* in Chap. 4 the method is thoroughly tested against problems such as the Rayleigh-Taylor instability in Chap. 5. While in Chap. 6 an additional contribution due to thermal fluctuations is considered. Although the focus is solemnly on thermal fluctuations, this chapter should serve as a guideline for the inclusion of further dynamics.

4 Swalbe.jl: A lattice Boltzmann solver for thin film hydrodynamics

*Okay die Eisbären gehen unter denn
der Wasserspiegel steigt, ist mir egal
in meinem Baccardi ist noch Eis*

Neodisco

This chapter has been published and can be found as: Zitz et al., (2022). Swalbe.jl: A lattice Boltzmann solver for thin film hydrodynamics. Journal of Open Source Software, 7(77), 4312

4.1 Summary

Small amounts of liquid deposited on a substrate are an everyday phenomenon. From a theoretical point of view this represents a modelling challenge, due to the multiple scales involved: from the molecular interactions among the three phases (solid substrate, liquid film and surrounding gas) to the hydrodynamic flows. An efficient way to deal with this problem is via the thin-film equation:

$$\partial_t h = \nabla \cdot (M(h) \nabla p), \quad (4.1)$$

where h is the film thickness, $M(h)$ is a thickness dependent mobility and p is the pressure inside the film. Solving the thin film equation directly is however a difficult task as it is a fourth order degenerate PDE [Bec+03]. *Swalbe.jl* approaches the problem from a different angle. Instead of directly solving the thin film equation we use a novel method based on a class lattice Boltzmann models [Krü+17], originally developed to simulate shallow water flows [Sal99]. This allows us to benefit from the simplicity of the lattice Boltzmann algorithm which makes it straightforward to parallelize the code and run it on accelerator devices. Choosing appropriate forces it is possible to simulate complex problems. Among them is the dewetting of a patterned substrates as shown in Fig. 4.1. It is as well possible to simulate low contact angle droplets out of equilibrium to probe relaxation experiments, e.g. the Cox-Voinov or Tanner's law [Bon+09]. Due to a disjoining pressure model for the three phase contact line droplets can not only relax towards their equilibrium they can slide as well [Zit+19]. All of this can be coupled with thermal fluctuations to study the stochastic thin film equation [Sha+19].

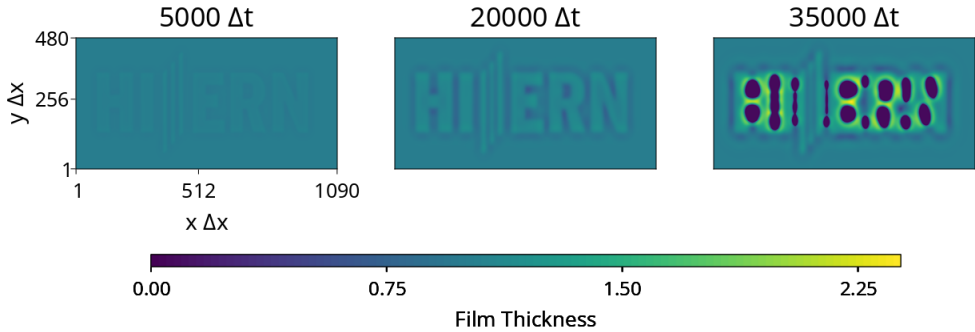


Figure 4.1: Dewetting simulation on a patterned substrate, letters have a higher wettability than the rest of the substrate.

4.2 Statement of need

Swalbe is written in Julia [Bez+17] and developed for a *script your experiment* workflow. For that reason an experiment is composed of three steps. First, the initial problem is defined by setting the system size and other input parameters, stored in a custom type. Followed by the lattice Boltzmann time loop where different force terms allow for different dynamics. To note here however is that some forces are mandatory for every experiment. This is on the one hand the friction with the substrate, the slip that helps regularizing the contact line and on the other hand the capillary- or filmpressure that accounts for the correct wetting behavior. After the time loop has ended an IO step can be included to store the data in files or to generate a plot. The package is written in pure Julia, therefore it can be easily coupled with other packages from the Julia ecosystem such as Plots.jl [Bre21] to visualize data and JLD2.jl [22] to store data in HDF5 format. Of course one future development goal is to interact with *SciML* environment to pair modelling with ML. *Swalbe.jl* is designed to approach two problems, first being the modelling itself and second the applicability to large system sizes. Ideas can be implemented quickly and tested with a two dimensional system, which is discretized in a single horizontal direction and offers a second computed dimension for the thickness. The hardware requirements to run these two dimensional simulations are comparably low and depending on the number of lattice Boltzmann iterations ranging from seconds to at most an hour on a single Core of a modern CPU. After testing it is possible to scale up and simulate the same or other problems in three dimensions with a slightly more complex discretization. Keeping the simulation time low is archived by using a Nvidia GPU. Most functions are written in a generic style and can be executed both on a CPU or GPU. For the GPU usage the high-level API of CUDA.jl [BFD19; Bes+19] is used, mostly CuArrays.

An older version of the numerical model (written in C++) has been tested and used for thin film simulations in previous publications [Zit+19; ZSH21]. While there is a small performance decrease when moving from C++ with OpenACC to Julia, the benefits of usability, straightforward documentation and automated testing outweighs

this issue. There are many thin film problems the authors will investigate in the future with *Swalbe.jl*. Among those are switchable substrate and their influence on a dewetting thin film, or the influence of thermal fluctuations on the coalescence of droplets.

4.3 State of the field

In the context of computational fluid dynamics low Reynolds number flows and especially thin film flows are a comparably small subsection. Therefore numerical tools that deal exclusively with the thin film problem are sparse. Two packages for simulations of thin film hydrodynamics are **ThinViscoelasticFilms** and **stochastic_thin_films** [Bar19; Nes17]. The core components are written in *Fortran* and at least the later package can be used according to BSD-2 license. Documentation however is only available through code comments and a short readme, leaving the user little guidance.

That said, the thin film equation is a fourth-order parabolic equation and can of course be solved with appropriate numerical schemes. Some of these schemes can be found in the refs. [Eng+16; DKB00; Bec+03; Pes+19]. Upon contacting the authors it should be possible to have access to a working version of the described approach.

Wilczek et al. used **DUNE** to study the dynamics of an ensemble of sliding drops in ref. [Wil+17]. DUNE is a software suite written in *C++* that solves partial differential equations with a grid based approach [San20]. Therefore DUNE is not limited to the problem of thin film flows, interested readers may visit the project's home page.

Another open source package with similar functionality that is used to solve thin film problems is **oomph-lib**. oomph-lib uses both *Fortran* as well *C* components to solve differential equations. The library's emphasis however are fluid dynamic problems as can be seen from refs. [HH15; Pih+15; Pih+13]. Of course, similar to DUNE, its capabilities are not limited to thin film problems.

Given the nature of the thin film problem one can, as well, use classical Navier-Stokes solvers with appropriate initial and boundary conditions. What comes to mind here is for example **OpenFOAM** a widely used open source CFD software with an active community. Another example utilizing a Navier-Stokes solver would be the **basilisk** software library, which is written in *C* and is the successor of **GERRIS**.

Lattice Boltzmann solvers offer another category to approximate the Navier-Stokes equation. Starting point of this method is not the Navier-Stokes equation but the Boltzmann equation. Using the Chapman-Enskog expansion [CC90; Ens17], it can be shown that the resulting system of equations recovers to the Navier-Stokes equation. The method is straightforward to implement and several small to large projects can be found with OSI-approved licence. To name just a few examples: **waLBerla**, **openLB** or some smaller project **STLBM**, **TLBfind** (explicitly written for GPU use).

Proprietary software, e.g. **COMSOL** can as well be used to simulate thin film dynamics. Wedershoven et al. used COMSOL to study the rupture of a thin film due to laser irradiation [Wed+14]. Berendsen et al. from the same group simulated the

dynamics an impinging air jet has on a thin film using COMSOL [Ber+12].

With the exclusion of **ThinViscoelasticFilms** every above mentioned project has a much wider purpose than *just* solving the thin film equation. However due to the generality of most libraries it can become quite complex to set up a simulation for a thin film problem. Especially concerning the Navier-Stokes solvers one uses a *sledge hammer to crack a nut*.

4.4 Use Case

An interesting problem in the domain of thin liquid films is the coalescence of sessile droplets, see references [ELS99; EWS13; Her+12; Aar+05]. The underlying idea is that two droplets placed on a hydrophilic substrate in close contact to each other will coalesce into a single droplet to minimize their surface area and therefore energy. The dynamics of this process can be explained using a self-similarity solution of the thin film equation. In fact, that the bridge height, the point that connects the two droplets, has to grow with a power law. We now show how to perform that simulation with the help of the *Swalbe.jl* package. The goal will be to observe a growth of the bridge height as

$$h_0(t) = kt^\alpha, \quad (4.2)$$

where the exponent α should be $2/3$ [Paw+19; Sui+13]. This experiment has been performed using the *Pluto notebook* Drop_coal.jl.

Just to outline the most important steps towards the simulation:

1. Define the initial conditions of the simulation
2. Define a function that performs the experiment
3. Run the experiment with varying parameters:

```
for gamma in enumerate(gammars)
    # System parameter, delta=50 can still considered small to
    # medium slippage (delta approx max(height))
    sys = Swalbe.SysConst_1D(L=1024,
                           Tmax=2000000,
                           delta=50.0,
                           gamma=gamma[2])
)
# The experiment
data_merge[:, :, gamma[1]] = run_drop_coal(sys,
                                             r1=sphere_rad,
                                             r2=sphere_rad)
)
end
```

4. Display the results, see Fig. 4.2

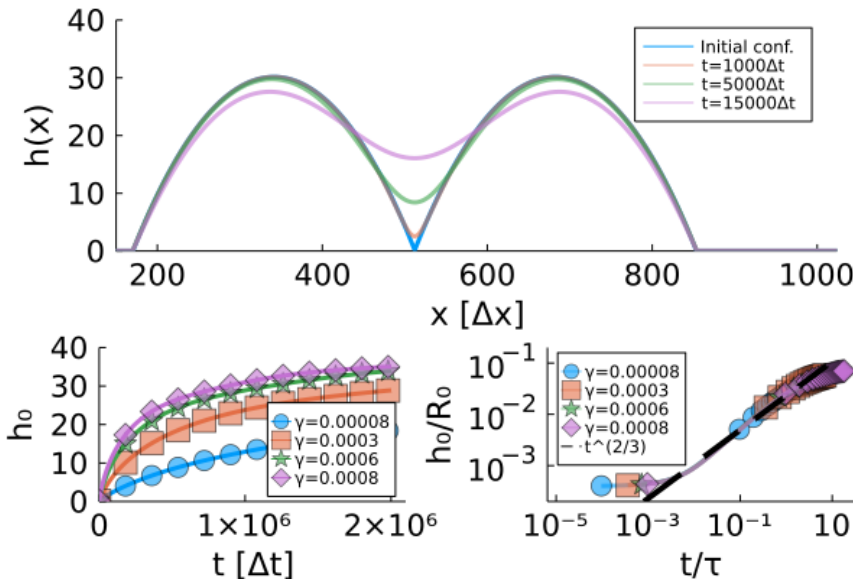


Figure 4.2: Coalescence of sessile droplets on a partially wetting substrate. The upper panel shows the time evolution for a single experiment (lowest surface tension). In the lower left panel we plot the evolution of the bridge height for the four different surface tensions. To the right we normalize the data with characteristic quantities and show that the bridge height grows as $\propto t^{2/3}$.

4.5 Author Contribution Statement

The authors confirm contribution to the paper as follows: S. Z. wrote the code, performed the simulations and set up the package. M. Z. contributed to the integration as well as the documentation. A. S. derived the mathematical approximations on which the packages is based on and J. H. served in an advisory role in the design and the execution of the research.

4.6 Acknowledgements

The authors acknowledge financial support by the Deutsche Forschungsgemeinschaft (DFG) within the priority program SPP2171 “Dynamic Wetting of Flexible, Adaptive, and Switchable Substrates”, within project HA-4382/11.

5 Lattice Boltzmann method for thin-liquid-film hydrodynamics

*Das Schicksal hat mich angelacht
und mir ein Geschenk gemacht.*

RAMMSTEIN

This chapter has been published and can be found as: Zitz, S., Scagliarini, A., Maddu, S., Darhuber, A. A., & Harting, J. (2019). Lattice Boltzmann method for thin-liquid-film hydrodynamics. Physical Review E, 100(3), 033313

We propose a novel approach to the numerical simulation of thin film flows, based on the lattice Boltzmann method. We outline the basic features of the method, show in which limits the expected thin film equations are recovered and perform validation tests. The numerical scheme is applied to the viscous Rayleigh-Taylor instability of a thin film and to the spreading of a sessile drop towards its equilibrium contact angle configuration. We show that the Cox-Voinov law is satisfied, and that the effect of a tunable slip length on the substrate is correctly captured. We address, then, the problem of a droplet sliding on an inclined plane, finding that the Capillary number scales linearly with the Bond number, in agreement with experimental results. At last, we demonstrate the ability of the method to handle heterogenous and complex systems by showcasing the controlled dewetting of a thin film on a chemically structured substrate.

5.1 Introduction

Thin layers of liquids on solid surfaces are frequently encountered in a host of natural and technological settings [dBQ04; Foc+10]. Therefore, understanding and controlling their stability and dynamics is a central problem for fundamental physics, as well as for applied research in process engineering and nanotechnology [ODB97; Uta+07]. Coating processes, for instance, rely crucially on the mutual affinity of liquid and surface (i.e. on wettability properties). When the liquid film is sufficiently thin, in fact, it can become unstable, leading to the dewetting of the coated area [Bon+09]. From the modelling point of view, the challenge consists in the fact that the physics of thin films is intrinsically multiscale, for it involves phenomena ranging from the

molecular scale at the three phase contact line, to the micro-/nano-metric size of the film thickness, to the size of the film as a whole, extending over the coated substrate area.

A fully resolved bottom-up atomistic approach would be, obviously, unfeasible, if hydrodynamic regimes are to be explored. It clearly appears that some degree of model order reduction is required. Most hydrodynamic models of thin liquid films, in the framework of the lubrication theory, simplify the complexity of the full 3D Navier-Stokes equations [Cla27; Sto48] to one scalar transport equation (the lubrication equation) for the film thickness field $h(x, t)$ [Rey86; ODB97; CM09; Mit93]:

$$\partial_t h = \nabla \cdot (Q(h) \nabla p_{\text{film}}) \quad (5.1)$$

Here, $Q(h)$ is the mobility function, whose explicit form depends on the boundary condition for the velocity at the surface (for a no-slip boundary, $Q(h) = h^3/(3\mu)$, with μ being the dynamic viscosity), and p_{film} is the film pressure at the free liquid surface. Stable and reliable direct numerical simulations of Eq. (5.1) require sophisticated numerical methods, whose execution is often computationally expensive [Bec+03]. Moreover, an ever-growing number of microfluidic problems requires to cope with complex fluids rather than simple liquids, i.e. fluids with non-trivial internal microstructure and/or complex non-Newtonian rheological behaviour (e.g. colloidal suspensions, polymer solutions, etc.). The quest for an efficient multiscale numerical method for simulating thin film hydrodynamics, versatile for the inclusion of multiphysics features, is, thus, an ongoing endeavour.

In this paper, we present a novel approach to the numerical study of thin liquid films, based on the lattice Boltzmann method (LBM) [Suc01]. Due to the built-in properties of the LBM, our method enjoys an outstanding computational performance, especially on parallel architectures and graphics processing units.

The paper is organized as follows. We first present the numerical model and discuss the equations of motion for the hydrodynamic fields that the model covers. We then show that these equations effectively correspond, under certain limits, to the lubrication equation of Reynolds. In section 5.3 we present validation results including the Rayleigh-Taylor instability of thin fluid films, the spreading of a sessile droplet on a substrate and the sliding of a droplet on an inclined plane. After showcasing the ability of our method to handle large and heterogeneous substrates, we present some computational aspects including the performance of our implementation for Graphics Processing Units (GPUs). An appendix is added to provide numerical tests of the validity of the correspondence with lubrication theory (appendix 5.7).

5.2 Numerical Model

When a layer of fluid is characterized by a vertical length scale H much smaller than the longitudinal one L , the equations of motion can be simplified under the approximation that the ratio of the length scales, $\varepsilon \equiv H/L$, is small ($\varepsilon \ll 1$, see Fig. 5.1). In this limit, and for small reduced Reynolds number, $\varepsilon^2 Re$ the lubrication

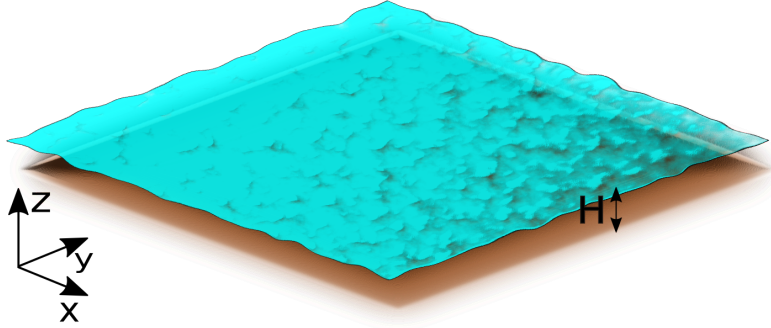


Figure 5.1: Schematic sketch of a model system: a thin liquid film deposited on a flat substrate. The air-liquid interface is represented by the *height* $h(x, y, t)$. The characteristic thickness of the film is given by H .

approximation tells that the dynamics is governed by equation (5.1). Instead of directly solving Eq. (5.1) numerically, we follow an alternative strategy. We build our numerical model on a class of LBMs originally proposed as solvers for the shallow water equations [Sal99; Del02; Zho04; van+10]. The lattice Boltzmann equation for the discrete probability density functions of a fluid system subject to a total force (that can include both internal and external forces) \mathbf{F}_{tot} , $f_l(\mathbf{x}, t)$, reads:

$$f_l(\mathbf{x} + \mathbf{c}^{(l)} \Delta t, t + \Delta t) = (1 - \omega) f_l(\mathbf{x}, t) + \omega f_l^{(eq)}(\mathbf{x}, t) + w_l \frac{\Delta t}{c_s^2} \mathbf{c}^{(l)} \cdot \mathbf{F}_{\text{tot}}, \quad (5.2)$$

where l labels the lattice velocities \mathbf{c}_l and runs from 0 to $Q - 1$, with Q being the number of velocities characterizing the scheme. Algorithmically, this equation can be seen as made up of two steps. A *local collision* step where the $f_l(\mathbf{x}, t)$ “relax” towards the local equilibrium distributions $f_l^{(eq)}(\mathbf{x}, t)$ with rate $\omega = \Delta t / \tau$ (where τ , the relaxation time, is proportional to the kinematic viscosity ν): the distribution functions are substituted by their weighted average (with weights ω and $1 - \omega$) with the equilibria, with an added so-called "source" term (the last term on the right hand side of Eq. (5.2)), when a force is present. A *non-local streaming* step where the updated distribution functions are scattered to the nearest neighbouring sites. The parameters c_s (the lattice speed of sound) and w_l (the so called "weights") depend on the geometry of the lattice and are determined under suitable constraints on the form of the tensorial moments in the lattice velocities up to fourth order [Wol04]. We work with two-dimensional square lattices of side length $N\Delta x$, with lattice constant Δx and $Q = 9$. For simplicity, we keep $\Delta t = \Delta x = 1$ throughout this paper and follow the standard notation, where $c_s = 1/\sqrt{3}$ and the $\mathbf{c}^{(l)} = (c_x^{(l)}, c_y^{(l)})$, $l = 0, 1, \dots, 8$, are [Qia97; SC93]

$$\mathbf{c}^{(l)} = \begin{cases} (0, 0) & l = 0 \\ \left[\cos \frac{(l-1)\pi}{4}, \sin \frac{(l-1)\pi}{4} \right] & l = 1, 3, 5, 7 \\ \sqrt{2} \left[\cos \frac{(l-1)\pi}{4}, \sin \frac{(l-1)\pi}{4} \right] & l = 2, 4, 6, 8 \end{cases}, \quad (5.3)$$

with the corresponding weights

$$w_l = \begin{cases} \frac{4}{9} & l = 0 \\ \frac{1}{9} & l = 1, 3, 5, 7 \\ \frac{1}{36} & l = 2, 4, 6, 8 \end{cases}. \quad (5.4)$$

The equilibrium distribution functions $f_l^{(eq)}$ have to be determined to recover the desired equations of motion for hydrodynamic fields in the long wavelength limit (we will return to this shortly). They have, therefore, to fulfill the following relations involving the liquid height

$$h = \sum_{l=0}^8 f_l^{(eq)}, \quad (5.5)$$

momentum

$$hu_i = \sum_{l=0}^8 c_i^{(l)} f_l^{(eq)} \quad (5.6)$$

and momentum flux tensor field

$$\frac{1}{2} gh^2 \delta_{ij} + hu_i u_j = \sum_{l=0}^8 c_i^{(l)} c_j^{(l)} f_l^{(eq)}, \quad (5.7)$$

where the left hand side coincides with the momentum flux of the shallow water equation, with the term $gh^2/2$ being the hydrostatic pressure in a thin fluid layer at rest [Del02]. With the usual *ansatz* of a quadratic polynomial in the velocity field \mathbf{u} , the equilibrium distribution functions read

$$f_l^{(eq)} = \begin{cases} h - \frac{5gh^2}{6c_s^2} - \frac{2hu^2}{3c_s^2} & l = 0 \\ \frac{gh^2}{6c_s^2} + \frac{h\mathbf{c}^{(l)} \cdot \mathbf{u}}{3c_s^2} + \frac{h(\mathbf{c}^{(l)} \cdot \mathbf{u})^2}{2c_s^4} - \frac{hu^2}{6c_s^2} & l = 1, 3, 5, 7 \\ \frac{gh^2}{24c_s^2} + \frac{h\mathbf{c}^{(l)} \cdot \mathbf{u}}{12c_s^2} + \frac{h(\mathbf{c}^{(l)} \cdot \mathbf{u})^2}{8c_s^4} - \frac{hu^2}{24c_s^2} & l = 2, 4, 6, 8 \end{cases}, \quad (5.8)$$

where $u^2 = |\mathbf{u}|^2$ is the magnitude of the velocity. The multiscale Chapman-Enskog expansion [CC90; Ens17] of such a LBM yields (for small ratios Ma/Fr of the Mach, $Ma = u/c_s$, and Froude, $Fr = u/\sqrt{gH}$, numbers, corresponding also to $\sqrt{gH}/c_s \ll 1$) the following equations for the height and velocity fields [Del02; van+10; Sal99]

$$\begin{cases} \partial_t h + \nabla \cdot (h\mathbf{u}) = 0 \\ \partial_t(h\mathbf{u}) + \nabla \cdot (h\mathbf{u}\mathbf{u}) = -gh\nabla h + \\ \quad + \nu \nabla^2(h\mathbf{u}) + 2\nu \nabla(\nabla \cdot (h\mathbf{u})) + \mathbf{F}_{\text{tot}} \end{cases}, \quad (5.9)$$

where ν , the kinematic viscosity, is related to the relaxation rate ω appearing in (5.2) via $\nu = c_s^2((2-\omega)/2\omega)\Delta t$. For stability of the scheme, the condition $Fr < 1$ is

also required, which is fulfilled in all our applications, given the low values of u (as discussed in more detail later on). Different terms contribute to the total (generalized) force¹ \mathbf{F}_{tot} :

$$\mathbf{F}_{\text{tot}} = \mathbf{F}_{\text{film}} + \mathbf{F}_{\text{fric}} + \mathbf{F}. \quad (5.10)$$

In the first term the film pressure appearing in (5.1) is included as $\mathbf{F}_{\text{film}} = -\frac{1}{\rho_0} h \nabla p_{\text{film}}$, where the film pressure p_{film} is written as

$$p_{\text{film}} = -\gamma(\nabla^2 h - \Pi(h)) \quad (5.11)$$

and ρ_0 is the (constant) liquid density (equal to 1, in LBM units). The first term in Eq. (5.11) represents the capillary Laplace pressure (with γ being the surface tension) while the second term is the disjoining pressure. Various forms have been proposed for $\Pi(h)$ in the literature [ODB97; Thi14], where here we use the expression

$$\Pi(h) = \kappa f(h) = \underbrace{(1 - \cos(\theta)) \frac{(n-1)(m-1)}{(n-m)h_*}}_{\kappa} \underbrace{\left[\left(\frac{h_*}{h} \right)^n - \left(\frac{h_*}{h} \right)^m \right]}_{f(h)}. \quad (5.12)$$

In Eq. (5.12), θ is the contact angle and h_* corresponds to the precursor film thickness. The integers n and m are set to be 3 and 9, respectively. These are commonly chosen values in the literature [ML13; ODB97] that correspond to a standard 6 – 12 Lennard-Jones intermolecular potential [FG18], though other pairs (n, m) can be used (e.g. (2, 3), (3, 6), (4, 10) [DGK09b; Wil+17; Wed+14]). By adjusting κ we are thus able to address the wetting properties of the substrate. The film pressure is specific to model thin film dynamics, in general however one can make use of other force terms e.g. to couple fluid layers which has been shown in [Roc+12]. The second term on the right hand side in Eq. (5.10) introduces a friction with the substrate of the form

$$\mathbf{F}_{\text{fric}} = -\nu \alpha_\delta(h) \mathbf{u} \quad (5.13)$$

with the coefficient $\alpha_\delta(h)$ given by

$$\alpha_\delta(h) = \frac{6h}{(2h^2 + 6\delta h + 3\delta^2)}. \quad (5.14)$$

Here, δ acts as a regularizing parameter, which can be identified with an effective slip length. Finally, the last term in Eq. (5.10), \mathbf{F} accounts for any other possible source of forcing (e.g. the gravity component parallel to the substrate in the case of a liquid film deposited on an inclined plate). Equipped with such extra terms, equations (5.9) become

$$\begin{cases} \partial_t h + \nabla \cdot (h \mathbf{u}) = 0 \\ \partial_t(h \mathbf{u}) + \nabla \cdot (h \mathbf{u} \mathbf{u}) = -gh \nabla h + \\ \quad + \nu \nabla^2(h \mathbf{u}) + 2\nu \nabla(\nabla \cdot (h \mathbf{u})) - \frac{1}{\rho_0} h \nabla p_{\text{film}} - \nu \alpha_\delta(h) \mathbf{u} + \mathbf{F}. \end{cases} \quad (5.15)$$

¹The generalized forces have indeed the dimensions of [length]²[time]⁻².

Let us notice at this point that for most microfluidic applications we are actually interested in, the advection term on the left hand side of the second equation of (5.15) is indeed negligible as compared to the right hand side (the Reynolds number [Rey83a; Som08] being much smaller than one). Analogously, the longitudinal viscous terms $\nu \nabla^2(h\mathbf{u})$ and $2\nu \nabla(\nabla \cdot (h\mathbf{u}))$ are of order ε^2 smaller in the ratio of length scales than the friction term $\nu \alpha(h)\mathbf{u}$ (since the former scale as $\nu H \frac{U}{L^2}$, whereas the latter as $\nu \frac{U}{H}$). Therefore they can also be neglected. The validity of these considerations has been numerically tested in some selected cases (representative of typical applications) and the results are shown and discussed in the appendix. Equations (5.15) reduce then to

$$\begin{cases} \partial_t h + \nabla \cdot (h\mathbf{u}) = 0 \\ \partial_t(h\mathbf{u}) = -gh\nabla h - \frac{1}{\rho_0}h\nabla p_{\text{film}} - \nu\alpha_\delta(h)\mathbf{u} + \mathbf{F}. \end{cases} \quad (5.16)$$

For processes evolving on time-scales \tilde{t} such that $\tilde{t} \gg \frac{h}{\alpha(h)\nu}$, one can consider the “quasi-steady” limit of the second of these equations (setting $\partial_t(h\mathbf{u}) \approx 0$), which yields

$$\mathbf{u} \approx \frac{1}{\nu\alpha_\delta(h)} \left(-gh\nabla h - \frac{1}{\rho_0}h\nabla p_{\text{film}} + \mathbf{F} \right), \quad (5.17)$$

effectively enslaving the dynamics of \mathbf{u} to that of h . In the no slip limit, $\delta \rightarrow 0$, and in absence of gravity and other forces, Eq. (5.17) simplifies into

$$\mathbf{u} \approx -\frac{h^2}{3\mu} \nabla p_{\text{film}}$$

with the dynamic viscosity $\mu = \rho_0\nu$. Inserting this result into the first equation of (5.16) leads to

$$\partial_t h \approx \nabla \cdot \left(\frac{h^3}{3\mu} \nabla p_{\text{film}} \right),$$

which is precisely the lubrication equation. In essence, our method is, therefore, an alternative solver of the lubrication equation (at least in the inertialess regime, $Re \ll 1$, and for very thin films, $\varepsilon \ll 1$), that brings in, from the computational point of view, the added values of excellent scalability of the corresponding LBM algorithm on parallel architectures, as we shall see in the following sections. Similar ideas have also been developed for reaction-diffusion equations [Cal+92; KS92; Che+95; WP96] and the modelling of surface tension effects by gradients of auxiliary fields [Swi+96; LCH03] based on the color gradient method [Gun+91].

Before concluding this section, let us notice that special care has to be taken in the implementation of the numerical scheme, when evaluating the forcing term since it contains higher order derivatives (the gradient p_{film} , which in turn includes the Laplace pressure $\gamma \nabla^2 h$, see Eq.(5.11) and, hence, spurious lattice effects may arise. We noticed, for example, that a centered scheme to calculate gradients [Zho04] does not guarantee the sufficient degree of isotropy on the lattice as, e.g., for the relaxation of a droplet (discussed in section 5.3), where it led to unphysical droplet shapes.

Therefore, we use the following expressions to compute the gradients

$$\nabla \phi(\mathbf{x}) = 3 \sum_{l=0}^8 w_l \mathbf{c}^{(l)} \phi(\mathbf{x} + \mathbf{c}^{(l)}) + O(\nabla^3), \quad (5.18)$$

and the Laplacian

$$\begin{aligned} \nabla^2 \phi(\mathbf{x}) = & \frac{1}{6} \left[4 \sum_{l=\text{odd}} w_l \phi(\mathbf{x} + \mathbf{c}^{(l)}) \right. \\ & \left. + 1 \sum_{l=\text{even}} w_l \phi(\mathbf{x} + \mathbf{c}^{(l)}) - 20\phi(\mathbf{x}) \right] + O(\nabla^4), \end{aligned} \quad (5.19)$$

respectively [JK00; Tha+13], for a generic scalar field ϕ (be it the height field h , the pressure p_{film} or a position dependent surface tension field). Besides the higher degree of the isotropy, the scheme (5.18-5.19) has the advantage of employing directly the set of lattice Boltzmann speeds.

5.3 Results

Below we present results from numerical simulations using the method introduced in the previous section. For all simulations, we apply periodic boundary conditions in the X - Y plane.

5.3.1 The Rayleigh-Taylor instability

The Rayleigh-Taylor instability occurs when a denser fluid is accelerated against a less dense one [Ray82; Tay50; Kul91; Sha84]. This can be the case, for instance, for a liquid film coating a ceiling, under the action of gravity. In such a configuration gravity tends, of course, to deform (and eventually disrupt) the film, while surface tension has a stabilizing effect. As a result of these competing mechanisms, any surface perturbation is stable or unstable depending on whether its characteristic wavenumber k is smaller or larger than a certain critical value k_c . Linear stability analysis calculations in the framework of lubrication theory provide the following growth rate $\sigma(k)$:

$$\sigma(k) = \frac{\rho g h_0^3}{3\mu} (k^2 - l_{\text{cap}}^2 k^4), \quad (5.20)$$

where $l_{\text{cap}} = (\gamma/g)^{1/2}$ is the capillary length. Unstable (stable) modes correspond to $\sigma(k) > 0$ ($\sigma(k) < 0$) and the critical wavenumber is, therefore, such that $\sigma(k_c) = 0$, i.e. $k_c = 1/l_{\text{cap}}$. On a lattice of size 2048×2048 nodes, we initialize the film height according to

$$h(\mathbf{x}, 0) = h_0(1 + \varepsilon(\mathbf{x})), \quad (5.21)$$

with ε a random variable homogeneously distributed in $[1 \cdot 10^{-4}, -1 \cdot 10^{-4}]$ and $h_0 = 1$. Forcing should always be below a certain threshold. Thus, for the gravitational

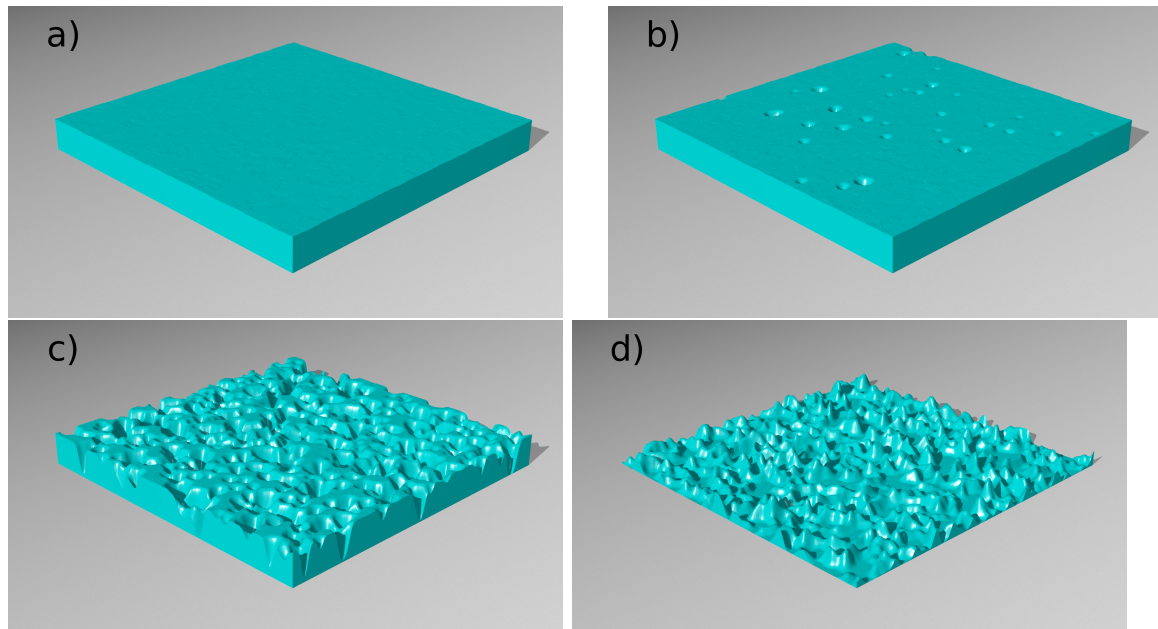


Figure 5.2: Time evolution of the free surface for the Rayleigh-Taylor instability at $\tau_{\text{cap}} \approx 50, 75, 100, 188$, corresponding to the lattice Boltzmann time steps $[9000, 14000, 19000, 35000] \Delta t$ in (a) - (d) respectively. For a more clear visualization we only show a small patch of size 256×256 centered in the middle of the 2048×2048 domain. The fluctuations of earlier states still follow the linear stability analysis (See Fig. 5.3 for the power spectrum of the height fluctuations versus wavenumber).

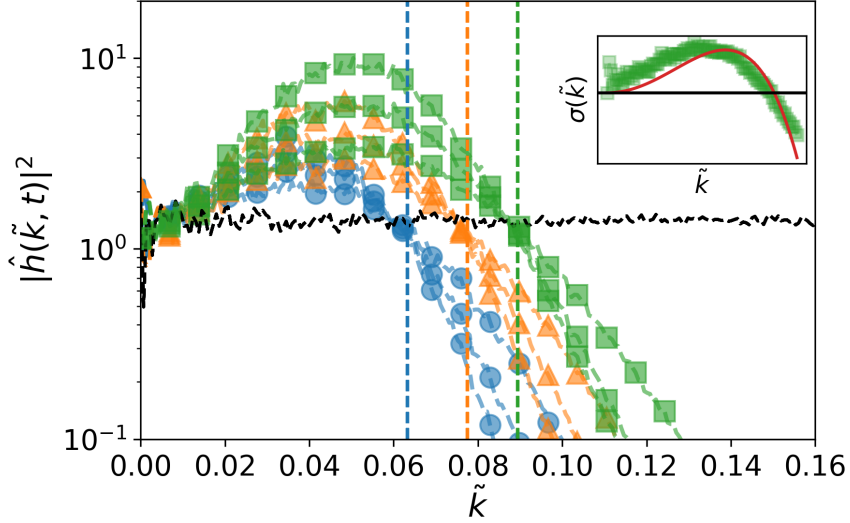


Figure 5.3: Power spectrum of the height fluctuations versus wavenumber.

The different colors and symbols belong to different values of gravitational acceleration, $g = 4 \cdot 10^{-5}$ is given by blue circles (\bullet), $g = 6 \cdot 10^{-5}$ by orange triangles (\blacktriangle) and $g = 8 \cdot 10^{-5}$ is given by green squares (\blacksquare). Same colored lines are taken at different time steps. In the inset we show the growth rate $\sigma(k)$ for the largest value of g (symbols) and the theoretical growth rate according to Eq. (5.20) (solid line).

acceleration we choose values within the interval $|g| = [4, 8] \cdot 10^{-5}$. Furthermore, we fix the surface tension to be $\gamma = 0.01$. This results in critical wavenumbers ranging from $k_c = 0.06$ to $k_c = 0.09$. Fig. 5.2 shows snapshots of the free surface from various time steps, where the growth of the perturbations is shown as time increases. The last panel is already beyond the linear regime.

We consider the time evolution of the power spectrum of the height field fluctuations (around the mean), defined as

$$E(k, t) = \oint_{\Omega_k} |\delta h(\mathbf{k}, t)|^2 d\Omega_k, \quad (5.22)$$

where

$$\delta h(\mathbf{k}, t) = \int e^{-2\pi i \mathbf{k} \cdot \mathbf{x}} (h(\mathbf{x}, t) - h_0) d\mathbf{k}, \quad (5.23)$$

with $\mathbf{k} = (k_x, k_y)$. Ω_k denotes the circle in \mathbf{k} -space (i.e. $\Omega_k = \{(k_x, k_y) | k_x^2 + k_y^2 = k^2\}$). Since we work in a discretized system we have to smear out the circle Ω_k with some small δk . Therefore, strictly speaking the integral is not computed around the circle Ω_k but around some small annulus $\Omega_{k+\delta k}$. The spectra are shown in Fig. 5.3. The various colors and symbols of Fig. 5.3 relate to different values of gravitational acceleration. For every set we consider the spectra at three equally scaled times $\tilde{t} = t/\tau_{\text{cap}}$, where

$$\tau_{\text{cap}} = \frac{\mu l_c}{\gamma}, \quad (5.24)$$

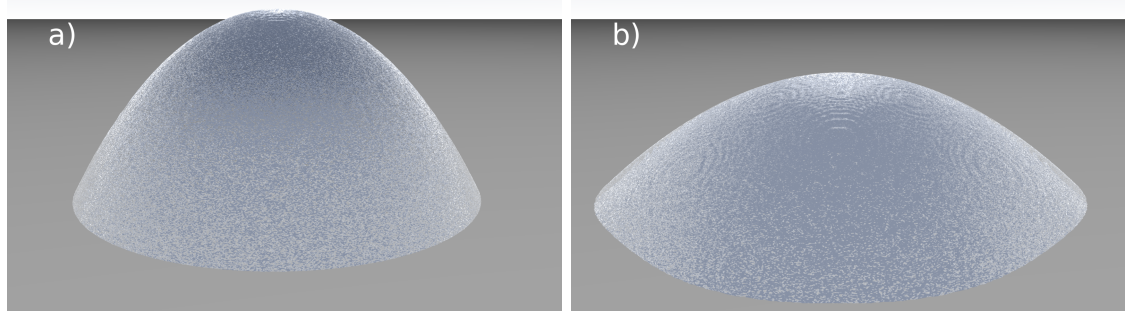


Figure 5.4: Relaxation of an out-of-equilibrium droplet. The initial state (a) is shown with a contact angle of $\theta = \pi/6$. Towards the end of the simulation (b) the droplet relaxes to the equilibrium contact angle.

$\tilde{t} = 50, 75, 100$. The values of k_c correspond to the points where the colored lines with symbols cut the black dashed line. The horizontal colored dashed lines mark the theoretical values for k_c . We observe good agreement of theoretical and numerical values. In the inset of Fig. 5.3 we plot the growth rate for the data of $g = 8 \cdot 10^{-5}$ together with the theoretical expression given by Eq. (5.20) (solid line).

Consistently with the random initialization, at $\tilde{t} = 0$ the spectrum is a constant (black dashed line). For $\tilde{t} > 0$, $E(k, t)$ develops a profile that grows in time for $k < k_c$, while it is damped out for $k > k_c$, in agreement with the expectation from the theory.

5.3.2 A spreading droplet

Let us consider the problem of a droplet, deposited on a smooth substrate with an apparent contact angle $\theta > \theta_{eq}$, which spreads to relax to a shape dictated by the equilibrium contact angle θ_{eq} . The equilibrium contact angle quantifies the wettability of a given substrate by a certain liquid and can be calculated using Young's equation [de 85]

$$\gamma \cos \theta_{eq} = \gamma_{SL} - \gamma_{SG}, \quad (5.25)$$

with γ_{SL} and γ_{SG} being the surface tensions between solid/liquid and solid/gas, respectively.

In our simulations we set the equilibrium contact angle through the disjoining pressure (Eq. (5.12)). In order to comply as much as possible with the thin film assumptions, we limit ourselves to relatively small contact angles.

To probe the spreading, on a 512×512 lattice we initialize a droplet, whose surface is given by the expression

$$h(x, y, 0) = \sqrt{R^2 - (x - x_0)^2 - (y - y_0)^2} - R \cos \theta, \quad (5.26)$$

with $R \sin \theta \approx 100 \Delta x$ ($\theta > \theta_{eq}$) being the radius of the droplet with a spherical cap shape, and (x_0, y_0) its center. The droplet is placed in the center of the lattice, i.e. $x_0 = y_0 = 256 \Delta x$.

In Fig. 5.4 we show such an initial shape, with contact angle $\theta = \pi/6$, and the equilibrium shape with contact angle $\theta_{eq} = \pi/12$.

To extract the contact angle from our data we impose that the shape at all times is close to the shape of a spherical cap, such that we are able to calculate the contact angle at any time using the initial angle and radius to obtain the volume

$$V = \frac{\pi}{3} R^3 (2 + \cos \theta) (1 - \cos \theta)^2. \quad (5.27)$$

Since our method is mass conserving, the volume of the droplet is by construction conserved. Measuring both the height of the droplet $h_d(t)$ and the diameter of the spherical cap $r(t)/2$ we are able to recalculate the time dependent sphere radius as

$$R(t) = \frac{r(t)^2 + h_d(t)^2}{2h_d(t)} \quad (5.28)$$

and can solve Eq.(5.27) again for the contact angle $\theta(t)$. We cross-checked our results with an alternative approach to calculate the angle given by

$$\theta(t) = \sin \left(\frac{r(t)}{R(t)} \right)^{-1}. \quad (5.29)$$

Let us stress that the shape is indeed very close to a spherical cap. As mentioned in Section 5.2, in fact, a sufficiently accurate finite difference scheme is required, as the one in Eqs. (5.18-5.19) [Tha+13]. In particular, we note that the isotropy of the pressure gradient is of utmost importance: a simple scheme with two-point centered derivatives [Zho04] yields squared equilibrium droplet shapes.

The spreading dynamics can be investigated even more quantitatively in terms of the so-called Cox-Voinov law and Tanner's law [Tan79]. The first one relates the apparent contact angle to the velocity U of the spreading front (the contact line), at various times, by $\theta^3 - \theta_{eq}^3 \propto Ca$. The capillary number Ca is defined as $Ca = \mu U / \gamma$ [SA13]. In Fig. 5.5 we plot $\theta^3(t) - \theta_{eq}^3$ vs $Ca(t)$ from a numerical simulation of a spreading drop: a good linear scaling, in agreement with the Cox-Voinov law, is observed, as highlighted by the dashed line.

The Tanner's law which states that the radius of the droplet grows with time as

$$R(t) \approx \left[\frac{10\gamma}{9B\mu} \left(\frac{4V}{\pi} \right)^3 t \right]^{1/10}, \quad (5.30)$$

with the constant B being such that $B^{1/10} \approx 1.2$. In Fig. 5.6 we plot the measured radius of the droplet divided by its initial radius R_0 as a function of the dimensionless time $\tilde{t} = t/\tau_{cap}$ (here $\tau_{cap} = \frac{\mu R}{\gamma}$). For the three viscosities considered in Figs. 5.5,5.6 our capillary times are $\tau_{cap} = [1333, 1667, 2333]\Delta t$. We see a saturation at $R/R_0 = 1.17$ because the droplet is very close to its equilibrium shape. During the growth phase the radius follows indeed a power law in \tilde{t} with exponent 1/10, which is shown by the red dashed line, in agreement with Tanner's prediction and experimental results [RMT02; Jam+18; CS86; Che88]. We further notice that within our simulations the droplet needs about $12\tau_{cap}$ to reach its equilibrium shape.

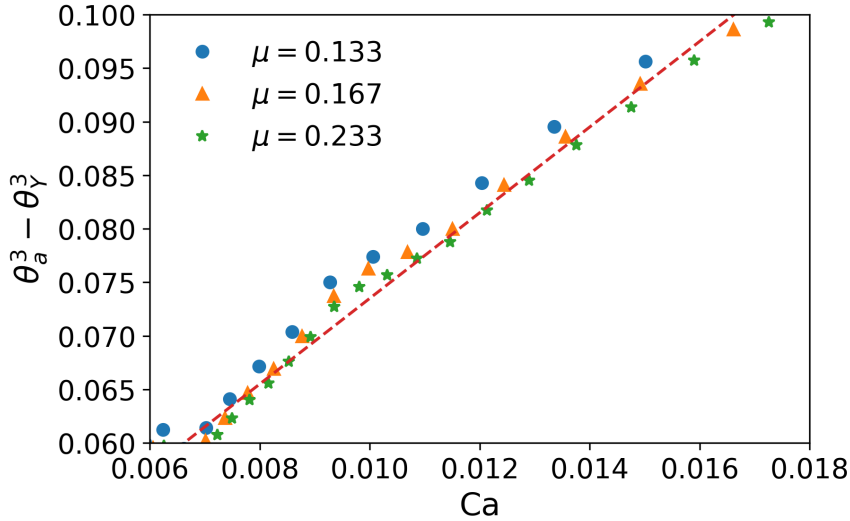


Figure 5.5: Difference of cubed instantaneous and equilibrium contact angles, $\theta_{num}^3 - \theta_{eq}^3$, vs. capillary number Ca for a spreading droplet; the dashed line shows a linear dependence (consistent with the Cox-Voinov law). The different symbols represent different viscosities, while the dashed line is a linear function of the capillary number.

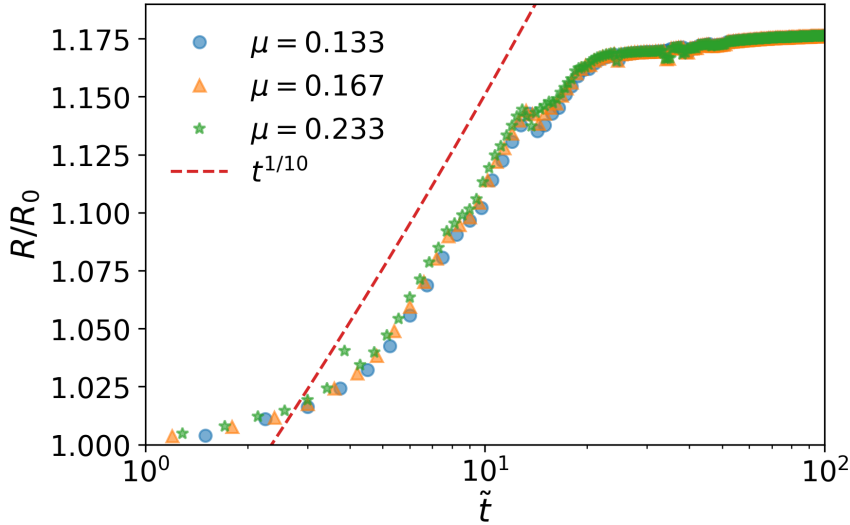


Figure 5.6: Time evolution of the droplet base radius of a spreading droplet; the dashed red line shows a $\tilde{t}^{1/10}$ power law (In consistence with Tanner's law). As in Fig. 5.5 different symbols refer to different viscosities. The radius clearly grows with the predicted power law until it saturates. Upon rescaling the time with τ_{cap} the curves of all three viscosities collapse into a single one.

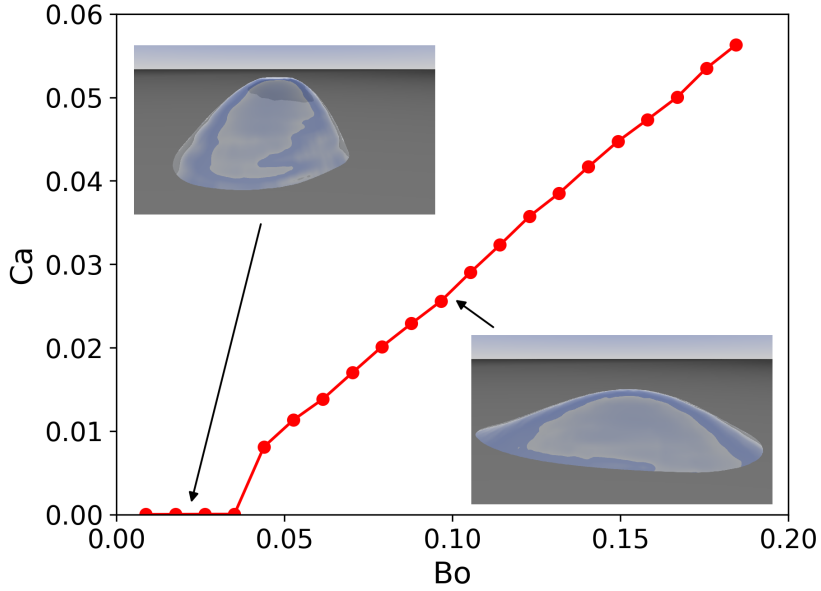


Figure 5.7: Ca vs Bo for a sliding droplet: notice that a finite minimum forcing (corresponding to Bo_c) is needed to actuate the droplet. For $Bo > Bo_c$ a linear relation, $Ca \sim Bo$, is observed. In the insets we show the shape of the droplet for both, the pinned (upper left) as well as the sliding (lower right) case.

5.3.3 A Sliding droplet

As a further validation case we consider the sliding of a droplet on an inclined plane. For a droplet to slide over an inclined plane, a minimum tilting angle $\alpha > 0$ of the substrate is required [Fur62], which in our case is due to the friction term Eq. (5.14). Until this critical angle is reached energy is stored in the deformation of the surface as the upper left inset in Fig. 5.7 shows. Above such a critical angle, a linear relation between the terminal sliding velocity U_∞ and the gravitational force $\propto mg \sin \alpha$ is observed [PFL01; KLK02; Sbr+14]; in dimensionless numbers such behaviour is expressed by

$$Ca \propto Bo - Bo_c, \quad (5.31)$$

where the capillary number is based on U_∞ and Bo is the so called Bond number, given by

$$Bo = (3V/4\pi)^{2/3} \rho g \frac{\sin \alpha}{\gamma}. \quad (5.32)$$

Bo_c is the critical Bond number, defined in terms of the critical tilting angle α_c . In Fig. 5.7 we plot Ca vs Bo from our numerical simulations, showing that the phenomenology described by Eq. (5.31) is indeed reproduced, i.e. the onset of sliding takes place at a finite forcing, beyond which the linear scaling $Ca \sim Bo$ is fulfilled.

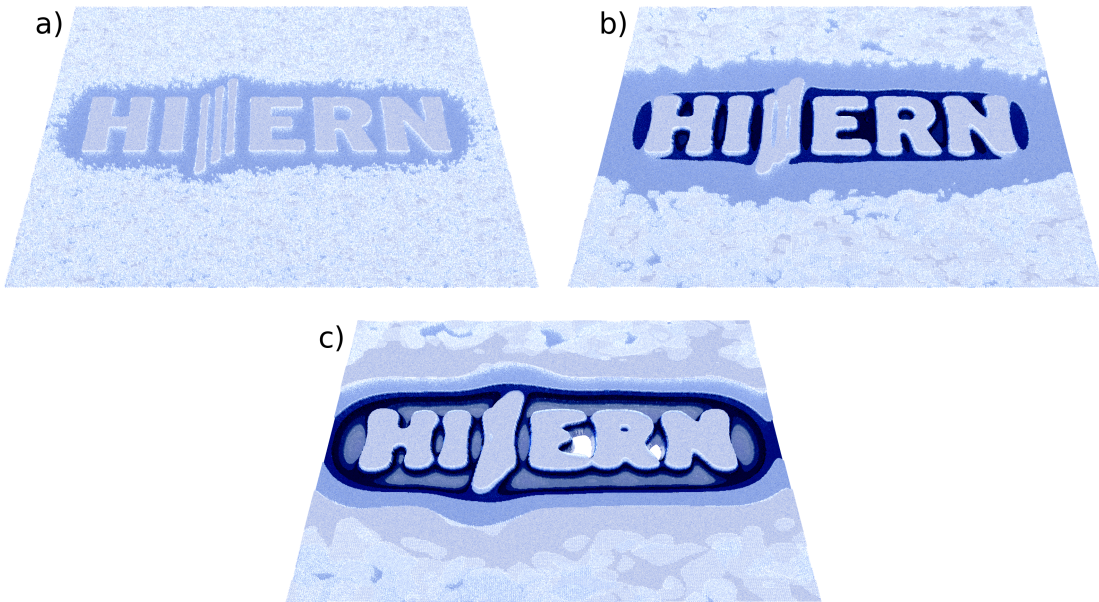


Figure 5.8: Time evolution of the free surface on a chemically patterned substrate on a $512 \times 512 \Delta x^2$ domain. Varying the contact angle between the letters and the rest of the substrate yields the shown dewetting pattern. The letters are more wettable than the rest. To emphasize the process we use a color gradient ranging from dark blue to light blue. Starting from a randomly perturbed film height, the fluid starts to dewet the pattern (a) and after $2400\Delta t$ the letters and a surrounding rim structure are clearly visible. In (b) at $16800\Delta t$ a depletion around the letters is already very prominent. Towards the end of the simulation (c) at $97200\Delta t$, the instability of the thin film also leads to film rupture. Holes form between the letters E, R and N.

5.3.4 Dewetting of liquid films

In order to show-case the capabilities of our method in handling more complex physics scenarios, we finally consider the dewetting of a chemically patterned substrate [KS02a; BGD13]. This is easily made possible within the code by introducing a space-varying equilibrium contact angle, $\theta_{eq}(x, y)$, in Eq. (5.12); in this way we can tune the local wettability of the substrate. Fig. 5.8 shows a liquid film which is initialized with thickness $h(x, y, 0)$ randomly fluctuating in space around its mean value h_0 , by a small percentage ($\approx 0.01\%$) of it (panel (a)). A partially wettable substrate is patterned in such a way that the contact angle is lower on a region defining a logo. The total domain contains 512x512 lattice nodes. With this domain size a letter contains around 130 lattice nodes in y-direction and about 60 lattice nodes in x-direction. Using the initial height h_0 of the film as characteristic length scale we get a capillary time of $\tau_{cap} \approx 20\Delta t$. As the film dewets, liquid moves toward the letters of the logo, the surrounding film becomes thinner and eventually the logo becomes visible.

5.4 Computational Aspects

We use *OpenACC* directives to allow our code to run on accelerator devices, such as Graphics Processing Units (GPUs), while being able, at the same time, to exploit the well known good scaling properties of the LBM on parallel machines [CJ17]. *OpenACC* is particularly versatile in terms of programmability since it only requires a few lines of code to allow us to harness the power of state of the art accelerators. In this sense *OpenACC* is very similar to *OpenMP* and more readable as well as much easier to program than *CUDA*.

The performance of a LBM code is commonly measured in Million Lattice Updates Per Second (**MLUPS**), defined as

$$\text{MLUPS} = \frac{A \times n}{t_{sim} \times 10^6}, \quad (5.33)$$

with $A = L_x \times L_y$ being the area of the lattice, where L_x, L_y are the number of lattice nodes in x and y directions. The number of iterations is given by n . The time needed to compute the n interations is called t_{sim} (in seconds). In Tab. 5.1 we provide benchmark data comparing the performance of a Nvidia GTX 1080TI, a Nvidia Quadro K2200 and a single core of an Intel i7-4790 @ 3.6GHz CPU. Due to the limited amount of memory available on the Quadro K2200, it is not possible to run a simulation of size 4096² on this card. Such a simulation requires about 4.8 GB local memory, while the Quadro K2200 only supplies 4 GB. In particular the speedup gained by using a GTX 1080TI is outstanding and corresponds to about 24-92 times the performance of a single core of the Intel CPU. Assuming perfect scaling on the CPU and using all 4 physical cores, the simulation on the GPU would be faster by a factor between 6 and 23. The speedup depends on the size of the lattice and in

Lattice/Accelerator	128^2	256^2	512^2	1024^2	2048^2	4096^2
GTX 1080TI	157.6	279.2	382.6	414.9	404.7	395.6
Quadro K2200	33.5	42.9	46.6	48.2	49.0	X
i7-4790	6.4	5.8	4.5	4.6	4.5	4.3

Table 5.1: Performance analysis based on a MLUPS measurement. The different columns relate to different lattice sizes, while the rows correspond to the two GPUs and one CPU used. All simulations are run for $100000\Delta t$ with FP64 double precision.

order to keep the pipelines on the GPU filled, a minimum loop size is needed. In addition, data transfer between *host* and *device* is a known bottleneck impacting the performance of GPU based simulations. This is obviously also the case for our code – even though such data transfer is only needed when files are written to disk.

5.5 Conclusions

We have presented a novel lattice Boltzmann model for the numerical simulation of thin liquid film hydrodynamics, featuring explicitly relevant properties of interface physics, such as surface tension and disjoining pressure.

We validated our method against a relevant test case, namely the Rayleigh-Taylor instability, where the critical wavenumber as well as the growth and damping of wave-modes are correctly reproduced. Our simulations of droplets on substrates showed that droplets initiated out of equilibrium attain their equilibrium contact angle and that our method correctly reproduces the Cox-Voinov law as well as Tanner’s law. Furthermore, our approach allows to simulate the dynamics of sliding droplets and even complex dewetting scenarios.

Our *OpenACC* enabled simulation code allows for a massive improvement of the performance: with modern GPU cards at hand simulations using large lattice sizes and requiring many time steps can be run on a single workstation without the need for access to high performance computing resources.

In the future, we plan to extend our work towards systems which could hardly be tackled by traditional methods: from the dynamics of individual droplets on complex shaped substrates we plan to move to large numbers of droplets in order to understand the statistical properties of collective droplet motion on chemically structured substrates. Finally, a possible application of our method could be the simulation of full lab-on-chip devices with highly resolved channels, junctions, etc..

5.6 Acknowledgements

The authors acknowledge financial support by the Deutsche Forschungsgemeinschaft (DFG) within the Cluster of Excellence “Engineering of Advanced Materials” (project

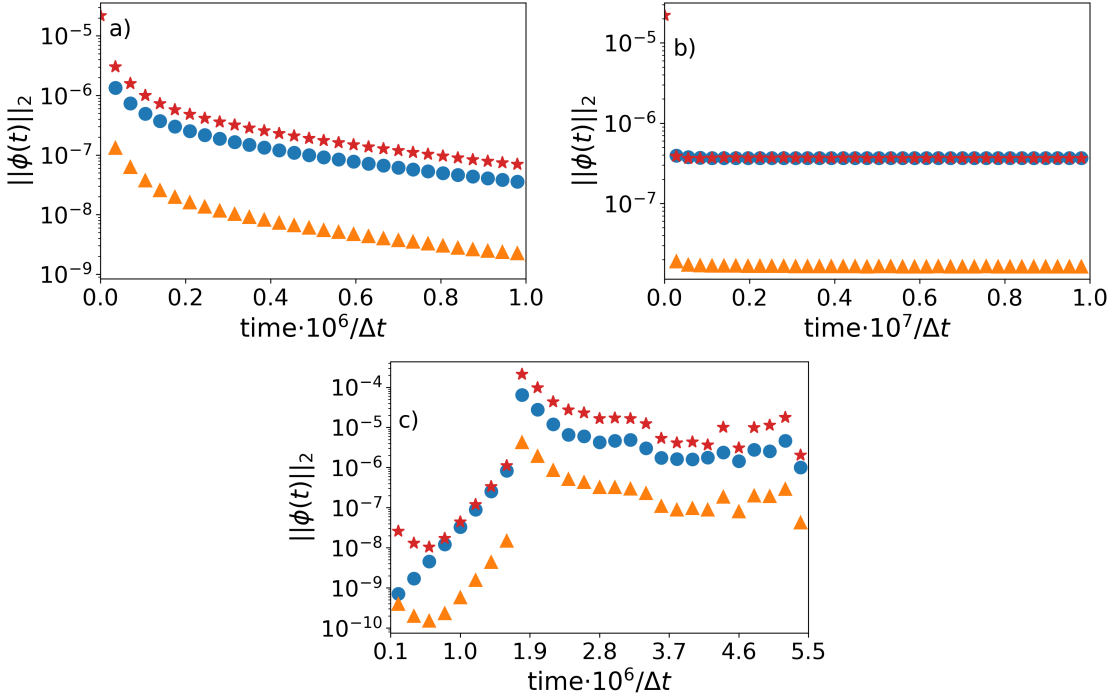


Figure 5.9: Time evolution of the \mathbf{L}_2 norm (as defined by equation (5.34)) of the x -component of the terms appearing on the right hand side of the second of equations (5.15). The plot is in log-lin scale. The panels refer to three different numerical experiments: (a) spreading droplet, (b) sliding droplet and (c) thin film dewetting. The symbols correspond to: film pressure gradient, $-h\partial_x p_{\text{film}}$, (\star); friction, $-\nu\alpha(h)u_x$, (\bullet); longitudinal dissipation terms $\nu\nabla^2(hu_x) + 2\nu\partial_x(\nabla \cdot (hu))$, (\blacktriangle).

EXC 315) (Bridge Funding). The work has been partly performed under the Project HPC-EUROPA3 (INFRAIA-2016-1-730897), with the support of the EC Research Innovation Action under the H2020 Programme; in particular, S. Z. gratefully acknowledges the support of Consiglio Nazionale delle Ricerche (CNR) and the computer resources and technical support provided by CINECA.

5.7 Appendix

As anticipated above, we provide here a numerical validation of the assumptions on effectively negligible terms that lead from Eq. (5.9) to Eq. (5.16). To this aim, we report in Fig. 5.9, for each of the term under scrutiny, the time evolution of a \mathbf{L}_2 -norm, defined for a generic scalar field $\phi(\mathbf{x}, t)$ as

$$\|\phi(t)\|_2 = \left(\frac{1}{N^2} \sum_{i=1}^N \sum_{j=1}^N (\phi(x_i, y_j, t))^2 \right)^{\frac{1}{2}}, \quad (5.34)$$

where the double sum is extended to the whole two-dimensional domain. Three case-studies are analyzed (corresponding to the three panels in Fig. 5.9), namely (a) a sessile droplet spreading on a substrate with an equilibrium contact angle smaller than the initial one, (b) a droplet sliding under the action of a body force and (c) the dewetting of a substrate. We compare, for each simulation, the $\|\phi(t)\|_2$ for the x -component² of the gradient of the film pressure, $-h\partial_x p_{\text{film}}$, of the friction term, $-\nu\alpha(h)u_x$, and of the longitudinal viscous terms, $\nu\nabla^2(hu_x) + 2\nu\partial_x(\nabla \cdot (h\mathbf{u}))$ (the advection term, $\nabla \cdot (h\mathbf{u}u_x)$ is for all cases orders of magnitude smaller than the other terms, therefore we decided to omit it from the comparisons in figure Fig. 5.9). We observe that the gradient of the film pressure and the friction are dominant, with the L_2 norm of the longitudinal dissipation term being always, roughly, less than 10% of the friction contribution.

²Similar results are found also for the y -component.

6 Lattice Boltzmann simulations of stochastic thin film dewetting

*Während um mich herum die Welt
im Akkord progressiert, bleibt
stumm, wer sich in Dissonanz
verliert*

Yukno

This chapter has been published and can be found as: Zitz, S., Scagliarini, A., & Harting, J. (2021). Lattice Boltzmann simulations of stochastic thin film dewetting. Physical Review E, 104(3), 034801.

We study numerically the effect of thermal fluctuations and of variable fluid-substrate interactions on the spontaneous dewetting of thin liquid films. To this aim, we use a recently developed lattice Boltzmann method for thin liquid film flows, equipped with a properly devised stochastic term. While it is known that thermal fluctuations yield shorter rupture times, we show that this is a general feature of hydrophilic substrates, irrespective of the contact angle θ . The ratio between deterministic and stochastic rupture times, though, decreases with θ . Finally, we discuss the case of fluctuating thin film dewetting on chemically patterned substrates and its dependence on the form of the wettability gradients.

6.1 Introduction

A liquid wetting a solid surface is a process that appears in many everyday life situations, like, e.g., when a rain drop hits the leaf of a plant or when coffee is spilt on a table. Wetting phenomena have an impact on areas as diverse as surface coatings, printing, plant treatment with pesticides, or even pandemics [ODB97; SA13; CB44; Len90; dQ98; Qué99; Ber+00; BA20]. Coating processes heavily rely on the affinity between a fluid and a substrate [Bon+09]. If this affinity is not sufficiently strong or the substrate is rather heterogeneous the liquid layer may eventually become unstable, leading to film rupture [ODB97; CM09] or wrinkling [da +99]. These instabilities are, of course, harmful to a uniform coating.

A successful mathematical modelling of the dynamics of thin liquid films is based on

the thin-film equation [Rey83a; ODB97]

$$\partial_t h(\mathbf{x}, t) = \nabla \cdot (M(h) \nabla p(\mathbf{x}, t)), \quad (6.1)$$

where $h(\mathbf{x}, t)$ is the height of the free surface at position $\mathbf{x} = (x, y)$ and time t , while $p(\mathbf{x}, t)$ is the pressure at the free surface. The function $M(h)$ denotes the mobility, whose functional form is determined by the fluid velocity boundary condition at the solid surface: for a no-slip condition [ODB97], in particular, $M(h) = \frac{h^3}{3\mu}$, where μ is the fluid dynamic viscosity. The film pressure p consists of the capillary pressure and the disjoining pressure, i.e.,

$$p = -\gamma \nabla^2 h + \Pi(h), \quad (6.2)$$

where γ is the surface tension. The disjoining pressure $\Pi(h)$ is the derivative, with respect to the height h , of the interfacial potential, which incorporates the interactions between liquid and substrate (i.e. wetting properties). The advantage of such approach in comparison with molecule-resolved methods such as Molecular Dynamics [Hai97; ZSL19; Wen+00; GG88] and Density Functional Theory [vH89; TE84; MK85; HTA14] is that these may quickly become computationally prohibitive, as the size of the film is increased above few nanometres in thickness and to the micrometric scale in the horizontal extension. However, when dealing with films of nanometric thickness, a hydrodynamic description may fall short due to thermal fluctuations. For instance, in the context of dewetting, rupture times measured in experiments are shorter than predicted by simulations of the thin-film equation [Bis+96; Her+98; Bec+03]. More in general, thermal fluctuations can accelerate the appearance of film instabilities [RD08; TR93; Fet+07b; ZSL19]. The first theoretical and experimental studies, by means of light scattering techniques, on film rupture influenced by thermal fluctuations date back to the 60s [VO68]. Almost half a century later, a stochastic version of Eq. (6.1) was derived [GMR06; MR05; DMS05], through a lubrication approximation of the Navier-Stokes-Landau-Lifshitz equations of fluctuating hydrodynamics [LL13]. A strong agreement between experiments and the stochastic thin-film equation was found in showing that the variance of the interfacial roughness cannot be explained without adding a fluctuating term [Fet+07b]. The influence of thermal fluctuations on the short and long time morphology of a film has been studied with simulations of the one and two dimensional stochastic thin-film equations [Nes+15; Pah+18]. Recently, new theoretical insights have been gained explaining film rupture as a consequence of the combined action of thermal fluctuations and drainage, both numerically [Sha+19] and experimentally [CV20].

To the best of our knowledge, the impact of thermal fluctuations on thin film dewetting of chemically patterned substrates has so far been overlooked. The purpose of this paper is to fill this gap, studying the role of heterogeneous substrate properties in the fluctuating dewetting dynamics. To this aim we perform numerical simulations of the deterministic and stochastic thin-film equations with space-varying contact angle (parametrizing the chemical patterning of the substrate). In particular, since we aim to simulate large systems, in order to achieve reliable statistics in terms of number of droplets, we specialize the study to the one-dimensional geometry, for computational feasibility.

This paper is organized as follows. In Sec. 6.2 we shortly discuss the stochastic thin-film equation and its linear stability analysis. Then, we introduce the key features of our lattice Boltzmann model for the thin-film equation and its extension to include thermal fluctuations in Sec. 6.3. The results are presented and discussed in Sec. 6.4. Finally, conclusions and summary are provided in Sec. 6.5.

6.2 Linear Stability Analysis of the Stochastic Thin-Film Equation

The one-dimensional stochastic thin-film equation reads [GMR06; MR05]:

$$\partial_t h = \partial_x \left[\frac{h^3}{3\mu} \partial_x p + \sqrt{\frac{2k_B T h^3}{3\mu}} \mathcal{N} \right], \quad (6.3)$$

where k_B is Boltzmann's constant, T is the temperature and \mathcal{N} is a Gaussian white noise with

$$\langle \mathcal{N}(x, t) \rangle = 0, \quad (6.4)$$

$$\langle \mathcal{N}(x, t) \mathcal{N}(x', t') \rangle = \delta(x - x') \delta(t - t'). \quad (6.5)$$

In order to understand the influence of thermal fluctuations on the temporal evolution of the film height, we cursory recall the linear stability analysis of Eq. (6.3) [ZSL19; DGF16]. Introducing the deviation δh from the mean height h_0 , such that $h = h_0 + \delta h$ and $\delta h \ll h_0$, the linearised stochastic thin-film equation is obtained

$$\partial_t \delta h = \frac{h_0^3}{3\mu} \left(\Pi'(h_0) \partial_x^2 \delta h - \gamma \partial_x^4 \delta h \right) + \sqrt{\frac{2k_B T h_0^3}{3\mu}} \partial_x \mathcal{N}, \quad (6.6)$$

where $\Pi'(h_0) \equiv \left. \frac{\partial \Pi(h)}{\partial h} \right|_{h=h_0}$. Here, it is assumed that also the noise is small, in the sense that $k_B T \ll \gamma h_0^2$. To derive a dispersion relation for this system, first the Fourier transforms of the perturbation δh

$$\tilde{\delta h}(q, t) = \int_{-\infty}^{\infty} \delta h(x, t) e^{-ixq} dx, \quad (6.7)$$

and the noise term \mathcal{N}

$$\tilde{\mathcal{N}}(q, t) = \int_{-\infty}^{\infty} \mathcal{N}(x, t) e^{-ixq} dx. \quad (6.8)$$

must be performed.

Inserting $\tilde{\delta h}$ and $\tilde{\mathcal{N}}$ in (6.6) yields

$$\partial_t \tilde{\delta h} = \omega(q) \tilde{\delta h} + i \sqrt{\frac{2k_B T h_0^3}{3\mu}} q \tilde{\mathcal{N}}, \quad (6.9)$$

with dispersion relation $\omega(q)$ given by

$$\omega(q) = \frac{1}{t_0} \left[2 \left(\frac{q}{q_0} \right)^2 - \left(\frac{q}{q_0} \right)^4 \right]. \quad (6.10)$$

The maximum, q_0 , of $\omega(q)$ and the characteristic time, t_0 , are specific to the substrate the film is deposited on and their expressions are [Fet+07b]

$$q_0^2 = \frac{1}{2\gamma} \frac{\partial \Pi(h)}{\partial h} \Big|_{h=h_0}, \quad (6.11)$$

and

$$t_0 = \frac{3\mu}{\gamma h_0^3 q_0^4}. \quad (6.12)$$

Solving Eq. (6.9) leads to the following expression for the spectrum [ZSL19; MR05], $S(q, t) = \langle |\tilde{h}(q, t)|^2 \rangle$ (where the brackets stand for the average over the noise):

$$S(q, t) = S_0(q) e^{2\omega(q)t} + \frac{k_B T h_0^3}{3\mu} \frac{q^2}{\omega(q)} (e^{2\omega(q)t} - 1). \quad (6.13)$$

For $q > \sqrt{2}q_0$, $S(q, t)$ tends to the capillary wave spectrum, $S \sim S_{\text{cw}} \propto \frac{k_B T}{\gamma q^2}$, as $t \rightarrow \infty$ (whereas it would decay exponentially to zero in the deterministic case) [Fet+07b; MR05]. Moreover, while the maximum q_0 is independent of time in the deterministic case, the maximum q_m of (6.13) approaches q_0 from the right as the time increases. It follows that the most unstable wavelength, $\lambda_{\max} = 2\pi/q_m$, grows with time. We will come back to this fact in Sec. 6.4 and show that indeed this behavior is reproduced and observed in our simulations.

6.3 Thin Film Lattice Boltzmann Model

Performing numerical simulations of the thin-film equation is challenging, even in the deterministic case; including stochastic terms adds a further level of complexity. To this aim, several sophisticated numerical methods have been developed, based on, e.g., finite differences [DKB00], finite elements [GMR06] and spectral schemes [Dur+19].

6.3.1 Lattice Boltzmann Method

To simulate the dynamics of thin liquid films described by Eq. (6.1), we employ a recently developed [Zit+19] lattice Boltzmann method (LBM), built on a class of models originally devised for the shallow water equations [Sal99; Del02; Zho04; van+10]. The one-dimensional lattice Boltzmann equation for the discrete particle distribution functions f_i reads

$$f_i(x + c^{(i)} \Delta t, t + \Delta t) = \left(1 - \frac{\Delta t}{\tau} \right) f_i(x, t) + \frac{\Delta t}{\tau} f_i^{(eq)}(x, t) + w_i \frac{\Delta t}{c_s^2} c^{(i)} F, \quad (6.14)$$

where i labels the lattice velocities $c^{(i)}$ and runs from 0 to $Q - 1$, with Q being the number of velocities characterizing the scheme, and F is a (generalised) force¹. Algorithmically, this equation is composed of two steps. In the local collision step, the distribution functions f_i relax towards their local equilibria $f_i^{(eq)}$ with a relaxation time τ . In the streaming step, the Q distribution functions f_i are moved over the lattice according to their lattice velocities $c^{(i)}$. We adopt here the standard one-dimensional D1Q3 scheme with 3 lattice velocities, given by

$$c^{(i)} = [0, c, -c], \quad i = 0, 1, 2, \quad (6.15)$$

where $c = \frac{\Delta x}{\Delta t}$, with weights

$$w_0 = \frac{2}{3}, \quad w_{1,2} = \frac{1}{6}, \quad (6.16)$$

and speed of sound $c_s^2 = \frac{c^2}{3}$. The equilibrium distribution functions $f_i^{(eq)}$ read [van+10]:

$$\begin{aligned} f_0^{eq} &= h \left(1 - \frac{1}{2c^2} gh - \frac{1}{c^2} u^2 \right), \\ f_1^{eq} &= h \left(\frac{1}{4c^2} gh + \frac{1}{2c} u + \frac{1}{2c^2} u^2 \right), \\ f_2^{eq} &= h \left(\frac{1}{4c^2} gh - \frac{1}{2c} u + \frac{1}{2c^2} u^2 \right), \end{aligned} \quad (6.17)$$

with g being the gravitational acceleration (which will be set to zero, hereafter, as it can be obviously neglected for nanoscale thin films). The hydrodynamic fields (film height h and velocity u) are expressed in terms of the distribution functions f_i as:

$$h = \sum_{i=0}^2 f_i \quad hu = \sum_{i=0}^2 c^{(i)} f_i. \quad (6.18)$$

The force F in (6.14) consists of two terms,

$$F = F_{\text{cap}} + F_{\text{fric}}. \quad (6.19)$$

In the first term the effect of the film pressure p , Eq. (6.2), is embedded, i.e.

$$F_{\text{cap}} = -\frac{1}{\rho_0} h \frac{\partial p}{\partial x}, \quad (6.20)$$

(ρ_0 being the fluid density) whereas the second one represents a viscous friction with the substrate:

$$F_{\text{fric}} = -\nu \alpha_\delta(h) u, \quad (6.21)$$

where $\nu = \mu/\rho_0$ is the fluid kinematic viscosity (related to the relaxation time τ by $\nu = c_s^2 (\tau - \frac{\Delta}{2})$) and the friction factor

$$\alpha_\delta(h) = \frac{6h}{2h^2 + 6h\delta + 3\delta^2}, \quad (6.22)$$

¹Strictly speaking its dimensions are [length]²[time]⁻²

depends on the film height and on the particular fluid velocity boundary condition at the substrate surface, parameterised by a slip length δ . It can be shown that in the limit of vanishing inertia, negligible gravity and small film thickness, the model defined by Eqs. (6.14-6.22) represents a numerical solver for the system of equations

$$\begin{cases} \partial_t h + \partial_x(hu) = 0 \\ \partial_t(hu) = -\frac{1}{\rho_0}h\partial_x p - \nu\alpha_\delta(h)u. \end{cases} \quad (6.23)$$

The left hand side of the second of Eqs. (6.23) can be neglected in the limits considered (small Reynolds number and film thickness). Thus, the equation reduces to $u \approx -\frac{h}{\mu\alpha_\delta(h)}\partial_x p$ that, plugged into the first of Eqs. (6.23), gives Eq. (6.1) (with a no-slip mobility $M(h) = \frac{h^3}{3\mu}$ if the further limit $\delta \rightarrow 0$ is taken).

6.3.2 Modelling Thermal Fluctuations

In order to enable our method to simulate the stochastic thin-film equation, we proceed in a constructive way, introducing a fluctuating force, F_{fluc} , in the velocity equation in (6.23) such that, in the limits previously discussed, Eq. (6.3) is recovered. The velocity entering the height equation in (6.23) then reads

$$u \approx -\frac{h}{\mu\alpha_\delta(h)}\partial_x p + \frac{\rho_0}{\mu\alpha_\delta(h)}F_{\text{fluc}}. \quad (6.24)$$

A term-by-term matching with Eq. (6.3) straightaway tells that the sought form for the fluctuating force is

$$F_{\text{fluc}} = \frac{1}{\rho_0}\sqrt{2k_B T \mu \alpha_\delta(h)} \mathcal{N} \quad (6.25)$$

(where we have omitted the sign since \mathcal{N} is a zero-mean random number), or also, in the no-slip limit $\delta \rightarrow 0$,

$$F_{\text{fluc}} = \frac{1}{\rho_0}\sqrt{\frac{6k_B T \mu}{h}} \mathcal{N}. \quad (6.26)$$

The fluctuating force F_{fluc} enters in the scheme by being added to the total force, Eq. (6.19), that becomes

$$F = F_{\text{cap}} + F_{\text{fric}} + F_{\text{fluc}} \quad (6.27)$$

and appears in the lattice Boltzmann equation (6.14).

6.3.3 Fluid-substrate interactions: the contact angle

For the disjoining pressure $\Pi(h)$ we use the following expression [CM09; Pes+19; Nes+15; ODB97]:

$$\Pi(h) = \kappa(\theta) \left[\left(\frac{h_*}{h + h_c} \right)^n - \left(\frac{h_*}{h + h_c} \right)^m \right], \quad (6.28)$$

θ	$n = 3, m = 2$			$n = 9, m = 3$		
	t_0	q_0	λ_{\max}	t_0	q_0	λ_{\max}
$\pi/9$	$5 \cdot 10^5$	0.101	62	$8.6 \cdot 10^6$	0.049	128
$5\pi/36$	$2 \cdot 10^5$	0.126	50	$3.5 \cdot 10^6$	0.061	103
$\pi/6$	10^5	0.151	42	$1.7 \cdot 10^6$	0.073	86
$7\pi/36$	$5 \cdot 10^4$	0.175	36	10^6	0.085	74
$2\pi/9$	$3 \cdot 10^4$	0.2	32	$6 \cdot 10^5$	0.097	65

Table 6.1: Numerical values (in lbu) of characteristic time, t_0 , most unstable wavenumber, q_0 , and corresponding wavelength, λ_{\max} , for the various contact angles θ and pairs (n, m) of the disjoining pressure exponents used (see Eq. (6.28)).

where the prefactor $\kappa(\theta) = \gamma(1 - \cos(\theta)) \frac{(n-1)(m-1)}{(n-m)h_*}$ is related to the Hamaker constant by $\mathcal{A} = 6\pi h_*^3 \kappa(\theta)$. θ is the contact angle, which effectively encodes the interfacial energies of the three-phase system and represents, therefore, a measure of the hydrophilicity/hydrophobicity of the substrate. Throughout the paper we restrict ourselves to low contact angles, $\theta < 1$, so to comply with the lubrication approximation, which requires the derivative of the height field to be small, $\partial_x h(x) \ll 1$, and hence limits the values of θ (since, at the contact point, $\partial_x h \sim \tan(\theta) \sim \theta$). To ensure numerical stability we introduce a regularizing term h_c ; the value $h_* - h_c > 0$, at which the disjoining pressure vanishes, sets the thickness of the precursor film covering the substrate.

6.4 Results

We simulate numerically the model (6.14-6.18), with forcing term (6.20-6.21-6.26-6.27) (and $\Delta x = \Delta t = 1$), on a domain of length $L = 4096$, with a relaxation time $\tau = 1$, corresponding to a kinematic viscosity $\nu = 1/6$. The surface tension γ is set to 0.01 and we use, as exponents appearing in the disjoining pressure (Eq. (6.28)), the pairs $(n, m) = (3, 2)$ (in section 6.4.1, 6.4.2 and 6.4.3) and $(n, m) = (9, 3)$ (in section 6.4.4). The thickness of the precursor film is $h_* - h_c = 0.05$ ($h_* = 0.1, h_c = 0.05$) and the numerical slip length δ (unless otherwise stated) is chosen to be in the weak slip regime, $\delta/h_0 = 1.0$. The system is initialised with zero velocity everywhere ($u(x, 0) = 0 \forall x \in [0, L]$) and with random perturbations of amplitude 10^{-3} around the value $h_0 = 1$ for the film height, i.e. $h(x, 0) = h_0 + 10^{-3}\varepsilon$ (ε being a random variable uniformly distributed in $[-1, +1]$). In the remainder of the manuscript all lengths will be given adimensionalised by h_0 . We vary the contact angle in the interval $[\pi/9, 2\pi/9]$; the numerical values (in lattice Boltzmann units, lbu) of the corresponding wavelength, λ_{\max} and wavenumber, q_0 , of the most unstable mode as well as the

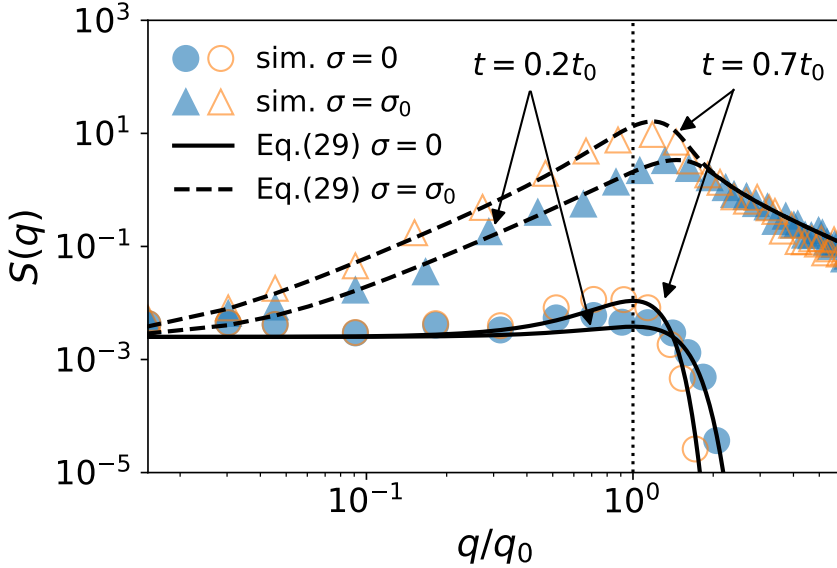


Figure 6.1: Height fluctuations spectra from deterministic (circles) and stochastic (triangles) simulations at $t = 0.2t_0$ (filled symbols) and $t = 0.7t_0$ (empty symbols), on a substrate with $\theta = \pi/9$. The theoretical predictions, Eq. (6.29), are reported with solid ($\sigma = 0$) and dashed ($\sigma = \sigma_0$) lines.

characteristic time, t_0 , can be found in Tab. 6.1. For each contact angle configuration we perform one simulation for the athermal system and a set of $O(30)$ runs for the fluctuating case, at changing the random seed (the data shown represent, then, an average over the noise realisations). We would like to stress, incidentally, that the inclusion of the stochastic term entails a computational overhead of, roughly, 20% of a typical deterministic run.

The numerical data will be indicated, hereafter, in terms of the dimensionless temperature $\sigma = \sqrt{\frac{k_B T}{\gamma h_0^2}}$, which is set either to $\sigma = 0$ (for the athermal dewetting) or to $\sigma = 3.16 \cdot 10^{-3} \equiv \sigma_0$, corresponding to a thermal energy of $k_B T = 10^{-7}$ lbu (for the fluctuating dewetting). For the sake of comparison, we remark that such a value lies well within the window $\sigma \in [10^{-3}, 10^{-2}]$, measured in experiments with polymeric and metallic thin films [Fet+07b; Gon+13].

6.4.1 Testing the stochastic term

In order to validate our model against the analytical results discussed in section 6.2, we first rewrite Eq. (6.29) in a form, involving the dimensionless temperature σ , which is more convenient for the forthcoming discussion, namely:

$$S(q, t) = S_0 e^{2\omega(q)t} + \frac{\sigma^2 h_0^2 L}{q_0^2} g\left(\frac{q}{q_0}\right) (e^{2\omega(q)t} - 1), \quad (6.29)$$

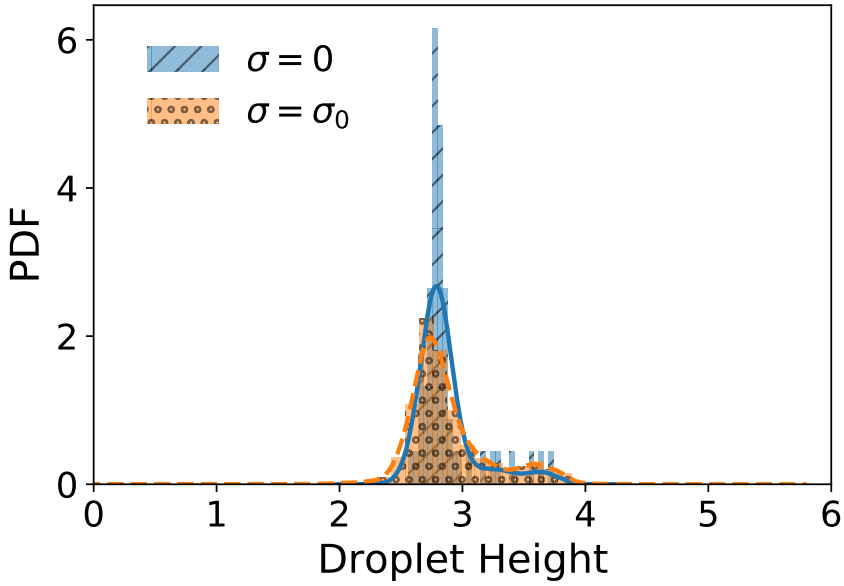


Figure 6.2: Histograms of the droplet height distributions from the deterministic (blue, line-patterned) and stochastic (orange, dot-patterned) simulations with $\theta = \pi/9$, at $t \approx 20t_0$; the corresponding Gaussian kernel density estimations are also plotted, as a guide to the eye, with solid blue (dashed orange) curve for the deterministic (stochastic) data.

where $g(\xi) = \frac{\xi^2}{2\xi^2 - \xi^4}$ and the appearance of the system size L stems from the noise amplitude, $\langle |\tilde{N}(q, t)|^2 \rangle = L$, resulting from discrete Fourier-transforming over a finite length [ZSL19; ZSL20]. To arrive at (6.29), use was made of the expression (6.12) for the characteristic time t_0 and we omitted the dependence on q of $S_0(q)$ because, with our initialization, the latter is just a constant, $S_0(q) \equiv S_0$. We measured, then, the spectra $S(q, t)$, at two instants of time, in the early stages of the growth of the instability, for both athermal and fluctuating dewetting on a substrate with $\theta = \pi/9$ (and strict no-slip, $\delta = 0$). The data, reported in Fig. 6.1, from both deterministic (circles) and fluctuating (triangles) simulations show good agreement with the theoretical curves, Eq. (6.29), depicted with solid ($\sigma = 0$) and dashed ($\sigma = \sigma_0$) lines. In particular, notice that the maximum of $S(q, t)$ is attained for $q = q_0$ independently of time, in the athermal case, and at $q = q_m > q_0$, with q_m tending to q_0 as the time goes by, when fluctuations are present; in the latter case, in addition, the capillary wave spectrum $S_{\text{cw}}(q) \propto q^{-2}$ is recovered for large q .

6.4.2 Droplet size distributions

In the early stage of the deterministic dewetting, we expect that the droplet size distribution, quantified in terms of the droplet height, will be strongly correlated to

the maximum unstable wavelength $\lambda_{\max} = 2\pi/q_0$:

$$\lambda_{\max} = \frac{2\pi}{q_0} = \sqrt{\frac{8\pi^2\gamma}{\Pi'(h)|_{h_0}}} \quad (6.30)$$

More quantitatively, in our one-dimensional case the equilibrium shape of a droplet is a circular arc, whose chord is the portion of droplet in contact with the substrate and equals $\lambda_{\max}/2$. Therefore, it can be shown, by means of simple geometrical arguments, that the droplet height is

$$h_{\text{drop}} = \frac{\lambda_{\max}}{4} \tan\left(\frac{\theta}{2}\right), \quad (6.31)$$

where θ is the contact angle. For $\theta = \pi/9$, we get $\lambda_{\max} \approx 62$ and $h_{\text{drop}} \approx 2.7$, which is the maximum around which the height values should be distributed. This is, indeed, what we observe in Fig. 6.2, where we show measurements of the droplet height distribution obtained from simulations with and without thermal fluctuations. In the deterministic case ($\sigma = 0$), the distribution (blue, line-patterned, histogram) sharply peaks around the theoretically predicted value $h_{\text{drop}} \approx 2.7$. As a guide to the eye we add a Gaussian kernel density estimation (solid blue curve) that shows the best fitting continuous distribution to the histogram. The data from the stochastic simulations ($\sigma = \sigma_0$), instead, show a broadening of the distribution (orange, dot-patterned, histogram and dashed orange curve). Adding thermal energy, then, on the one hand, facilitates the system to explore higher energetic states, whereas on the other hand it reduces the coarsening time scales [GMR06]: this is reflected in the tails of the distribution for both small and large values of h , respectively. These findings are in agreement with what was reported by Nesic et al. [Nes+15].

6.4.3 Rupture times and role of contact angle

Let us focus, now, on the dependence of the rupture times of the spinodally dewetting film on temperature and contact angle. To this aim, we compare, in Fig. 6.3, the evolution in time of height perturbations, $\Delta h(t) = \max_x\{h(x, t)\} - \min_x\{h(x, t)\}$, from deterministic (bullets (\bullet , \circ , \bullet)) and stochastic (triangles (\blacktriangle , \blacktriangledown , \blacktriangleup)) simulations, for three different contact angles, $\theta = \{\pi/9, \pi/6, 2\pi/9\}$ (color-coded). A similar analysis can also be found in Ref. [Pah+18]. As predicted by the linear stability analysis (see Eq (6.9)), the perturbations initially follow an exponential growth law (highlighted by the dashed-dotted blue line, fitting the deterministic data for $\theta = \pi/9$); at later times, the data start to deviate from the linear stability prediction and a kink in the curves appears, signalling the film rupture. As expected, in the fluctuating case the rupture occurs earlier.

A deeper insight can be achieved looking at the dependence of the rupture events on the contact angle. Defining the rupture time τ_r as the earliest instant of time at which the free surface "touches" the substrate

$$\tau_r = \min\{t | h(x, t) = h_* - h_c\},$$

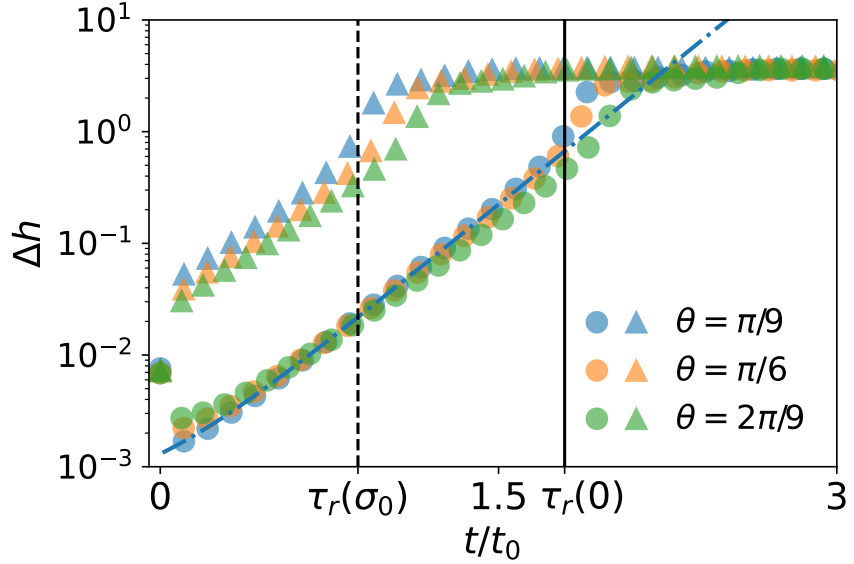


Figure 6.3: Time evolution of $\Delta h(t) = \max_x\{h(x,t)\} - \min_x\{h(x,t)\}$ for the athermal (bullets) and fluctuating (triangles) systems with $\theta = \pi/9$. The blue dashed-dotted line depicts an exponential fit of the data for the athermal case ($\sigma = 0$). The vertical lines mark the rupture times for the deterministic (solid) and stochastic (dotted) simulations.

we have seen that, with thermal fluctuations ($\sigma \neq 0$), τ_r is shorter than the athermal counterpart. The latter feature holds true irrespective of the contact angle, i.e.

$$\tau_r^{(\sigma=\sigma_0)}(\theta) < \tau_r^{(\sigma=0)}(\theta) \quad \forall \theta,$$

as it can be better appreciated from Fig. 6.4, where we plot the ratio

$$\chi_{\sigma_0}(\theta) \stackrel{\text{def}}{=} \frac{\tau_r^{(\sigma=0)}(\theta)}{\tau_r^{(\sigma=\sigma_0)}(\theta)} \quad (6.32)$$

as a function of θ and we see that it is always larger than one. Remarkably, moreover, while in the athermal system the ratio $\tau_r^{(\sigma=0)}(\theta)/t_0$ is basically independent of θ , in the fluctuating case a weak growth of $\tau_r^{(\sigma=\sigma_0)}(\theta)/t_0$ can be detected (see inset of Fig. 6.4); consequently, $\chi_{\sigma_0}(\theta)$ is a (monotonically) decreasing function of the contact angle. These findings can be understood as follows. The rupture time is such that $\Delta h(\tau_r) \sim h_0$; if we assume the validity of the linear regime (or, equivalently, an exponential evolution) up to rupture (as it looks reasonable from Fig. 6.3), we can estimate $\Delta h(t)$ as

$$\Delta h(t) \sim \left(\frac{S(q_m, t)}{L} \right)^{1/2}$$

(where it is also assumed that the growth rate is dominated by the maximum of the spectrum, q_m ²). At the rupture time we have

$$\left(\frac{S(q_m, \tau_r)}{L}\right)^{1/2} \sim h_0; \quad (6.33)$$

in the deterministic case $q_m = q_0$ and $S(q_0, t) = S_0 e^{2t/t_0}$, whence

$$\tau_r^{(\sigma=0)} \sim t_0 \log\left(\frac{h_0 L^{1/2}}{S_0^{1/2}}\right). \quad (6.34)$$

In the stochastic case, the time dependence of $S(q_m, t)$ is slightly more complicated, but it can be simplified noticing that, when $t \sim t_0$ (i.e. close to rupture), $q_m \approx q_0$ (see Fig. 6.5) and, therefore, in Eq. (6.29), $g(q_m/q_0) \approx g(1) = 1$ and $(e^{2\omega(q_m)t} - 1) \approx (e^{2t/t_0} - 1) \approx e^{2t/t_0}$. The spectrum, then, reduces to

$$S(q_m, t) \approx \left(S_0 + \frac{\sigma^2 h_0^2 L}{q_0^2}\right) e^{2t/t_0},$$

which, by virtue of (6.33) and neglecting S_0 (for $S_0 \ll \frac{\sigma^2 h_0^2 L}{q_0^2}$), delivers:

$$\tau_r^{(\sigma)} \sim t_0 \log\left(\frac{q_0}{\sigma}\right) \approx t_0 \log\left(\frac{a\theta}{\sigma}\right), \quad (6.35)$$

where we have used the expression for the deterministic maximum wavenumber q_0 , i.e. (from Eqs. (6.11) and (6.28))

$$q_0^2 = \frac{1 - \cos \theta}{2h_*^2(n-m)}(n-1)(m-1) \left[m \left(\frac{h_*}{h_0}\right)^{m+1} - n \left(\frac{h_*}{h_0}\right)^{n+1} \right],$$

that can be written, in the small angle approximation $1 - \cos \theta \approx \frac{\theta^2}{2}$, as $q_0^2 \approx a^2 \theta^2$. Taking the ratio of (6.34) and (6.35) we get:

$$\chi_\sigma(\theta) \sim \frac{\log\left(\frac{h_0 L^{1/2}}{S_0^{1/2}}\right)}{\log\left(\frac{a\theta}{\sigma}\right)} \propto \frac{1}{\log(\theta/\sigma)}; \quad (6.36)$$

the latter relation tells us that $\chi_\sigma(\theta)$, indeed, increases with the temperature (confirming that the rupture times are shorter for the fluctuating systems), but decreases with the contact angle. Eq. (6.36) is plotted in Fig. 6.4 (dashed line), showing a nice agreement with the numerical data. Fig. 6.5 depicts the evolution of the maximum wavenumber q_m with time for different values of the contact angle. The solid lines show the theoretical curves $q_m(t)$ derived from Eq. (6.29). In compliance with the theory exposed in 6.2, we see that, for each θ , q_m decreases in time and tends asymptotically to the corresponding $q_0(\theta)$, indicated with dashed lines.

²The factor $1/L$ ensures the fulfillment of the discrete Parseval-Plancherel's theorem

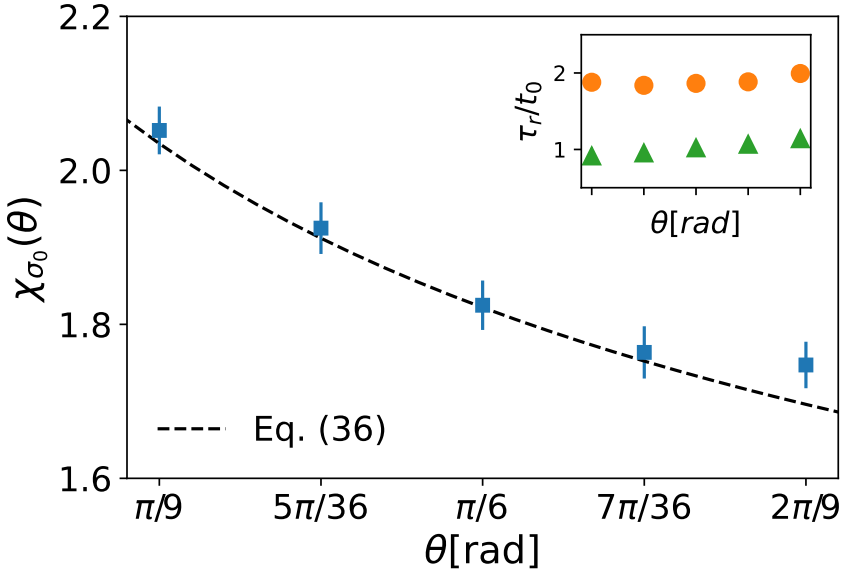


Figure 6.4: Ratio of rupture times from athermal and fluctuating dewetting, $\chi_{\sigma_0}(\theta)$ (Eq. (6.32), as a function of the contact angle θ . The dashed line is Eq. (6.36) for $\sigma = \sigma_0$. Inset: Rupture times τ_r normalized by t_0 (see Tab. 6.1) vs θ , for the deterministic (orange bullets \bullet) and stochastic (green triangles \blacktriangle) simulations.

6.4.4 Patterned substrates

On patterned substrates one generally observes that a fluid prefers to wet regions with lower contact angle, thus the modulated wettability induces a net force (effectively entering in our model through a space-varying contact angle, $\theta = \theta(x)$, in Eq. (6.20)). We will now show how simple patterns can substantially change the droplet distribution, with and without thermal fluctuations, thus allowing, in principle, to control both the size and the number of droplets generated during the dewetting process. We consider two kinds of patterns: a sine wave and a square wave (the latter mimicking the effect of spatially confined defects that induce contact angle "jumps"). In the following we show data obtained using the disjoining pressure exponents (9, 3) instead of (3, 2). The reason for this choice is that although the overall behavior is the same, the characteristic time scale t_0 is larger, as indicated in Tab. 6.1, thus extending the duration of the height field evolution and, therefore, allowing for a much clearer presentation of the data.

6.4.4.1 Sine wave pattern

The sine wave pattern is defined by

$$\theta^{(1)}(x) = \frac{5\pi}{36} + \frac{\pi}{36} \sin(q_\theta x), \quad (6.37)$$

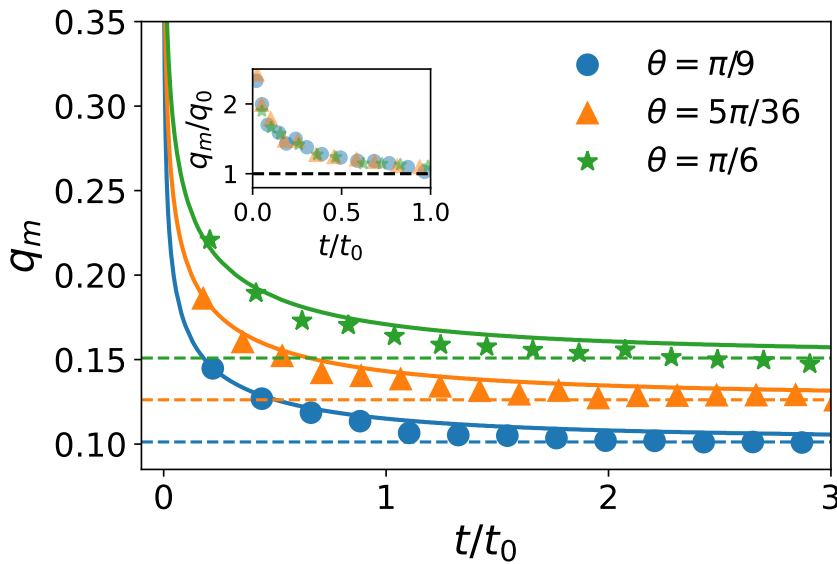


Figure 6.5: Time dependence of the maximum wavenumber q_m for various contact angles θ and $\sigma = \sigma_0$, using $\delta = 0$. The full blue, orange and green lines correspond to theoretical curve $q_m(t)$ derived from Eq. (6.29) for $\theta = \pi/9, 5\pi/36, \pi/6$. The dashed lines show the corresponding $q_0(\theta)$. In the inset we show that the data collapse onto a single curve upon rescaling each q_m by its respective q_0 .

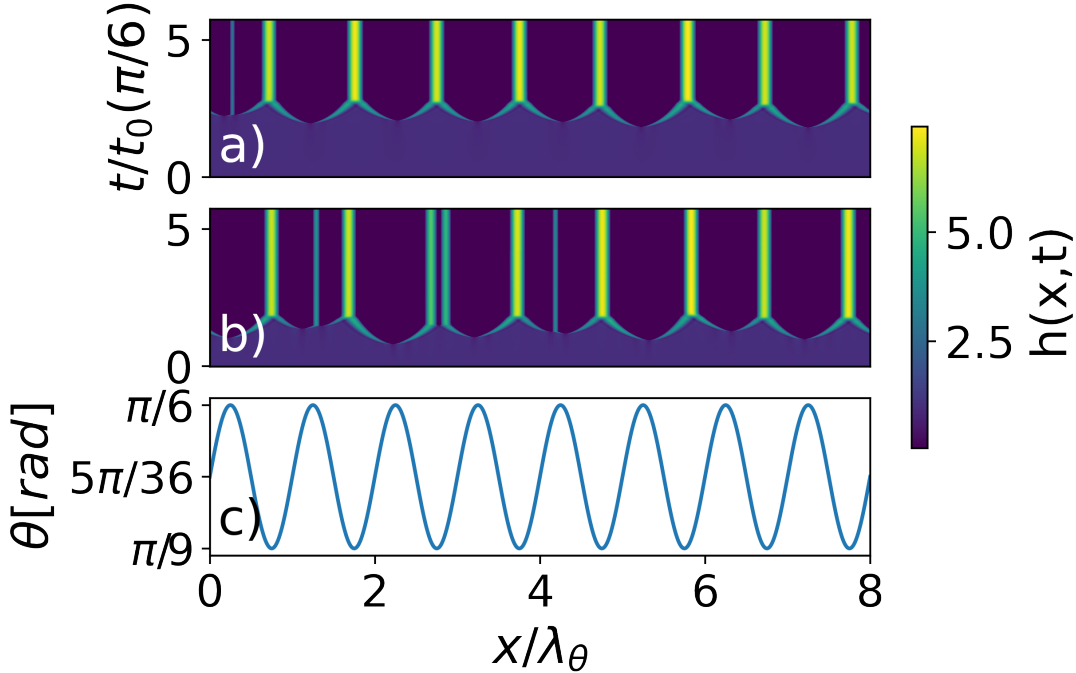


Figure 6.6: Space-time plot of the height field $h(x, t)$ evolution over a sinusoidally patterned substrate undergoing athermal (panel (a)) and fluctuating (panel (b)) dewetting, respectively. In panel (c) we report the contact angle profile $\theta(x)$ (Eq. (6.37)).

where the wavenumber is set to $q_\theta = 2\pi/512$ (thus the wavelength is $\lambda_\theta = 512$), such that the contact angle ranges between $\pi/9$ (20°) and $\pi/6$ (30°). We plot the space-time evolution of the height field on this kind of patterned substrate in Figs. 6.6(a) (deterministic) and 6.6(b) (stochastic). Both show, as expected, that the film starts to rupture prevelently in regions of high contact angle and droplet nucleation occurs in regions of low contact angle; indeed, the deterministic dewetting leads to the formation of precisely L/λ_θ droplets. However, in the stochastic case, the morphology of the dewetting process seems to be less bound to the subjacent pattern: we report, indeed, the formation of few droplets ($\approx 0.2(L/\lambda_\theta)$, on average) in regions of high contact angle ($\theta(x) \approx \pi/6$). We also notice that thermal fluctuations are able to induce defects in the *stable* droplet state, i.e. in regions of low contact angle ($\theta(x) \approx \pi/9$). This is shown by the double droplet state in panel 6.6(b) at $x \approx 3\lambda_\theta$ and happens in about 20% of our stochastic simulations. Concerning the time scales involved, it must be stressed that, owing to the contact angle inhomogeneity, a characteristic time as in Eq. (6.12) is not anymore uniquely defined. Still, it is natural to assume that the most unstable regions of the substrate, where the contact angle is the highest ($\max_x(\theta_{\text{eq}}(x)) = \pi/6$), are the main drive to the dewetting and, hence, determine the relevant time scales; we set, therefore, $t_0 \equiv t_0(\pi/6)$. With such choice, we observe that the film starts to rupture at around $t \equiv \tau_r \gtrsim 2t_0$ in the derministic simulation, which is indeed comparable

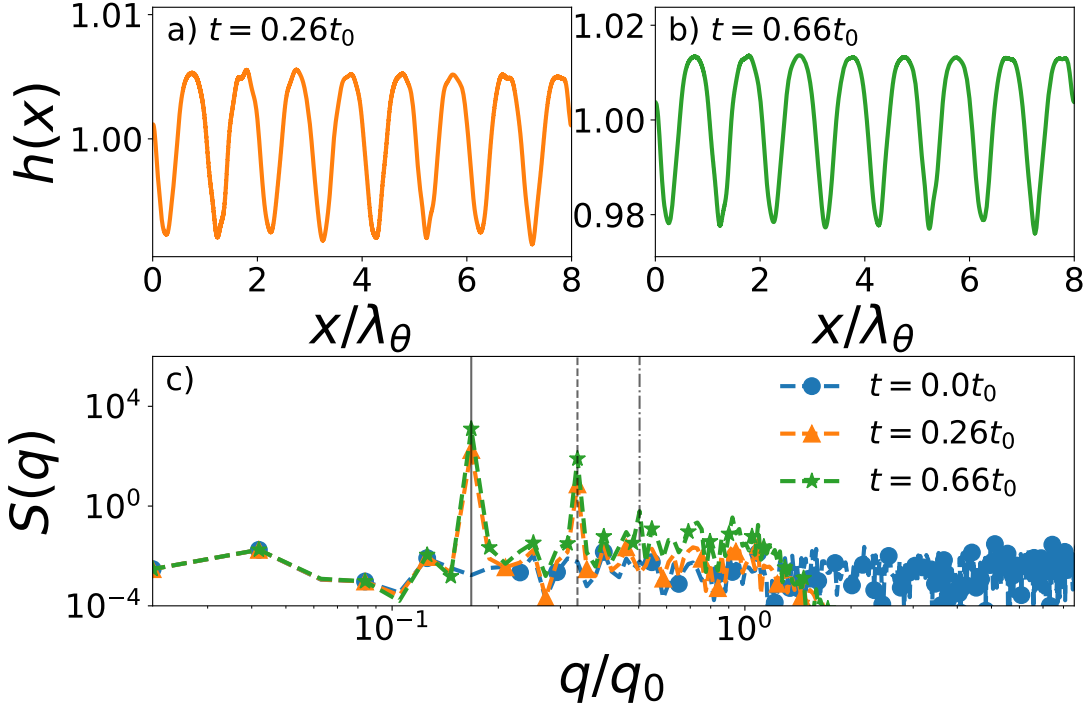


Figure 6.7: Height profiles from deterministic dewetting ($\sigma = 0$) over the sinusoidally patterned substrate, Eq.(6.37) at $t = 0.26t_0$ (panel a)) and $t = 0.66t_0$ (panel b)) and corresponding spectra (panel c)). In panel c) also the initial spectrum, $S_0(q)$, is reported; the vertical lines indicate the pattern wavemode q_θ (solid) and its multiples $2q_\theta$ (dashed) and $3q_\theta$ (dashed dotted). As explained in the text, the convention $t_0 = t_0(\pi/6)$ and $q_0 = q_0(\pi/6)$ applies.

with the homogeneous substrate (see Fig. 6.4). By analogy we take as the reference wavenumber $q_0 = q_0(\pi/6)$; consequently, since q_0 decreases with θ , we should expect the actual most unstable wavenumber to be slightly below q_0 . The influence of the substrate wettability modulation shows up already in the early stages of dewetting ($t < t_0$), as reflected in the shape and evolution of the spectra (Figs. 6.7-6.8). The maximum of the spectrum from the athermal system (Fig. 6.7(c)), in fact, is not located at $q \approx q_0$ anymore. Instead, the wavenumber of the substrate pattern sets the (absolute) maximum at $q = q_\theta$. Interestingly, further local maxima (of progressively decreasing amplitude) can be detected at integer multiples of q_θ , namely for $q = 2q_\theta$ and $q = 3q_\theta$ (indicated, in the figure, by the gray dashed and dashed-dotted lines, respectively). For higher values of q , the spectrum tends to that of spinodal dewetting, with a small local maximum at $q \lesssim q_0$ (consistently with the above discussion about the choice of q_0) and a fast decay for $q/q_0 > \sqrt{2}$. The strong correlation between the patterning ($\theta(x)$) and the height field evolution may be further highlighted by visual inspection of the profiles in Fig. 6.7(a-b), where a precise phase-shift of $\pi/2$, as compared to the contact angle profile, Fig. 6.6(c), can be observed. Such shift, mathematically, stems from the fact that the height is forced by the pressure gradient

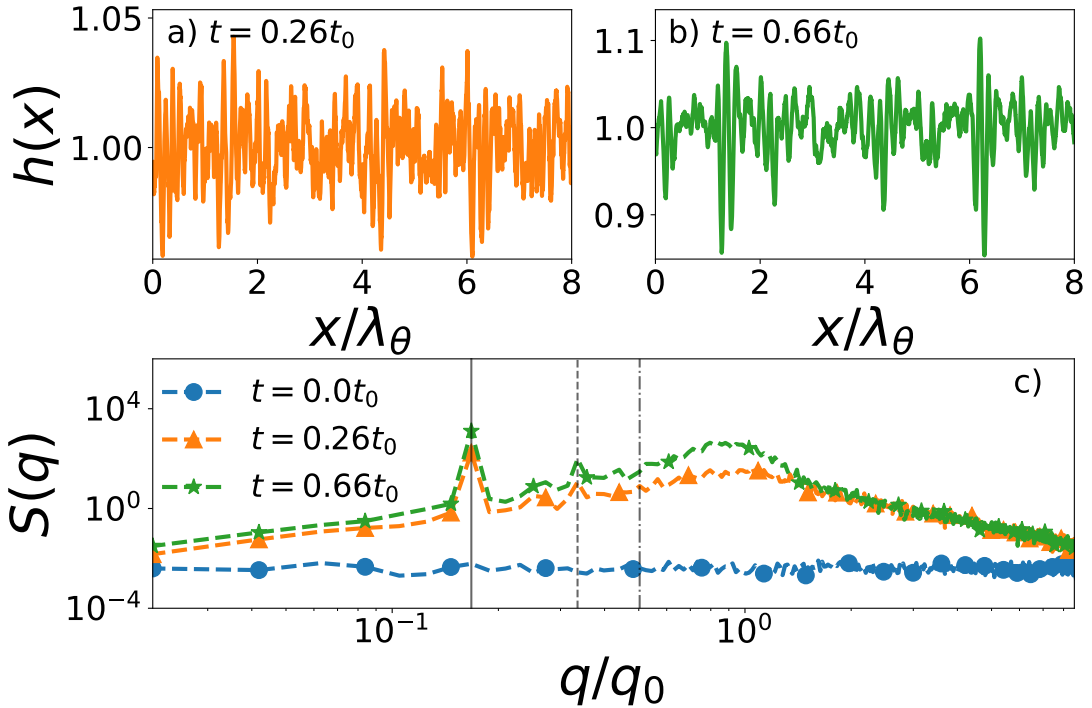


Figure 6.8: Height profiles from stochastic dewetting ($\sigma = \sigma_0$) over the sinusoidally patterned substrate, Eq.(6.37) at $t = 0.26t_0$ (panel a)) and $t = 0.66t_0$ (panel b)) and corresponding spectra (panel c)). In panel c) also the initial spectrum, $S_0(q)$, is reported; the vertical lines indicate the pattern wavemode q_θ (solid) and its multiples $2q_\theta$ (dashed) and $3q_\theta$ (dashed dotted).

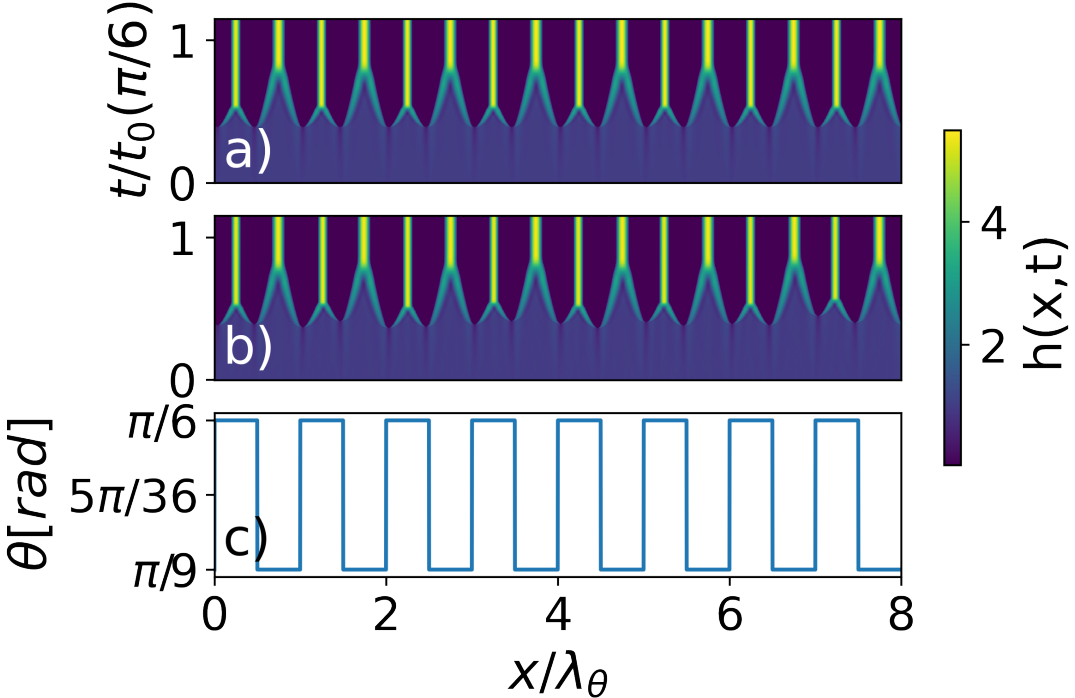


Figure 6.9: Space-time plot of the height field $h(x,t)$ evolution over a square-wave patterned substrate undergoing athermal (panel (a)) and fluctuating (panel (b)) dewetting, respectively. In panel (c) we report the contact angle profile $\theta(x)$ (Eq. (6.38)).

and, hence, by the gradient of the disjoining pressure, which contains the contact angle dependence as $\Pi \propto \cos(\theta(x))$. In the fluctuating dewetting, instead, the stochastic dynamics shadows the correlation, as it can be appreciated from Figs. 6.8(a-b), where the height field is reported. Correspondingly, we see in the spectra, Fig. 6.8(c), that the "spinodal" maximum at $q \lesssim q_0$ is much more enhanced, than it was in the athermal case, and it is of comparable to the "pattern" maximum at $q = q_\theta$.

6.4.4.2 Square wave pattern

In the following we focus on the dewetting process on a substrate with a contact angle pattern given by

$$\theta^{(2)}(x) = \begin{cases} \frac{\pi}{9} & \text{if } \sin(q_\theta x) \leq 0, \\ \frac{\pi}{6} & \text{otherwise} \end{cases} . \quad (6.38)$$

Looking at Fig. 6.9, one can immediately notice two main differences in comparison to the sinusoidal pattern (cf. Fig. 6.6). The first one is that the impact of thermal fluctuations on the global dewetting morphology looks much weaker; in particular, in both deterministic and stochastic simulations, the film ruptures exactly at the wettability discontinuities. Secondly, stable droplets are formed also in regions of

high contact angle. As a consequence, a total amount of $2\frac{L}{\lambda_\theta}$ droplets are observed, which is twice as many as for the pattern $\theta^{(1)}(x)$.

The characteristic time scale of formation process, however, is not the same for all droplets, since it depends on the local contact angle. We observe, indeed, that, droplets nucleate faster in regions of higher contact angle. Specifically, if we define the droplet formation time as the delay between the, θ -dependent, droplet nucleation time, $t_d(\theta)$, and the film rupture time, $\tau_r(\theta)$, i.e.

$$\tau_d(\theta) = t_d(\theta) - \tau_r(\theta), \quad (6.39)$$

and measure the ratio

$$\Xi = \frac{\tau_d(\pi/6)}{\tau_d(\pi/9)} \quad (6.40)$$

of formation times over patches of different contact angle, we find $\Xi \approx 0.3$. Theoretically, this can be explained according to a retracting film scenario. We expect, in fact, that the characteristic time (6.39) will be inversely proportional to the speed of the receding contact line over a particular substrate patch, namely $t_d \propto U^{-1}$; such speed, in turn, is known to depend on the contact angle as $U(\theta) \sim \theta^3$ [SE10], therefore we get for the ratio Ξ :

$$\Xi = \frac{\tau_d(\pi/6)}{\tau_d(\pi/9)} \propto \frac{U(\pi/9)}{U(\pi/6)} \sim \frac{(\pi/9)^3}{(\pi/6)^3} = \left(\frac{2}{3}\right)^3 = 0.296..., \quad (6.41)$$

in excellent agreement with the measured value.

The rupture times from the athermal and fluctuating dewetting films are shorter than their counterparts on the $\theta^{(1)}(x)$ pattern (Eq. (6.37)), and, unlike those, they are comparable to each other, hinting at a stronger bond to the substrate modulation (also in the fluctuating case). However, a difference arises in the full time distributions of rupture events, shown, as histograms, in Fig. 6.10(c) (in Fig. 6.10(a) and Fig. 6.10(b) we highlight the rupture events with red bullets in the time-space evolution diagram). The blue (orange) bars are the data from the deterministic (stochastic) simulation. We see that, while in the athermal case rupture events are concentrated in a very narrow time frame (i.e. they all occur almost simultaneously along the whole domain), the distribution is broadened when thermal fluctuations are switched on (analogously to what happened with the droplet height distributions over the unstructured substrates). Here, the rupture events are scattered over a time frame of $0.08 t_0$ as compared to $0.003 t_0$ in the deterministic simulation.

As a final analysis we discuss the short time (pre-rupture) spectra on this substrate as well (see Fig. 6.11). We show the deterministic (blue dashed line with bullets) and stochastic (orange dashed line with triangles) data at the same time $t = 0.1 t_0$. Under the light of what obtained with the sine wave pattern and given the dewetting morphology shown in Fig. 6.9, we would guess to find the absolute maximum of the spectrum at $q = 2q_\theta$. Surprisingly, instead, the figure shows that, although a local maximum located at $2q_\theta$ can indeed be detected, there are several higher peaks at nq_θ , with a global maximum at $7q_\theta \approx 1.2q_0$; this probably suggests that the early time

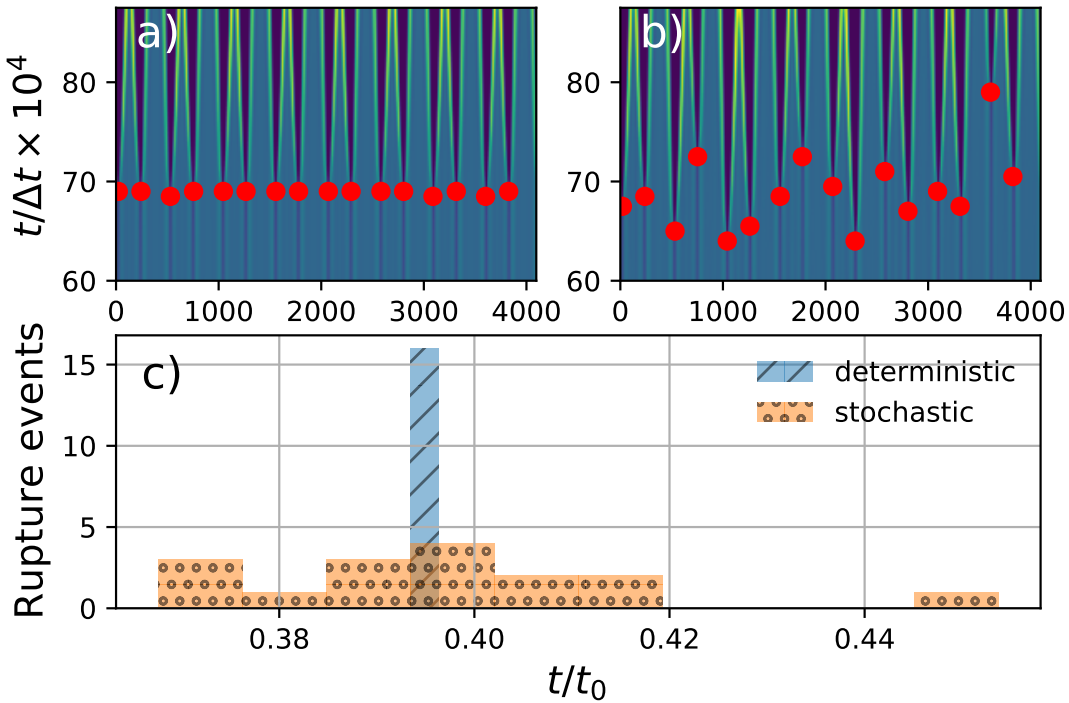


Figure 6.10: Panel a) and b): Space-time plots showing the evolution of the height field for athermal, a), and fluctuating, b), dewetting over the square-wave patterned substrate, in a neighbourhood of the instant of time at which the first rupture event (in the athermal case) occurred; for the sake of visualization we mark the rupture events with red bullets (\bullet). Panel c): Distribution of times of occurrence of rupture events for the athermal ($\sigma = 0$, blue, line-patterned) and fluctuating ($\sigma = \sigma_0$, orange, dot-patterned) dewetting.

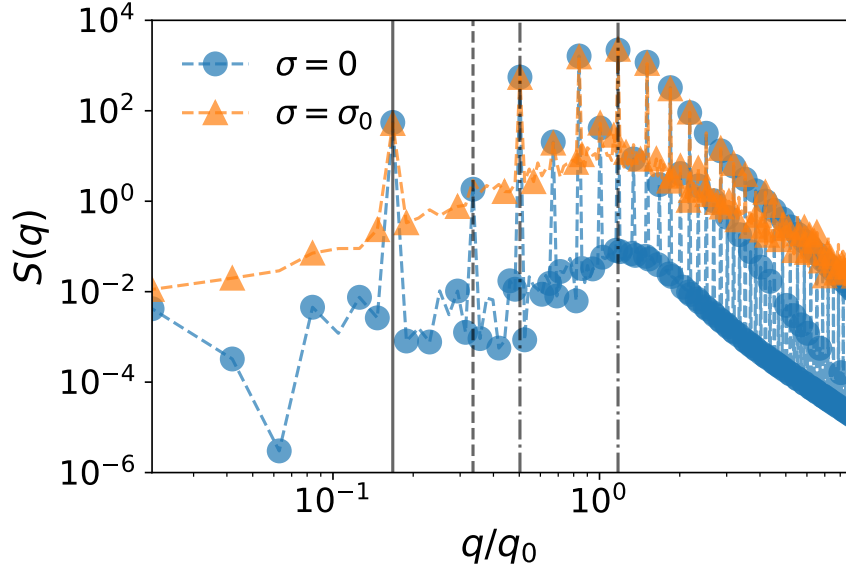


Figure 6.11: Spectra of the dewetting film on the $\theta^{(2)}(x)$ pattern, Eq.(6.38), at $t = 0.1t_0(\pi/6)$, with ($\sigma = \sigma_0$, \blacktriangle) and without ($\sigma = 0$, \bullet) thermal fluctuations. The vertical lines indicate the substrate wavemode q_θ (solid) and its multiples $2q_\theta$ (dashed), $3q_\theta$ (thin dashed-dotted) and $7q_\theta$ (thick dashed-dotted).

dewetting on this kind of substrate is still reminiscent of the spinodal background. Nevertheless, the strong bond of the dynamics with the pattern is evident and it is further pointed out by the unexpected observation that corresponding maxima from the deterministic and stochastic spectra are all of the same magnitude.

6.5 Summary and Conclusions

We have presented a lattice Boltzmann method for the simulation of the stochastic thin-film equation. The method has been tested against exact results on the height fluctuations spectrum of a dewetting film. We observed, in agreement with previous studies, that the inclusion of thermal fluctuations accelerates the dewetting and reduces the rupture times [GMR06]. Furthermore, we have shown that the distribution of droplet sizes measured in the stochastic simulations is more spread out than its deterministic counterpart [Nes+15].

A central contribution of our work concerned the study of the role of the liquid-substrate interactions, parametrised by the contact angle θ , on the dewetting process, with and without thermal fluctuations. We reported, and justified theoretically, that the ratio of the deterministic and stochastic rupture times decreases monotonically with the contact angle, though being always larger than one (i.e. the fluctuating dewetting occurs faster than the athermal one, irrespective of the substrate wettability). We then performed simulations with a chemically patterned substrate, modelled

as a space-dependent contact angle $\theta(x)$. Depending on the pattern, a smoothly varying profile (a sine wave) and a sequence of alternate stripes (segments, in 1-d), one can control the number of droplets formed, which differ by a factor two, in spite of the two patterns having the same "wavelength". In both cases, on the other hand, the dynamics appears strongly enslaved to the wettability modulation, so much that the effect of thermal fluctuations is significantly hindered, even in the early stages of dewetting, as inferable from the inspection of the spectra. Before concluding, let us make two last remarks. Firstly, it is worth mentioning that we do not expect that the results presented would differ too much in two dimensions (i.e. for real substrates). The physical observables discussed, in fact, pertain essentially to the early dewetting (spectra, rupture times, droplet size distributions), whereby the dynamics is mostly determined by the spectral properties of the linearized equations and by the characteristics of the free energy. The signature of the dimensionality should, instead, emerge in the morphology of the dewetting pattern, especially in the long time evolution, when coarsening and droplet coalescence dominate. These aspects will be subject of a forthcoming study. In the second place, we underline that the versatility of the numerical scheme would allow, in principle, to extend the method to simulate the dynamics of thin film of more complex liquids, such as non-Newtonian and active fluids [Egg97; Car+19].

6.6 Acknowledgements

The authors acknowledge financial support by the Deutsche Forschungsgemeinschaft (DFG) within the Cluster of Excellence "Engineering of Advanced Materials" (project EXC 315) (Bridge Funding). The work has been partly performed under the Project HPC-EUROPA3 (INFRAIA-2016-1-730897), with the support of the EC Research Innovation Action under the H2020 Programme; in particular, S. Z. gratefully acknowledges the support of Consiglio Nazionale delle Ricerche (CNR) and the computer resources and technical support provided by CINECA. We thank Paolo Malgaretti, Massimo Bernaschi and Mauro Sbragaglia for fruitful discussions.

7 Controlling the dewetting morphologies of thin liquid films by switchable substrates

Du wirst nicht enttäuscht, wenn du nie etwas erwartest und bevor du etwas falsch machst, dann mach mal lieber gar nichts.

Kraftklub

This chapter has been submitted as a regular contribution to Physical Review Letters.

Switchable and adaptive substrates emerged as valuable tools for the control of wetting and actuation of droplet motion. Here we report a computational study of the dynamics of an unstable thin liquid film deposited on a switchable substrate, modelled with a space and time varying contact angle. With a static pattern, all the fluid is drained into droplets located around contact angle minima, whereas for a sufficiently large rate of wettability variation a state consisting of metastable rivulets is observed. A criterion discriminating whether rivulets can be observed or not is identified in terms of a single dimensionless parameter. Finally, we show and explain theoretically how the film rupture times, droplet shape and rivulet life time depend on the pattern wavelength and speed.

7.1 Introduction

Wet surfaces and droplets are part of our every-day experience and of numerous industrial processes including coating, tribology, painting and printing, to name but a few [Gro+80; Sze10; dQ98; Qué99; da +99; Sin+10; Jo+09; Wij10]. Moreover, the continuously growing technological interest for lab-on-a-chip devices [STH16; Foc+10] as well as for printable electronics [KM05; LAS08] and printable photovoltaics [BSH01; RH20], whose efficiency relies crucially on a precise control of material deposition upon (de-)wetting of liquid films, drew the attention to applications where the substrate is adaptive or switchable, i.e. it is not inert but responds dynamically to external stimuli or to the evolution of the coating liquid film itself [But+18; GG16]. Several realizations of switchable and adaptive substrates have been proposed [Liu+05;

XH10], involving smart materials such as polymer brushes [Stu+10; ABB07; Yon+18], thermal-responsive hydrogels [Che+10], light-responsive molecules and microstructures [ION00; Del+05; Osc+17] or processes such as electrowetting [Mug+05]. Probably the simplest, yet non-trivial, modelling of a switchable substrate can be realized by a space and time dependent wettability pattern [GS21b]. While a consistent body of theoretical/computational work has been devoted to processes on static heterogeneous substrates, though, the time dependent case is still almost unexplored, with few relevant exceptions focusing on single droplet spreading and sliding [GS21b; GS21a; TH20] or limited to an analysis of the linear regime [SK06].

In this Letter, we study, by means of numerical simulations, the full dewetting dynamics of a thin liquid film deposited over a substrate with a time varying wettability pattern, from rupture to the long time morphology. We identify two regimes where the rupture times grow with the pattern wavelength either linearly (on the static pattern) or attain a constant value (in the time dependent case), for short wavelengths, and approach a quadratic law as the wavelength increases. These observations are then explained theoretically. We show that, by tuning the rate of change (the “speed”) of the underlying pattern, it is possible to control, to some extent, the dewetting morphology. In particular, for large enough pattern speeds, we detect a metastable state, where the film retracts into metastable rivulets, eventually breaking up into multiple droplets. We introduce a control parameter that discriminates whether rivulets or just droplets (as in the static situation) can be observed and we propose a phenomenological argument that justifies the logarithmic dependence of the rivulets life time on the pattern speed.

7.2 Method

In order to simulate the dewetting dynamics on patterned, “switchable”, substrates, we integrate numerically the thin-film equation [Rey86; ODB97; CM09]

$$\partial_t h(\mathbf{x}, t) = \nabla \cdot (M_\delta(h) \nabla p(\mathbf{x}, t)), \quad (7.1)$$

by means of a recently developed method, based on a lattice Boltzmann (LB) scheme [Zit+19; ZSH21; Zit+22]. Eq. (7.1) describes, in a lubrication approximation spirit, the evolution of the height field (film thickness) $h(\mathbf{x}, t)$, denoting the location of the liquid/air interface. The mobility function $M_\delta(h) = \frac{2h^3 + 6\delta h^2 + 3\delta^2 h}{6\mu}$ depends on the velocity boundary condition at the substrate, parameterized by an effective slip length δ (for $\delta \rightarrow 0$ it reduces to the no-slip form $h^3/(3\mu)$). Here, μ is the fluid dynamic viscosity. The film pressure $p(\mathbf{x}, t)$ consists of the sum of the Laplace and disjoining pressures, that is $p(\mathbf{x}, t) = -\gamma \nabla^2 h - \Pi$ ¹, where γ is the surface tension. The disjoining pressure Π can be seen as (minus) the derivative, with respect to the film thickness, of an effective

¹The Laplace pressure is the product of the surface tension and the local curvature, therefore its full expression reads $p_L = -\gamma \nabla^2 h / \sqrt{1 + |\nabla h|^2}$; since we are in the lubrication regime, though, whereby $|\nabla h| \ll 1$, the denominator can be safely neglected and the pressure reduces to the form involving only the Laplacian of the thickness field [Ben+14; Pah+18].

interfacial potential. As such, it contains the information on the liquid/solid and solid/gas interactions and, hence, on the wettability, which is parameterized in terms of the contact angle θ [Bon+09; SE98]. The expression adopted for Π is

$$\Pi(h, \theta) = \frac{2\gamma}{h_*} (1 - \cos(\theta(\mathbf{x}, t))) f\left(\frac{h}{h_*}\right), \quad (7.2)$$

where $f(\xi) = \xi^{-3} - \xi^{-2}$ and h_* is the height at which the disjoining pressure vanishes and sets the precursor layer thickness ². The time variation of the patterned substrate then enters the model precisely through the disjoining pressure, by making the contact angle space and time dependent, i.e. $\theta = \theta(\mathbf{x}, t)$. We decorate the substrate with a checkerboard pattern, a common choice that generalizes the broken homogeneity of the stripes to two directions [KS03; Jal+18; NZ20; DJP20]. In particular, we employ the sinusoidal form

$$\theta(\mathbf{x}, t) = \theta_0 + \delta\theta [\sin(q_\theta(x + v_{\theta x}t)) \sin(q_\theta(y + v_{\theta y}t))], \quad (7.3)$$

where $q_\theta = 2\pi/\lambda$, i.e. the pattern evolves in time as a plane wave. A possible laboratory experiment for the here mentioned approach consists of a light switchable substrate with a thin film cast on it [Bec+03; ION00]. The external stimulus, our moving pattern, can be realized, e.g., by using a digital multimirror device (DMD) [Vie+12; Sah+19]. We fix the velocity direction to one diagonal, namely $\mathbf{v}_\theta = (v_{\theta x}, v_{\theta y}) = v_\theta(1/\sqrt{2}, -1/\sqrt{2})$ (we will return later on the importance of this choice), and we set $\theta_0 = 20^\circ$ and $\delta\theta = 10^\circ$ ³. Lengths and time scales will be expressed, respectively, in units of the mean film height, h_0 (which is constant in time, due to mass conservation), and of $t_0 = \frac{3\mu}{\gamma h_0^3 q_0^4}$, the inverse growth rate of the most unstable mode, whose wavenumber is q_0 , of a spinodally dewetting film [MR05]. On a uniform substrate, with constant contact angle $\theta^{(u)}$, the wavenumber reads $(q_0^{(u)})^2 = h_*^{-2}(1 - \cos\theta^{(u)})f'(h_0/h_*)$ [MR05; ZSL19]. In our patterned case, we define $q_0^2 = h_*^{-2}(1 - \cos\theta_0)f'(h_0/h_*)$. Correspondingly, we choose as a velocity scale $v_0 = \lambda_s/t_0$, where $\lambda_s = 2\pi/q_0$. To give a flavour of how to compare with actual experimental systems, let us notice first that the expression of t_0 depends on the disjoining pressure (through its dependence $q_0 = \sqrt{\frac{1}{2\gamma}\Pi'(h_0)}$) and contains, therefore, energetic details, namely the Hamaker constant A_H . Consider, for instance, the problem studied in

²Expressions of the general form $\Pi(h) = \gamma(1 - \cos\theta)(n - 1)(m - 1)/(n - m)((h_*/h)^n - (h_*/h)^m)/h_*$ are frequently found in the literature, with various combination of exponents (n, m) ($n > m$), depending on the type of interactions among fluid molecules and between fluid and substrate [SE98; Mit93; TTS87]. A common choice, for instance, is the pair $(9, 3)$, which can be derived from molecular interactions of Lennard-Jones type. Here, the use of the $(3, 2)$ pair is motivated mainly by the computational advantage of keeping the characteristic dewetting time shorter. We have run also a single case ($\lambda = 256h_0$ and $\Gamma = 1.5$) with $(9, 3)$ and observed that the dynamics remains essentially the same, but for a shift in the time scale (see also [ZSH21])

³Notice that, since a typical velocity is such that $v_\theta\Delta t \ll \Delta x$ (in one LB time step Δt the wave would travel a distance much smaller than a lattice spacing Δx), the time update needs to be interpreted in an integer part sense, that is the pattern is shifted by one Δx every $1/v_{\theta x}$ time steps (and equivalently in the y -direction).

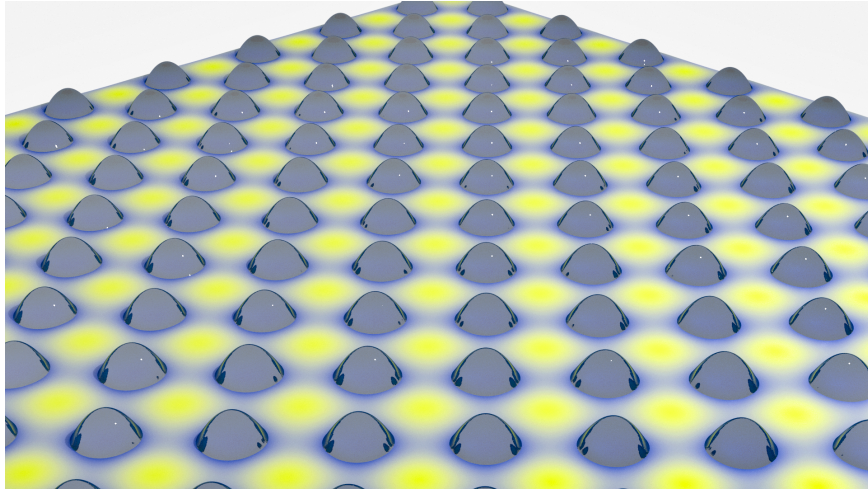


Figure 7.1: Stationary film thickness field ($t > t_0$) showing the formation of droplets. The color map indicates the contact angle pattern (Eq. (7.3) with $v_\theta = 0$), with lower (higher) values coded in light blue (yellow).

[Bec+03]: the dewetting of a polystyrene film of thickness $h_0 \approx 4\text{ nm}$ deposited on a silicon dioxide substrate, where $A_H = 2.2 \times 10^{-20}\text{ J}$ and $\gamma = 0.03\text{ N/m}$. Neglecting the short range part of the interface potential (such that $\Pi(h) = -\frac{A_H}{6\pi h^3}$) [MR05; Bec+03], one gets $q_0^2 \approx \frac{A_H}{4\pi\gamma h_0^4} \approx 2.5 \times 10^{-4}\text{ nm}^{-2}$. The characteristic time of the growth of the instability for these experiments, then, reads [Fet+07b] (the dynamic viscosity of polystyrene is $\mu = 1.2 \times 10^4\text{ Pa} \cdot \text{s}$) $t_0 = \frac{3\mu}{\gamma h_0^3 q_0^4} \approx 300\text{ s}$ and it can be seen that indeed film rupture occurs within time scales of the order of t_0 ($\approx 2t_0$) [Bec+03], as in our simulation for the largest pattern wavelength, $\lambda = L$ (see also our previous work with homogeneous substrates [ZSH21]). All our simulations are run on a bi-periodic square domain of size $L \times L$ with $L/h_0 = 512$. The numerical values in lattice Boltzmann units of the mean film thickness, dynamics viscosity and surface tension are, respectively, $h_0 = 1$, $\mu = 1/6$ and $\gamma = 0.01$. To regularize the contact line divergence [HS71] we use a precursor layer thickness $h_* / h_0 = 0.07$ and a slip length $\delta / h_0 = 1$, a value which lies within the weak/intermediate slip regime [Pes+19; Fet+07a; MWW05] (we have tried also a value four times smaller, without observing any major qualitative change in the results). The liquid film is initialized with a height field slightly perturbed around the mean value h_0 , i.e. $h(\mathbf{x}, 0) = h_0 \left[1 + 0.1 \left(\sin \left(\frac{2\pi x}{L} \right) \sin \left(\frac{2\pi y}{L} \right) \right) \right]$. Various wavelengths, in the range $\lambda / h_0 \in [64, 512]$, and velocities, $v_\theta / v_0 \in [0, 200]$, are considered for the wettability pattern, Eq. (7.3). A few comments on these ranges are noteworthy at this point. The wavelengths are obviously limited from above by the size of the computational domain. On the other extreme, too short wavelengths are prevented by the energetic cost of accomodating droplets on too small patches, since the local contact angle (that increases with decreasing λ 7.6) would possibly exceed the largest substrate contact angle, such that the patterning itself would loose meaning. It has been, in fact, proven, both theoretically and experimentally, that for the confinement to be

effective, the pattern characteristic size should not be much smaller than the spinodal length scale on the less wettable substrate [KS02b; KKS00a; Nis+99; Kar+98]. We keep, therefore, $\lambda \gtrsim \lambda_s \approx 70h_0$. The pattern speeds, on the other hand, are limited by the intrinsic LB bound of the lattice speed of sound [Suc01].

The Reynolds number, Re , is of the order of $Re \sim 10^{-2}$ on the static substrate and never exceeds the value ≈ 0.2 in the time dependent case. In Fig. 7.1 we show $h(\mathbf{x}, t)$ (droplets) and $\theta(\mathbf{x})$ (color coded) for $v_\theta = 0$ (i.e. the static case) and $\lambda = 256h_0^4$, in late stages of dewetting. As expected, droplets form in regions of small contact angles (blue) while the regions of high contact angles (yellow) dewet.

7.3 Results

We start our analysis studying, first, how the rupture times depend on the parameters characterising the wettability pattern, namely the wavelength of the contact angle variation, λ , and wave speed, v_θ . The film rupture time, τ_r , is defined as the least t such that $h(\mathbf{x}, \tau_r) = h_*$ (that is, when the free surface "touches" the substrate). In Fig. 7.2 we report the rupture times, as a function of the wavelength, for stationary ($v_\theta = 0$) and time-dependent ($v_\theta = 20v_0$) patterns. It is conveyed that, overall, rupture occurs earlier on the static substrate, suggesting that the time variation tends to stabilize the film, in agreement with linear stability analysis results [SK06]. We observe that τ_r grows linearly with λ , for short wavelengths, and quadratically for longer λ . These facts can be explained, qualitatively, as follows. Let us first notice that the film rupture consists of two processes, each with its associated time scale: the growth of unstable interface perturbation with rate t_θ^{-1} , and the retraction of liquid from more hydrophobic regions, occurring in a characteristic time t_R . For longer pattern wavelengths, the dewetting instability amplifies more slowly, such that it is reasonable to take it as the process determining the rupture time, $\tau_r \sim t_\theta$. In this case, from the linearized thin-film equation (in one spatial dimension, for simplicity), obtained setting $h = h_0 + \delta h$ with $\delta h \ll h_0$, we can easily see that the exponential growth of the height perturbation is affected by the wettability pattern (variable contact angle) in such a way that $\partial_t(\delta h) \propto (\partial_x^2(\partial_h \Pi(h_0)))\delta h$. Therefore, since the characteristic time t_θ can be estimated dimensionally as $t_\theta \sim \delta h / (\dot{\delta h})$, the rupture time should go as

$$\tau_r \sim t_\theta \sim \delta h / (\dot{\delta h}) \propto \frac{3\mu}{h_0^3} (\partial_x^2(\partial_h \Pi(h_0)))^{-1} \sim t_0 \left(\frac{q_\theta}{q_0} \right)^{-2} \propto t_0 q_0^2 \lambda^2. \quad (7.4)$$

Conversely, for fast growths ($t_\theta \ll t_R$), retraction dominates and fixes the time scale, $\tau_r \sim t_R$. The latter is related to the time the liquid takes to flow out of regions of high contact angle, whose size is $\sim \lambda$. Hence we have

$$\tau_r \sim \tau_R \propto \frac{1}{U_\Theta} \lambda, \quad (7.5)$$

⁴For a better visualization we take twice the domain length L and periodically continue the image.

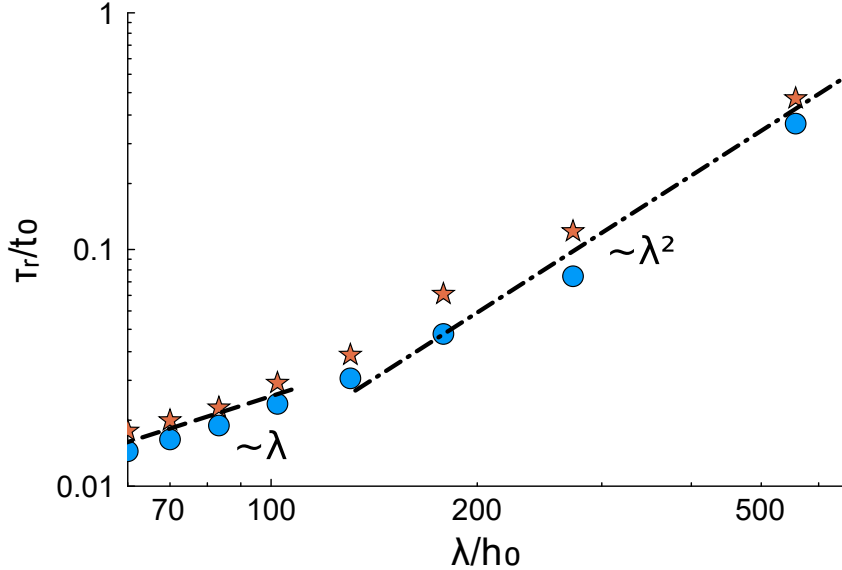


Figure 7.2: Rupture times, τ_r , as a function of the pattern wavelength λ , for $v_\theta = 0$ (●) and $v_\theta = 20v_0$ (★). The continuous and dashed lines indicate the linear, $\sim \lambda$, and quadratic, $\sim \lambda^2$, scaling laws, respectively.

where U_Θ is the retraction speed $U_\Theta = \frac{\gamma\Theta^3}{9\mu}$ [Edw+16], with $\Theta = \max_{\mathbf{x}}\theta(\mathbf{x})$. We now focus on the long time dynamics and in particular on the characterization of the dewetting morphologies and how they are affected by the speed of the wettability wave. On the stationary substrate, after rupture all the fluid accumulates in droplets centered at contact angle minima. Consequently, as we see from the inset of Fig. 7.3, where we plot the number of droplets $N(t)$ in time⁵, in the steady state ($t \gg t_0$) $N(t)$ attains the value $N_\infty = 2(L/\lambda)^2$ (reported as horizontal lines), which equals the minima of Eq. (7.3), for $v_\theta = 0$. Notice that the number of droplets converges faster for smaller pattern wavelengths, in line with the observation reported and justified in the previous section that the characteristic dewetting time decreases with the wavelength.

In the main panel of the same figure, we see that the height fluctuations $\Delta h(t) = \max_{\mathbf{x}}\{h(\mathbf{x}, t)\} - \min_{\mathbf{x}}\{h(\mathbf{x}, t)\}$ grow in time until film rupture and then settle to a constant value, which represents a measure of the mean droplet height h_d (since droplets are essentially monodisperse), decreasing with the pattern wavelength (as expectable, due to the decrease of the droplet volume, $V_d = \frac{h_0\lambda^2}{2}$).

A time-dependent pattern affects the dewetting morphology quite substantially. For $v_\theta = 0.2v_0$ we still observe the formation of droplets, similarly to the stationary case ($v_\theta = 0$). However, these are transported with the contact angle minima, reproducing a somehow similar behaviour recently described in a numerical study of a droplet on a

⁵A droplet is identified by the set (“cluster”) of points, in the plane, constituting each of the connected components of the set $\{\mathbf{x} \in [0, L]^2 | h(\mathbf{x}, t) \geq h_*\}$; the clusters are determined by means of an algorithm of Hoshen-Kopelman type [HK76].

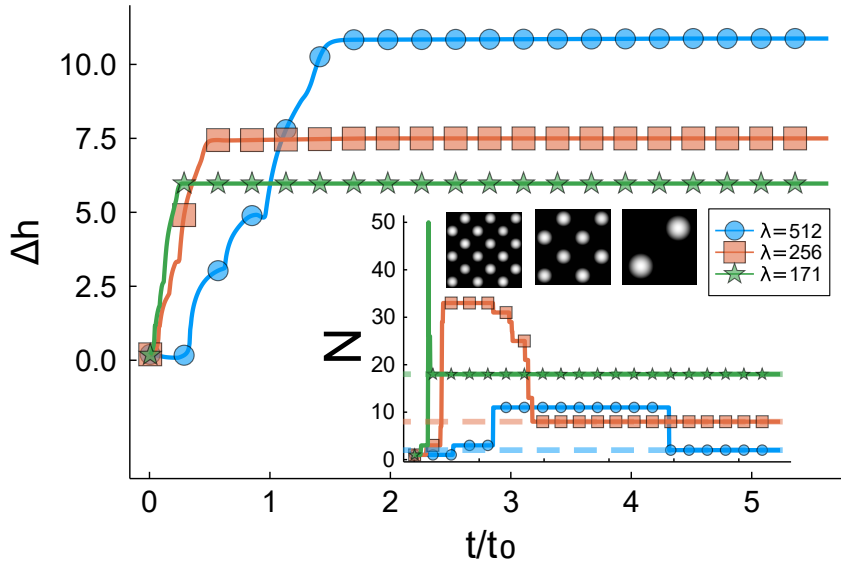


Figure 7.3: MAIN PANEL: Time evolution of the height fluctuations, $\Delta h(t)$, during the dewetting process on the patterned substrate given by Eq. (7.3) with $v_\theta = 0$ and $\lambda = 512h_0$ (blue circles), $\lambda = 256h_0$ (orange squares) and $\lambda = 170h_0$ (green stars). The dashed lines indicate the geometrically expected values of the droplet height h_d , assuming monodispersity and a perfect spherical cap shape. INSET: Number of droplets, $N(t)$, as a function of time. The three horizontal dashed lines indicate the number of minima of Eq. (7.3), which is $2(\frac{L}{\lambda})^2$. In the insets, we display snapshots of the stationary droplet states as grey-scale images of the film thickness field, $h(\mathbf{x}, t)$.

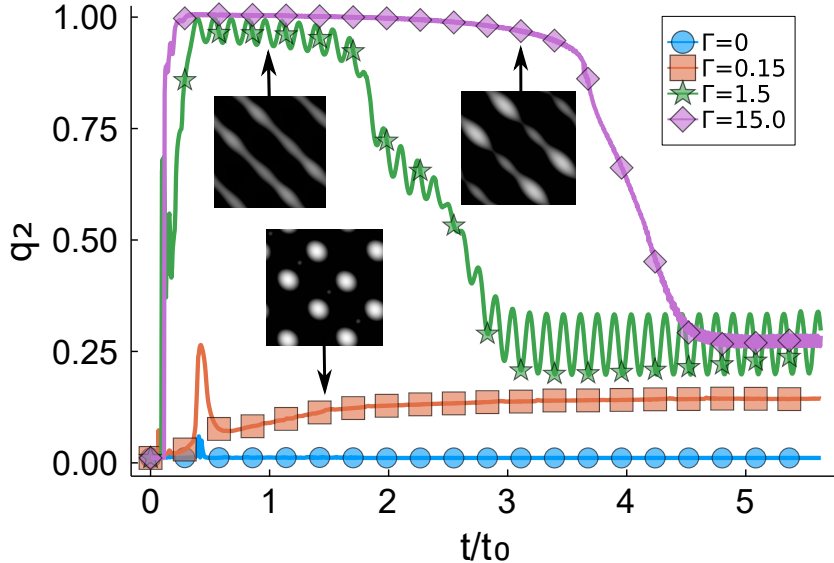


Figure 7.4: Time evolution of the second order Minkowski structure metric, $q_2(t)$ (see text for details), for different Γ values, on a substrate with pattern wavelength $\lambda = 256h_0$. The grey-scale insets supply snapshots of the film thickness field associated to the various curves.

moving wettability step [GS21b]. If the pattern speed is further increased, for $v_\theta = 2v_0$ we observe the development of rivulet-like structures, aligned with \mathbf{v}_θ . The film, in fact, while dewetting in the direction normal to the pattern velocity, is exposed, in the direction of the velocity, to a periodic potential with alternating minima and saddle points, which partially (as we will see) stabilizes the film over “preferential” lanes along the diagonals. This makes the chosen velocity direction, $(1/\sqrt{2}, -1/\sqrt{2})$ (or, equivalently, the orthogonal one $(1/\sqrt{2}, 1/\sqrt{2})$), optimal for the formation of rivulets.

In order to better characterize the various morphologies we apply the theory of Minkowski’s functionals. In particular, we employ the second order Minkowski structure metric, q_2 [Mic+13; SWK20], which can be computed from a Voronoi tessellation of the set of discrete points (x_i, y_i) on the 2D lattice, such that the height field lies above a certain threshold⁶. The q_2 metric quantifies the degree of anisotropy of the dewetting morphology, so it takes relatively large values if the structures formed display a preferential direction. Measuring q_2 then enables us to clearly distinguish between the formation of droplets and rivulets: much larger q_2 values are attained for the latter type of structure, as we can see in Fig. 7.4. We observe, on the other hand, that such rivulets are metastable and eventually break up into droplets, as indicated by the collapse of q_2 at later times. Notice, though, that the q_2 signal for any $v_\theta > 0$ always stays above the one for the static case, suggesting that even the

⁶The expression is: $q_2 = \frac{1}{N} \sum_j \frac{1}{P_j} |\sum_k L_k^{(j)} e^{2i\phi_k^{(j)}}|$, where the inner sum runs over the edges of length $L_k^{(j)}$, of the j -th Voronoi cell, whose perimeter is P_j , and $\phi_k^{(j)}$ is the polar angle of the normal to the k -th edge. The outer sum represents an ensemble average over the N points in the set.

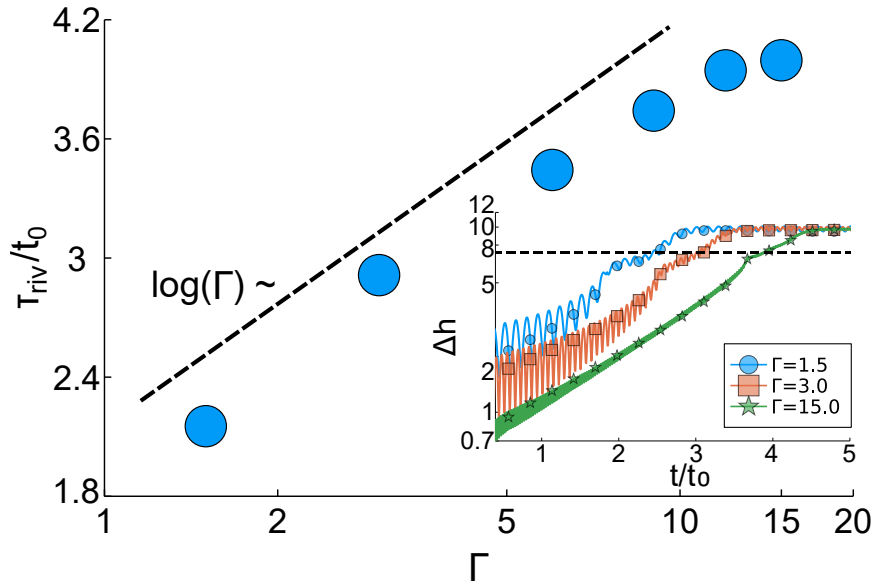


Figure 7.5: MAIN PANEL: Rivulets life-times, τ_{riv} , for various Γ values. The dashed line is plotted as a guide to the eye to highlight the logarithmic dependence, in agreement with the theoretical prediction, Eq. (7.6). INSET: Height fluctuations, $\Delta h(t)$, vs time, computed along the rivulet axis, for three different Γ values.

smallest pattern velocity introduces a sizeable deformation of the spherical cap shape. The breakup is the result of a varicose mode of the rivulet [DGK09a; MRD08], whose wavelength is $\approx \lambda$, such that only $N_\infty/2$ droplets are counted after breakup. These droplets show a peculiar dynamics, characterized by a periodic sequence of spreading and retraction, driven by the pattern, that we dub "pumping state" ⁷.

We argue that the emergence of rivulets is controlled by the competition of two characteristic velocities: the pattern wave speed, v_θ , and the retraction speed, U_Θ , introduced in Eq. (7.5). If U_Θ is large as compared to v_θ , the film retraction is faster than the transport due to the contact angle field and thus droplets form. However, if v_θ is larger than U_Θ , then the retracting film has too little time to form droplets and ends up in the metastable rivulet state. It appears, therefore, natural to consider the ratio of these two velocities, $\Gamma \equiv v_\theta/U_\theta$, as the discriminating parameter. We see from Fig. 7.4 that indeed rivulets form only for $\Gamma > 1$. Moreover, the larger Γ , the more stable the rivulets are; in other words, the rivulet life-time, τ_{riv} , that can be conventionally taken as the time at which the drop of q_2 occurs, grows with v_θ (see Fig. 7.5). The rivulet itself is, in fact, prone to dewetting, with the liquid accumulating over patches around contact angle minima. However, as the pattern moves, the instability is tamed due to configurations whereby higher contact angle regions underlie height field maxima, thus tending to revert the fluid flow. Heuristically speaking, this means that, if we evaluate $\Delta h(t)$ restricted on the rivulet axis, this should grow

⁷see movie file ligament_formation_and_breakup.mp4 in 7.6.

exponentially (with a certain growth rate $\alpha \propto t_0$) only when the system is in the unstable configuration. Namely, $\Delta h(t)/\Delta h_0 \propto e^{\alpha t}$ (see inset of Fig. 7.5) with a prefactor proportional to the time spent by the rivulet in such a configuration, which goes as $\sim \lambda/v_\theta$, therefore $\Delta h(t)/\Delta h_0 \sim \alpha(\lambda/v_\theta)e^{\alpha t}$. The rivulet life-time can be seen as the rupture time of the structure along its axis, hence such that $\Delta h(\tau_{\text{riv}}) \sim h_0$ [ZSH21], which yields

$$\tau_{\text{riv}} \sim \alpha \log(v_\theta) \propto t_0 \log(\Gamma). \quad (7.6)$$

This logarithmic dependence is indeed observed in the numerical data as shown in Fig. 7.5.

Before concluding, we would like to envisage a possible realization of a dewetting experiment on a switchable substrate of the type modelled by the spatio-temporal contact angle (7.3). One may think of a thin liquid film cast on a light responsive substrate [ION00], under the action of controlled external stimuli (a light emitter). An ideal candidate could be a digital multimirror device (DMD). This technology has effectively been used for thin film experiments and additive manufacturing [Vie+12; Sah+19], it allows for fast temporal modulations of the optical signal (with frequencies up to ≈ 16 kHz) with spatial resolution of $\approx 10 \times 10 \mu\text{m}^2$ (the size of a pixel). Considering as a reference, for instance, the system studied in [Bec+03; Fet+07b], namely a ~ 4 nm thick film of polystyrene deposited on an oxidized silicon wafer, we evaluate the retraction speed $U_\Theta = \frac{\Theta^3 \gamma}{9\mu}$ to be $U_\Theta \approx 10^{-2} \mu\text{m/s}$. The (minimum) *pattern speed* can be estimated, from the pixel size with frame rate $\sim 1\text{s}^{-1}$, as $v_\theta \sim 10 \mu\text{m/s}$, that would give $\Gamma \sim 10^3$, i.e. well within the rivulet regime ($\Gamma > 1$). We note, also, that both U_Θ and v_θ can be widely modulated: the former, playing either with the (temperature and molecular weight dependent) viscosity or tailoring the substrate to making it more hydrophobic (i.e. increasing the contact angle); the latter, tuning the spatial resolution and frame rate of the DMD. We expect, thus, the range of achievable Γ 's to be feasibly extended both to very high ($\Gamma \gg 1$) and very low ($\Gamma \ll 1$) values.

7.4 Conclusions

We have presented results, from numerical simulations and theoretical analysis, on the dewetting of thin liquid films on a switchable substrate, modelled with a space and time periodically varying contact angle in the thin-film equation. Studying how the stability of the film depends on the underlying static pattern, we found that the rupture times grow linearly with the pattern wavelength, for short wavelengths, and quadratically in the long wavelength limit. In the time-dependent case, the rupture times are in general longer, indicating an induced greater film stability, and, while the quadratic growth is preserved at long wavelengths, a plateauing behaviour is observed as the wavelength decreases. A theoretical explanation has been provided for all these various regimes. Furthermore, we showed that, at increasing the wettability wave speed, a transition occurs in the dewetting morphology from a multi-droplet to a metastable multi-rivulet state. A dimensionless parameter, Γ , controlling the

transition has been identified in the ratio of the pattern speed and the typical film retraction speed over the substrate. The rivulets life-time itself grows with the pattern speed, displaying a logarithmic dependence that has been captured by means of phenomenological arguments. On a broader perspective, our work suggests that switchable substrates offer a new avenue to control thin film dewetting, with obviously relevant implications, for instance, for open microfluidic devices, and paves the way to future studies in this direction, exploiting more complex and dedicated space-time dependencies.

7.5 Acknowledgements

SZ and JH acknowledge financial support from the Deutsche Forschungsgemeinschaft (DFG) within the priority program SPP2171 “Dynamic Wetting of Flexible, Adaptive, and Switchable Substrates”, project HA-4382/11.

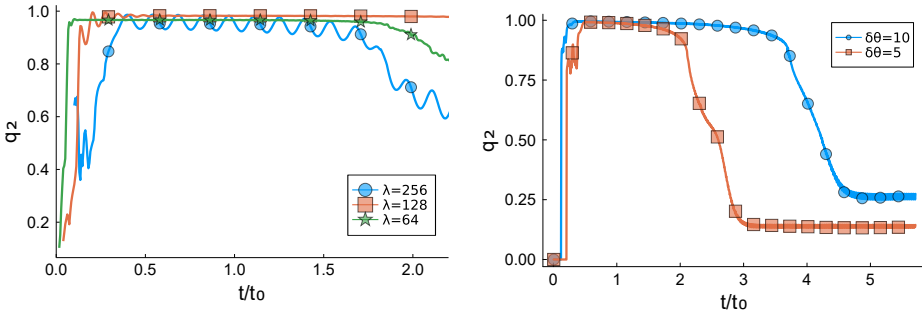


Figure 7.6: LEFT PANEL. Minkowski's structure metric q_2 for three different wavelengths $\lambda = 64h_0$, $\lambda = 128h_0$ and $\lambda = 256h_0$ (as in figure 4 of the main text) and for $\Gamma = 1.5$ (all other parameters are as in the main text). The time interval during which $q_2 \approx 1$ signals the emergence of rivulets, also for $\lambda = 64h_0$ which is comparable with the spinodal wavelength $\lambda_s \approx 70h_0$. RIGHT PANEL. Comparison of the Minkowski's structure metric q_2 for $\delta\theta = 5^\circ$ and $\delta\theta = 10^\circ$, $\Gamma = 15$ and $\lambda = 256h_0$.

7.6 Supplemental Material

7.6.1 Minkowski's structure metric q_2 in an extended parameter space.

In this section we test the robustness of the observation of the rivulet state over a wider parameter space and in particular at changing: 1) the pattern wavelength λ and 2) the heterogeneity amplitude $\delta\theta$. To this aim we have run simulations with $\Gamma = 1.5$, $\lambda/h_0 = 64, 128$, and with $\Gamma = 15$, $\lambda = 256h_0$, $\delta\theta = 5^\circ$, respectively. In Fig. 7.6 (left panel) we report the measurements of the Minkowski's structure metric q_2 , whose increase from zero up to a plateauing value of $q_2 \approx 1$ indicates the emergence of rivulets, for the different λ 's ($\lambda = 256h_0$, which is the value considered in the main text, is also reported for comparison). Analogously, in the right panel, we report q_2 as a function of time for $\delta\theta = 5^\circ$ and $\delta\theta = 10^\circ$ (the value used in the main text). We see that the q_2 metric attains the value $q_2 \approx 1$, signalling the rivulet state, albeit over a time interval shorter than for $\delta\theta = 10^\circ$, i.e. the rivulets lifetime decreases with $\delta\theta$. This was somehow expected, since obviously (and also in the static case) the patterning loses effectiveness as the contact angle mismatch is reduced (see, e.g. [KKS00b]).

7.6.2 Droplet shape

We investigate, here, how the local contact angle of droplets, formed on the more hydrophilic patches after dewetting, depends on the pattern wavelength. We recall, in fact, that the patterning is such that the contact angle is not piecewise constant,

but varies with continuity. The droplet shape is determined by minimization of the total interfacial energy

$$E = \gamma_{lg} A_{lg} + \int_{A_{sl}} (\gamma_{sl} - \gamma_{sg}) d\sigma, \quad (7.7)$$

where A_{lg} and A_{sl} are the liquid/gas and solid/liquid interface areas, and γ_{lg} , γ_{sl} , γ_{sg} are the liquid/gas, solid/liquid and solid/gas interface energies per unit area [Wu+20]. In particular, $\gamma_{lg} \equiv \gamma$ is the surface tension. Setting $A_{lg} \equiv A$ and $A_{sl} \equiv S$, by Young's equation $\cos \theta = \frac{\gamma_{sg} - \gamma_{sl}}{\gamma}$, Eq. (7.7) can be rewritten as

$$\tilde{E} \equiv \frac{E}{\gamma} = A - \int_S \cos \theta dx dy. \quad (7.8)$$

Droplets will form around minima of the contact angle pattern

$$\theta(x, y) = \theta_0 + \delta\theta \sin(q_\theta x) \sin(q_\theta y) \quad q_\theta = \frac{2\pi}{\lambda}, \quad (7.9)$$

namely $(x_n, y_n) = ((2n+1)\frac{\lambda}{4}, (2n+3)\frac{\lambda}{4})$, with $n = 0, \pm 1, \pm 2, \dots$. If we consider large wavelengths ($q_\theta h_0 \ll 1$) and heterogeneity ($\delta\theta \ll 1$) such that the contact angle gradients are small, the expression (7.9) can be expanded as

$$\theta(x, y) \approx \theta_m + \delta\theta q_\theta^2 ((x - x_n)^2 + (y - y_n)^2) + o(|\mathbf{x} - \mathbf{x}_n|^2), \quad (7.10)$$

where $\theta_m = \theta_0 - \delta\theta$. This local radial symmetry allows to approximate the equilibrium droplet shape as a spherical cap of height h and base radius a , whose area is $A = \pi(a^2 + h^2)$; inserting the expression for A and (7.10), neglecting higher than second order terms, in (7.8) gives

$$\tilde{E}(h, a) = \pi(a^2 + h^2) - \int_{C_a(\mathbf{x}_n)} \cos[\theta_m + \delta\theta q_\theta^2 ((x - x_n)^2 + (y - y_n)^2)] dx dy, \quad (7.11)$$

where $C_a(\mathbf{x}_n) = \{(x, y) \in [0, L]^2 | (x - x_n)^2 + (y - y_n)^2 \leq a^2\}$ is the circle of centre \mathbf{x}_n and radius a . Due to global volume conservation and assuming the droplets to be monodisperse, the droplet volume is $V_d = h_0 L^2 / N_d = h_0 \lambda^2 / 2$, where N_d is the number of droplets, which equals the number of minima of (7.9) in the domain $[0, L]^2$, i.e. $N_d = 2(L/\lambda)^2$. Enforcing the volume of the spherical cap to be equal to V_d relates h and a by

$$\frac{\pi h}{6} (3a^2 + h^2) \approx \frac{\pi}{2} a^2 h = \frac{h_0 \lambda^2}{2} \quad (7.12)$$

in the “lubrication approximation” $h \ll a$, whence

$$h \approx \left(\frac{h_0}{\pi} \right) \left(\frac{\lambda}{a} \right)^2. \quad (7.13)$$

Inserting the latter expression in (7.11) and performing the integral, the energy (that we indicate now as $E(a)$ to lighten the notation) reads

$$E(a) = \pi \left(a^2 + \frac{h_0^2 \lambda^4}{\pi^2 a^4} \right) - \frac{2\pi}{\delta\theta q_\theta^2} \left[\sin \left(\theta_m + \frac{\delta\theta}{2} q_\theta^2 a^2 \right) - \sin \theta_m \right]. \quad (7.14)$$

We expand, then, the sine in the second term up to second order in $\delta\theta$ (such that the energy is first order) and we finally get

$$E(a) \approx \pi \left((1 - \cos \theta_m) a^2 + \frac{h_0^2 \lambda^4}{\pi^2 a^4} \right) + \delta\theta \frac{\pi}{4} \sin \theta_m q_\theta^2 a^4 \equiv E_0(a) + \delta\theta E_1(a). \quad (7.15)$$

The minimum condition $\frac{\partial E}{\partial a} = 0$ ⁸ yields

$$2\pi(1 - \cos \theta_m)a^6 - 4h_0\lambda^4 + \delta\theta\pi^2 \sin \theta_m q_\theta^2 a^8 = 0. \quad (7.16)$$

The solution of (7.16) at zero-th order in $\delta\theta$ is

$$a_0 = \left[\frac{2h_0\lambda^4}{\pi^2(1 - \cos \theta_m)} \right]^{1/6}. \quad (7.17)$$

To this order the droplet contact angle $\tan(\theta_d/2) = h/a$ reads

$$\tan\left(\frac{\theta_d}{2}\right) = \frac{h}{a} \approx \left(\frac{h_0}{\pi}\right) \frac{\lambda^2}{a_0^3} = \left(\frac{1 - \cos \theta_m}{2}\right)^{1/2} \frac{\lambda^2}{(\lambda^{2/3})^3} \approx \frac{\theta_m}{2} \Rightarrow \theta_d \approx \theta_m, \quad (7.18)$$

i.e., it does not depend on λ . We move, then, to the next order. We seek a solution to (7.16) in the form $a = a^{(0)} + \delta\theta a^{(1)} + \dots$, where $a^{(0)} \equiv a_0$. At the first order in $\delta\theta$ we get

$$a^{(1)} = -q_\theta^2 a_0^3 \frac{\sin \theta_m}{6(1 - \cos \theta_m)}, \quad (7.19)$$

such that the correction to the droplet contact angle provides

$$\tan\left(\frac{\theta_d}{2}\right) \approx \frac{h_0\lambda^2}{\pi a_0^3} \left(1 + \delta\theta q_\theta^2 a_0^2 \frac{\sin \theta_m}{12(1 - \cos \theta_m)} \right) \Rightarrow \theta_d \approx \theta_m \left(1 + \frac{\delta\theta}{\theta_m} \frac{b}{\lambda^{2/3}} \right), \quad (7.20)$$

where $b = \left(\frac{32h_0^2\pi^4}{27\theta_m^5}\right)^{1/3}$, i.e. the droplet contact angle grows at decreasing pattern wavelength as $\theta_d \sim \lambda^{-2/3}$.

⁸It can be easily checked that $\frac{\partial^2 E}{\partial a^2} > 0$ for $a > 0$

8 Conclusion and outlook

*Wenn du dann am Boden bist,
weißt du wo du hingehörst
Wenn du ganz alleine bist, weißt du
dass du es noch so lange sein wirst.*

Faber

Thin liquid film flows are a prominent phenomenon that we encounter in our daily life, e.g. the rain droplets on the windows or the water soap film when we wash our hands. Interestingly most of the time we do not recognize them as such, although they are used in a lot of industrial process and applications as motivated in Chap. 1. A few vivid examples of thin film flows have been shown in Fig. 1.1. Both the life time and shape of a soap bubble can in fact be explained with the theoretical framework derived in Chap. 2.

That said and in the spirit of the Helmholtz Institute Erlangen-Nürnberg for Renewable Energy, the greater goal of this project is to understand the dynamics needed for mass production of cheap organic/perovskite photovoltaic cells (OPV/PSC). While these cells are still lacking in efficiency as compared to silica based ones they offer great usability features. The underlying structure does not need to be stiff and as such they can be printed on e.g. plastic foil. Printing on soft and elastic substrates with blends of complex liquids is however a hideous problem, more so from a theoretical point of view. Instead of searching from the very first step for a solution to the full problem, this thesis addresses one issue of this complex process, which is the film formation. A step of crucial importance that happens after the coating, be it with a slot die or other coating methods. Numerical simulations based on the thin film equation may help to understand at least this part of the process. In the long run the found results should help to improve both the process itself as well as the efficiency of the final product.

To this end a novel approach for modelling the dynamics of thin liquid films has been developed, see Chap. 2-6. It is important to highlight that this model consists of two parts. There is the theoretical work, where we use shallow water theory and find matching conditions that allow us to solve the thin film equation. In Chap. 2 we discuss both theories and some overlap between them, we however like to point out that we are not the first ones to discuss this overlap. What makes our approach novel is the step from the continuum to a discrete system. Instead of solving the (stiff) degenerate fourth order partial differential equation for the evolution of the film thickness we solve a modified shallow water system using the lattice Boltzmann

method. A very thorough referee called this approach hyperbolization of the thin film equation. The second part is therefore the numerical tool or solver that we created during this project.

To summarize the results of this thesis, we should first address the elephant in the room: “Do we need yet another solver for the thin film equation?” Although it might be tempting to answer this question with a clear “Yes” or “No”, it is more complicated than that. Computational fluid dynamics is a rich scientific field populated with several methods build on truly stunning results. It is not just the finite volume method or the lattice Boltzmann method, but a vast collection of different approaches, many more than mentioned in this work. There are various reasons why there are so many tools doing essentially the same. Some reasons grew historically, others developed with advances in mathematics. One thing to mention is that it is of scientific value when a new method can reproduce known results. That is because all methods suffer shortcomings and there is no single method that is better suited in all hydrodynamic regimes than another one. In Chap. 3 we introduced the idea behind the Chapman-Enskog expansion and found that the lattice Boltzmann method best works in the low $Kn & Ma$ number regime. Finite volume methods are highly dependent on the quality of the mesh and developing self-consistent boundary conditions can be a tedious task, e.g. contact angle dynamics. Molecular dynamics simulations are inherently noisy and computationally demanding for large volumes, and yet all of those three methods can be used to simulate thin film problems. Each method can address different aspects of a problem and yet all have to satisfy the underlying physical boundary conditions, e.g. mass conservation. We briefly addressed why our method fits well into the current landscape of thin film solvers in Sec 1.4 of Chap. 4.

This statement of need covers only the positive sides of our method, but as written above all methods have their shortcomings and so does ours. All the numerical experiments conducted in this thesis don’t rely on the lattice Boltzmann approach we developed. It would have been in fact helpful to use a suited finite difference scheme because the lattice Boltzmann method is certainly not the most beloved CFD tool. One reason why the lattice Boltzmann method is less appealing than other methods are the model parameters. For the simulation of a sliding droplet with **oomph-lib** we would use model parameters which relate to a laboratory experiment. Doing the same with the lattice Boltzmann method we likely have a harder time matching parameters. We have seen in Chap. 3 that e.g. the viscosity is related to the relaxation time τ . This relaxation time τ has a lower limit which is $\tau = 1/2$ and it should not be too large for stability and convergence reasons (at least for a single relaxation time collision operator, such as the BGK operator). The viscosity is therefore not a simple model parameter that can be changed to arbitrary values and the problem associated with it is called under- and over relaxation. Another difference to classical solvers is the idea of particle distributions and particle collisions. A lattice Boltzmann time step consists of a collision operation and a streaming step, both happen on rather short physical time scales, usually orders smaller than a second. Another flaw of the here developed method is its simplicity. Currently, the method allows simulating a single fluid on a flat substrate. Additional dynamics such as the coupling with particles

or the interaction of multiple fluids are not implemented. Evaporation, for example, plays an important role in many film forming processes, however as of now we do not supply a model for phase changes. The same is true for problems where inertia is non-negligible, such as spin coating. And then there is the novelty of this method. Novelty is a double-edged sword, because something novel requires a lot of creativity and novel results should enhance our current understanding. Developing a new numerical tool that can solve problems which have been solved is, as said, important but not considered novel. Using a new tool to create new results usually comes with a heavy price to pay. Any new method must show that it agrees with previous work, be it theoretical, experimental or other simulations. Before we were able to show that we can use the here developed method for novel problems, we had to make sure that relevant known results, e.g. relaxation of a droplet, can be reproduced with the correct physical behaviour. Therefore, there is a lot of *overhead* which simply would not exist when using an established finite difference scheme.

Picking up the question from above, “Do we need yet another solver...?”, we found some arguments for the “No” answer, let us discuss some arguments for the “Yes” answer. One rather unscientific strength of this solver is the transparent nature of the software. The code base is available under an open source licence and everyone interested can fork the repository and use (and develop) our method. It is becoming harder and harder to validate numerical simulations and argue about data, we think that transparency of our source code is at least a baby step into the right direction. The package approach, similar to e.g. Python, Matlab or R, makes it simple to share and collaborate with colleagues. Apart from these quality of life/usability features there are few things that make the derived model special and scientifically interesting. In contrast to various numerical methods used in the literature of thin film dynamics, *Swalbe.jl* is built upon the lattice Boltzmann method as described in Chaps 3-5. It is therefore not intended as a general tool to approximate differential equations, but only for the hydrodynamics of thin liquid films. While the term simplicity was used earlier as weakness, one of the nineteen guiding principles of python reads: “Simple is better than complex”. A small codebase is maintainable, it is possible to write tests for every function and add documentation, all of this would be harder for general purpose solvers with much more lines of code. In Chap. 5 we show that our simple approach is in fact more than capable to simulate relevant physical problems. Multiple tests with analytical results have been used to validate the method, see Tanner’s law and Cox-Voinov relation. Another benefit of the here presented approach is the dimensional reduction. While it is restricting on the one hand, e.g. contact angles smaller than $\pi/2$, it reduces the demand for computational resources quite significant. That in fact allows us to introduce various additions to our model and still have reasonable fast running simulations. All simulations presented in this thesis can be computed on a laptop with dedicated GPU, there is no real need for HPC resources. While the model does not account for e.g. surfactants, we supply a matching condition between our method and thin film like theories in Chaps. 5-6. The seemingly simple “Yes” or “No” question could be discussed in even more detail, but it is a subjective open question. Therefore we would like to have a look at Chaps.6-7 and their findings.

In Chap. 6 we introduce thermal fluctuations to our model. These fluctuations lead to a constant excitement of the fluid air interface that is smoothed out by the surface tension, leading to the appearance of thermo-capillary waves. Their amplitude however is usually so small that they can be neglected in experimental analysis or numerical simulations. However having a dewetting thin film it can be assumed that the thickness of the film will be comparable to the amplitude of the fluctuations, at least in regions where the film ruptures. As shown in Chap. 6 these fluctuations can be added to the model using a matching condition for a fluctuating force term. The fluctuating force term is then tested against the theory of capillary waves and does show in fact good agreement with the predicted spectrum. In the following it is shown that the stability difference, as measured in rupture times, between fluctuating and deterministic thin film¹ does inversely depend on the logarithm of the wettability. By the virtue of the model a combination of a spatially varying wettability as well as the addition of thermal fluctuations is studied using a dewetting thin film. Depending on the chosen function of the wettability it is possible to create numerical experiments where the deterministic simulation is almost indistinguishable from the fluctuating one. At the beginning of this chapter we discuss the underlying theory and the modification to the thin film equation. The constructive approach we use to match our model with the stochastic thin film equation should in fact serve as a blueprint for other additions e.g. surfactant dynamics.

In Chap. 7 a simple toy model is developed to study dewetting dynamics under the influence of “switchable” substrates. The model is build on the idea that the wettability, e.g. the equilibrium contact angle $\theta_{\text{eq.}}$, can be changed based on external stimuli. We assume that the these stimuli can be modelled by an arbitrary function. In the here discussed case the arbitrary function is a trigonometric function ($\theta(x, t) \propto \sin(xt)$) that admits not only a spatial gradient but also a time dependent behaviour. Due to this wettability gradient fluid is driven into regions of high wettability, or low contact angles. Therefore the stationary state for vanishing time dependency, $\partial_t \theta = 0$, is simply an array of droplets formed in the minima of the contact angle field. Adding a temporal component to the contact angle field introduces a stabilizing effect to the dewetting film, which lead to an increase in rupture time. Most interestingly is the morphological transition that emerges when the dynamics of the contact angle field becomes fast as compared to the capillary retraction. This means that the film finds itself in a metastable energy minimum where all fluid accumulates in rivulets. Metastable because the rivulets are prone to an instability. In fact, independent of the parameters we vary rupture of these rivulets can be observed. The stationary state after the breakup is again a multi-droplet state, however with fewer droplets than in the static case.

Somewhat unexpected to the author of this thesis the lattice Boltzmann model for thin film hydrodynamics does in fact work very well. Unexpected because this model is build from parts that work well individually, e.g. shallow water theory and the lattice Boltzmann method, but that does not necessarily mean that their combination

¹ $k_B T > 0$ fluctuating thin film, $k_B T = 0$ deterministic thin film

is appropriate to solve thin film problems. We did show that the method is capable of performing numerical experiments in the desired fluid dynamic regimes ($Re < 1$, $Ca < 1$) without too much superficial parameter tuning, leaving aside the discussion of hydrodynamic slip. Matching with characteristic quantities such as the most unstable mode of the film (q_0) does allow comparing with experiments, theory and even other simulations. The here presented work should be understood as a baseline to what the model is currently able to do.

The title of the chapter is **Conclusion and outlook** and so far we have not touched the outlook that we foresee. In the pros and cons paragraphs earlier in the conclusion we stated that there is no model for evaporation at the moment of writing. There is however a lot of literature on evaporation in thin films, and a model would be to introduce a constant evaporation flux (scaled with the water-vapour interface). A modification that in principle would violate mass conservation if we do not account for the vapour phase, but the flux can be tuned to agree with experimental findings. Another important aspect in the production of OPV cells is the crystallization during drying. Again we are able to find relevant research for crystallization be it as theoretical approach in thin film theory or as a model for the lattice Boltzmann method. Further problems that would require minor extensions to *Swalbe.jl* are surfactants, particle-fluid coupling and active colloids to name just a few. Among this short list of topics first steps were taken to study the dynamics of thin liquid films with immersed active colloids. While the model does not allow to have a height resolved distribution of colloids inside the film, it in fact allows having a scalar density of colloids. Depending on the activity of these colloids the density can be coupled to the film with e.g. a modified film pressure. The colloids on the other hand have internal degrees of freedom allowing for their own system of equations. Within the limit of slow change of colloidal density (flowing with the film) the integration of evolution equation can simply be coupled to the lattice Boltzmann time iteration.

Similar to the development of complex software, scientific problems are always in an evolving state. One theory is not wrong but rather replaced by another one that creates a deeper understanding. Therefore although this is the scientific end of my work as a PhD student, I personally hope that possible successors will achieve novel and interesting results based on the here presented model and ideas.

“Talent is cheap, you have to be possessed or obsessed, rather. You really have to feel like you cannot not do art, and that is something you can’t will.” - John Baldessari.

Bibliography

- [22] *JLD2*. JuliaIO. Dec. 2022.
- [Aar+05] Dirk G. A. L. Aarts et al. “Hydrodynamics of Droplet Coalescence”. In: *Phys. Rev. Lett.* 95.16 (Oct. 2005), p. 164503. DOI: 10.1103/PhysRevLett.95.164503.
- [ABB07] Neil Ayres, Stephen G. Boyes, and William J. Brittain. “Stimuli-Responsive Polyelectrolyte Polymer Brushes Prepared via Atom-Transfer Radical Polymerization”. In: *Langmuir* 23.1 (Jan. 2007), pp. 182–189. ISSN: 0743-7463. DOI: 10.1021/la0615261.
- [AM21] Sebastian Aland and Dominic Mokbel. “A Unified Numerical Model for Wetting of Soft Substrates”. In: *Int. J. Numer. Methods Eng.* 122.4 (2021), pp. 903–918. ISSN: 1097-0207. DOI: 10.1002/nme.6567.
- [APM10] Anton A. Darhuber, Joseph P. Valentino, and Sandra M. Troian. “Planar Digital Nanoliter Dispensing System Based on Thermocapillary Actuation”. In: *Lab. Chip* 10.8 (2010), pp. 1061–1071. DOI: 10.1039/B921759B.
- [AR18] Daron Acemoglu and Pascual Restrepo. “Artificial Intelligence, Automation, and Work”. In: *The Economics of Artificial Intelligence: An Agenda*. University of Chicago Press, Jan. 2018, pp. 197–236.
- [AS20] Bruno Andreotti and Jacco H. Snoeijer. “Statics and Dynamics of Soft Wetting”. In: *Annu. Rev. Fluid Mech.* 52.1 (2020), pp. 285–308. DOI: 10.1146/annurev-fluid-010719-060147.
- [Ava11] A Avagadro. “Essai d’une maniere de determiner les masses relatives des molecules elementaires des corps, et les proportions selon lesquelles elles entrent dans ces combinaisons”. In: *J. Physique* 73 (1811), pp. 58–76.
- [B71] De St Venant B. “Theorie Du Mouvement Non-Permanent Des Eaux Avec Application Aux Crues Des Rivers et a l’introduuntion Des Marees Dans Leur Lit”. In: *Acad. Sci Comptes Redus* 73.99 (1871), pp. 148–154.
- [BA20] Rajneesh Bhardwaj and Amit Agrawal. “Likelihood of Survival of Coronavirus in a Respiratory Droplet Deposited on a Solid Surface”. In: *Phys. Fluids* 32.6 (June 2020), p. 061704. ISSN: 1070-6631. DOI: 10.1063/5.0012009.
- [Bar19] Valeria Barra. *valeriabarra/ThinViscoelasticFilms: v0.1*. Version v0.1. Dec. 2019. DOI: 10.5281/zenodo.3561225. URL: <https://doi.org/10.5281/zenodo.3561225>.

- [Bar22] Valeria Barra. *Code for Thin Viscoelastic Film Simulations on Flat Substrates*. Jan. 2022.
- [BB13] François Bouchut and Sébastien Boyaval. “A New Model for Shallow Viscoelastic Fluids”. In: *Math. Models Methods Appl. Sci.* 23.08 (July 2013), pp. 1479–1526. ISSN: 0218-2025. DOI: 10.1142/S0218202513500140.
- [BB67] C. K. Batchelor and G. K. Batchelor. *An Introduction to Fluid Dynamics*. Cambridge University Press, 1967. ISBN: 978-0-521-66396-0.
- [Bec+03] Jürgen Becker et al. “Complex Dewetting Scenarios Captured by Thin-Film Models”. In: *Nature Mater.* 2.1 (Jan. 2003), pp. 59–63. ISSN: 1476-4660. DOI: 10.1038/nmat788.
- [Bec03] Kent Beck. *Test-Driven Development: By Example*. Addison-Wesley Professional, 2003. ISBN: 978-0-321-14653-3.
- [Bei+20] Gerben Beintema et al. “Controlling Rayleigh–Bénard Convection via Reinforcement Learning”. In: *J. Turbul.* 21.9-10 (Oct. 2020), pp. 585–605. DOI: 10.1080/14685248.2020.1797059.
- [Ben+14] Jorge Benet et al. “Disjoining Pressure, Healing Distance, and Film Height Dependent Surface Tension of Thin Wetting Films”. In: *J. Phys. Chem. C* 118.38 (Sept. 2014), pp. 22079–22089. ISSN: 1932-7447. DOI: 10.1021/jp506534b.
- [Ber+00] Vance Bergeron et al. “Controlling Droplet Deposition with Polymer Additives”. In: *Nature* 405.6788 (June 2000), pp. 772–775. ISSN: 1476-4687. DOI: 10.1038/35015525.
- [Ber+07] E. Bertrand et al. “Dynamics of Dewetting at the Nanoscale Using Molecular Dynamics”. In: *Langmuir* 23.7 (Mar. 2007), pp. 3774–3785. ISSN: 0743-7463. DOI: 10.1021/la062920m. (Visited on 07/27/2023).
- [Ber+12] Christian W. J. Berendsen et al. “Rupture of Thin Liquid Films Induced by Impinging Air-Jets”. In: *Langmuir* 28.26 (July 2012), pp. 9977–9985. ISSN: 0743-7463. DOI: 10.1021/la301353f.
- [Bes+19] Tim Besard et al. “Rapid Software Prototyping for Heterogeneous and Distributed Platforms”. In: *Advances in Engineering Software* 132 (June 2019), pp. 29–46. ISSN: 0965-9978. DOI: 10.1016/j.advengsoft.2019.02.002.
- [Bez+17] Jeff Bezanson et al. “Julia: A Fresh Approach to Numerical Computing”. In: *SIAM Rev.* 59.1 (Jan. 2017), pp. 65–98. ISSN: 0036-1445. DOI: 10.1137/141000671.
- [BFD19] Tim Besard, Christophe Foket, and Bjorn De Sutter. “Effective Extensible Programming: Unleashing Julia on GPUs”. In: *IEEE Trans. Parallel Distrib. Syst.* 30.4 (Apr. 2019), pp. 827–841. ISSN: 1558-2183. DOI: 10.1109/TPDS.2018.2872064.

- [BG05] Jürgen Becker and Günther Grün. “The Thin-Film Equation: Recent Advances and Some New Perspectives”. In: *J. Phys.: Condens. Matter* 17.9 (Feb. 2005), S291. ISSN: 0953-8984. DOI: 10.1088/0953-8984/17/9/002. (Visited on 07/19/2023).
- [BG91] B. J. Briscoe and K. P. Galvin. “Growth with Coalescence during Condensation”. In: *Phys. Rev. A* 43.4 (Feb. 1991), pp. 1906–1917. DOI: 10.1103/PhysRevA.43.1906.
- [BGD13] Berend J. Brasjen, Hao Gu, and Anton A. Darhuber. “Dewetting of Thin Liquid Films on Chemically Patterned Substrates: Front Propagation along Narrow Lyophobic Stripes and Stripe Arrays”. In: *Microfluid Nanofluid* 14.3 (Mar. 2013), pp. 669–682. ISSN: 1613-4990. DOI: 10.1007/s10404-012-1086-4.
- [BGK54] P. L. Bhatnagar, E. P. Gross, and M. Krook. “A Model for Collision Processes in Gases. I. Small Amplitude Processes in Charged and Neutral One-Component Systems”. In: *Phys. Rev.* 94.3 (May 1954), pp. 511–525. DOI: 10.1103/PhysRev.94.511.
- [BGW07] John B. Bell, Alejandro L. Garcia, and Sarah A. Williams. “Numerical Methods for the Stochastic Landau-Lifshitz Navier-Stokes Equations”. In: *Phys. Rev. E* 76.1 (July 2007), p. 016708. DOI: 10.1103/PhysRevE.76.016708. (Visited on 07/13/2023).
- [Bil06] Filiz Bilge. “Examining the Burnout of Academics in Relation to Job Satisfaction and Other Factors”. In: *Social Behavior and Personality: an international journal* 34.9 (Jan. 2006), pp. 1151–1160. DOI: 10.2224/sbp.2006.34.9.1151.
- [Bis+96] J. Bischof et al. “Dewetting Modes of Thin Metallic Films: Nucleation of Holes and Spinodal Dewetting”. In: *Phys. Rev. Lett.* 77.8 (Aug. 1996), pp. 1536–1539. DOI: 10.1103/PhysRevLett.77.1536.
- [BM72] George Boole and John Fletcher Moulton. *A Treatise on the Calculus of Finite Differences*. MacMillan and Company, 1872.
- [Bon+09] Daniel Bonn et al. “Wetting and Spreading”. In: *Rev. Mod. Phys.* 81.2 (May 2009), pp. 739–805. DOI: 10.1103/RevModPhys.81.739.
- [BPT03] M. Bestehorn, A. Pototsky, and U. Thiele. “3D Large Scale Marangoni Convectionin Liquid Films”. In: *Eur. Phys. J. B* 33.4 (June 2003), pp. 457–467. ISSN: 1434-6036. DOI: 10.1140/epjb/e2003-00186-3.
- [Bre08] Yann Brenier. “Generalized Solutions and Hydrostatic Approximation of the Euler Equations”. In: *Physica D: Nonlinear Phenomena. Euler Equations: 250 Years On* 237.14 (Aug. 2008), pp. 1982–1988. ISSN: 0167-2789. DOI: 10.1016/j.physd.2008.02.026.
- [Bre21] Tom Breloff. *Plots.Jl*. Zenodo. June 2021. DOI: 10.5281/zenodo.4907285. (Visited on 08/09/2023).

- [BSH01] C. J. Brabec, N. S. Sariciftci, and J. C. Hummelen. “Plastic Solar Cells”. In: *Adv. Funct. Mater.* 11.1 (2001), pp. 15–26. ISSN: 1616-3028. DOI: 10.1002/1616-3028(200102)11:1<15::AID-ADFM15>3.0.CO;2-A.
- [But+18] Hans-Jürgen Butt et al. “Adaptive Wetting—Adaptation in Wetting”. In: *Langmuir* 34.38 (Sept. 2018), pp. 11292–11304. ISSN: 0743-7463. DOI: 10.1021/acs.langmuir.8b01783.
- [Bvv95] H. J. C. Berendsen, D. van der Spoel, and R. van Drunen. “GROMACS: A Message-Passing Parallel Molecular Dynamics Implementation”. In: *Computer Physics Communications* 91.1 (Sept. 1995), pp. 43–56. ISSN: 0010-4655. DOI: 10.1016/0010-4655(95)00042-E.
- [BW12] C. Brezinski and L. Wuytack. *Numerical Analysis: Historical Developments in the 20th Century*. Elsevier, Dec. 2012. ISBN: 978-0-444-59858-5.
- [Cal+92] A. Calì et al. “Diffusion and Hydrodynamic Dispersion with the Lattice Boltzmann Method”. In: *Phys. Rev. A* 45.8 (Apr. 1992), pp. 5771–5774. DOI: 10.1103/PhysRevA.45.5771.
- [Car+19] Livio Nicola Carenza et al. “Lattice Boltzmann Methods and Active Fluids”. In: *Eur. Phys. J. E* 42.6 (June 2019), p. 81. ISSN: 1292-895X. DOI: 10.1140/epje/i2019-11843-6. (Visited on 08/10/2023).
- [CB44] A. B. D. Cassie and S. Baxter. “Wettability of Porous Surfaces”. In: *Trans. Faraday Soc.* 40 (1944), p. 546. ISSN: 0014-7672. DOI: 10.1039/tf9444000546.
- [CC90] Sydney Chapman and T. G. Cowling. *The Mathematical Theory of Non-uniform Gases: An Account of the Kinetic Theory of Viscosity, Thermal Conduction and Diffusion in Gases*. Cambridge University Press, 1990. ISBN: 978-0-521-40844-8.
- [CD21] P. Cardiff and I. Demirdžić. “Thirty Years of the Finite Volume Method for Solid Mechanics”. In: *Arch. Comput. Methods Eng.* 28.5 (Aug. 2021), pp. 3721–3780. ISSN: 1886-1784. DOI: 10.1007/s11831-020-09523-0. (Visited on 07/25/2023).
- [CD98] Shiyi Chen and Gary D. Doolen. “Lattice Boltzmann Method for Fluid Flows”. In: *Annu. Rev. Fluid Mech.* 30.1 (Jan. 1998), pp. 329–364. ISSN: 0066-4189, 1545-4479. DOI: 10.1146/annurev.fluid.30.1.329.
- [Cer88] Carlo Cercignani. “The Boltzmann Equation”. In: *The Boltzmann Equation and Its Applications*. Ed. by Carlo Cercignani. Applied Mathematical Sciences. New York, NY: Springer, 1988, pp. 40–103. ISBN: 978-1-4612-1039-9. DOI: 10.1007/978-1-4612-1039-9_2.
- [CFL28] R. Courant, K. Friedrichs, and H. Lewy. “Über die partiellen Differenzengleichungen der mathematischen Physik”. In: *Math. Ann.* 100.1 (Dec. 1928), pp. 32–74. ISSN: 1432-1807. DOI: 10.1007/BF01448839.

- [Che+10] Li Chen et al. “Thermal-Responsive Hydrogel Surface: Tunable Wettability and Adhesion to Oil at the Water /Solid Interface”. In: *Soft Matter* 6.12 (2010), pp. 2708–2712. DOI: 10.1039/C002543G.
- [Che+14] Goong Chen et al. “OpenFOAM for Computational Fluid Dynamics”. In: *Notices Amer. Math. Soc.* 61.4 (Apr. 2014), p. 354. ISSN: 0002-9920, 1088-9477. DOI: 10.1090/noti1095.
- [Che+95] S. Chen et al. “Lattice Methods and Their Applications to Reacting Systems”. In: *Comput. Chem. Eng.* Applications of Parallel Computing 19.6 (June 1995), pp. 617–646. ISSN: 0098-1354. DOI: 10.1016/0098-1354(94)00072-7.
- [Che88] Jing-Den Chen. “Experiments on a Spreading Drop and Its Contact Angle on a Solid”. In: *J. Colloid Interface Sci.* 122.1 (Mar. 1988), pp. 60–72. ISSN: 0021-9797. DOI: 10.1016/0021-9797(88)90287-1.
- [CJ17] Sunita Chandrasekaran and Guido Juckeland. *OpenACC for Programmers: Concepts and Strategies*. Addison-Wesley Professional, Sept. 2017. ISBN: 978-0-13-469434-4.
- [CKB11] Longquan Chen, Günter K. Auernhammer, and Elmar Bonaccurso. “Short Time Wetting Dynamics on Soft Surfaces”. In: *Soft Matter* 7.19 (2011), pp. 9084–9089. DOI: 10.1039/C1SM05967J.
- [Cla27] Navier (M Claude-Louis-Marie-Henri). *Mémoire sur les lois du mouvement des fluides*. 1827.
- [CM09] R. V. Craster and O. K. Matar. “Dynamics and Stability of Thin Liquid Films”. In: *Rev. Mod. Phys.* 81.3 (Aug. 2009), pp. 1131–1198. DOI: 10.1103/RevModPhys.81.1131.
- [CMM15] Andrea Cavalli, Michiel Musterd, and Frieder Mugele. “Numerical Investigation of Dynamic Effects for Sliding Drops on Wetting Defects”. In: *Phys. Rev. E* 91.2 (Feb. 2015), p. 023013. DOI: 10.1103/PhysRevE.91.023013.
- [CN47] J. Crank and P. Nicolson. “A Practical Method for Numerical Evaluation of Solutions of Partial Differential Equations of the Heat-Conduction Type”. In: *Math. Proc. Camb. Philos. Soc.* 43.1 (Jan. 1947), pp. 50–67. ISSN: 1469-8064, 0305-0041. DOI: 10.1017/S0305004100023197.
- [CS20] Steffen Christgau and Thomas Steinke. “Porting a Legacy CUDA Stencil Code to oneAPI”. In: *2020 IEEE Int. Parallel Distrib. Process. Symp. Workshop IPDPSW*. May 2020, pp. 359–367. DOI: 10.1109/IPDPSW50202.2020.00070.
- [CS86] A. M. Cazabat and M. A. Cohen Stuart. “Dynamics of Wetting: Effects of Surface Roughness”. In: *J. Phys. Chem.* 90.22 (Oct. 1986), pp. 5845–5849. ISSN: 0022-3654, 1541-5740. DOI: 10.1021/j100280a075.

- [CV20] Emmanuil Chatzigiannakis and Jan Vermant. “Breakup of Thin Liquid Films: From Stochastic to Deterministic”. In: *Phys. Rev. Lett.* 125.15 (Oct. 2020), p. 158001. DOI: [10.1103/PhysRevLett.125.158001](https://doi.org/10.1103/PhysRevLett.125.158001).
- [da +99] A. S. da Silva Sobrinho et al. “A Study of Defects in Ultra-Thin Transparent Coatings on Polymers”. In: *Surf. Coat. Technol.* 116–119 (Sept. 1999), pp. 1204–1210. ISSN: 0257-8972. DOI: [10.1016/S0257-8972\(99\)00152-8](https://doi.org/10.1016/S0257-8972(99)00152-8).
- [Dar+00] Anton A. Darhuber et al. “Selective Dip-Coating of Chemically Micropatterned Surfaces”. In: *J. Appl. Phys.* 88.9 (Nov. 2000), pp. 5119–5126. ISSN: 0021-8979. DOI: [10.1063/1.1317238](https://doi.org/10.1063/1.1317238).
- [dBQ04] Pierre-Gilles de Gennes, Françoise Brochard-Wyart, and David Quéré. *Capillarity and Wetting Phenomena*. New York, NY: Springer, 2004. ISBN: 978-1-4419-1833-8. DOI: [10.1007/978-0-387-21656-0](https://doi.org/10.1007/978-0-387-21656-0).
- [de 02] P. G. de Gennes. “On Fluid/Wall Slippage”. In: *Langmuir* 18.9 (Apr. 2002), pp. 3413–3414. ISSN: 0743-7463. DOI: [10.1021/la0116342](https://doi.org/10.1021/la0116342).
- [de 85] P. G. de Gennes. “Wetting: Statics and Dynamics”. In: *Rev. Mod. Phys.* 57.3 (July 1985), pp. 827–863. DOI: [10.1103/RevModPhys.57.827](https://doi.org/10.1103/RevModPhys.57.827).
- [DEJ03] L. Duchemin, J. Eggers, and C. Josserand. “Inviscid Coalescence of Drops”. In: *J. Fluid Mech.* 487 (June 2003), pp. 167–178. ISSN: 1469-7645, 0022-1120. DOI: [10.1017/S0022112003004646](https://doi.org/10.1017/S0022112003004646).
- [Del+05] N. Delorme et al. “Azobenzene-Containing Monolayer with Photoswitchable Wettability”. In: *Langmuir* 21.26 (Dec. 2005), pp. 12278–12282. ISSN: 0743-7463. DOI: [10.1021/la051517x](https://doi.org/10.1021/la051517x).
- [Del02] Paul J. Dellar. “Nonhydrodynamic Modes and a Priori Construction of Shallow Water Lattice Boltzmann Equations”. In: *Phys. Rev. E* 65.3 (Feb. 2002), p. 036309. DOI: [10.1103/PhysRevE.65.036309](https://doi.org/10.1103/PhysRevE.65.036309).
- [Der93] B. Derjaguin. “On the Thickness of the Liquid Film Adhering to the Walls of a Vessel after Emptying”. In: *Prog. Surf. Sci.* 43.1 (May 1993), pp. 134–137. ISSN: 0079-6816. DOI: [10.1016/0079-6816\(93\)90022-N](https://doi.org/10.1016/0079-6816(93)90022-N).
- [DGF16] Javier A. Diez, Alejandro G. González, and Roberto Fernández. “Metallic-Thin-Film Instability with Spatially Correlated Thermal Noise”. In: *Phys. Rev. E* 93.1 (Jan. 2016), p. 013120. DOI: [10.1103/PhysRevE.93.013120](https://doi.org/10.1103/PhysRevE.93.013120).
- [DGK09a] Javier A. Diez, Alejandro G. González, and Lou Kondic. “On the Breakup of Fluid Rivulets”. In: *Phys. Fluids* 21.8 (Aug. 2009), p. 082105. ISSN: 1070-6631. DOI: [10.1063/1.3211248](https://doi.org/10.1063/1.3211248).
- [DGK09b] Javier A. Diez, Alejandro G. González, and Lou Kondic. “Stability of a Finite-Length Rivulet under Partial Wetting Conditions”. In: *J. Phys.: Conf. Ser.* 166.1 (May 2009), p. 012009. ISSN: 1742-6596. DOI: [10.1088/1742-6596/166/1/012009](https://doi.org/10.1088/1742-6596/166/1/012009).

- [DJP20] Prasenjit Das, Prabhat K. Jaiswal, and Sanjay Puri. “Surface-Directed Spinodal Decomposition on Chemically Patterned Substrates”. In: *Phys. Rev. E* 102.1 (July 2020), p. 012803. DOI: [10.1103/PhysRevE.102.012803](https://doi.org/10.1103/PhysRevE.102.012803).
- [DKB00] Javier A. Diez, L. Kondic, and Andrea Bertozzi. “Global Models for Moving Contact Lines”. In: *Phys. Rev. E* 63.1 (Dec. 2000), p. 011208. DOI: [10.1103/PhysRevE.63.011208](https://doi.org/10.1103/PhysRevE.63.011208).
- [DMS05] Benny Davidovitch, Esteban Moro, and Howard A. Stone. “Spreading of Viscous Fluid Drops on a Solid Substrate Assisted by Thermal Fluctuations”. In: *Phys. Rev. Lett.* 95.24 (Dec. 2005), p. 244505. DOI: [10.1103/PhysRevLett.95.244505](https://doi.org/10.1103/PhysRevLett.95.244505).
- [dQ98] Alain de Ryck and David Quéré. “Gravity and Inertia Effects in Plate Coating”. In: *J. Colloid Interface Sci.* 203.2 (July 1998), pp. 278–285. ISSN: 0021-9797. DOI: [10.1006/jcis.1998.5444](https://doi.org/10.1006/jcis.1998.5444).
- [DS05] Paul J. Dellar and Rick Salmon. “Shallow Water Equations with a Complete Coriolis Force and Topography”. In: *Phys. Fluids* 17.10 (Oct. 2005), p. 106601. ISSN: 1070-6631. DOI: [10.1063/1.2116747](https://doi.org/10.1063/1.2116747).
- [DS15] Camille Duprat and Howard A. Stone. *Fluid-Structure Interactions in Low-Reynolds-Number Flows*. Royal Society of Chemistry, Nov. 2015. ISBN: 978-1-78262-849-1.
- [Dur+19] Miguel A. Durán-Olivencia et al. “Instability, Rupture and Fluctuations in Thin Liquid Films: Theory and Computations”. In: *J. Stat. Phys.* 174.3 (Feb. 2019), pp. 579–604. ISSN: 1572-9613. DOI: [10.1007/s10955-018-2200-0](https://doi.org/10.1007/s10955-018-2200-0).
- [Edw+16] Andrew M. J. Edwards et al. “Not Spreading in Reverse: The Dewetting of a Liquid Film into a Single Drop”. In: *Sci. Adv.* 2.9 (Sept. 2016), e1600183. DOI: [10.1126/sciadv.1600183](https://doi.org/10.1126/sciadv.1600183).
- [EG04] Alexandre Ern and Jean-Luc Guermond. *Theory and Practice of Finite Elements*. Ed. by S. S. Antman, J. E. Marsden, and L. Sirovich. Vol. 159. Applied Mathematical Sciences. New York, NY: Springer, 2004. ISBN: 978-1-4419-1918-2. DOI: [10.1007/978-1-4757-4355-5](https://doi.org/10.1007/978-1-4757-4355-5). (Visited on 07/27/2023).
- [Egg97] Jens Eggers. “Nonlinear Dynamics and Breakup of Free-Surface Flows”. In: *Rev. Mod. Phys.* 69.3 (July 1997), pp. 865–930. DOI: [10.1103/RevModPhys.69.865](https://doi.org/10.1103/RevModPhys.69.865).
- [ELS99] Jens Eggers, John R. Lister, and Howard A. Stone. “Coalescence of Liquid Drops”. In: *J. Fluid Mech.* 401 (Dec. 1999), pp. 293–310. ISSN: 1469-7645, 0022-1120. DOI: [10.1017/S002211209900662X](https://doi.org/10.1017/S002211209900662X).

- [Eng+16] Sebastian Engelnkemper et al. “Morphological Transitions of Sliding Drops: Dynamics and Bifurcations”. In: *Phys. Rev. Fluids* 1.7 (Nov. 2016), p. 073901. DOI: [10.1103/PhysRevFluids.1.073901](https://doi.org/10.1103/PhysRevFluids.1.073901).
- [Ens17] David Enskog. *Kinetische Theorie Der Vorgänge in Mässig Verdünnten Gasen 1 Allgemeiner Teil*. Uppsala: Almqvist & Wiksell, 1917.
- [EWS13] A. Eddi, K. G. Winkels, and J. H. Snoeijer. “Influence of Droplet Geometry on the Coalescence of Low Viscosity Drops”. In: *Phys. Rev. Lett.* 111.14 (Oct. 2013), p. 144502. DOI: [10.1103/PhysRevLett.111.144502](https://doi.org/10.1103/PhysRevLett.111.144502).
- [FC98] X. Fanton and A. M. Cazabat. “Spreading and Instabilities Induced by a Solutal Marangoni Effect”. In: *Langmuir* 14.9 (Apr. 1998), pp. 2554–2561. ISSN: 0743-7463. DOI: [10.1021/la971292t](https://doi.org/10.1021/la971292t).
- [FCQ96] X. Fanton, A. M. Cazabat, and D. Quéré. “Thickness and Shape of Films Driven by a Marangoni Flow”. In: *Langmuir* 12.24 (Jan. 1996), pp. 5875–5880. ISSN: 0743-7463. DOI: [10.1021/la960488a](https://doi.org/10.1021/la960488a).
- [Fet+05] R. Fetzer et al. “New Slip Regimes and the Shape of Dewetting Thin Liquid Films”. In: *Phys. Rev. Lett.* 95.12 (Sept. 2005), p. 127801. DOI: [10.1103/PhysRevLett.95.127801](https://doi.org/10.1103/PhysRevLett.95.127801).
- [Fet+07a] R. Fetzer et al. “Quantifying Hydrodynamic Slip: A Comprehensive Analysis of Dewetting Profiles”. In: *Langmuir* 23.21 (Oct. 2007), pp. 10559–10566. ISSN: 0743-7463. DOI: [10.1021/la7010698](https://doi.org/10.1021/la7010698).
- [Fet+07b] R. Fetzer et al. “Thermal Noise Influences Fluid Flow in Thin Films during Spinodal Dewetting”. In: *Phys. Rev. Lett.* 99.11 (Sept. 2007), p. 114503. DOI: [10.1103/PhysRevLett.99.114503](https://doi.org/10.1103/PhysRevLett.99.114503).
- [FG18] Julian Fischer and Günther Grün. “Existence of Positive Solutions to Stochastic Thin-Film Equations”. In: *SIAM J. Math. Anal.* 50.1 (Jan. 2018), pp. 411–455. ISSN: 0036-1410. DOI: [10.1137/16M1098796](https://doi.org/10.1137/16M1098796).
- [FH21] A. I. Fedorchenko and J. Hruba. “On Formation of Dry Spots in Heated Liquid Films”. In: *Phys. Fluids* 33.2 (Feb. 2021), p. 023601. ISSN: 1070-6631. DOI: [10.1063/5.0035547](https://doi.org/10.1063/5.0035547).
- [FHP86] U. Frisch, B. Hasslacher, and Y. Pomeau. “Lattice-Gas Automata for the Navier-Stokes Equation”. In: *Phys. Rev. Lett.* 56.14 (Apr. 1986), pp. 1505–1508. DOI: [10.1103/PhysRevLett.56.1505](https://doi.org/10.1103/PhysRevLett.56.1505). (Visited on 07/25/2023).
- [Foc+10] Maximilian Focke et al. “Lab-on-a-Foil: Microfluidics on Thin and Flexible Films”. In: *Lab. Chip* 10.11 (2010), pp. 1365–1386. DOI: [10.1039/C001195A](https://doi.org/10.1039/C001195A).
- [Fur62] C. G. L. Furmidge. “Studies at Phase Interfaces. I. The Sliding of Liquid Drops on Solid Surfaces and a Theory for Spray Retention”. In: *Journal of Colloid Science* 17.4 (Apr. 1962), pp. 309–324. ISSN: 0095-8522. DOI: [10.1016/0095-8522\(62\)90011-9](https://doi.org/10.1016/0095-8522(62)90011-9).

- [Gew21] Virginia Gewin. “Pandemic Burnout Is Rampant in Academia”. In: *Nature* 591.7850 (Mar. 2021), pp. 489–491. DOI: 10.1038/d41586-021-00663-2.
- [GG16] Fei Guo and Zhiguang Guo. “Inspired Smart Materials with External Stimuli Responsive Wettability: A Review”. In: *RSC Adv.* 6.43 (2016), pp. 36623–36641. DOI: 10.1039/C6RA04079A.
- [GG88] Marcia H. Grabow and George H. Gilmer. “Thin Film Growth Modes, Wetting and Cluster Nucleation”. In: *Surface Science* 194.3 (Jan. 1988), pp. 333–346. ISSN: 0039-6028. DOI: 10.1016/0039-6028(88)90858-8.
- [GMR06] Günther Grün, Klaus Mecke, and Markus Rauscher. “Thin-Film Flow Influenced by Thermal Noise”. In: *J. Stat. Phys.* 122.6 (Mar. 2006), pp. 1261–1291. ISSN: 1572-9613. DOI: 10.1007/s10955-006-9028-8.
- [Gon+13] Alejandro G. González et al. “Instability of Liquid Cu Films on a SiO₂ Substrate”. In: *Langmuir* 29.30 (July 2013), pp. 9378–9387. ISSN: 0743-7463. DOI: 10.1021/la4009784.
- [Gra97] Julia B. Graf. *The Colorado River in Grand Canyon: How Fast Does It Flow?* USGS Numbered Series 168-97. U.S. Geological Survey, 1997, p. 4. DOI: 10.3133/fs16897. (Visited on 07/19/2023).
- [Gre89] George Green. *An Essay on the Application of Mathematical Analysis to the Theories of Electricity and Magnetism*. author, 1889.
- [Gri13] David J. Griffiths. *Introduction to Electrodynamics*. Fourth edition. Boston: Pearson, 2013. ISBN: 978-0-321-85656-2.
- [Gro+80] W. A. Gross et al. “Fluid Film Lubrication”. In: DOE/TIC-11301 (Jan. 1980).
- [Gro11] David Gross. “How to Exploit the Full Potential of the Dip-Coating Process to Better Control Film Formation”. In: *J. Mater. Chem.* 21.43 (2011), pp. 17033–17038. DOI: 10.1039/C1JM12837J.
- [Gro94] J B Grotberg. “Pulmonary Flow and Transport Phenomena”. In: *Annu. Rev. Fluid Mech.* 26.1 (1994), pp. 529–571. DOI: 10.1146/annurev.fl.26.010194.002525. eprint: <https://doi.org/10.1146/annurev.fl.26.010194.002525>.
- [GS21a] Josua Grawitter and Holger Stark. “Droplets on Substrates with Oscillating Wettability”. In: *Soft Matter* 17.41 (2021), pp. 9469–9479. DOI: 10.1039/D1SM01113H.
- [GS21b] Josua Grawitter and Holger Stark. “Steering Droplets on Substrates Using Moving Steps in Wettability”. In: *Soft Matter* 17.9 (Mar. 2021), pp. 2454–2467. ISSN: 1744-6848. DOI: 10.1039/D0SM02082F.
- [Gun+91] Andrew K. Gunstensen et al. “Lattice Boltzmann Model of Immiscible Fluids”. In: *Phys. Rev. A* 43.8 (Apr. 1991), pp. 4320–4327. DOI: 10.1103/PhysRevA.43.4320.

- [Gur02] Guru P. Guruswamy. “A Review of Numerical Fluids/Structures Interface Methods for Computations Using High-Fidelity Equations”. In: *Computers & Structures* 80.1 (Jan. 2002), pp. 31–41. ISSN: 0045-7949. DOI: [10.1016/S0045-7949\(01\)00164-X](https://doi.org/10.1016/S0045-7949(01)00164-X).
- [GZS02] Zhaoli Guo, Chuguang Zheng, and Baochang Shi. “Discrete Lattice Effects on the Forcing Term in the Lattice Boltzmann Method”. In: *Phys. Rev. E* 65.4 (Apr. 2002), p. 046308. DOI: [10.1103/PhysRevE.65.046308](https://doi.org/10.1103/PhysRevE.65.046308).
- [Hac+20] Michiel A. Hack et al. “Self-Similar Liquid Lens Coalescence”. In: *Phys. Rev. Lett.* 124.19 (May 2020), p. 194502. DOI: [10.1103/PhysRevLett.124.194502](https://doi.org/10.1103/PhysRevLett.124.194502).
- [Hae+15] Sabrina Haefner et al. “Influence of Slip on the Plateau–Rayleigh Instability on a Fibre”. In: *Nat Commun* 6.1 (June 2015), p. 7409. ISSN: 2041-1723. DOI: [10.1038/ncomms8409](https://doi.org/10.1038/ncomms8409).
- [Hai97] J. M. Haile. *Molecular Dynamics Simulation: Elementary Methods*. 1st edition. New York, NY: Wiley-Interscience, Mar. 1997. ISBN: 978-0-471-18439-3.
- [Ham37] H. C. Hamaker. “The London—van Der Waals Attraction between Spherical Particles”. In: *Physica* 4.10 (Oct. 1937), pp. 1058–1072. ISSN: 0031-8914. DOI: [10.1016/S0031-8914\(37\)80203-7](https://doi.org/10.1016/S0031-8914(37)80203-7). (Visited on 07/19/2023).
- [HC85] L. J. Harrison and F. E. Cunningham. “Factors Influencing the Quality of Mayonnaise: A Review”. In: *J. Food Qual.* 8.1 (1985), pp. 1–20. ISSN: 1745-4557. DOI: [10.1111/j.1745-4557.1985.tb00828.x](https://doi.org/10.1111/j.1745-4557.1985.tb00828.x).
- [Her+12] J. F. Hernández-Sánchez et al. “Symmetric and Asymmetric Coalescence of Drops on a Substrate”. In: *Phys. Rev. Lett.* 109.18 (Nov. 2012), p. 184502. DOI: [10.1103/PhysRevLett.109.184502](https://doi.org/10.1103/PhysRevLett.109.184502).
- [Her+15] Eline Hermans et al. “Lung Surfactants and Different Contributions to Thin Film Stability”. In: *Soft Matter* 11.41 (2015), pp. 8048–8057. DOI: [10.1039/C5SM01603G](https://doi.org/10.1039/C5SM01603G).
- [Her+98] Stephan Herminghaus et al. “Spinodal Dewetting in Liquid Crystal and Liquid Metal Films”. In: *Science* 282.5390 (Oct. 1998), pp. 916–919. DOI: [10.1126/science.282.5390.916](https://doi.org/10.1126/science.282.5390.916).
- [HH15] Matthias Heil and Andrew L. Hazel. “Flow in Flexible/Collapsible Tubes”. In: *Fluid–Structure Interactions in Low-Reynolds-Number Flows*. The Royal Society of Chemistry, Nov. 2015. ISBN: 978-1-84973-813-2. DOI: [10.1039/9781782628491-00280](https://doi.org/10.1039/9781782628491-00280).
- [HK76] J. Hoshen and R. Kopelman. “Percolation and Cluster Distribution. I. Cluster Multiple Labeling Technique and Critical Concentration Algorithm”. In: *Phys. Rev. B* 14.8 (Oct. 1976), pp. 3438–3445. DOI: [10.1103/PhysRevB.14.3438](https://doi.org/10.1103/PhysRevB.14.3438).

- [HL97] Xiaoyi He and Li-Shi Luo. “Theory of the Lattice Boltzmann Method: From the Boltzmann Equation to the Lattice Boltzmann Equation”. In: *Phys. Rev. E* 56.6 (Dec. 1997), pp. 6811–6817. DOI: [10.1103/PhysRevE.56.6811](https://doi.org/10.1103/PhysRevE.56.6811).
- [HS71] Chun Huh and L. E Scriven. “Hydrodynamic Model of Steady Movement of a Solid/Liquid/Fluid Contact Line”. In: *J. Colloid Interface Sci.* 35.1 (Jan. 1971), pp. 85–101. ISSN: 0021-9797. DOI: [10.1016/0021-9797\(71\)90188-3](https://doi.org/10.1016/0021-9797(71)90188-3).
- [HTA14] Adam P. Hughes, Uwe Thiele, and Andrew J. Archer. “An Introduction to Inhomogeneous Liquids, Density Functional Theory, and the Wetting Transition”. In: *Am. J. Phys.* 82.12 (Dec. 2014), pp. 1119–1129. ISSN: 0002-9505. DOI: [10.1119/1.4890823](https://doi.org/10.1119/1.4890823).
- [ION00] Kunihiro Ichimura, Sang-Keun Oh, and Masaru Nakagawa. “Light-Driven Motion of Liquids on a Photoresponsive Surface”. In: *Science* 288.5471 (June 2000), pp. 1624–1626. DOI: [10.1126/science.288.5471.1624](https://doi.org/10.1126/science.288.5471.1624).
- [JA98] John D. Anderson Jr and John David Anderson. *A History of Aerodynamics: And Its Impact on Flying Machines*. Cambridge University Press, 1998. ISBN: 978-0-521-66955-9.
- [Jac21] John David Jackson. *Classical Electrodynamics*. John Wiley & Sons, May 2021. ISBN: 978-1-119-77076-3.
- [Jal+18] Maryam Jalali et al. “Fabrication and Characterization of a Scalable Surface Textured with Pico-Liter Oil Drops for Mechanistic Studies of Bacteria-Oil Interactions”. In: *Sci Rep* 8.1 (May 2018), p. 7612. ISSN: 2045-2322. DOI: [10.1038/s41598-018-25812-y](https://doi.org/10.1038/s41598-018-25812-y).
- [Jam+18] Etienne Jambon-Puillet et al. “Spreading Dynamics and Contact Angle of Completely Wetting Volatile Drops”. In: *J. Fluid Mech.* 844 (June 2018), pp. 817–830. ISSN: 0022-1120, 1469-7645. DOI: [10.1017/jfm.2018.142](https://doi.org/10.1017/jfm.2018.142).
- [Jam+19] François James et al. “Towards a New Friction Model for Shallow Water Equations through an Interactive Viscous Layer”. In: *ESAIM: M2AN* 53.1 (Jan. 2019), pp. 269–299. ISSN: 0764-583X, 1290-3841. DOI: [10.1051/m2an/2018076](https://doi.org/10.1051/m2an/2018076).
- [Jas09] Hrvoje Jasak. “OpenFOAM: Open Source CFD in Research and Industry”. In: *International Journal of Naval Architecture and Ocean Engineering* 1.2 (Dec. 2009), pp. 89–94. ISSN: 2092-6782. DOI: [10.2478/IJNAOE-2013-0011](https://doi.org/10.2478/IJNAOE-2013-0011).
- [JAT99] A. Jabbarzadeh, J. D. Atkinson, and R. I. Tanner. “Wall Slip in the Molecular Dynamics Simulation of Thin Films of Hexadecane”. In: *J. Chem. Phys.* 110.5 (Feb. 1999), pp. 2612–2620. ISSN: 0021-9606. DOI: [10.1063/1.477982](https://doi.org/10.1063/1.477982).

- [JJ65] Charles Jordan and Károly Jordán. *Calculus of Finite Differences*. American Mathematical Soc., 1965. ISBN: 978-0-8284-0033-6.
- [JJT] Hrvoje Jasak, Aleksandar Jemcov, and Zeljko Tukovic. “OpenFOAM: A C++ Library for Complex Physics Simulations”. In: ().
- [JK00] Michael Junk and Axel Klar. “Discretizations for the Incompressible Navier–Stokes Equations Based on the Lattice Boltzmann Method”. In: *SIAM J. Sci. Comput.* 22.1 (Jan. 2000), pp. 1–19. ISSN: 1064-8275. DOI: 10.1137/S1064827599357188.
- [JM95] Jos M. H. Janssen and Han. E. H. Meijer. “Dynamics of Liquid-Liquid Mixing: A 2-Zone Model”. In: *Polym. Eng. Sci.* 35.22 (1995), pp. 1766–1780. ISSN: 1548-2634. DOI: 10.1002/pen.760352206.
- [Jo+09] Byoung Wook Jo et al. “Evaluation of Jet Performance in Drop-on-Demand (DOD) Inkjet Printing”. In: *Korean J. Chem. Eng.* 26.2 (Mar. 2009), pp. 339–348. ISSN: 1975-7220. DOI: 10.1007/s11814-009-0057-2.
- [Kar+14] Stefan Karpitschka et al. “Coalescence and Noncoalescence of Sessile Drops: Impact of Surface Forces”. In: *Langmuir* 30.23 (June 2014), pp. 6826–6830. ISSN: 0743-7463. DOI: 10.1021/la500459v.
- [Kar+98] A. Karim et al. “Phase Separation of Ultrathin Polymer-Blend Films on Patterned Substrates”. In: *Phys. Rev. E* 57.6 (June 1998), R6273–R6276. DOI: 10.1103/PhysRevE.57.R6273.
- [KE20] Christoph Klopp and Alexey Eremin. “On Droplet Coalescence in Quasi-Two-Dimensional Fluids”. In: *Langmuir* 36.35 (Sept. 2020), pp. 10615–10621. ISSN: 0743-7463. DOI: 10.1021/acs.langmuir.0c02139.
- [Kim07] Jungho Kim. “Spray Cooling Heat Transfer: The State of the Art”. In: *International Journal of Heat and Fluid Flow*. Including Special Issue of Conference on Modelling Fluid Flow (CMFF’06), Budapest 28.4 (Aug. 2007), pp. 753–767. ISSN: 0142-727X. DOI: 10.1016/j.ijheatfluidflow.2006.09.003.
- [KKS00a] Kajari Kargupta, Rahul Konnur, and Ashutosh Sharma. “Instability and Pattern Formation in Thin Liquid Films on Chemically Heterogeneous Substrates”. In: *Langmuir* 16.26 (Dec. 2000), pp. 10243–10253. ISSN: 0743-7463. DOI: 10.1021/la000759o.
- [KKS00b] Rahul Konnur, Kajari Kargupta, and Ashutosh Sharma. “Instability and Morphology of Thin Liquid Films on Chemically Heterogeneous Substrates”. In: *Phys. Rev. Lett.* 84.5 (Jan. 2000), pp. 931–934. DOI: 10.1103/PhysRevLett.84.931.
- [KLK02] Ho-Young Kim, Heon Ju Lee, and Byung Ha Kang. “Sliding of Liquid Drops Down an Inclined Solid Surface”. In: *J. Colloid Interface Sci.* 247.2 (Mar. 2002), pp. 372–380. ISSN: 0021-9797. DOI: 10.1006/jcis.2001.8156.

- [KM05] Dongjo Kim and Jooho Moon. “Highly Conductive Ink Jet Printed Films of Nanosilver Particles for Printable Electronics”. In: *Electrochem. Solid-State Lett.* 8.11 (Sept. 2005), J30. ISSN: 1944-8775. DOI: 10.1149/1.2073670.
- [KMV02] Joseph B. Keller, Paul A. Milewski, and Jean-Marc Vanden-Broeck. “Breaking and Merging of Liquid Sheets and Filaments”. In: *Journal of Engineering Mathematics* 42.3 (Apr. 2002), pp. 283–290. ISSN: 1573-2703. DOI: 10.1023/A:1016127027751.
- [Kön11] Königliche Gesellschaft der Wissenschaften zu Göttingen. *Commentationes Societatis Regiae Scientiarum Gottingensis recentiores*. Göttingen, Germany, 1811. (Visited on 07/17/2023).
- [Kop+06] J. Koplik et al. “Pearling Instability of Nanoscale Fluid Flow Confined to a Chemical Channel”. In: *Physics of Fluids* 18.3 (Mar. 2006), p. 032104. ISSN: 1070-6631. DOI: 10.1063/1.2178786. (Visited on 07/27/2023).
- [KR12] Stefan Karpitschka and Hans Riegler. “Noncoalescence of Sessile Drops from Different but Miscible Liquids: Hydrodynamic Analysis of the Twin Drop Contour as a Self-Stabilizing Traveling Wave”. In: *Phys. Rev. Lett.* 109.6 (Aug. 2012), p. 066103. DOI: 10.1103/PhysRevLett.109.066103.
- [KR14] Stefan Karpitschka and Hans Riegler. “Sharp Transition between Coalescence and Non-Coalescence of Sessile Drops”. In: *J. Fluid Mech.* 743 (Mar. 2014), R1. ISSN: 0022-1120, 1469-7645. DOI: 10.1017/jfm.2014.73.
- [Krü+17] Timm Krüger et al. *The Lattice Boltzmann Method: Principles and Practice*. Graduate Texts in Physics. Cham: Springer International Publishing, 2017. ISBN: 978-3-319-44647-9. DOI: 10.1007/978-3-319-44649-3.
- [KS02a] Kajari Kargupta and Ashutosh Sharma. “Dewetting of Thin Films on Periodic Physically and Chemically Patterned Surfaces”. In: *Langmuir* 18.5 (Mar. 2002), pp. 1893–1903. ISSN: 0743-7463. DOI: 10.1021/la010469n.
- [KS02b] Kajari Kargupta and Ashutosh Sharma. “Morphological Self-Organization by Dewetting in Thin Films on Chemically Patterned Substrates”. In: *J. Chem. Phys.* 116.7 (Feb. 2002), pp. 3042–3051. ISSN: 0021-9606. DOI: 10.1063/1.1434949.
- [KS03] Kajari Kargupta and Ashutosh Sharma. “Mesopatterning of Thin Liquid Films by Templating on Chemically Patterned Complex Substrates”. In: *Langmuir* 19.12 (June 2003), pp. 5153–5163. ISSN: 0743-7463. DOI: 10.1021/la026634w.
- [KS92] R. D. Kingdon and P. Schofield. “A Reaction-Flow Lattice Boltzmann Model”. In: *J. Phys. A: Math. Gen.* 25.14 (July 1992), p. L907. ISSN: 0305-4470. DOI: 10.1088/0305-4470/25/14/008.

- [KTS20] Christoph Klopp, Torsten Trittel, and Ralf Stannarius. “Self Similarity of Liquid Droplet Coalescence in a Quasi-2D Free-Standing Liquid-Crystal Film”. In: *Soft Matter* 16.19 (2020), pp. 4607–4614. DOI: [10.1039/DOSM00457J](https://doi.org/10.1039/DOSM00457J).
- [Kul91] H. J. Kull. “Theory of the Rayleigh-Taylor Instability”. In: *Physics Reports* 206.5 (Aug. 1991), pp. 197–325. ISSN: 0370-1573. DOI: [10.1016/0370-1573\(91\)90153-D](https://doi.org/10.1016/0370-1573(91)90153-D).
- [LAS08] Norman A. Luechinger, Evangelos K. Athanassiou, and Wendelin J. Stark. “Graphene-Stabilized Copper Nanoparticles as an Air-Stable Substitute for Silver and Gold in Low-Cost Ink-Jet Printable Electronics”. In: *Nanotechnology* 19.44 (Sept. 2008), p. 445201. ISSN: 0957-4484. DOI: [10.1088/0957-4484/19/44/445201](https://doi.org/10.1088/0957-4484/19/44/445201).
- [LCH03] S. V. Lishchuk, C. M. Care, and I. Halliday. “Lattice Boltzmann Algorithm for Surface Tension with Greatly Reduced Microcurrents”. In: *Phys. Rev. E* 67.3 (Mar. 2003), p. 036701. DOI: [10.1103/PhysRevE.67.036701](https://doi.org/10.1103/PhysRevE.67.036701).
- [Lea07] L. Gary Leal. *Advanced Transport Phenomena: Fluid Mechanics and Convective Transport Processes*. Cambridge University Press, June 2007. ISBN: 978-1-139-46206-8.
- [Len90] R. Lenormand. “Liquids in Porous Media”. In: *J. Phys.: Condens. Matter* 2.S (Dec. 1990), SA79. ISSN: 0953-8984. DOI: [10.1088/0953-8984/2/S/008](https://doi.org/10.1088/0953-8984/2/S/008).
- [LHv01] Erik Lindahl, Berk Hess, and David van der Spoel. “GROMACS 3.0: A Package for Molecular Simulation and Trajectory Analysis”. In: *J Mol Model* 7.8 (Aug. 2001), pp. 306–317. ISSN: 0948-5023. DOI: [10.1007/s008940100045](https://doi.org/10.1007/s008940100045).
- [Li+19] Shaotian Li et al. “An Evaluation of Force Terms in the Lattice Boltzmann Models in Simulating Shallow Water Flows over Complex Topography”. In: *Int. J. Numer. Methods Fluids* 90.7 (2019), pp. 357–373. ISSN: 1097-0363. DOI: [10.1002/fld.4726](https://doi.org/10.1002/fld.4726).
- [Li+20] Lin Li et al. “Lattice Boltzmann Method for Fluid-Thermal Systems: Status, Hotspots, Trends and Outlook”. In: *IEEE Access* 8 (2020), pp. 27649–27675. ISSN: 2169-3536. DOI: [10.1109/ACCESS.2020.2971546](https://doi.org/10.1109/ACCESS.2020.2971546).
- [Li+21] Xiaomei Li et al. “Adaptation of a Styrene–Acrylic Acid Copolymer Surface to Water”. In: *Langmuir* 37.4 (Feb. 2021), pp. 1571–1577. ISSN: 0743-7463. DOI: [10.1021/acs.langmuir.0c03226](https://doi.org/10.1021/acs.langmuir.0c03226).
- [Liu+05] Ying Liu et al. “Controlled Switchable Surface”. In: *Chem. – Eur. J.* 11.9 (2005), pp. 2622–2631. ISSN: 1521-3765. DOI: [10.1002/chem.200400931](https://doi.org/10.1002/chem.200400931).

- [Liu+16] Haihu Liu et al. “Multiphase Lattice Boltzmann Simulations for Porous Media Applications”. In: *Comput Geosci* 20.4 (Aug. 2016), pp. 777–805. ISSN: 1573-1499. DOI: 10.1007/s10596-015-9542-3.
- [LL13] L. D. Landau and E. M. Lifshitz. *Fluid Mechanics: Landau and Lifshitz: Course of Theoretical Physics, Volume 6*. Elsevier, Sept. 2013. ISBN: 978-1-4831-6104-4.
- [LL88] L. Landau and B. Levich. “Dragging of a Liquid by a Moving Plate”. In: *Dynamics of Curved Fronts*. Ed. by Pierre Pelcé. San Diego: Academic Press, Jan. 1988, pp. 141–153. ISBN: 978-0-12-550355-6. DOI: 10.1016/B978-0-08-092523-3.50016-2.
- [Los66] Josef Loschmidt. “Zur Grösse der Luftmoleküle”. In: *Sitzungsberichte der kaiserlichen Akademie der Wissenschaften Wien, Mathem.-naturwiss. Klasse*. Vol. Abt. II, 52. 1866, pp. 395–413.
- [LP00] R. S. Laugesen and M. C. Pugh. “Linear Stability of Steady States for Thin Film and Cahn-Hilliard Type Equations”. In: *Arch. Rational Mech. Anal* 154.1 (Aug. 2000), pp. 3–51. ISSN: 1432-0673. DOI: 10.1007/PL00004234.
- [LX15] Qingchang Liu and Baoxing Xu. “Actuating Water Droplets on Graphene via Surface Wettability Gradients”. In: *Langmuir* 31.33 (Aug. 2015), pp. 9070–9075. ISSN: 0743-7463. DOI: 10.1021/acs.langmuir.5b02335.
- [Mah+13] K. Mahady et al. “Comparison of Navier-Stokes Simulations with Long-Wave Theory: Study of Wetting and Dewetting”. In: *Phys. Fluids* 25.11 (Nov. 2013), p. 112103. ISSN: 1070-6631. DOI: 10.1063/1.4828721.
- [MAK15] Kyle Mahady, Shahriar Afkhami, and Lou Kondic. “A Volume of Fluid Method for Simulating Fluid/Fluid Interfaces in Contact with Solid Boundaries”. In: *Journal of Computational Physics* 294 (Aug. 2015), pp. 243–257. ISSN: 0021-9991. DOI: 10.1016/j.jcp.2015.03.051.
- [Mar07] Fabien Marche. “Derivation of a New Two-Dimensional Viscous Shallow Water Model with Varying Topography, Bottom Friction and Capillary Effects”. In: *European Journal of Mechanics - B/Fluids* 26.1 (Jan. 2007), pp. 49–63. ISSN: 0997-7546. DOI: 10.1016/j.euromechflu.2006.04.007.
- [Mat22] John E. Matsson. *An Introduction to ANSYS Fluent 2022*. SDC Publications, Aug. 2022. ISBN: 978-1-63057-569-4.
- [Mic+13] Walter Mickel et al. “Shortcomings of the Bond Orientational Order Parameters for the Analysis of Disordered Particulate Matter”. In: *J. Chem. Phys.* 138.4 (Jan. 2013), p. 044501. ISSN: 0021-9606. DOI: 10.1063/1.4774084.
- [Mil96] Louis Melville Milne-Thomson. *Theoretical Hydrodynamics*. Courier Corporation, Jan. 1996. ISBN: 978-0-486-68970-8.

- [Mit93] Vladimir S. Mitlin. “Dewetting of Solid Surface: Analogy with Spinodal Decomposition”. In: *J. Colloid Interface Sci.* 156.2 (Mar. 1993), pp. 491–497. ISSN: 0021-9797. DOI: 10.1006/jcis.1993.1142.
- [MK85] T. F. Meister and D. M. Kroll. “Density-Functional Theory for Inhomogeneous Fluids: Application to Wetting”. In: *Phys. Rev. A* 31.6 (June 1985), pp. 4055–4057. DOI: 10.1103/PhysRevA.31.4055.
- [ML13] D. E. Moulton and J. Lega. “Effect of Disjoining Pressure in a Thin Film Equation with Non-Uniform Forcing”. In: *Eur. J. Appl. Math.* 24.6 (Dec. 2013), pp. 887–920. ISSN: 0956-7925, 1469-4425. DOI: 10.1017/S0956792513000235.
- [MM94] Istvan Montvay and Gernot Münster. *Quantum Fields on a Lattice*. Cambridge University Press, 1994. ISBN: 978-0-521-59917-7.
- [MR05] Klaus Mecke and Markus Rauscher. “On Thermal Fluctuations in Thin Film Flow”. In: *J. Phys.: Condens. Matter* 17.45 (Oct. 2005), S3515. ISSN: 0953-8984. DOI: 10.1088/0953-8984/17/45/042.
- [MRD08] S. Mechkov, M. Rauscher, and S. Dietrich. “Stability of Liquid Ridges on Chemical Micro- and Nanostripes”. In: *Phys. Rev. E* 77.6 (June 2008), p. 061605. DOI: 10.1103/PhysRevE.77.061605.
- [Mug+05] F. Muggele et al. “Electrowetting: A Convenient Way to Switchable Wettability Patterns”. In: *J. Phys.: Condens. Matter* 17.9 (Feb. 2005), S559. ISSN: 0953-8984. DOI: 10.1088/0953-8984/17/9/016.
- [Mün05] A. Münch. “Dewetting Rates of Thin Liquid Films”. In: *J. Phys.: Condens. Matter* 17.9 (Feb. 2005), S309. ISSN: 0953-8984. DOI: 10.1088/0953-8984/17/9/003.
- [MWW05] A. Münch, B. A. Wagner, and T. P. Witelski. “Lubrication Models with Small to Large Slip Lengths”. In: *J Eng Math* 53.3 (Dec. 2005), pp. 359–383. ISSN: 1573-2703. DOI: 10.1007/s10665-005-9020-3.
- [Mye05] T. G. Myers. “Application of Non-Newtonian Models to Thin Film Flow”. In: *Phys. Rev. E* 72.6 (Dec. 2005), p. 066302. DOI: 10.1103/PhysRevE.72.066302.
- [MZ88] Guy R. McNamara and Gianluigi Zanetti. “Use of the Boltzmann Equation to Simulate Lattice-Gas Automata”. In: *Phys. Rev. Lett.* 61.20 (Nov. 1988), pp. 2332–2335. DOI: 10.1103/PhysRevLett.61.2332. (Visited on 08/02/2023).
- [Nav23] Claude L.M.H. Navier. “Mémoire Sur Les Lois Du Mouvement Des Fluides”. In: *Mém. Académie Sci. Inst. Fr.* 6 (1823), pp. 389–440.
- [Nes+15] S. Nesic et al. “Fully Nonlinear Dynamics of Stochastic Thin-Film Dewetting”. In: *Phys. Rev. E* 92.6 (Dec. 2015), p. 061002. DOI: 10.1103/PhysRevE.92.061002.

- [Nes17] S. Nesic. *stochastic thin films*. 2017. URL: https://github.com/snesic/stochastic_thin_films.
- [Nik+02] Alex D Nikolov et al. “Superspreading Driven by Marangoni Flow”. In: *Advances in Colloid and Interface Science*. A Collection of Papers in Honour of Nikolay Churaev on the Occasion of His 80th Birthday 96.1 (Feb. 2002), pp. 325–338. ISSN: 0001-8686. DOI: 10.1016/S0001-8686(01)00087-2.
- [Nis+99] Giovanni Nisato et al. “Excitation of Surface Deformation Modes of a Phase-Separating Polymer Blend on a Patterned Substrate”. In: *Macromolecules* 32.7 (Apr. 1999), pp. 2356–2364. ISSN: 0024-9297. DOI: 10.1021/ma981546x.
- [NS19] Noel De Nevers and G. D. Silcox. *Fluid Mechanics for Chemical Engineers*. McGraw-Hill Higher Education, 2019. ISBN: 978-1-260-47552-4.
- [NZ20] Gyoko Nagayama and Dejian Zhang. “Intermediate Wetting State at Nano/Microstructured Surfaces”. In: *Soft Matter* 16.14 (2020), pp. 3514–3521. DOI: 10.1039/C9SM02513H.
- [ODB97] Alexander Oron, Stephen H. Davis, and S. George Bankoff. “Long-Scale Evolution of Thin Liquid Films”. In: *Rev. Mod. Phys.* 69.3 (July 1997), pp. 931–980. DOI: 10.1103/RevModPhys.69.931.
- [Osc+17] Stefano Luigi Oscurato et al. “Light-Driven Wettability Tailoring of Azopolymer Surfaces with Reconfigured Three-Dimensional Posts”. In: *ACS Appl. Mater. Interfaces* 9.35 (Sept. 2017), pp. 30133–30142. ISSN: 1944-8244. DOI: 10.1021/acsami.7b08025.
- [Pah+18] A. Alizadeh Pahlavan et al. “Thin Films in Partial Wetting: Stability, Dewetting and Coarsening”. In: *J. Fluid Mech.* 845 (June 2018), pp. 642–681. ISSN: 0022-1120, 1469-7645. DOI: 10.1017/jfm.2018.255.
- [Paw+19] Nilesh D. Pawar et al. “Symmetric and Asymmetric Coalescence of Droplets on a Solid Surface in the Inertia-Dominated Regime”. In: *Phys. Fluids* 31.9 (Sept. 2019), p. 092106. ISSN: 1070-6631. DOI: 10.1063/1.5119014.
- [PBN11] Joseph D. Paulsen, Justin C. Burton, and Sidney R. Nagel. “Viscous to Inertial Crossover in Liquid Drop Coalescence”. In: *Phys. Rev. Lett.* 106.11 (Mar. 2011), p. 114501. DOI: 10.1103/PhysRevLett.106.114501.
- [Pel06] Efim Pelinovsky. “Hydrodynamics of Tsunami Waves”. In: *Waves in Geophysical Fluids: Tsunamis, Rogue Waves, Internal Waves and Internal Tides*. Ed. by John Grue and Karsten Trulsen. CISM International Centre for Mechanical Sciences. Vienna: Springer, 2006, pp. 1–48. ISBN: 978-3-211-69356-8. DOI: 10.1007/978-3-211-69356-8_1.
- [Pes+19] Dirk Peschka et al. “Signatures of Slip in Dewetting Polymer Films”. In: *Proc. Natl. Acad. Sci.* 116.19 (May 2019), pp. 9275–9284. DOI: 10.1073/pnas.1820487116.

- [Peschka] Dirk Peschka. “Variational Approach to Dynamic Contact Angles for Thin Films”. In: *Physics of Fluids* 30.8 (Aug. 2018), p. 082115. ISSN: 1070-6631. DOI: 10.1063/1.5040985. (Visited on 07/24/2023).
- [Peskin] Michael Peskin. *An Introduction To Quantum Field Theory*. CRC Press, May 2018. ISBN: 978-0-429-50355-9. DOI: 10.1201/9780429503559.
- [Podgorski et al.] T. Podgorski, J.-M. Flesselles, and L. Limat. “Corners, Cusps, and Pearls in Running Drops”. In: *Phys. Rev. Lett.* 87.3 (June 2001), p. 036102. DOI: 10.1103/PhysRevLett.87.036102.
- [Pihler-Puzović et al.] Draga Pihler-Puzović et al. “Modelling the Suppression of Viscous Fingering in Elastic-Walled Hele-Shaw Cells”. In: *J. Fluid Mech.* 731 (Sept. 2013), pp. 162–183. ISSN: 0022-1120, 1469-7645. DOI: 10.1017/jfm.2013.375.
- [Pihler-Puzović et al.] Draga Pihler-Puzović et al. “Displacement Flows under Elastic Membranes. Part 1. Experiments and Direct Numerical Simulations”. In: *J. Fluid Mech.* 784 (Dec. 2015), pp. 487–511. ISSN: 0022-1120, 1469-7645. DOI: 10.1017/jfm.2015.590.
- [Plimpton] Steve Plimpton. “Fast Parallel Algorithms for Short-Range Molecular Dynamics”. In: *Journal of Computational Physics* 117.1 (Mar. 1995), pp. 1–19. ISSN: 0021-9991. DOI: 10.1006/jcph.1995.1039.
- [Poisson] S. D. de Poisson. “Nouvelle théorie de l’action capillaire.” In: 1831.7 (Jan. 1831), pp. 170–175. ISSN: 1435-5345. DOI: 10.1515/crll.1831.7.170.
- [Press et al.] William H. Press et al. *Numerical Recipes 3rd Edition: The Art of Scientific Computing*. Cambridge University Press, Sept. 2007. ISBN: 978-0-521-88068-8.
- [Prestininzi et al.] Pietro Prestininzi, Giampiero Sciortino, and Michele La Rocca. “On the Effect of the Intrinsic Viscosity in a Two-Layer Shallow Water Lattice Boltzmann Model of Axisymmetric Density Currents”. In: *J. Hydraul. Res.* 51.6 (Dec. 2013), pp. 668–680. ISSN: 0022-1686. DOI: 10.1080/00221686.2013.819532.
- [Qian] Yue-Hong Qian. “Fractional Propagation and the Elimination of Staggered Invariants in Lattice-BGK Models”. In: *Int. J. Mod. Phys. C* 08.04 (Aug. 1997), pp. 753–761. ISSN: 0129-1831. DOI: 10.1142/S0129183197000643.
- [Quéré] David Quéré. “Fluid Coating on a Fiber”. In: *Annu. Rev. Fluid Mech.* 31.1 (1999), pp. 347–384. DOI: 10.1146/annurev.fluid.31.1.347. (Visited on 08/10/2023).
- [Raabe] D. Raabe. “Overview of the Lattice Boltzmann Method for Nano- and Microscale Fluid Dynamics in Materials Science and Engineering”. In: *Modelling Simul. Mater. Sci. Eng.* 12.6 (Sept. 2004), R13. ISSN: 0965-0393. DOI: 10.1088/0965-0393/12/6/R01.

- [Ray82] Rayleigh. “Investigation of the Character of the Equilibrium of an Incompressible Heavy Fluid of Variable Density”. In: *Proc. Lond. Math. Soc.* s1-14.1 (1882), pp. 170–177. ISSN: 1460-244X. DOI: 10.1112/plms/s1-14.1.170. (Visited on 08/10/2023).
- [RD08] M. Rauscher and S. Dietrich. “Wetting Phenomena in Nanofluidics”. In: *Annu. Rev. Mater. Res.* 38.1 (2008), pp. 143–172. DOI: 10.1146/annurev.matsci.38.060407.132451.
- [Rey83a] Osborne Reynolds. “III. An Experimental Investigation of the Circumstances Which Determine Whether the Motion of Water Shall Be Direct or Sinuous, and of the Law of Resistance in Parallel Channels”. In: *Proc. R. Soc. Lond.* 35.224-226 (Jan. 1883), pp. 84–99. DOI: 10.1098/rsp1.1883.0018.
- [Rey83b] Osborne Reynolds. “XXIX. An Experimental Investigation of the Circumstances Which Determine Whether the Motion of Water Shall Be Direct or Sinuous, and of the Law of Resistance in Parallel Channels”. In: *Philos. Trans. R. Soc. Lond.* 174 (Jan. 1883), pp. 935–982. DOI: 10.1098/rstl.1883.0029.
- [Rey86] Osborne Reynolds. “I. On the Theory of Lubrication and Its Application to Mr. Beauchamp Tower’s Experiments, Including an Experimental Determination of the Viscosity of Olive Oil”. In: *Proc. R. Soc. Lond.* 40.242-245 (Jan. 1886), pp. 191–203. DOI: 10.1098/rsp1.1886.0021.
- [RH20] Olivier J. J. Ronsin and Jens Harting. “Role of the Interplay between Spinodal Decomposition and Crystal Growth in the Morphological Evolution of Crystalline Bulk Heterojunctions”. In: *Energy Technol.* 8.12 (2020), p. 1901468. ISSN: 2194-4296. DOI: 10.1002/ente.201901468.
- [Ric73] S. Richardson. “On the No-Slip Boundary Condition”. In: *J. Fluid Mech.* 59.4 (Aug. 1973), pp. 707–719. ISSN: 1469-7645, 0022-1120. DOI: 10.1017/S0022112073001801.
- [RL08] Robert Rubinstein and Li-Shi Luo. “Theory of the Lattice Boltzmann Equation: Symmetry Properties of Discrete Velocity Sets”. In: *Phys. Rev. E* 77.3 (Mar. 2008), p. 036709. DOI: 10.1103/PhysRevE.77.036709.
- [RMT02] R. Rioboo, M. Marengo, and C. Tropea. “Time Evolution of Liquid Drop Impact onto Solid, Dry Surfaces”. In: *Exp Fluids* 33.1 (July 2002), pp. 112–124. ISSN: 1432-1114. DOI: 10.1007/s00348-002-0431-x.
- [Roc+12] Michele La Rocca et al. “Development of a Lattice Boltzmann Method for Two-Layered Shallow-Water Flow”. In: *Int. J. Numer. Methods Fluids* 70.8 (2012), pp. 1048–1072. ISSN: 1097-0363. DOI: 10.1002/fld.2742.
- [Run95] C. Runge. “Ueber die numerische Auflösung von Differentialgleichungen”. In: *Math. Ann.* 46.2 (June 1895), pp. 167–178. ISSN: 1432-1807. DOI: 10.1007/BF01446807.

- [Rus76] Kenneth J. Ruschak. “Limiting Flow in a Pre-Metered Coating Device”. In: *Chemical Engineering Science* 31.11 (Jan. 1976), pp. 1057–1060. ISSN: 0009-2509. DOI: 10.1016/0009-2509(76)87026-1.
- [Ruz08] M. C. Ruzicka. “On Dimensionless Numbers”. In: *Chemical Engineering Research and Design* 86.8 (Aug. 2008), pp. 835–868. ISSN: 0263-8762. DOI: 10.1016/j.cherd.2008.03.007.
- [Ryk+11] Konrad Rykaczewski et al. “Three Dimensional Aspects of Droplet Coalescence during Dropwise Condensation on Superhydrophobic Surfaces”. In: *Soft Matter* 7.19 (2011), pp. 8749–8752. DOI: 10.1039/C1SM06219K.
- [SA13] Jacco H. Snoeijer and Bruno Andreotti. “Moving Contact Lines: Scales, Regimes, and Dynamical Transitions”. In: *Annu. Rev. Fluid Mech.* 45.1 (Jan. 2013), pp. 269–292. ISSN: 0066-4189, 1545-4479. DOI: 10.1146/annurev-fluid-011212-140734.
- [Sah+19] Sourabh K. Saha et al. “Scalable Submicrometer Additive Manufacturing”. In: *Science* 366.6461 (Oct. 2019), pp. 105–109. DOI: 10.1126/science.aax8760.
- [Sai43] Barre de Saint-Venant. “Note á joindre au mémoire sur la dynamique des fluides”. In: *Comptes rendus* 17.1240 (1843), p. 1843.
- [Sal99] Rick Salmon. “The Lattice Boltzmann Method as a Basis for Ocean Circulation Modeling”. In: *Journal of Marine Research* 57.3 (May 1999), pp. 503–535. DOI: 10.1357/002224099764805174.
- [San20] Oliver Sander. *DUNE — The Distributed and Unified Numerics Environment*. Springer Nature, Dec. 2020. ISBN: 978-3-030-59702-3.
- [Sat+21] Emily N. Satinsky et al. “Systematic Review and Meta-Analysis of Depression, Anxiety, and Suicidal Ideation among Ph.D. Students”. In: *Sci Rep* 11.1 (July 2021), p. 14370. ISSN: 2045-2322. DOI: 10.1038/s41598-021-93687-7.
- [SB09] Nikos Savva and John W. M. Bush. “Viscous Sheet Retraction”. In: *J. Fluid Mech.* 626 (May 2009), pp. 211–240. ISSN: 1469-7645, 0022-1120. DOI: 10.1017/S0022112009005795. (Visited on 07/24/2023).
- [SBA05] Eric Sultan, Arezki Boudaoud, and Martine Ben Amar. “Evaporation of a Thin Film: Diffusion of the Vapour and Marangoni Instabilities”. In: *J. Fluid Mech.* 543 (Nov. 2005), pp. 183–202. ISSN: 1469-7645, 0022-1120. DOI: 10.1017/S0022112005006348.
- [Sbr+14] M. Sbragaglia et al. “Sliding Drops across Alternating Hydrophobic and Hydrophilic Stripes”. In: *Phys. Rev. E* 89.1 (Jan. 2014), p. 012406. DOI: 10.1103/PhysRevE.89.012406.
- [SC93] Xiaowen Shan and Hudong Chen. “Lattice Boltzmann Model for Simulating Flows with Multiple Phases and Components”. In: *Phys. Rev. E* 47.3 (Mar. 1993), pp. 1815–1819. DOI: 10.1103/PhysRevE.47.1815.

- [Sch06] Franz Schwabl. *Statistical Mechanics*. Springer Science & Business Media, Sept. 2006. ISBN: 978-3-540-36217-3.
- [Sch11] Stephen R. Schach. *Object-Oriented and Classical Software Engineering*. 8th ed. New York: McGraw-Hill, 2011. ISBN: 978-0-07-337618-9.
- [Sch97] R.R. Schaller. “Moore’s Law: Past, Present and Future”. In: *IEEE Spectr.* 34.6 (June 1997), pp. 52–59. ISSN: 1939-9340. DOI: 10.1109/6.591665.
- [Scr88] L. E. Scriven. “Physics and Applications of DIP Coating and Spin Coating”. In: *MRS Online Proc. Libr. OPL* 121 (1988), p. 717. ISSN: 0272-9172, 1946-4274. DOI: 10.1557/PROC-121-717.
- [SE10] Jacco H. Snoeijer and Jens Eggers. “Asymptotic Analysis of the Dewetting Rim”. In: *Phys. Rev. E* 82.5 (Nov. 2010), p. 056314. DOI: 10.1103/PhysRevE.82.056314.
- [SE98] Leonard W. Schwartz and Richard R. Eley. “Simulation of Droplet Motion on Low-Energy and Heterogeneous Surfaces”. In: *J. Colloid Interface Sci.* 202.1 (June 1998), pp. 173–188. ISSN: 0021-9797. DOI: 10.1006/jcis.1998.5448.
- [Sec+16] Eleonora Secchi et al. “Massive Radius-Dependent Flow Slippage in Carbon Nanotubes”. In: *Nature* 537.7619 (Sept. 2016), pp. 210–213. ISSN: 1476-4687. DOI: 10.1038/nature19315.
- [Seg+13] Marcello Sega et al. “Regularization of the Slip Length Divergence in Water Nanoflows by Inhomogeneities at the Angstrom Scale”. In: *Soft Matter* 9.35 (2013), pp. 8526–8531. DOI: 10.1039/C3SM51508G.
- [Sek18] Takahiro Seki. “A Wide Array of Photoinduced Motions in Molecular and Macromolecular Assemblies at Interfaces”. In: *BCSJ* 91.7 (July 2018), pp. 1026–1057. ISSN: 0009-2673. DOI: 10.1246/bcsj.20180076.
- [Sha+19] Maulik S. Shah et al. “Thermal Fluctuations in Capillary Thinning of Thin Liquid Films”. In: *J. Fluid Mech.* 876 (Oct. 2019), pp. 1090–1107. ISSN: 0022-1120, 1469-7645. DOI: 10.1017/jfm.2019.595.
- [Sha06] Xiaowen Shan. “Analysis and Reduction of the Spurious Current in a Class of Multiphase Lattice Boltzmann Models”. In: *Phys. Rev. E* 73.4 (Apr. 2006), p. 047701. DOI: 10.1103/PhysRevE.73.047701.
- [Sha84] D.H. Sharp. “An Overview of Rayleigh-Taylor Instability”. In: *Physica D: Nonlinear Phenomena* 12.1-3 (July 1984), pp. 3–18. ISSN: 01672789. DOI: 10.1016/0167-2789(84)90510-4.
- [Shi+18] Weiwei Shi et al. “Fog Harvesting with Harps”. In: *ACS Appl. Mater. Interfaces* 10.14 (Apr. 2018), pp. 11979–11986. ISSN: 1944-8244. DOI: 10.1021/acsami.7b17488.
- [Sin+10] Madhusudan Singh et al. “Inkjet Printing—Process and Its Applications”. In: *Adv. Mater.* 22.6 (2010), pp. 673–685. ISSN: 1521-4095. DOI: 10.1002/adma.200901141.

- [SJ06] Andrew D. Sommers and Anthony M. Jacobi. “Creating Micro-Scale Surface Topology to Achieve Anisotropic Wettability on an Aluminum Surface”. In: *J. Micromech. Microeng.* 16.8 (June 2006), p. 1571. ISSN: 0960-1317. DOI: 10.1088/0960-1317/16/8/018.
- [SK06] Balram Suman and Satish Kumar. “Dynamics of Thin Liquid Films on Surfaces with a Time-Periodic Wettability”. In: *J. Colloid Interface Sci.* 304.1 (Dec. 2006), pp. 208–213. ISSN: 0021-9797. DOI: 10.1016/j.jcis.2006.08.061.
- [Som08] Arnold Sommerfeld. “Ein Beitrag zur hydrodynamische Erklärung der turbulenten Flüssigkeitsbewegungen”. In: *Atti del IV Congresso Internazionale dei Matematici*. IV Congresso Internazionale dei Matematici (Rome). Ed. by G. Castelnuovo. Vol. IV. Tipografia della R. Accademia dei Lincei, 1908, pp. 116–124.
- [Som15] Ian Sommerville. *Software Engineering*. 10th edition. Boston: Pearson, Mar. 2015. ISBN: 978-0-13-394303-0.
- [SSA04] H.A. Stone, A.D. Stroock, and A. Ajdari. “Engineering Flows in Small Devices: Microfluidics Toward a Lab-on-a-Chip”. In: *Annu. Rev. Fluid Mech.* 36.1 (2004), pp. 381–411. DOI: 10.1146/annurev.fluid.36.050802.122124.
- [STH16] Ehsan Samiei, Maryam Tabrizian, and Mina Hoorfar. “A Review of Digital Microfluidics as Portable Platforms for Lab-on a-Chip Applications”. In: *Lab. Chip* 16.13 (2016), pp. 2376–2396. DOI: 10.1039/C6LC00387G.
- [Sto42] George G. Stokes. “On the steady motion of incompressible fluids”. In: *Transactions of the Cambridge Philosophical Society* 7 (1842), pp. 439–453.
- [Sto48] G. G. Stokes. “On the Steady Motion of Incompressible Fluids”. In: *Trans. Camb. Philos. Soc.* 7 (Jan. 1848), p. 439.
- [Stu+10] Martien A. Cohen Stuart et al. “Emerging Applications of Stimuli-Responsive Polymer Materials”. In: *Nature Mater* 9.2 (Feb. 2010), pp. 101–113. ISSN: 1476-4660. DOI: 10.1038/nmat2614.
- [Stu21] Terry W. Sturm. *Open Channel Hydraulics*. McGraw-Hill Education, 2021. ISBN: 978-1-260-46970-7.
- [Suc01] Sauro Succi. *The Lattice Boltzmann Equation: For Fluid Dynamics and Beyond*. Clarendon Press, June 2001. ISBN: 978-0-19-850398-9.
- [Sui+13] Yi Sui et al. “Inertial Coalescence of Droplets on a Partially Wetting Substrate”. In: *Phys. Fluids* 25.10 (Oct. 2013), p. 101701. ISSN: 1070-6631. DOI: 10.1063/1.4824108.
- [Sut93] S P Sutera. “The History of Poiseuille’s Law”. In: *Annu. Rev. Fluid Mech.* 25.1 (1993), pp. 1–20.

- [Suz+08] Shunsuke Suzuki et al. “Sliding Behavior of Water Droplets on Line-Patterned Hydrophobic Surfaces”. In: *Applied Surface Science* 254.6 (Jan. 2008), pp. 1797–1805. ISSN: 0169-4332. DOI: [10.1016/j.apsusc.2007.07.171](https://doi.org/10.1016/j.apsusc.2007.07.171).
- [SWB04] Jeanman Sur, Thomas P. Witelski, and Robert P. Behringer. “Steady-Profile Fingering Flows in Marangoni Driven Thin Films”. In: *Phys. Rev. Lett.* 93.24 (Dec. 2004), p. 247803. DOI: [10.1103/PhysRevLett.93.247803](https://doi.org/10.1103/PhysRevLett.93.247803).
- [Swi+96] Michael R. Swift et al. “Lattice Boltzmann Simulations of Liquid-Gas and Binary Fluid Systems”. In: *Phys. Rev. E* 54.5 (Nov. 1996), pp. 5041–5052. DOI: [10.1103/PhysRevE.54.5041](https://doi.org/10.1103/PhysRevE.54.5041).
- [SWK20] Fabian Schaller, Jenny Wagner, and Sebastian Kapfer. “Papaya2: 2D Irreducible Minkowski Tensor Computation”. In: *JOSS* 5.54 (Oct. 2020), p. 2538. ISSN: 2475-9066. DOI: [10.21105/joss.02538](https://doi.org/10.21105/joss.02538).
- [SYC06] Xiaowen Shan, Xue-Feng Yuan, and Hudong Chen. “Kinetic Theory Representation of Hydrodynamics: A Way beyond the Navier–Stokes Equation”. In: *J. Fluid Mech.* 550 (Mar. 2006), pp. 413–441. ISSN: 1469-7645, 0022-1120. DOI: [10.1017/S0022112005008153](https://doi.org/10.1017/S0022112005008153).
- [Sze10] Andras Z. Szeri. *Fluid Film Lubrication*. Cambridge University Press, Dec. 2010. ISBN: 978-1-139-49519-6.
- [Tan79] L. H. Tanner. “The Spreading of Silicone Oil Drops on Horizontal Surfaces”. In: *J. Phys. D: Appl. Phys.* 12.9 (Sept. 1979), p. 1473. ISSN: 0022-3727. DOI: [10.1088/0022-3727/12/9/009](https://doi.org/10.1088/0022-3727/12/9/009).
- [Tan92] W. Y. Tan. *Shallow Water Hydrodynamics: Mathematical Theory and Numerical Solution for a Two-dimensional System of Shallow-water Equations*. Elsevier, Aug. 1992. ISBN: 978-0-08-087093-9.
- [Tay50] Geoffrey Ingram Taylor. “The Instability of Liquid Surfaces When Accelerated in a Direction Perpendicular to Their Planes. I”. In: *Proc. R. Soc. Lond. Ser. Math. Phys. Sci.* 201.1065 (Jan. 1950), pp. 192–196. DOI: [10.1098/rspa.1950.0052](https://doi.org/10.1098/rspa.1950.0052). (Visited on 08/10/2023).
- [TE84] P. Tarazona and R. Evans. “A Simple Density Functional Theory for Inhomogeneous Liquids”. In: *Mol. Phys.* 52.4 (July 1984), pp. 847–857. ISSN: 0026-8976. DOI: [10.1080/00268978400101601](https://doi.org/10.1080/00268978400101601).
- [TH20] Uwe Thiele and Simon Hartmann. “Gradient Dynamics Model for Drops Spreading on Polymer Brushes”. In: *Eur. Phys. J. Spec. Top.* 229.10 (Sept. 2020), pp. 1819–1832. ISSN: 1951-6401. DOI: [10.1140/epjst/e2020-900231-2](https://doi.org/10.1140/epjst/e2020-900231-2).
- [Tha+13] Sumesh P. Thampi et al. “Isotropic Discrete Laplacian Operators from Lattice Hydrodynamics”. In: *Journal of Computational Physics* 234 (Feb. 2013), pp. 1–7. ISSN: 0021-9991. DOI: [10.1016/j.jcp.2012.07.037](https://doi.org/10.1016/j.jcp.2012.07.037).

- [Thi14] Uwe Thiele. “Patterned Deposition at Moving Contact Lines”. In: *Advances in Colloid and Interface Science*. Manuel G. Velarde 206 (Apr. 2014), pp. 399–413. ISSN: 0001-8686. DOI: 10.1016/j.cis.2013.11.002.
- [TR93] Roumen Tsekov and Eli Ruckenstein. “Effect of Thermal Fluctuations on the Stability of Draining Thin Films”. In: *Langmuir* 9.11 (Nov. 1993), pp. 3264–3269. ISSN: 0743-7463, 1520-5827. DOI: 10.1021/la00035a082.
- [TSB07] Guido Thömmes, Mohammed Seaïd, and Mapundi K. Banda. “Lattice Boltzmann Methods for Shallow Water Flow Applications”. In: *Int. J. Numer. Methods Fluids* 55.7 (2007), pp. 673–692. ISSN: 1097-0363. DOI: 10.1002/fld.1489.
- [TT09] Kevin R. Tubbs and Frank T. -C. Tsai. “Multilayer Shallow Water Flow Using Lattice Boltzmann Method with High Performance Computing”. In: *Advances in Water Resources* 32.12 (Dec. 2009), pp. 1767–1776. ISSN: 0309-1708. DOI: 10.1016/j.advwatres.2009.09.008.
- [TTS87] GARY F. TELETZKE, H. TED DAVIS, and L.E. SCRIVEN. “How Liquids Spread on Solids”. In: *Chem. Eng. Commun.* 55.1-6 (May 1987), pp. 41–82. ISSN: 0098-6445. DOI: 10.1080/00986448708911919.
- [Uta+07] A. S. Utada et al. “Dripping, Jetting, Drops, and Wetting: The Magic of Microfluidics”. In: *MRS Bull.* 32.9 (Sept. 2007), pp. 702–708. ISSN: 1938-1425, 0883-7694. DOI: 10.1557/mrs2007.145.
- [V41] Derjaguin B. V. “Acta Physicochim”. In: *USSR* 14 (1941).
- [van+10] Pham van Thang et al. “Study of the 1D Lattice Boltzmann Shallow Water Equation and Its Coupling to Build a Canal Network”. In: *Journal of Computational Physics* 229.19 (Sept. 2010), pp. 7373–7400. ISSN: 0021-9991. DOI: 10.1016/j.jcp.2010.06.022.
- [VCG88] Carel J. Van Oss, Manoj K. Chaudhury, and Robert J. Good. “Interfacial Lifshitz-van Der Waals and Polar Interactions in Macroscopic Systems”. In: *Chem. Rev.* 88.6 (Sept. 1988), pp. 927–941. ISSN: 0009-2665, 1520-6890. DOI: 10.1021/cr00088a006.
- [Ver] E J W Verwey. “Theory of the Stability of Lyophobic Colloids.” In: () .
- [vH89] Frank van Swol and J. R. Henderson. “Wetting and Drying Transitions at a Fluid-Wall Interface: Density-functional Theory versus Computer Simulation”. In: *Phys. Rev. A* 40.5 (Sept. 1989), pp. 2567–2578. DOI: 10.1103/PhysRevA.40.2567.
- [Vie+12] Jorge A. Vieyra Salas et al. “Active Control of Evaporative Solution Deposition by Modulated Infrared Illumination”. In: *J. Phys. Chem. C* 116.22 (June 2012), pp. 12038–12047. ISSN: 1932-7447. DOI: 10.1021/jp301092y.

- [VO68] A. Vrij and J. Th. G. Overbeek. “Rupture of Thin Liquid Films Due to Spontaneous Fluctuations in Thickness”. In: *J. Am. Chem. Soc.* 90.12 (June 1968), pp. 3074–3078. ISSN: 0002-7863, 1520-5126. DOI: 10.1021/ja01014a015.
- [W01] Kutta W. “Beitrag Zur Naherungsweisen Integration Totaler Differentialgleichungen”. In: *Z. Math. Phys.* 46 (1901), pp. 435–453.
- [Wan+15] Bing-Bing Wang et al. “Molecular Dynamics Simulations on Coalescence and Non-coalescence of Conducting Droplets”. In: *Langmuir* 31.27 (July 2015), pp. 7457–7462. ISSN: 0743-7463. DOI: 10.1021/acs.langmuir.5b01574. (Visited on 07/27/2023).
- [WBS08] Gene Whyman, Edward Bormashenko, and Tamir Stein. “The Rigorous Derivation of Young, Cassie–Baxter and Wenzel Equations and the Analysis of the Contact Angle Hysteresis Phenomenon”. In: *Chemical Physics Letters* 450.4 (Jan. 2008), pp. 355–359. ISSN: 0009-2614. DOI: 10.1016/j.cplett.2007.11.033.
- [WD82] Malcolm B Williams and Stephen H Davis. “Nonlinear Theory of Film Rupture”. In: *J. Colloid Interface Sci.* 90.1 (Nov. 1982), pp. 220–228. ISSN: 0021-9797. DOI: 10.1016/0021-9797(82)90415-5.
- [Wed+14] H. M. J. M. Wedershoven et al. “Infrared Laser Induced Rupture of Thin Liquid Films on Stationary Substrates”. In: *Appl. Phys. Lett.* 104.5 (Feb. 2014), p. 054101. ISSN: 0003-6951. DOI: 10.1063/1.4863318.
- [Wen+00] Jian-Gang Weng et al. “Molecular Dynamics Investigation of Thickness Effect on Liquid Films”. In: *J. Chem. Phys.* 113.14 (Oct. 2000), pp. 5917–5923. ISSN: 0021-9606. DOI: 10.1063/1.1290698.
- [Wij10] Herman Wijshoff. “The Dynamics of the Piezo Inkjet Printhead Operation”. In: *Physics Reports* 491.4 (June 2010), pp. 77–177. ISSN: 0370-1573. DOI: 10.1016/j.physrep.2010.03.003.
- [Wil+17] Markus Wilczek et al. “Sliding Drops: Ensemble Statistics from Single Drop Bifurcations”. In: *Phys. Rev. Lett.* 119.20 (Nov. 2017), p. 204501. DOI: 10.1103/PhysRevLett.119.204501.
- [Wil+92] David L. Williamson et al. “A Standard Test Set for Numerical Approximations to the Shallow Water Equations in Spherical Geometry”. In: *Journal of Computational Physics* 102.1 (Sept. 1992), pp. 211–224. ISSN: 0021-9991. DOI: 10.1016/S0021-9991(05)80016-6.
- [Wol04] Dieter A. Wolf-Gladrow. *Lattice-Gas Cellular Automata and Lattice Boltzmann Models: An Introduction*. Springer, Oct. 2004. ISBN: 978-3-540-46586-7.

- [Won+20] William S. Y. Wong et al. “Microdroplet Contaminants: When and Why Superamphiphobic Surfaces Are Not Self-Cleaning”. In: *ACS Nano* 14.4 (Apr. 2020), pp. 3836–3846. ISSN: 1936-0851. DOI: 10.1021/acsnano.9b08211.
- [WP96] Jörg R. Weimar and Jean Pierre Boon. “Nonlinear Reactions Adveected by a Flow”. In: *Physica A: Statistical Mechanics and its Applications. Dynamics of Complex Systems* 224.1 (Feb. 1996), pp. 207–215. ISSN: 0378-4371. DOI: 10.1016/0378-4371(95)00355-X.
- [WR11] J. Watts and N. Robertson. “Burnout in University Teaching Staff: A Systematic Literature Review”. In: *Educ. Res.* 53.1 (Mar. 2011), pp. 33–50. ISSN: 0013-1881. DOI: 10.1080/00131881.2011.552235.
- [WSJ07] Shutao Wang, Yanlin Song, and Lei Jiang. “Photoresponsive Surfaces with Controllable Wettability”. In: *Journal of Photochemistry and Photobiology C: Photochemistry Reviews* 8.1 (Mar. 2007), pp. 18–29. ISSN: 1389-5567. DOI: 10.1016/j.jphotochemrev.2007.03.001.
- [Wu+20] Yanchen Wu et al. “How Do Chemical Patterns Affect Equilibrium Droplet Shapes?” In: *Soft Matter* 16.26 (2020), pp. 6115–6127. DOI: 10.1039/DOSM00196A.
- [XH10] Bingwei Xin and Jingcheng Hao. “Reversibly Switchable Wettability”. In: *Chem. Soc. Rev.* 39.2 (2010), pp. 769–782. DOI: 10.1039/B913622C.
- [Xie+98] R. Xie et al. “Spinodal Dewetting of Thin Polymer Films”. In: *Phys. Rev. Lett.* 81.6 (Aug. 1998), pp. 1251–1254. DOI: 10.1103/PhysRevLett.81.1251.
- [Xu99] Kun Xu. “UNSPLITTING BGK-TYPE SCHEMES FOR THE SHALLOW WATER EQUATIONS”. In: *Int. J. Mod. Phys. C* (Apr. 1999). DOI: 10.1142/S0129183199000395. (Visited on 08/07/2023).
- [YO86] Victor Yakhot and Steven A. Orszag. “Renormalization Group Analysis of Turbulence. I. Basic Theory”. In: *J Sci Comput* 1.1 (Mar. 1986), pp. 3–51. ISSN: 1573-7691. DOI: 10.1007/BF01061452.
- [Yon+18] Huaisong Yong et al. “Cononsolvency Transition of Polymer Brushes: A Combined Experimental and Theoretical Study”. In: *Materials* 11.6 (June 2018), p. 991. ISSN: 1996-1944. DOI: 10.3390/ma11060991.
- [You05] Thomas Young. “III. An Essay on the Cohesion of Fluids”. In: *Philos. Trans. R. Soc. Lond.* 95 (Jan. 1805), pp. 65–87. DOI: 10.1098/rstl.1805.0005.
- [Zha+15] Lianbin Zhang et al. “Inkjet Printing for Direct Micropatterning of a Superhydrophobic Surface: Toward Biomimetic Fog Harvesting Surfaces”. In: *J. Mater. Chem. A* 3.6 (Jan. 2015), pp. 2844–2852. ISSN: 2050-7496. DOI: 10.1039/C4TA05862C.

- [Zho04] Jian Guo Zhou. *Lattice Boltzmann Methods for Shallow Water Flows*. Berlin, Heidelberg: Springer, 2004. ISBN: 978-3-642-07393-9. DOI: 10.1007/978-3-662-08276-8.
- [Zit+19] S. Zitz et al. “Lattice Boltzmann Method for Thin-Liquid-Film Hydrodynamics”. In: *Phys. Rev. E* 100.3 (Sept. 2019), p. 033313. DOI: 10.1103/PhysRevE.100.033313.
- [Zit+22] Stefan Zitz et al. “Swalbe.Jl: A Lattice Boltzmann Solver for Thin Film Hydrodynamics”. In: *J. Open Source Softw.* 7.77 (Sept. 2022), p. 4312. ISSN: 2475-9066. DOI: 10.21105/joss.04312.
- [ZL05] Rong Zhang and Xin Kai Li. “Non-Newtonian Effects on Lubricant Thin Film Flows”. In: *J Eng Math* 51.1 (Jan. 2005), pp. 1–13. ISSN: 1573-2703. DOI: 10.1007/s10665-004-1342-z.
- [ZSH21] S. Zitz, A. Scagliarini, and J. Harting. “Lattice Boltzmann Simulations of Stochastic Thin Film Dewetting”. In: *Phys. Rev. E* 104.3 (Sept. 2021), p. 034801. DOI: 10.1103/PhysRevE.104.034801.
- [ZSL19] Yixin Zhang, James E. Sprittles, and Duncan A. Lockerby. “Molecular Simulation of Thin Liquid Films: Thermal Fluctuations and Instability”. In: *Phys. Rev. E* 100.2 (Aug. 2019), p. 023108. DOI: 10.1103/PhysRevE.100.023108.
- [ZSL20] Yixin Zhang, James E. Sprittles, and Duncan A. Lockerby. “Nanoscale Thin-Film Flows with Thermal Fluctuations and Slip”. In: *Phys. Rev. E* 102.5 (Nov. 2020), p. 053105. DOI: 10.1103/PhysRevE.102.053105.

Acknowledgments

“Doing a PhD is not a sprint but a marathon”, is an often written quote. I did not hear that one personally, but I do understand it. Coming with a master’s degree and having an idealistic view of science and academia is motivating and encouraging. But this initial emotional rush quite naturally fades out with time. To keep the train on track and finally write this thesis I have to thank many people that help during this episode of my life.

I’d like to start by thanking Dr. Andrea Scagliarini. He was the initiator of the project that led to my thesis. Even though he was only physically around for the first month of my PhD he kept helping me out for the full duration. Needless to say that not even Corona and the therefore resulting home office period did not stop our collaboration. His deep understanding of hydrodynamics and physics in general was always very insightful. I am especially thankful for his positive review of my HPC-europa proposal. Due to this I had a fruitful and productive research stay in Rome.

Of course, I could only reach this point due to constant support of my supervisor Prof. Dr. Jens Harting. He was brave enough to hire someone that had little to no prior knowledge with fluid dynamics and scientific computing. While it was not always easy, because different characters see different problems I thank him wholeheartedly for his supervision. He offered me all the freedom to learn new things and being creative with computational experiments. His trust allowed me to visit and present my work at several international conferences and let me engage with the community.

As my mood was not always the best during this time I have to thank the one person who always stood with me, Leonie. Not only had she to listen to my rants about work, but she also endured my negative attitude during setbacks. She was always supportive during this time and kept me functional. Due to her I got a very different perspective on problem solving and acquired a little taste for art.

I also thank my whole family who supported me not only for the last few years but during my whole life. For the longest time in my life I could ask my parents for help and without hesitation they would have helped me. That changed with my relocation to Nürnberg as there was *suddenly* distance between us. They tried to keep up with me and my life, with more and less success. On the same note I thank both my grandparents for being in my life. Both although very different care deeply for me and I am very lucky that they are still around. Supporting me with care packages I received from time to time, which were always filled with delicious goods.

Thanks to my friend, Clemens, and my brother Thomas who although in different country I am in contact on an almost daily base. The same holds for my colleagues and friends that I made during my time in Nürnberg. To name just a few Nico, David,

Bibliography

Daniel, Nadiia, Alex, Mathias, Marcello, Björn, Oliver, Thomas and Othmane you made the office always a nice place to be. One person that deserves his own sentence is Manuel our former IT admin and live saver. Thanks to his engaging lectures on coding and scientific computing as well as version control I quickly caught up with building my own usable software.

There were so many people who supported me on my journey and I am very sorry for those who I have not mentioned here. I could not have done this alone and I know that. Therefore I am in dept to so many people. Thank you very much Leonie, family, friends, Andrea, Jens and many more.